UAB
Universitat Autònoma de Barcelona

Searches for new neutral and charged scalars with multiple top and bottom quarks in Run 2pp collisions at 13 TeV with the ATLAS detector

Adrian Salvador Salas

Universitat Autònoma de Barcelona
Facultat de Ciències
Departament de Física

Searches for new neutral and charged scalars with multiple top and bottom quarks in Run 2 pp collisions at 13 TeV with the ATLAS detector

Ph.D. dissertation

Adrian Salvador Salas

Thesis director
Immaculada Riu Dachs
Institut de Física d'Altes Energies
Universitat Autònoma de Barcelona
Edifici Cn E-08193 Bellaterra (Barcelona)

Thesis tutor
Maria Pilar Casado Lechuga
Institut de Física d'Altes Energies
Universitat Autònoma de Barcelona
Edifici Cn E-08193 Bellaterra (Barcelona)

March 2023

Somewhere, something incredible is waiting to be known.

– Carl Sagan

Abstract

This thesis presents two searches for new scalars using the 139 fb^{-1} proton-proton collision data at a center-of-mass energy of 13 TeV collected by the ATLAS detector at the CERN Large Hadron Collider (LHC) during Run 2. Both searches look for multi-jet final states with one electron or muon and events are categorised according to the multiplicity of jets and how likely these are to have originated from the hadronisation of a bottom quark. Parameterised feed-forward neural networks are used to discriminate between signal and background and included in maximum-likelihood fits to the data for the various mass hypotheses.

The first search is dedicated to charged Higgs bosons, predicted by various theories Beyond the Standard Model and motivated by the inadequacy of the Standard Model to explain some experimental phenomena. The work focuses on heavy charged Higgs bosons, heavier than the top quark, decaying to a pair of top and bottom quarks, $H^{\pm} \to tb$. They are assumed to be produced in association with a top and a bottom quarks, $pp \to tbH^{\pm}$. The search is performed in the mass range between 200 and 2000 GeV. No significant excess of events above the expected Standard Model background is observed, hence upper limits are set for the cross-section of the charged Higgs boson production times the branching fraction of its decay. Results are interpreted in the context of hMSSM, various Mh125 scenarios and 2HDM+a.

The second search targets flavour-changing neutral-currents decays of top quarks into a new scalar decaying into a pair of bottom quarks, $t \to u/cX(bb)$. This novel study probes for a scalar on a broad mass range between 20 and 160 GeV and branching ratios below 10^{-3}. In the case of the Higgs boson, branching ratios for $t \to u/cH$ are predicted within the Standard Model to be of $\mathcal{O}(10^{-17})/\mathcal{O}(10^{-15})$. Several Beyond the Standard Model theoretical models predict new particles and enhanced branching ratios. In particular, simple extensions involve the Froggatt-Nielsen mechanism, which introduces a scalar field with flavour charge, the so-called flavon, featuring flavour violating interactions. As no significant excess is observed, upper limits for both FCNC decays $t \to uX$ and $t \to cX$ are extracted. In addition, limits are set for the process involving the Standard Model Higgs.

Contents

Introduction

The discovery of the Higgs boson in 2012 by ATLAS and CMS [1, 2] is one of the most recent historic milestones in the field of particle physics. CERN hosts the LHC, whose physics program included the hunt for the Higgs boson. After this achievement, all particles predicted by the Standard Model (SM), the theory which describes the fundamental particles and their interactions, have been discovered. Nevertheless, the ATLAS experiment continues to scrutinise the Standard Model of particle physics by analysing the ever-increasing amount of particle collisions delivered by the LHC. There are many phenomena not covered by the current theory and any measurement that deviates from the predictions or reveals a hint of a new particle could pave the way for new discoveries in particle physics.

The theory of the Standard Model has successfully guided the experiments with the prediction of particles and their interactions. However, the theory does not address gravity, the non-zero neutrino masses, dark matter, or other phenomena. One significant concern with the Standard Model is the hierarchy problem, which refers to the apparent unnaturalness of the Higgs mass being at the electroweak scale despite the inexistence of a constraint on its value within the theory. One possible theoretical solution involves expanding the Standard Model to include additional scalar particles. In Two Higgs Doublet Models (2HDM), the Higgs sector is built with one extra doublet and a total of five scalars are predicted instead of a single Higgs boson, and includes Higgs bosons with electrical charge. Another feature of the Standard Model is known as the so-called flavour problem, as fermions can be grouped in three families with different mixing patterns, and this is seen as an arbitrary choice. The flavour problem can be addressed by introducing a new particle called the flavon, which arises from a broken flavour symmetry and introduces flavour-violating interactions. Flavour-changing neutral current (FCNC) interactions are heavily suppressed in the Standard Model and fall below the sensitivity of current experiments. These interactions are hence very sensitive to new physics as they can be enhanced with new interactions outside the Standard Model.

This thesis presents a direct search for charged Higgs bosons with masses greater than the top quark and a direct search for neutral scalars with masses lighter than the top quark. The charged Higgs process is searched in the $200 - 2000$ GeV mass range, produced in association with top and bottom quarks and decaying into a top-bottom pair. Limits on the production of charged Higgs bosons in the same channel have been previously obtained by ATLAS with only the data from 2015 and 2016 in the same mass range [3], and more recently by CMS in the $200 - 3000$ GeV mass range using the full Run-2, setting upper limits at 95% confidence level on the production cross-section of $2.9 - 0.070$ pb and $9.6 - 0.01$ pb, respectively. The neutral scalar is searched for in the $20 - 160$ GeV mass range, produced in a FCNC decay of a top quark involving a c- or a u-quark, and finally decaying into a pair of b-quarks. This is the first time either ATLAS or CMS perform this measurement,

however both experiments have searched for the top FCNC decay into the SM Higgs, $t \to qH$ with q being either a c- or u-quark. The most recent analysis from ATLAS being in the $H \to \tau\tau$ channel [4] while the CMS results with 137 fb^{-1} data combines several channels and sets limits to B($t \to uH$)< 0.079 and B($t \to cH$)< 0.094 [5].

Both searches in this thesis use the full Run-2 proton-proton collisions collected by the ATLAS experiment from 2015 to 2018 at a center-of-mass energy of 13 TeV. Events are required to have either one reconstructed electron or muon and multiple jets, including those originated from the hadronisation of a bottom quark. Results are obtained by performing binned maximum-likelihood fits of the different simulated signal samples and SM backgrounds to the recorded data. The fits are performed using discriminants obtained by combining several kinematic variables through parameterised feed-forward neural networks, developed to optimise the sensitivity to separate signal and background events.

This document is structured into three main parts: the first part describes the theoretical and experimental setup, while the second and third parts include the $H^\pm \to tb$ and $t \to qX$ analyses, respectively, both with a detailed description of the strategy and their results. Chapter 1 focuses on the Standard Model and the models that motivate the searches. Chapter 2 provides an overview of the LHC and the ATLAS experiment. Chapters 3 and 4 present the main aspects of the simulation and reconstruction of simulated proton-proton collisions, while Chapter 5 presents the machine learning techniques and statistical tools used in the different analyses. Chapter 6 introduces and explains the details of the $H^\pm \to tb$, with the results summarised in Chapter 7. Similarly, the details and results of the $t \to qX$ search are discussed in Chapters 8 and 9. A summary and conclusions of the work are provided in Chapter 10.

Theoretical and experimental setup

The Standard Model of Particle Physics and beyond

1

The Standard Model (SM) of particle physics [6–8] is the theoretical framework that so far best describes subatomic particles and their interactions. It is a Quantum Field Theory (QFT) and since its initial development in the 1960s, the model has been overwhelmingly successful, guiding many experimental achievements including the discovery of the top quark [9, 10] in 1995 and the Higgs boson at the LH1C in 2012 [1, 2]. Despite its success, there are known phenomena not accounted for by the model and other questions which clearly point to the need of a new theory.

This chapter starts with an overview of the SM, building it with its mathematical formalism, and presenting a summary of the particle content and their interactions. Then, it continues with a summary of the current success of the theory, as well as its shortcomings and alternative models. The focus is given to models that include charged Higgs bosons or top FCNC interactions involving a scalar.

Throughout this dissertation, natural units are used: the speed of light and the reduced Planck constant are set to unity ($c = \hbar = 1$), electric charges are expressed in units of the electron electric charge ($-e$) and masses are expressed in terms of energy (eV). Throughout this chapter's theoretical developments, the Einstein summation convention is used by default.

1.1 The Standard Model of Particle Physics

From the mathematical point of view, the SM is a renormalisable non-abelian gauge QFT based on the symmetry group,

$$SU(3)_C \otimes SU(2)_L \otimes U(1)_Y \tag{1.1}$$

where $SU(3)_C$ is the group described by Quantum Chromodynamics (QCD) [11] that represents the strong interactions of colored quarks and gluons (strong force), while $SU(2)_L \times U(1)_Y$ is the inclusive representation of both electromagnetic (EM) and weak interactions described by the ElectroWeak (EW) theory [6, 7, 12]. The SM describes all the interactions between elementary particles except gravity, for which no renormalisable QFT has been formulated so far. The following sections introduce the particles of the SM and the theories that describe their interactions.

1.1.1 Particle content of the Standard Model

In the SM, elementary particles are described as excitations of quantum fields. There are two main classes of particles within the theory: *fermions* and *bosons*. The main difference between the two is the spin: fermions have half-integer spin and therefore obey the Pauli exclusion principle [13], while bosons have integer spin.

Fermions

Fermions can be divided further into two categories: quarks and leptons, based on their interactions, or their charges. Both types manifest in EW interactions, having a weak isospin $T_3 = \pm 1/2$ while only the quarks experience the strong interaction. Quarks have a fractional electric charge $|Q| = 2/3$ or $1/3$, and the *colour* charge. The last one is the charge associated to the strong interaction and its values are denoted as *red*, *green* and *blue*. Table 1.1 presents a summary of the fundamental fermions and their characteristics.

Table 1.1: Table of the different quarks and leptons of the SM grouped in families with their mass and electric charge according to the Particle Data Group [14]. The uncertainties on the electron and the muon masses are below 10^{-10} and 10^{-6} MeV, respectively. The anti-matter states are not shown.

Generation	Name	Symbol	Mass	Charge
		Quarks		
1st	Up	u	$2.15^{+0.49}_{-0.26}$ MeV	+2/3
	Down	d	$4.67^{+0.48}_{-0.17}$ MeV	−1/3
2nd	Charm	c	1.27 ± 0.02 GeV	+2/3
	Strange	s	$93.4^{+8.6}_{-3.4}$ MeV	−1/3
3rd	Top	t	172.69 ± 0.30 GeV	+2/3
	Bottom	b	$4.18^{+0.03}_{-0.02}$ GeV	−1/3
		Leptons		
1st	Electron	e^-	0.511 MeV	−1
	Electron neutrino	ν_e	< 1.1 eV 90% CL	0
2nd	Muon	μ^-	0.106 GeV	−1
	Muon neutrino	ν_μ	< 0.19 MeV 90% CL	0
3rd	Tau	τ^-	1776.86 ± 0.12 MeV	−1
	Tau neutrino	ν_τ	< 18.2 MeV 95% CL	0

There is a total of six quark types, named *flavours*, and are split into three generations. The first generation consists in the *up* and the *down* quark, the former with $Q = +2/3$ and $T_3 = +1/2$, while the latter $Q = -1/3$, $T_3 = -1/2$ and a slightly lower mass. The next two generations are copies of the first one with increasing mass, with a pair of an *up*-type quark and a *down*-type quark. The second generation consists in *charm* and *strange* quarks, and the third of *top* and *bottom* quarks. In addition, all the six quark flavours have antimatter states with the same mass, but opposite quantum numbers, as an example, an anti-*up*-type quark has $Q = -2/3$, $T_3 = -1/2$ and can carry anti-*red* colour.

Leptons are also similarly divided into six different types and in three separate generations named *electron* (e), *muon* (μ) and *tau* (τ), also with increasing mass. Each generation contains a lepton with $Q = -1$ and $T_3 = +1/2$ named after its generation, and an associated electrically neutral lepton with $T_3 = -1/2$ named neutrino (ν). The neutrino is assumed to be massless in the formulation of the SM, however the phenomena of neutrino oscillations is experimental proof of these

actually having very small, but non-zero, mass values. This apparent failure of the theory is discussed in Section 1.2.4. As before, the associated antimatter states have the same mass but opposite quantum numbers.

All the stable SM matter in the universe is constituted by the massive particles of the first generations of quarks and leptons, as the heavier versions eventually decay to lighter ones through their disclosed interactions. While it is possible to observe free leptons, quarks exist only in bound states, or hadrons, like the neutron or the proton. This is a feature of the strong interaction called confinement, discussed in Section 1.1.3. Only colour-less bounded states of quarks are observable, and can be built from three quarks with overall half-integer spin, named baryons, or by two quarks with integer spin, named mesons.

In the context of particle physics, the formulation of the classical Lagrangian, $\mathcal{L}$, is used to describe physics systems. A generic free fermion field ψ with mass m, can be described by the Dirac Lagrangian,

$$\mathcal{L} = \bar{\psi}(i\gamma^\mu \partial_\mu - m)\psi, \tag{1.2}$$

where γ^μ are Dirac matrices and ∂_μ is the four-momentum derivative.

Bosons

Particles with integer spin are referred to as bosons. The bosonic sector with spin-1 gauge fields are force carriers that naturally follow from imposing the requirement of local gauge invariance on Equation 1.2 under symmetry groups, in this case Equation 1.1. In Section 1.1.2 the nature and origins of the gauge bosons will be detailed. Table 1.2 presents a summary of the bosons of the SM.

Table 1.2: Table of the different bosons of the SM with their mass and electric charge according to the Particle Data Group [14]. The Higgs boson has spin 0 and does not mediate an interaction, while the rest have spin 1 and mediate an interaction.

Name	Mass [GeV]	Charge	Interaction
Photon (γ)	0	0	Electromagnetic
Z	91.1876 ± 0.0021 GeV	0	Weak
$W^\pm$	80.377 ± 0.012 GeV	±1	
Gluon (g)	0	0	Strong
Higgs	125.25 ± 0.17 GeV	0	-

In summary, the photon (γ) is the carrier of the electromagnetic force, being a massless and electrically neutral particle. The weak force carriers are the W^+, W^- and Z bosons, all massive with the Z boson being electrically neutral and the $W^\pm$ with either $Q = \pm 1$. Gluons (g) are the strong force carriers which are massless and with no electric charge. Instead, there are eight different gluons representing each possible colour exchange.

The SM also includes a neutral spin-0 particle, or *scalar*, the Higgs boson. The

Higgs field is responsible for all SM particles acquiring mass through the Higgs mechanism, as described in Section 1.1.5. The kinematics of a generic scalar ϕ with mass m, is described by the Klein-Gordon Lagrangian,

$$\mathcal{L} = \frac{1}{2}\partial^\mu\phi\partial_\mu\phi - m^2\phi^2 \tag{1.3}$$

Charged scalars can be described instead through a complex field and the expression of the Lagrangian is slightly modified,

$$\mathcal{L} = \partial^\mu\phi\partial_\mu\phi^* - m^2\phi\phi^* \tag{1.4}$$

Vector fields A^μ, which represent spin-1 bosons, are described by the Proca Lagrangian,

$$\mathcal{L} = -\frac{1}{4}F^{\mu\nu}F_{\mu\nu} + \frac{1}{2}m^2A^\mu A_\mu \tag{1.5}$$

with $F^{\mu\nu} = \partial^\mu A_\nu - \partial^\nu A_\mu$ the field strength tensor. In the case of massless particles, the previous expression with $m = 0$ is known as the Maxwell Lagrangian.

1.1.2 Interactions of the Standard Model

The Lagrangian of the SM is defined to be locally invariant to the Equation 1.1 symmetry group, condition that generates and defines the interactions of the corresponding particles as representations of the symmetry transformations.

For a generic Lagrangian, the physical system can have symmetries, so its Lagrangian is invariant under different types of transformations. These transformations can be either time-space independent, called global transformations, or dependent, called gauge or local transformations. Any invariant transformation of a Lagrangian describes a physical system which conserves a physical quantity, as described by the Noether theorem [15]. Then, the interactions are introduced in the Lagrangian as additional terms by promoting an already existing global symmetry, ϕ, of the Lagrangian to a local gauge symmetry, $\phi(x)$. The physical motivation behind introducing gauge symmetries is to be able to describe vector bosons in QFT. The procedure expands the theory with additional fields that mediate the resulting interactions, which properties depend on the characteristics of the symmetry group.

An example of the process is shown to afterwards derive the SM interactions of the strong and electroweak sectors.

Gauging a symmetry to interaction

A general global transformation θ which acts upon the field ψ is described as,

$$\psi \rightarrow e^{ig\theta^a T^a}\psi \tag{1.6}$$

with g the coupling constant and T^a the generators of the Lie group associated to the transformation (like $SU(n)$ or $U(n)$), with a ranging from 1 to $n^2 - 1$, for $n > 1$, the corresponding number of the Lie algebra. The generators can be characterised by their commutation relation,

$$[T^a, T^b] = if^{abc}T^c \tag{1.7}$$

where f^{abc} are the structure constants of the group. Following Noether's theorem, there are as many conserved quantities as generators of the Lagrangian's symmetries. As an example, it is straightforward to see that a Lagrangian like Equation 1.2 is invariant to a $U(1)$ transformation where θ is just a constant and hence, a constant phase change. One can obtain the current, j^μ,

$$j^\mu = \bar{\psi}\gamma^\mu\psi \tag{1.8}$$

that is conserved, $\partial_\mu j^\mu = 0$, with the conserved charge,

$$Q = \int \mathrm{d}^3x j^0 = \int \mathrm{d}^3x \psi^\dagger\psi \tag{1.9}$$

With some algebra and introducing solutions in momentum space, ψ can be interpreted as annihilating a fermion and creating an anti-fermion (the other way around with $\psi^\dagger$) in the Fock space and then, the product becomes the difference of the number of fermion and anti-fermion leading to the conservation of the fermion number.

Promoting the global symmetry to a local symmetry is done by introducing locality in the θ transformation, $\theta \to \theta(x)$, which introduces new $\partial_\mu\theta$ terms in the Lagrangian. A way to counter the new terms and, hence, keep the Lagrangian invariant, is to introduce gauge vector fields A^a_μ, following Yang-Mills theory [16]. In the most generalised approach, there have to be as many A^a_μ as generators of the symmetry, that transform as,

$$A^a_\mu \to A^a_\mu + \partial_\mu\theta^a + gf^{abc}A^b_\mu\theta^c \tag{1.10}$$

Note that the last term proportional to the structure constant is relating the gauge field to the conserved symmetry charge. The next step is to replace the standard derivative in the Lagrangian by the covariant derivative,

$$D_\mu \equiv \partial_\mu - igT^aA^a_\mu \tag{1.11}$$

The final ingredient is to complete the Lagrangian with the the kinematic Lagrangian for the massless vector fields, the Maxwell Lagrangian from Equation 1.5 with a slightly different field strength tensor,

$$F^a_{\mu\nu} = \partial_\mu A^a_\nu - \partial_\nu A^a_\mu + gf^{abc}A^b_\mu A^c_\nu \tag{1.12}$$

The last term is present only for non-abelian symmetry groups, since it is proportional to the structure constants, and has huge consequences in the resulting interactions as discussed in the next section. Another remark is that the gauge fields have to be massless, as a mass term proportional to $A^c_\mu A^{\mu c}$ is not gauge invariant.

As an example, the promotion of the global $U(1)$ symmetry seen in Equation 1.2

results in the upgraded Lagrangian,

$$\begin{aligned} \mathcal{L} &= \bar{\psi}(i\gamma^\mu D_\mu - m)\psi - \frac{1}{4}F_{\mu\nu}F^{\mu\nu} \\ D_\mu &\equiv \partial_\mu - igA_\mu \\ F_{\mu\nu} &\equiv \partial_\mu A_\nu - \partial_\nu A_\mu \end{aligned} \tag{1.13}$$

introducing just one massless gauge field that interacts with the field ψ. The interaction term between the two fields is $g\bar{\psi}\gamma^\mu A_\mu \psi$, hidden in the covariant derivative definition and proportional to the coupling constant g.

The Lagrangian of the SM is built from imposing local invariance under $SU(3)_C$ transformations, which leads to strong interactions; and $SU(2)_L \times U(1)_Y$ transformations, which brings EW interactions,

$$\mathcal{L}_{SM} = \mathcal{L}_{QCD} + \mathcal{L}_{EW} \tag{1.14}$$

After this introduction on field theory, the theories of the two orthogonal sectors can now be described and then, the mechanism to introduce mass terms in the Lagrangian, the spontaneous symmetry breaking.

1.1.3 Quantum Chromodynamics

The quantum field theory that describes quarks, gluons and their interactions is named *quantum chronodynamics*. Each quark has an internal degree of freedom, the colour charge, and it is defined by a triplet of fields,

$$q = \begin{pmatrix} q_{\text{red}} \\ q_{\text{blue}} \\ q_{\text{green}} \end{pmatrix} \tag{1.15}$$

where each of the components is a Dirac spinor associated to the corresponding colour state (red, blue and green). In addition, there are a total of six quarks, so the fields are labelled as $q_{f\alpha}$ with f indicating the quark flavour ($f = u, d, c, s, t, b$) and α the colour. Note that there is an anti-quark of each flavour carrying an anti-colour charge.

The theory is based on the $SU(3)$ symmetry group, whose algebra is characterised by the non-abelian commutation relation from Equation 1.7 with a total of eight generators, T^a. The generators can be written as $T^a = \lambda^a/2$ where λ^a denote the Gell-Mann matrices [17]. Because of the eight generators, the interaction is mediated by a total of eight gauge bosons, called gluons G^a_μ. There are different matrix representation for the colour states of the gluons, following the Gell-Mann matrices, taking,

$$\lambda^1 = \begin{pmatrix} 0 & 1 & 0 \\ 1 & 0 & 0 \\ 0 & 0 & 0 \end{pmatrix} \tag{1.16}$$

and applying it to a general quark triplet like Equation 1.15, it can be seen that the transformation switches the red and blue charges. To do so, the gluon has to carry

a colour/anti-colour pair, to be able to "remove" the red charge (r) and "add" the blue charge (b), and the other way around. There are nine possible combinations of colour/anti-colour pairs, which can be used to re-write the λ^1 transformation as,

$$\frac{r\bar{b} + b\bar{r}}{\sqrt{2}} \tag{1.17}$$

known as the first state of the gluon colour octet. The rest of the states are equivalent to the other Gell-Mann matrices and all conserve the three different colour flows.

The QCD Lagrangian can be obtained from modifying the Dirac Lagrangian (Equation 1.2) to achieve gauge invariance under $SU(3)_C$ transformations, following the definitions from Section 1.1.2. The resulting Lagrangian is,

$$\begin{aligned} \mathcal{L}_{QCD} &= i \sum_f \bar{q}_f \gamma^\mu D_\mu q_f - \frac{1}{4} G^a_{\mu\nu} G^{a\ \mu\nu} \\ D_\mu &\equiv \partial_\mu - i g_s T^a G^a_\mu \\ G^a_{\mu\nu} &\equiv \partial_\mu G^a_\nu - \partial_\nu G^a_\mu + g_s f^{abc} G^b_\mu G^c_\nu \end{aligned} \tag{1.18}$$

with g_s being the strong force coupling constant and where the covariant derivative has been introduced with the G^a_μ gluons fields, together with the kinematic term for the gluons, with the gluon tensor $G^a_{\mu\nu}$. As described in Section 1.1.2, gluons are massless because the term in the Lagrangian is not gauge invariant. Notice that the masses of the quarks are also not present, not because it would break the symmetry, but for convention. The masses in the SM come from the electro-weak sector. Another remark is that the addition of a charge conjugation and parity symmetry (CP) violating interaction term is allowed under local gauge invariance, but such an interaction has been experimentally observed to be effectively zero [18].

The possible interactions in the Lagrangian are shown in Figure 1.1, consisting of couplings between quarks and gluons[1], and three- and four-point gluon self-interactions. As foreshadowed in Section 1.1.2, for non-abelian groups the gauge bosons have the self-interacting terms in the tensor.
There are two more important characteristics of this theory: asymptotic freedom and confinement [19, 20]. Asymptotic freedom refers to the fact that at very high energies (in momentum transfer), or short distances, quarks and gluons interact weakly with each other allowing predictions to be obtained using perturbation theory. Confinement is the name given to the impossibility of directly observing quarks, and are only confined in hadrons, which are colourless composite states[2].

The idea is that for high distances, the strong coupling becomes larger, so when the distance between two quarks is increased, the energy of the gluon field is larger, up to the point where a quark/anti-quark pair is created from the vacuum and thus forming a new hadron. These characteristics arise from the non-abelian nature

[1] Equivalent to the interaction obtained from the gauge $U(1)$ symmetry.
[2] Color singlets are quantum states that are invariant under all eight generators of $SU(3)$, and therefore carry vanishing values of all colour conserved charges.

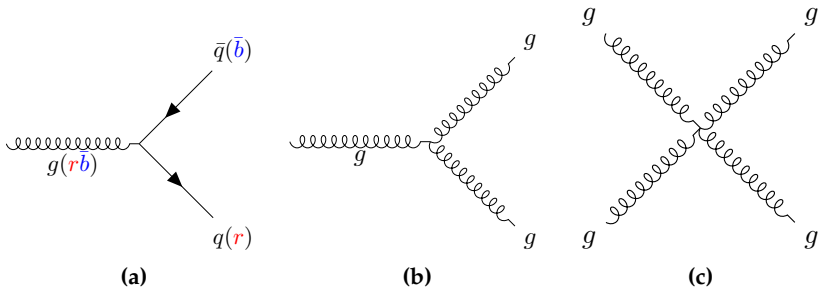

Figure 1.1: Vertices allowed in QCD: (a) quark-gluon coupling, (b) three-point gluon self-coupling, and (c) four-point gluon self-coupling. The color charge is depicted in the the quark-gluon vertex to depict an example of the interaction.

of the symmetry, which prompt the coupling to decrease with the energy of the interaction.

Running coupling

To understand the fact that the couplings can vary with the energy, the topics of QFT renormalisation and regularisation have to be introduced. The quantity known as the matrix amplitude has to be computed for the prediction of physical quantities of a given process. Observables are proportional to the square sum of the amplitude of every possible Feynman diagram that yields the same initial and final particles of the process being predicted. However, the computation in diagrams with loops leads to the integration of all possible four-momentum of the virtual particles involved, which are divergent. Nevertheless, these divergences can be isolated with regularisation techniques, which renders them finite by introducing a parameter Λ such that for a given value of the parameter the divergence is recovered. This allows the computation of any quantity in terms of the *bare* quantities that appear in the Lagrangian, such as masses and couplings, along the regularisation parameter. The other key point is renormalisation, from the idea that the physical quantities measured in experiments (masses and couplings), are different from the bare quantities (masses and couplings that appear in the lagrangian). Therefore, one has the freedom to apply renormalisation conditions which cause the expressions to depend only on the physical quantities if the theory is renormalisable, removing the divergent sources.

As an example, to compute the gluon two-point function, an infinite sum of loop contributions is needed,

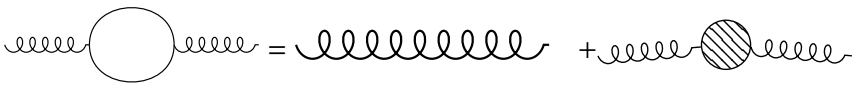

(1.19)

Focusing on the one loop contribution, the result is obtained at first order from three different diagrams,

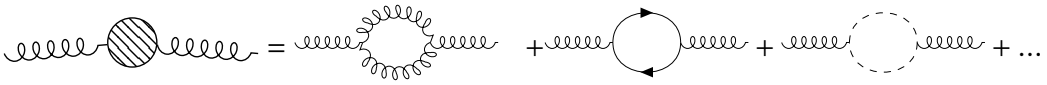

(1.20)

which includes the loop involving gluons, quarks and a third one with a new propagator, the ghost. This propagator is a regularisation artifact to compensate unphysical degrees of freedom[3]. Focusing on the gluon loop contribution,

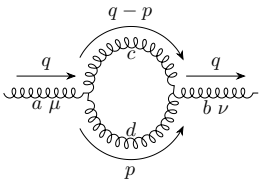

(1.21)

leads to a badly divergent integral in its computation with Feynman rules,

$$\frac{1}{2}g_s^2 f^{acd} f^{bcd} \int \frac{d^4p}{(2\pi)^4} \frac{1}{(q-p)^2 + i\epsilon} \frac{1}{p^2 + i\epsilon} \left[g^{\mu\alpha}(p-2q)^\beta + g^{\alpha\beta}(q-2p)^\mu + g^{\beta\mu}(p+q)^\alpha \right] \left[\delta^\nu_\alpha (p-2q)_\beta + g_{\alpha\beta}(q-2p)^\nu + \delta^\nu_\beta (p+q)_\alpha \right] \tag{1.22}$$

which can be worked around with a regularisation parameter μ,

$$\int \frac{d^4p}{(2\pi)^4} \to \int \frac{d^Dp}{(2\pi)^D} \mu^{2\varepsilon}.$$

and $D = 4 - 2\varepsilon$ with later $\varepsilon \to 0$. After the computation of all main contributions, the divergent term can be summarised as,

$$\frac{g_s^2}{24\pi} \left[11 n_c - 2 n_f \right] \frac{1}{\epsilon} + \mathcal{O}(g_s^4) \tag{1.23}$$

with n_c the number of colours, n_f the number of quark flavours and $\varepsilon \to 0$ the condition to recover the original divergence. Hence the bare coupling constant can be rewritten to account for this divergence, completing the regularisation process for the gluon self-energy.

The final strong coupling constant is commonly given by,

$$\alpha_s(Q^2) = \frac{12\pi}{(11 n_c - 2 n_f) \log \frac{Q^2}{\Lambda^2_{\text{QCD}}}} \tag{1.24}$$

which depends on the energy scale Q at which is evaluated and Λ_{QCD} the infrared cutoff scale which sets the validity of the perturbative regime of QCD. As $n_c = 3$,

[3] There are other methods to avoid the unphysical degrees of freedom, as choosing a physical gauge in the axial direction.

for n_f<16 the coupling constant decreases with the energy scale, the key feature of QCD that causes asymptotic freedom and confinement.

1.1.4 Electroweak theory

The quantum field theory that describes both the electromagnetic and weak interactions is called *electroweak* theory. The theory is based on the $SU(2)_L \otimes U(1)_Y$ symmetry group[4], which is a product that yields a non-abelian group, like $SU(3)_C$, and chiral. It will spawn four mediators, corresponding to the number of generators.

The symmetry spontaneously breaks down through *symmetry breaking* giving rise to the electromagnetic interaction, mediated by the photon, and to the weak interaction, mediated by the Z and $W^{\pm}$ bosons. This process is described by the *EW symmetry breaking* (EWSB), which occurs at ~100 GeV, defined as the EW scale, and after which only the $U(1)_Q$ symmetry is unbroken. The process of the EWSB, and the resulting effects are described in more detail in Section 1.1.5.

The interactions for the EW sector can be obtained following the procedure described in general in Section 1.1.2; already used in Section 1.1.3 for QCD. First, only left-handed fermion fields interact via the weak interaction[5], transforming as doublets under $SU(2)_L$, whereas right-handed fermion fields do not interact weakly and thus transform as singlets,

$$\begin{aligned} \psi_L^i &= \begin{pmatrix} \ell_L^i \\ \nu_L^i \end{pmatrix}, \begin{pmatrix} u_L^i \\ d_L^i \end{pmatrix} \\ \psi_R^i &= \ell_R^i, u_R^i, d_R^i \end{aligned} \tag{1.25}$$

with i corresponding to the number of the generation. Fields with subscripts L/R are left- and right-handed fields that can be defined through the chirality operators P_L and P_R, projecting a generic field into only its left- and right-handed components, respectively,

$$\begin{aligned} \psi_L &= P_L\psi = \frac{1}{2}(1-\gamma_5)\psi \\ \psi_R &= P_R\psi = \frac{1}{2}(1+\gamma_5)\psi \end{aligned} \tag{1.26}$$

with γ_5 defined from the Dirac matrices $\gamma_5 \equiv i\gamma^0\gamma^1\gamma^2\gamma^3$. Notice that there are no right-handed fields associated to the neutrinos. This convention exists to avoid the prediction of right-handed neutrinos, which would not interact with any of the forces described in the SM.

The $SU(2)_L$ group consists of three generators $\hat{T}_i$, which can be written as $\hat{T}_i = \sigma_i/2$ where σ_i denotes the Pauli matrices. Also, the quantum number associated is the weak isospin, T. On the other side, the $U(1)_Y$ group introduces the weak hypercharge

[4] L refers to the left-handed chirality and Y to the weak hypercharge
[5] As a consequence, parity can be violated in weak interactions [21, 22].

quantum number, Y. After EWSB, the Gell-Mann-Nishijima equation relates Y to the third component of the weak isospin operator, T_3, and the electric charge Q,

$$Q = Y + T_3 \tag{1.27}$$

Regarding the EW Lagrangian, four gauge fields need to be introduced to achieve invariance under $SU(2)_L \otimes U(1)_Y$: $W^i_{\mu\nu}$ (i=1,2,3) from $SU(2)_L$, and B_μ from $U(1)_Y$. The resulting Lagrangian is,

$$\begin{aligned}
\mathcal{L}_{EW} &= i \sum_{f=l,q} \bar{f}(\gamma^\mu D_\mu) f - \frac{1}{4} W^i_{\mu\nu} W^{i\,\mu\nu} - \frac{1}{4} B_{\mu\nu} B^{\mu\nu} \\
D_\mu &\equiv \partial_\mu - ig\frac{\sigma}{2} W^i_\mu - ig' Y B_\mu \\
W^i_{\mu\nu} &\equiv \partial_\mu W^i_\nu - \partial_\nu W^i_\mu + g\epsilon^{ijk} W^j_\mu W^k_\nu \\
B_{\mu\nu} &\equiv \partial_\mu B_\nu - \partial_\nu B_\mu
\end{aligned} \tag{1.28}$$

with ϵ^{ijk} the Levi-Civita symbol, an antisymmetric tensor defined as $\epsilon^{ijk}\epsilon_{imn} = \delta^j_m \delta^k_n - \delta^j_n \delta^m_k$ with $i, j, k, l, m, n \in [1, 2, 3]$. Also, the $W^i_{\mu\nu}$ and $B_{\mu\nu}$ field tensors are defined to introduce the additional kinetic terms to the Lagrangian. The former contains a quadratic piece, due to the non-abelian nature of $SU(2)_L$, hence the full Lagrangian contains cubic and quartic self-interactions, as seen for the gluons in QCD. In contrast, the coupling constant g increases rapidly with the energy scale. As encountered before, mass terms for the gauge boson would break the gauge invariance. In this case, terms for the fermion masses would also break the symmetry as they would mix left- and right-handed fields, which transforms distinctively under $SU(2)_L$.

Summing all the interactions described, the SM Lagrangian for all the fermions before EWSB becomes,

$$\begin{aligned}
\mathcal{L}_{SM} = &\sum_f \sum_{\psi=L,e_R,Q_L,u_R,d_R} i\bar{\psi}^f \gamma^\mu D_\mu \psi^f \\
&- \frac{1}{4} G^a_{\mu\nu} G^{a_\mu\nu} - \frac{1}{4} W^i_{\mu\nu} W^{i_\mu\nu} - \frac{1}{4} B_{\mu\nu} B^{\mu\nu} \\
D_\mu = &\partial_\mu - ig_s T^a G^a_\mu - ig\frac{\sigma^i}{2} W^i_\mu - ig' Y B_\mu
\end{aligned} \tag{1.29}$$

1.1.5 Spontaneous symmetry breaking and the Higgs mechanism

The model described so far cannot reproduce measured results; first, the different fermions and the weak force mediators have mass and second, the $SU(2)_L \times U(1)_Y$ symmetry is not preserved in nature.

Even if somehow the EW gauge bosons are allowed to have mass, it leads to the lack of renormalisability and the violation of unitarity. Renormalisation is a collection of techniques that allows for the computation of measurable observables in QFT, managing the various sources of infinities within the theory, such as those from

self-interactions. Unitarity is needed more in general in quantum mechanics, to ensure proper time-evolution predictions of a quantum state. The longitudinal component of the massive boson is the cause of the problem, as in a boosted frame where $p^\mu = (p^0, 0, 0, |\mathbf{p}|)$, the parallel polarisation component of a massive boson, given by $\epsilon_\mu = (|\mathbf{p}|/m, 0, 0, p^0)$, grows indefinitely with the energy of the system. When computing the cross-section of the corresponding boson scattering, the value will indefinitely grow breaking the mentioned unitarity. If computed explicitly for the $W^\pm$ bosons, the energy scale where this occurs is around the TeV scale, which highlights a fundamental problem in the theory's ability to describe that scale.

The solution is provided by the EWSB and the Higgs-Englert-Brout mechanism, discussed next, after showing the spontaneous symmetry breaking process for a simple gauge theory.

How to break a symmetry

Spontaneous symmetry breaking is a phenomenon where a symmetry of the theory is unstable and the vacuum, or fundamental state, is degenerate. In the process, new interactions appear and a field obtains a non-zero vacuum expectation value.

The topic is broad as there are many symmetries and representations to potentially break, to illustrate the mechanism for the SM, lets consider a system with a scalar field ϕ, a gauge field A_μ, and the following Lagrangian with a gauge symmetry,

$$\begin{aligned} \mathcal{L} &= (D^\mu\phi)^\dagger D_\mu\phi - V(\phi) - \frac{1}{4}F_{\mu\nu}F^{\mu\nu} \\ D_\mu &\equiv \partial_\mu - igA_\mu \\ F_{\mu\nu} &\equiv \partial_\mu A_\nu - \partial_\nu A_\mu \end{aligned} \tag{1.30}$$

with a general potential $V(\phi)$ given by,

$$V(\phi) = \frac{1}{2}\mu^2\phi^\dagger\phi + \frac{1}{4}\lambda(\phi^\dagger\phi)^2 \tag{1.31}$$

with the real parameters μ^2 and λ relating respectively to the mass term and the strength of the self-interaction. There are two sensible ranges for these parameters, depicted in Figure 1.2, the first one is the case $\lambda, \mu^2 > 0$, similar to the previous theories and only one solution in the minimisation. The second one is for $\lambda > 0$ and $\mu^2 < 0$, where the $\mu^2\phi^\dagger\phi$ term cannot be understood as a mass term and the solution $\phi = 0$ is a local maximum, physically unstable. The minimum of the potential is degenerate and identified by the complex plane circle, $\phi^\dagger\phi = v^2/2$ with $v^2 \equiv -\mu^2/\lambda$ and

$$\phi = ve^{-i\theta} \tag{1.32}$$

The symmetry is broken spontaneously when the system chooses the fundamental state. Suppose $\phi = 0$, then the *Vacuum Expectation Value* (VEV) of ϕ is set to,

$$\langle 0|\phi|0\rangle = \frac{v}{\sqrt{2}} \tag{1.33}$$

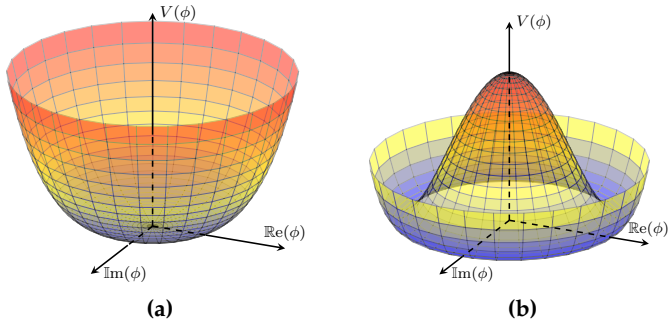

Figure 1.2: Shape of the potential $V(\phi)$ for $\lambda > 0$ and (a) $\mu^2 > 0$ or (b) $\mu^2 < 0$.

Next, lets suppose the following change of variables to center the new fundamental state,

$$\phi(x) = \left(\frac{v + \eta(x)}{\sqrt{2}}\right) e^{i\zeta(x)/v} \tag{1.34}$$

the Lagrangian can be expressed as,

$$\begin{aligned}\mathcal{L} = &\frac{1}{2}(\partial_\mu \eta)^2 + \frac{1}{2}(\partial_\mu \zeta)^2 - \frac{1}{4}F_{\mu\nu}F^{\mu\nu} \\ &+ \mu^2\eta^2 + \frac{1}{2}g^2v^2A_\mu A^\mu - gvA\mu\partial^\mu\zeta + \text{ interactions}\end{aligned} \tag{1.35}$$

which now contains the η and ζ fields, additional to the gauge A_μ. Also, square terms appear for η and A_μ, which can be identified as mass terms, $\frac{m_\eta}{2}\eta^2$ and $\frac{m_A}{2}A_\mu A^\mu$, resulting in $m_\eta = \sqrt{-2\mu^2}$ and $m_A = gv$. $\zeta(x)$ is massless and a particular resulting type of field named *Goldstone boson*, which the *Goldstone theorem* predicts. The theorem states that a massless boson appears for every symmetry that the VEV spontaneously breaks. In this abelian case, the VEV is not invariant under the $U(1)$ transformation. $\zeta(x)$ does not appear explicitly in the potential, therefore can take any value without affecting the energy of the system, which is not very physical. In addition, it appears in a strange mixing term with A_μ, $-gvA_\mu\partial^\mu\zeta$.

A way to remove the unphysical term is to choose the gauge,

$$\begin{aligned}\phi &\rightarrow \phi' = e^{-i\zeta/v}\phi \\ A_\mu &\rightarrow A'_\mu = A_\mu - \frac{1}{gv}\partial_\mu\zeta\end{aligned} \tag{1.36}$$

together with the previous change of variable for ϕ. Essentially the gauge freedom of the Lagrangian is being used to remove ζ, which becomes the longitudinal component of the transformed gauge boson A_μ. The gauge chosen is the so-called *unitary gauge*, which makes the physical content of the Lagrangian explicit[6].

[6] As a parallel, the ghost gluons in the context of regularisation also remove the problematic unphysical degrees of freedom.

In summary, this process of acquiring mass by means of absorbing a Goldstone boson is known as the *Higgs mechanism*.

The Higgs-Englert-Brout Mechanism in the Electroweak Sector

The Higgs-Englert-Brout mechanism [23–25] solved the contradictions found between massive particles and the requirement of gauge invariance. The mechanism is based on a spontaneous symmetry breaking of the $SU(2)_L \otimes U(1)_Y$ to $U(1)_{EM}$, gives mass to the different particles involved in the EW interactions except the photon.

A similar procedure can be applied to the EW Lagrangian derived in Equation 1.29, first by introducing an isospin doublet (Y=+1/2) of complex scalar fields Φ, the Higgs field,

$$\Phi \equiv \begin{pmatrix} \phi^+ \\ \phi^0 \end{pmatrix} = \frac{1}{\sqrt{2}} \begin{pmatrix} \phi_1 + i\phi_2 \\ \phi_3 + i\phi_4 \end{pmatrix} \tag{1.37}$$

where ϕ^+ corresponds to an electrically charged field (T_3=+1/2) and ϕ^0 to a neutral one (T_3=-1/2). This field transforms under $SU(2)_L$ and the Lagrangian, the Higgs Lagrangian,

$$\mathcal{L}_\Phi = (D_\mu \Phi)^\dagger (D^\mu \Phi) - V(\Phi) \tag{1.38}$$

with the same covariant derivative as in Equation 1.29 and the Higgs potential given by,

$$V(\Phi) = \mu^2 \Phi^\dagger \Phi + \lambda (\Phi^\dagger \Phi)^2 \tag{1.39}$$

which shape depends on the parameters μ^2 and λ. As seen before, choosing the case where $\lambda > 0$ and $\mu^2 < 0$, the potential at $\Phi = 0$ is unstable, and a continuous collection of possible minimum values appear defined by the circle,

$$\Phi^\dagger \Phi = \frac{1}{2} \frac{-\mu^2}{\lambda} \equiv \frac{1}{2} v^2 \tag{1.40}$$

Following, the spontaneous symmetry breaking with the choice of the new vacuum state,

$$\langle 0|\Phi|0\rangle = \frac{1}{\sqrt{2}} \begin{pmatrix} 0 \\ v \end{pmatrix} \tag{1.41}$$

This vacuum is not invariant to any of the $SU(2)_L$ and the $U(1)$ transformations, however, the $Q = T_3 + Y$ transformation is not affected,

$$Q\,\langle 0|\Phi|0\rangle = \frac{1}{2\sqrt{2}} \sigma_3 \begin{pmatrix} 0 \\ v \end{pmatrix} + \frac{1}{2\sqrt{2}} Y \begin{pmatrix} 0 \\ v \end{pmatrix} = \frac{1}{2\sqrt{2}} \left[\begin{pmatrix} 0 \\ -v \end{pmatrix} + \begin{pmatrix} 0 \\ v \end{pmatrix} \right] = \begin{pmatrix} 0 \\ 0 \end{pmatrix} \tag{1.42}$$

The field is rewritten in the unitary gauge, which automatically removes the extra non-physical Goldstone bosons,

$$\Phi(x) = \frac{1}{\sqrt{2}} \begin{pmatrix} 0 \\ v + H(x) \end{pmatrix} \tag{1.43}$$

where $H(x)$ is centered around the vacuum state. With this change the Higgs potential becomes,

$$V(\Phi) = \frac{1}{4}\lambda v^2 H^2 + \frac{1}{4}\lambda v H^3 + \frac{1}{16}\lambda H^4 \tag{1.44}$$

spawning the Higgs boson mass $m_H^2 = \lambda v^2/2 = -\mu^2/2$, in the quadratic H term. The cubic and quartic terms correspond to the three- and four-point Higgs boson self-interactions.
The EWSB generates new interactions and mass terms for the different particles involved in the EW interactions. Gluons are not affected as the scalar field is a doublet and does not transform under $SU(3)$.

The effects on the boson and fermion sectors of the SM are discussed in the following, individually.

Boson sector

The gauge boson masses arise from the covariant derivative, $(D_\mu\Phi)^\dagger(D^\mu\Phi)$, which includes the gauge fields. Expanding,

$$\mathcal{L}_{mass} = \frac{v^2}{8} V_\mu \begin{pmatrix} g^2 & 0 & & \\ 0 & g^2 & & 0_{2\times2} \\ & & g^2 & -gg' \\ & 0_{2\times2} & -gg' & g'^2 \end{pmatrix} V^\mu \tag{1.45}$$

with $V_\mu = \begin{pmatrix} W_\mu^1 & W_\mu^2 & W_\mu^3 & B_\mu \end{pmatrix}$. The next step is to diagonalise the matrix and finde the following eigenvectors,

$$\begin{aligned} A_\mu &\equiv \sin\theta_W W_\mu^3 + \cos\theta_W B_\mu \\ Z_\mu &\equiv \cos\theta_W W_\mu^3 - \sin\theta_W B_\mu \end{aligned} \tag{1.46}$$

where the Weinberg angle, or weak mixing angle, is defined by $\tan\theta_W \equiv g'/g$. The corresponding eigenvalues, the square masses, for the A_μ and Z_μ fields are zero and $v^2(g^2 + g'^2)/8$. In contrast, W_μ^1 and W_μ^2 are well-defined mass states but not charge states. This is due to T_1 and T_2 being not diagonal, connecting the different states of T_3 (hence of Q). The operator $T_\pm = T_1 \mp iT_2$ can be defined, which increases or decreases one unit of T_3 (hence of Q). In addition, the fields can be redefined,

$$W_\mu^\pm = \frac{1}{\sqrt{2}}(W_\mu^1 \mp iW_\mu^2) \tag{1.47}$$

In summary the Lagrangian in Equation 1.45 can now be written as

$$\mathcal{L}_{mass} = \frac{g^2 v^2}{4} W_\mu^+ W^{-\mu} - \frac{v^2}{8}(g^2 + g'^2) Z_\mu Z^\mu \tag{1.48}$$

where the mass terms of the different bosons can be identified,

$$\begin{aligned} m_A &= 0 \\ m_Z &= \frac{v}{2}\sqrt{g^2 + g'^2} \\ m_W &= \frac{vg}{2} = m_Z \cos\theta_W \end{aligned} \tag{1.49}$$

Note that the remaining symmetry after breaking $SU(2)_L \otimes U(1)_L$ is $U(1)_{EM}$. The associated A_μ field is massless, the photon, which is a combination of the W^3_μ and B_μ fields. The associated quantum number, the electric charge, has been defined previously in the chapter, $Q = T_3 - Y$.

As for interactions, the covariant derivative can be expressed in terms of the new bosons,

$$\partial_\mu - igW^3_\mu = \partial_\mu - ig\sin\theta_W A_\mu - ig\cos\theta_W Z_\mu \tag{1.50}$$

where the electromagnetic coupling constant e can be defined as $e = g\sin\theta_W$. In addition, the field tensors can be rewritten as,

$$\begin{aligned} W^3_{\mu\nu} &= \partial_\mu W^3_\nu - \partial_\nu W^3_\mu - ig(W^+_\mu W^-_\nu - W^+_\nu W^-_\mu) \\ &= \sin\theta_W F_{\mu\nu} + \cos\theta_W Z_{\mu\nu} - ig(W^+_\mu W^-_\nu - W^+_\nu W^-_\mu) \\ B_{\mu\nu} &= \cos\theta_W F_{\mu\nu} - \sin\theta_W Z_{\mu\nu} \end{aligned} \tag{1.51}$$

where the field strength tensors for the photons and the Z boson, $F_{\mu\nu}$ and $Z_{\mu\nu}$ are defined.

Fermion sector

The procedure required to obtain the fermion masses is more complicated than for the gauge bosons. Instead of just expanding the kinematic term with the new Higgs field, Yukawa [26] interactions that couple left- and right-handed fermions with the Higgs need to be introduced.

As seen in this chapter, only $q^i_{\alpha L}$ and l^i_L fields are $SU(2)_L$ doublets,

$$q^i_{\alpha L} = \begin{pmatrix} u^i_{\alpha L} \\ d^i_{\alpha L} \end{pmatrix},\ l^i_L = \begin{pmatrix} \nu^i_L \\ \ell^i_L \end{pmatrix} \tag{1.52}$$

where the i refers to the generation and α to the colour. It has been already pointed out that is not possible to construct a well defined $mf^\dagger f$ term that transforms under the SM group, necessary for gauge invariance.

The solution is provided by introducing Yukawa interactions between the fermion fields and the Higgs field Φ, also a doublet under $SU(2)$,

$$\mathcal{L}_{Yukawa} = -y^{ab}\bar{q}^a_{\alpha\ L}\Phi d^b_{\alpha\ R} - y'^{ab}\bar{q}^a_{\alpha\ L}\tilde{\Phi}u^b_{\alpha\ R} - y''^{ab}\bar{l}^a_L\Phi\ell^b_R + \text{ h.c} \tag{1.53}$$

where y, y′ and y″ are the Yukawa matrices, 3×3 matrices with one dimension for each generation. Also, $\tilde{\Phi}\equiv i\sigma_2\Phi^*$. Note that there is no second term for the leptons, as the SM does not contemplate the right handed neutrino, ν_R. Also, this Lagrangian breaks explicitly the chiral symmetry but yields a singlet representation, safe for gauge invariance.

Next, writing the field Φ in terms of the unitary gauge as in the EWSB, $\phi^0(x) = v + H(x)$,

$$\begin{aligned}\mathcal{L}_{Yukawa} &= -\frac{1}{\sqrt{2}}(v+H)y^{ab}\bar{q}^a_{\alpha\ L}d^b_{\alpha\ R} - \frac{1}{\sqrt{2}}(v+H)y'^{ab}\bar{q}^a_{\alpha\ L}u^b_{\alpha\ R}\\ &\quad -\frac{1}{\sqrt{2}}(v+H)y''^{ab}\bar{l}^a_L\ell^b_R + \text{ h.c}\\ &= -\frac{1}{\sqrt{2}}(v+H)y^{ab}\bar{D}^a_\alpha D^b_\alpha - \frac{1}{\sqrt{2}}(v+H)y'^{ab}\bar{U}^a_\alpha U^b_\alpha\\ &\quad -\frac{1}{\sqrt{2}}(v+H)y''^{ab}\bar{L}^a L^b + \text{ h.c}\end{aligned} \tag{1.54}$$

where the expression has been rearranged to define Dirac fields in spinor notation,

$$D^a_\alpha = \begin{pmatrix} d^a_\alpha \\ \bar{d}^{\dagger a}_\alpha\end{pmatrix},\ U^a_\alpha = \begin{pmatrix} u^a_\alpha \\ \bar{u}^{\dagger a}_\alpha\end{pmatrix},\ L^a_\alpha = \begin{pmatrix} \ell^a_\alpha \\ \bar{\ell}^{\dagger a}_\alpha\end{pmatrix} \tag{1.55}$$

After diagonalising the three Yukawa matrices, the eigenvalue terms are related to the masses, which can be identified for each generation as,

$$\begin{aligned} m_{d^i} &= y^{ii}v/\sqrt{2}\\ m_{u^i} &= y'^{ii}v/\sqrt{2}\\ m_{\ell^i} &= y''^{ii}v/\sqrt{2}\\ m_{\nu^i} &= 0\end{aligned} \tag{1.56}$$

There is a major consequence of the differences between the representation in the generator space (Equation 1.52, $SU(2)_L$ doublets), and in mass space, after diagonalising the Yukawa matrices. D^a_α and U^a_α are rotated to diagonalise their corresponding Yukawa matrix, so affected by different transformations. However, the individual $d^a_{\alpha\ L}$ and $u^a_{\alpha\ L}$ fields are part of the same $SU(2)_L$ doublet.

The effect can be seen writing the $W^\pm$ interactions in the mass state representation of the fields which become off-diagonal,

$$\frac{-g}{\sqrt{2}}\begin{pmatrix}\bar{u}_L & \bar{c}_L & \bar{t}_L\end{pmatrix}\gamma^\mu W^+_\mu V_{CKM}\begin{pmatrix} d_L \\ s_L \\ b_L\end{pmatrix} + \text{ h.c} \tag{1.57}$$

$$\begin{pmatrix} d'_L \\ s'_L \\ b'_L \end{pmatrix} = V_{CKM} \begin{pmatrix} d_L \\ s_L \\ b_L \end{pmatrix} = \begin{pmatrix} V_{ud} & V_{us} & V_{ub} \\ V_{cd} & V_{cs} & V_{cb} \\ V_{td} & V_{ts} & V_{tb} \end{pmatrix} \begin{pmatrix} d_L \\ s_L \\ b_L \end{pmatrix} \tag{1.58}$$

where the superscript ' denotes the mass representation and V_{CKM} is the Cabibbo-Kobayashi-Maskawa matrix [27, 28]. This unitary matrix is the product of the transformations that diagonalise the y and y' Yukawa matrices, which encodes the mixing of the different generations of fields in charged-mediated weak interactions. This is known as flavour violation, where a weak interaction of a quark can result on changing its flavour. On the other side, leptons are represented with the same $SU(2)_L$ doublet, so any mixing of lepton generations is not present in the theory.

There is still another interesting feature that arises from the CKM matrix. The standard representation [29] of the matrix takes into account invariant phase rotations of the fields, leaving as free parameters three angles θ_{12}, θ_{23} and θ_{13} (chosen to lie in the first quadrant so $\sin\theta, \cos\theta \geq 0$), and a single complex phase δ that cannot be rotated to zero. The matrix reads,

$$\begin{aligned} V_{CKM} &= \begin{pmatrix} 1 & 0 & 0 \\ 0 & c_{23} & s_{23} \\ 0 & -s_{23} & c_{23} \end{pmatrix} \begin{pmatrix} c_{13} & 0 & s_{13}e^{-i\delta} \\ 0 & 1 & 0 \\ -s_{13}e^{i\delta} & 0 & c_{13} \end{pmatrix} \begin{pmatrix} c_{12} & s_{12} & 0 \\ -s_{12} & c_{12} & 0 \\ 0 & 0 & 1 \end{pmatrix} \\ &= \begin{pmatrix} c_{12}c_{13} & s_{12}c_{13} & s_{13}e^{-i\delta} \\ -s_{12}c_{23} - c_{12}s_{23}s_{13}e^{i\delta} & c_{12}c_{23} - s_{12}s_{23}s_{13}e^{i\delta} & s_{23}c_{13} \\ s_{12}s_{23} - c_{12}c_{23}s_{13}e^{i\delta} & -c_{12}s_{23} - s_{12}c_{23}s_{13}e^{i\delta} & c_{23}c_{13} \end{pmatrix} \end{aligned} \tag{1.59}$$

where $s_{ij} = \sin\theta_{ij}$ and $c_{ij} = \cos\theta_{ij}$. The presence of the complex phase leads to different couplings for anti-matter, as the complex phase will switch sign, thus leading to matter/anti-matter asymmetry. This asymmetry in flavour-changing processes is the only source in the SM of CP violation, or T violation (from the time-reversal symmetry[7]) however, as discussed in Section 1.2.4, fails to describe the current matter/anti-matter content of the universe. The CKM matrix is predicted and measured to be almost diagonal, with very small sources of CP violation, or V_{ub} and V_{td}.

The current matrix as in 2022 [14] reads,

$$V_{CKM} = \begin{pmatrix} 0.97401 \pm 0.00011 & 0.22650 \pm 0.00048 & 0.00361^{+0.00011}_{-0.00009} \\ 0.22636 \pm 0.00048 & 0.97320 \pm 0.00011 & 0.04053^{+0.00083}_{-0.00061} \\ 0.00854^{+0.00023}_{-0.00016} & 0.03978^{+0.00082}_{-0.00060} & 0.999172^{+0.000024}_{-0.000035} \end{pmatrix} \tag{1.60}$$

1.1.6 Flavour Changing Neutral Currents interactions

Flavour Changing Neutral Currents (FCNC) are the processes that involve the change of a fermion flavour through a neutral boson. In the electroweak sector, the neutral current interactions are mediated by the Z boson. Contrary to the $W^\pm$ case, the interactions involving the Z boson involve fields with the same associated Yukawa

[7] The three symmetries are related as the combination, CPT symmetry, which must always be respected in theory.

matrix, from the same spinors of the mass representation (Equation 1.55). Hence, no mixing matrix is spawned and thus no explicit FCNC appear in the SM Lagrangian.

The existence of charged flavour changing currents is allowed at tree level but their associated couplings are proportional to the off-diagonal elements of the CKM matrix, which are especially small for the interactions between the first and third generation leptons. However, FCNC processes can be obtained from consecutive flavour changing interactions in higher order diagrams. Figure 1.3 shows example FCNC processes involving the two types of first order Feynman diagrams, known as *box* and *penguin* diagrams.

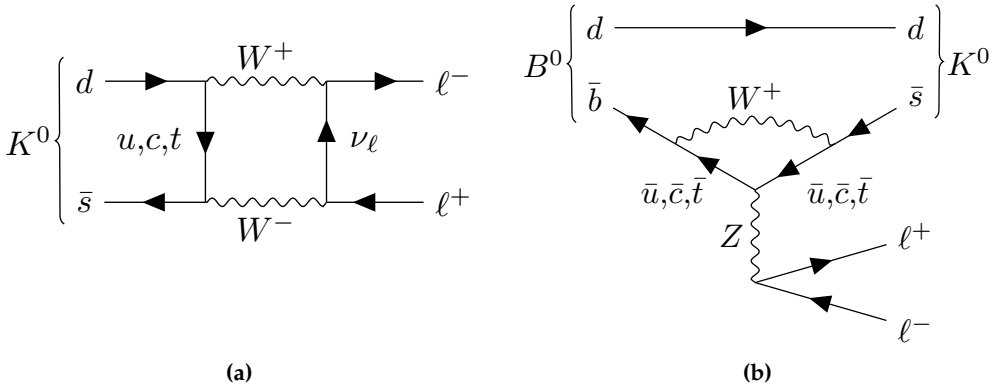

Figure 1.3: Example first-order Feynman diagrams of a box diagram for the $K^0 \to \ell^+\ell^-$ process (a) and of a penguin diagram for the $B^0 \to K^0\ell^+\ell^-$ process (b).

The high-order contributions are suppressed further by the Glashow, Iliopoulos and Maiani (GIM) mechanism [30]. In order to illustrate this mechanism, the example penguin diagram is discussed in the following. The diagram depicts a top FCNC decay that involves the $t \to b$ and $b \to c$ types of interactions, thus the interaction will be proportional to $V^*_{cb}V_{tb}$. Adding up the other two possible diagrams with d and s in the loop,

$$V^*_{cd}V_{td} + V^*_{cs}V_{ts} + V^*_{cb}V_{tb} \tag{1.61}$$

which assumes that the quarks have the same mass. The value of this expression can be obtained from the CKM matrix. As the matrix is unitary ($V_{CKM}V^\dagger_{CKM} = V^\dagger_{CKM}V_{CKM} = \mathbb{1}$), a total of 18 constraints appear, relating the different vertices:

$$\begin{aligned} V^2_{ud}+V^2_{cd}+V^2_{td} &= 1, & V^2_{ud}+V^2_{us}+V^2_{ub} &= 1 \\ V^2_{us}+V^2_{cs}+V^2_{ts} &= 1, & V^2_{cd}+V^2_{cs}+V^2_{cb} &= 1 \\ V^2_{ub}+V^2_{cb}+V^2_{tb} &= 1, & V^2_{td}+V^2_{ts}+V^2_{tb} &= 1 \end{aligned}$$

$$
\begin{aligned}
V_{ud}^* V_{us} + V_{cd}^* V_{cs} + V_{td}^* V_{ts} &= 0, & V_{ud}^* V_{cd} + V_{us}^* V_{cs} + V_{ub}^* V_{cb} &= 0 \\
V_{ud}^* V_{ub} + V_{cd}^* V_{cb} + V_{td}^* V_{tb} &= 0, & V_{ud}^* V_{td} + V_{us}^* V_{ts} + V_{ub}^* V_{tb} &= 0 \\
V_{us}^* V_{ud} + V_{cs}^* V_{cd} + V_{ts}^* V_{td} &= 0, & V_{cd}^* V_{ud} + V_{cs}^* V_{us} + V_{cb}^* V_{ub} &= 0 \\
V_{us}^* V_{ub} + V_{cs}^* V_{cb} + V_{ts}^* V_{tb} &= 0, & V_{cd}^* V_{td} + V_{cs}^* V_{ts} + V_{cb}^* V_{tb} &= 0 \\
V_{ub}^* V_{ud} + V_{cb}^* V_{cd} + V_{tb}^* V_{td} &= 0, & V_{td}^* V_{ud} + V_{ts}^* V_{us} + V_{tb}^* V_{ub} &= 0 \\
V_{ub}^* V_{us} + V_{cb}^* V_{cs} + V_{tb}^* V_{ts} &= 0, & V_{td}^* V_{cd} + V_{ts}^* V_{cs} + V_{tb}^* V_{cb} &= 0
\end{aligned}
\tag{1.62}
$$

The equation is exactly one of the constraints and equals zero. However, as the different quarks are not degenerate in mass, every term would be proportional to $1/m_q$ (q being the quark inside the loop). This is the origin of the GIM mechanism and results in a non-zero but very suppressed contribution of FCNC in the SM. In addition, this suppression is larger for loops involving down-type quarks as their masses are more similar to each other than for the up-type quarks.

1.2 Standard Model measurements and top physics

Since the formulation of the SM, most experimental observations and measurements have been described successfully by the model. Throughout the years, predicted particles have been found and multiple precision measurements have tested its validity. However, there are theoretical and experimental issues that are not solved, leading to the conclusion that the SM is an effective theory and there is a more complete theory that can explain the whole range of observations.

In this section, a summary of the measurements of the SM is presented, focusing on processes involving the top quark and FCNC. Then, different main open questions of the SM are briefly reviewed.

1.2.1 Experimental measurements

Decades of experiments have performed measurements of parameters that define the SM. The SM can be summarised with nineteen parameters, which have been described in this chapter: nine fermion masses (six for quarks, three for leptons), the three gauge couplings (g_S, g and g'), the Higgs vacuum expectation value (v), the Higgs mass, four parameters of the CKM matrix (three angles and a complex phase) and the QCD CP-violating phase. There is no underlying relation between these parameters, only being set from experimental observations. With these parameters measured, theoretical predictions of observables can be tested with experimental data in order to explore new physics.

One typical observable in particle physics is the cross-section σ, the expected interaction rate between two interacting particles in terms of the effective surface area typically measured in pb (picobarn, 1pb = 10^{-40} m^2). The cross-section of a process depends on the interacting forces involved, as well as the energy and momentum of the interacting particles, which can be calculated from the S-matrix (scattering matrix) using relativistic mechanics. Feynman diagrams are a tool to translate a visual description of a process to a mathematical expression, the matrix amplitude,

which is proportional to the probability of the specific process happening and is needed for the computation.

The decay width, Γ, can be computed in similar fashion to obtain another common observable, the Branching Ratio (BR). The BR of an unstable particle is the probability for it to decay into specific particles among all possible states. It is computed by dividing the Γ of the specific process with respect to the sum of all the possible processes. Both σ and Γ are calculated from perturbation approximations, as the actual process is not the product of just one Feynman diagram, but all the possible interactions that lead to the same final state including loops, interferences and radiative corrections, refereed to as high order corrections. However, each particle interaction is proportional to the probability making higher order corrections become less important. Typically, *leading-order* (LO) calculations use only the leading order terms from the perturbation expansion, while if complemented by higher order corrections are referred to next-to-leading-order (NLO) or next-to-NLO (NNLO) calculations.

Figure 1.4 shows a summary of a wide range of cross-section measurements by the ATLAS Collaboration compared to the theoretical predictions, showing excellent agreement between data and theory. On the other side, the Higgs boson has been scrutinised since its discovery to characterise all its properties. Figure 1.5 shows a summary of Higgs boson production cross-sections and branching ratios by the ATLAS Collaboration, including the coupling strengths to other SM particles. It shows that the coupling is proportional to the mass of the resulting particle, as expected from the Higgs mechanism. As the Higgs couples with any particle that acquires mass through its field, it is an excellent candidate to study any other particle still to be discovered.

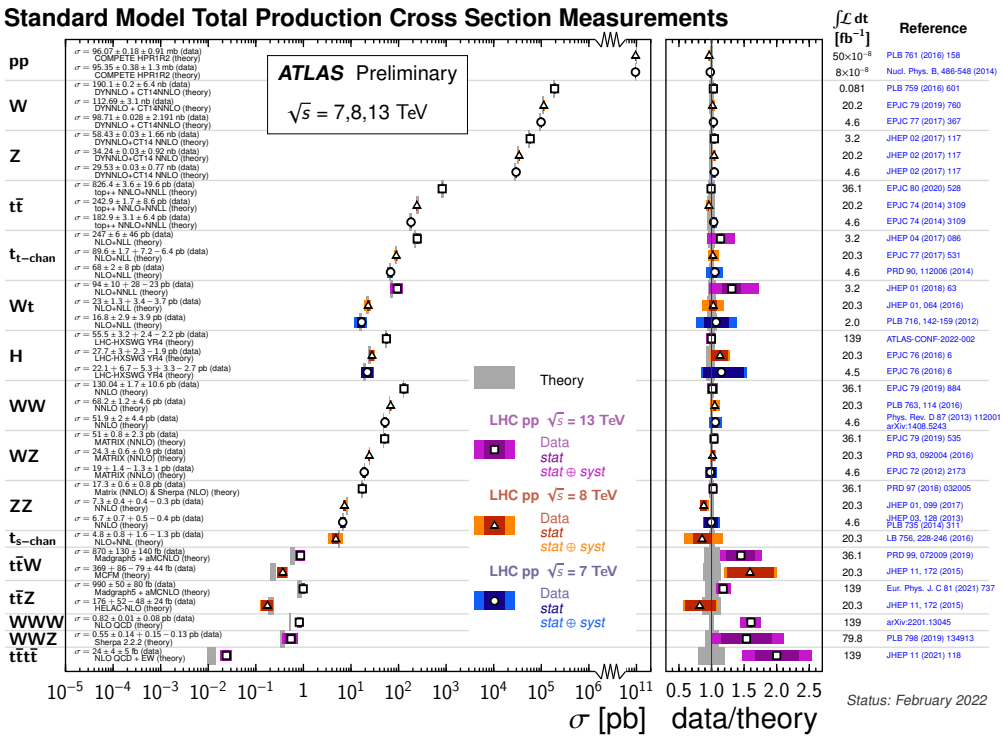

Figure 1.4: Summary of several SM total production cross-section measurements, corrected for branching fractions, compared to the corresponding theoretical predictions and ratio with respect to theory [31].

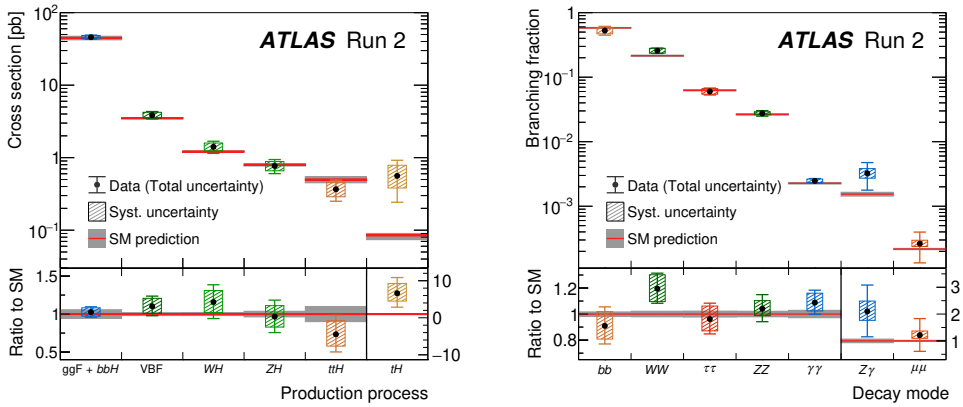

(a) (b)

Figure 1.5: Observed and predicted Higgs boson production cross-sections for different production processes (a) and for different decay modes (b). The lower panels show the ratios of the measured values to their SM predictions. The vertical bar on each point denotes the 68% confidence interval. The p-value for compatibility of the measurement and the SM prediction is 65% (a) or 56% (b) [32].

1.2.2 Top quark physics

The top quark is the most massive known elementary particle, discovered in 1995 at Fermilab [9, 10]. This characteristic makes the top quark the only one that decays before hadronisation and hence, properties like the spin are directly transferred to the decay products. The main top quark decay is $t \rightarrow Wb$ with a branching ratio close to 1, determined by the $V_{tb} = 0.97401 \pm 0.00011$ (element of the CKM matrix [14]) being very close to 1. Due to its high mass, the top quark strongly couples with the Higgs boson as the Yukawa coupling (Equation 1.56) $y_t = \sqrt{2}m_t/v \simeq 1$.

Altogether, the top quark plays a key role in the study of the SM. The precise measurements of its properties put the theory to test and any deviation would point to new physics. It is also an excellent candidate for searches involving either much more massive particles that might decay to the top quark, or decay into other lighter exotic particles. Even if these new particles are too heavy to be produced at the LHC, they can still be detected indirectly through their effects on the properties of the top quark. This makes the top quark an important tool for searching for new physics beyond the SM. The top quark can be produced either in top quark pairs, namely $t\bar{t}$ production, or together with other particles, called single-top production.

The single-top production has three different channels, which involve electroweak interactions: $t-$channel, from W or gluon fusion; $Wt-$channel, with an associated W; and $s-$channel, from $q\bar{q}' \rightarrow tb$.

Figure 1.6 shows a comparison of theoretical and experimental values for the cross-sections involving the production of different top processes, showing an excellent agreement between them. Also, that the $t\bar{t}$ production is larger than the single-top.

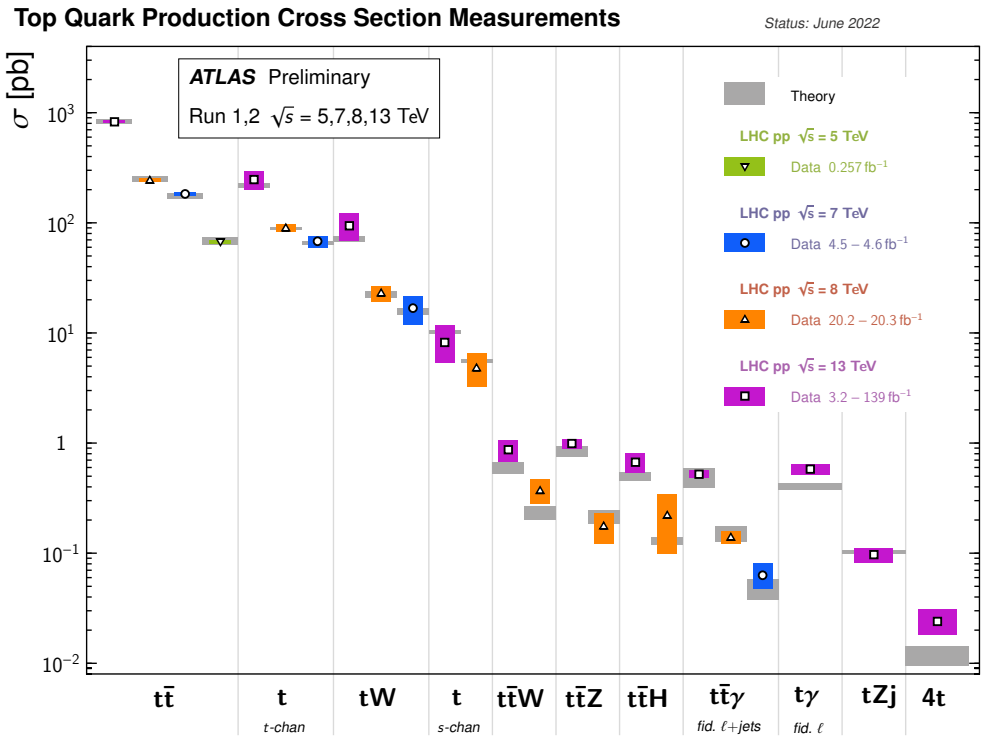

Figure 1.6: Summary of several top-quark related production cross-section measurements, compared to the corresponding theoretical expectations. All theoretical expectations were calculated at NLO or higher [33].

1.2.3 FCNC measurements

A FCNC process stands for an interaction with a change in the fermion (quark or lepton) flavour through the emission or absorption of a neutral boson. As seen in Section 1.1.6, such processes are not allowed at tree-level in the SM and the one-loop contributions are heavily suppressed by the GIM mechanism.

As the branching ratio of the top quark is mainly $t \to Wb$, together with the heavily suppressed FCNC contributions, the predicted branching ratio for the top FCNC decays in the SM is below 10^{-14}. This very small value is far away from the achievable sensitivity at the LHC, and makes the precise measurement of FCNC interactions an excellent test of the SM.

Table 1.3 shows the SM predictions for all the FCNC top quark decays, together with the experimental results from the SM and CMS collaborations.

Table 1.3: Theoretical predictions for the branching ratios of FCNC top decays predicted with the SM [34] and the most recent experimental limits from the ATLAS [4, 35, 36] and the CMS [37–40] collaborations.

Process	SM	ATLAS	CMS
$t \to u\gamma$	$4 \cdot 10^{-16}$	$0.85 \cdot 10^{-5}$ (139 fb^{-1})	$1.3 \cdot 10^{-4}$ (8 TeV, 19.8 fb^{-1})
$t \to c\gamma$	$5 \cdot 10^{-14}$	$4.2 \cdot 10^{-5}$ (139 fb^{-1})	$1.7 \cdot 10^{-4}$ (8 TeV, 19.8 fb^{-1})
$t \to ug$	$4 \cdot 10^{-14}$	$0.61 \cdot 10^{-4}$ (139 fb^{-1})	$2.0 \cdot 10^{-4}$ (7+8 TeV, 24.7 fb^{-1})
$t \to cg$	$5 \cdot 10^{-12}$	$3.7 \cdot 10^{-4}$ (139 fb^{-1})	$4.1 \cdot 10^{-4}$ (7+8 TeV, 24.7 fb^{-1})
$t \to uZ$	$8 \cdot 10^{-17}$	$6.2 \cdot 10^{-5}$ (139 fb^{-1})	$2.4 \cdot 10^{-4}$ (35.9 fb^{-1})
$t \to cZ$	$1 \cdot 10^{-14}$	$13 \cdot 10^{-5}$ (139 fb^{-1})	$4.5 \cdot 10^{-4}$ (35.9 fb^{-1})
$t \to uH$	$2 \cdot 10^{-17}$	$6.9 \cdot 10^{-4}$ ($H \to \tau\tau$, 139 fb^{-1})	$1.9 \cdot 10^{-4}$ ($H \to \gamma\gamma$, 137 fb^{-1})
$t \to cH$	$3 \cdot 10^{-15}$	$9.4 \cdot 10^{-4}$ ($H \to \tau\tau$, 139 fb^{-1})	$7.3 \cdot 10^{-4}$ ($H \to \gamma\gamma$, 137 fb^{-1})

1.2.4 Open questions

The SM has been successful in describing the fundamental particles and their interactions in nature. However, it is not a complete theory and leaves many open questions about the nature of the universe.

One of the most popular issues with the theory is the lack of neutrino mass terms. The observation of neutrino oscillations [41] implies the existence of mass differences between the three neutrino generations, but the SM does not account for this directly. Different approaches have been proposed, such as adding right-handed neutrinos or describing neutrinos as Majorana particles [42]. However, the SM would require at least seven additional parameters: three neutrino masses, three mixing angles and one CP violating phase for the Pontecorvo-Maki-Nakagawa-Sakata (PMNS) matrix [43, 44], the neutrino mixing matrix similar to the CKM quark flavour matrix.

Another open question concerns the anomalous magnetic dipole moment of the muon. The high-order corrections from QCD that appear in this quantity are in

tension with the prediction of the SM. In 2021, the muon g-2 experiment found a greater deviation [45] from the prediction, highlighting this discrepancy even further.

The SM also fails to describe the other fundamental force in nature: gravity. While general relativity has provided a good description of gravity in macroscopic systems, there is no renomalisable quantum field theory for gravity, and the SM does not account for it. Theoretical frameworks like string theory have been proposed as alternatives, but these are difficult to test experimentally. The SM is understood as an effective theory of a more complete unified theory and is only valid at low energies. In the most extreme scenario, the SM is expected to break around the Planck scale ($M_P = \sqrt{\hbar/(8\pi G_N)} \sim 2.4\ 10^{18}$ GeV), where gravitational effects are expected to become as important as the other forces in the SM.

Furthermore, the SM only describes what is known as baryonic matter, which accounts for about 5% of the energy density of the universe. Cosmological observations suggest the existence of large amounts of *dark matter* (DM) and *dark energy*, phenomena not accounted for by the SM. The existence of DM was postulated as extra non-luminous matter needed to explain the clustering of galaxies [46]. Rotation curves of galaxies not matching the gravitational pull of observed stars [47] and gravitational lensing effects observed in some galaxy collisions [48] also provide evidence for large concentrations of invisible mass. More recently, the WMAP and Planck collaborations have studied anisotropies in the cosmic microwave background (CMB) [49, 50] and postulated the existence of cold DM. Meanwhile, observations suggest that the universe is expanding at an accelerated rate, compatible with the existence of dark energy, understood to be the product of an intrinsic space-time energy density or cosmological constant that causes the expansion. Observation of the red-shift of light from supernovae, used as standard candles, indicates that cosmological objects are moving away at an increasingly faster rate with the distance [51]. Studies of the CMB provide additional measurements of the accelerated expansion [50]. Overall, baryonic matter accounts for only 4.9% of the total energy density of the universe, dark matter for 26.8% and dark energy for 68.3% [50].

The universe appears to be composed entirely of matter. However, to explain the observed imbalance in the abundance of matter and anti-matter, referred to as matter/anti-matter asymmetry, the SM only provides one source of CP violation in the quark weak interactions, which is not sufficient. Additional sources, such as the complex phase in the PMNS matrix have been proposed. However, it is clear that more phenomena are needed to account for the current net balance of matter. Possible baryon number-violating effects at high energy scales may have played a role in generating this imbalance.

Besides the natural phenomena uncovered by the SM, there are also naturalness problems, which are aesthetic concerns regarding the precise values of some of the SM parameters. These values seem "unnatural" if there is no underlying mechanism to explain them. The general consensus is that a theory is more natural if it requires fewer fine-tunings. Although these issues are completely subjective, they could be a hint for the existence of a new underlying mechanism that complements the SM.

The first problem, commonly known as the hierarchy problem, arises because the cutoff energy of the SM (Λ_{SM}) is usually set to the Planck scale, $\sim 10^{18}$ GeV, whereas the EW scale ($v \sim 246$ GeV) is much smaller. This problem can be understood as the lack of a clear reason why the EWSB occurs at a sclae orders of magnitude smaller than the Plank scale. High-order corrections from the SM suggest that the leading radiation corrections for fermion masses are of the order of $\log \Lambda_{\text{SM}}$ and thus sensitive to the scale, but the fine-tuning is considered small. On the other hand, the physical Higgs mass including radiation corrections, is given by,

$$m_H^2 = m_0^2 + \frac{3}{8\pi^2 v^2}\Lambda_{\text{SM}}^2[m_0^2 + 2m_W^2 + M_Z^2 - 4m_t^2] + \mathcal{O}(\ln \frac{\Lambda_{\text{SM}}}{m_0}) \tag{1.63}$$

with m_0 the bare Higgs mass. The nature of the hierarchy problem is evident as the correction is more sensitive to the cutoff scale and requires substantial tuning to counter the Λ_{SM} term and achieve such a low measured physical mass. It can also be observed that the most important correction is given by the top quark, and it is often questioned whether the reason for the huge mass of this quark could provide a solution. Although the Higgs mass and the EW scale are difficult to justify, it can be argued that the appearance of the Λ_{SM} is related to the chosen regularisation scheme, and cutoffs play no physical role.

Another related problem is the fermion mass hierarchy; the fact that the masses of the SM particles range from ~1 MeV to ~173 GeV is not understood. Similarly, there is no clear reason for the existence of the three mass families of quarks and leptons with different mixing patterns, with FCNC interactions being heavily suppressed. This problem is known as the flavour problem and might also be related to renormalisation, as fermion masses also have correction terms with the logarithm of the cutoff scale.

Another naturalness problem is the strong CP problem, which is related to QCD. The most general QCD Lagrangian can contain a CP-violating angle that does not break any symmetry or the renormalisability of the theory. This term would introduce a prediction of axion particles and the neutron having non-zero electric dipole moment. However, the experimental measures of ultracold neutrons and mercury have constrained the CP-violating term to be very small, $|\theta| < 6 \cdot 10^{-11}$ [18], which is an incredibly low value for a parameter that could have any value in the theory. The problem suggests that there may be a yet-unkown symmetry or mechanism that cancels out the CP-violating term.

1.3 Beyond the Standard Model

Beyond the SM (BSM) theories aim to extend or replace the SM by addessing its limitations and shortcomings. Several theories have been proposed to address some of the gaps mentioned in the previous section, and among them are the extended Higgs sectors and flavon models. Overall, BSM theories provide a rich landscape of new physics, and their predictions can be tested by current and future experiments.

1.3.1 Two Higgs Doublet Model

The Two Higgs Doublet Model (2HDM) extends the SM by adding a second Higgs doublet. With two scalar Higgs doublets, the electroweak symmetry can be broken differently and the type of model can be defined depending on which fermions couple to each doublet. One of the most studied is the Type-II 2HDM, in which up-type quarks couple to one doublet while the down-type quarks and charged leptons couple to the other,

$$\Phi_1 \equiv H_u = \begin{pmatrix} H_u^+ \\ H_u^0 \end{pmatrix} = \frac{1}{\sqrt{2}} \begin{pmatrix} 0 \\ v_u \end{pmatrix}, \qquad \Phi_2 \equiv H_d = \begin{pmatrix} H_d^- \\ H_d^0 \end{pmatrix} = \frac{1}{\sqrt{2}} \begin{pmatrix} 0 \\ v_d \end{pmatrix} \tag{1.64}$$

with v_u and v_d being the VEV of each doublet field. This scalar sector has eight initial degrees of freedom, four more than in the SM, yielding a total of five physical scalars instead of just the SM Higgs. The predicted particles are two neutral CP-even scalars h and H ($m_h < m_H$), one CP-odd pseudo-scalar A and two charged Higgs bosons $H^\pm$. This type of models have six free parameters: m_h, m_H, m_A, $m_{H^\pm}$, $\tan\beta$ and α. The last two are the ratio of the two VEV, $\tan\beta = \frac{v_u}{v_d}$, and a mixing angle α that diagonalises the mass matrix of the CP even states.

1.3.2 Supersymmetry

Supersymmetry (SUSY) is a popular theoretical extension of the SM, very atractive solving many issues of the SM like the hierarchy problem or DM. It is a framework of theories that introduce a symmetry between the fermion and boson sectors (supersymmetry), predicting a superpartner particle with different spin for each SM particle. No new particles or other experimental evidence has been found so far; however, there are many SUSY models with different assumptions and parameters that still remain consistent with the current experimental data and could potentially be discovered.

The simplest realization of SUSY is the Minimal Supersymmetic SM (MSSM), one of the models best studied and motivated. The model introduces the minimal amount of degrees of freedom with respect to the SM, with new particles and no new interactions. Every SM particle has an associated superpartner with different spin: the SUSY particles related to the SM gauge bosons are known as gauginos, the squarks are related to quarks, sleptons to leptons and Higgsinos to the Higgs bosons. The MSSM has an additional Higgs doublet to prevent anomalies from the Higgsino, therefore it is a 2HDM theory and predicts five physical scalars, as mentioned before.

In addition, a new quantum number is introduced, the R-parity,

$$R = (-1)^{3(B-L)+2S} \tag{1.65}$$

where B is the baryon number, L is the lepton number, and S is the spin. The parity has a value of +1 for SM particles and -1 for the SUSY particles. The R-parity is conserved in the MSSM and, as one of the consequences, the lightest SUSY particle (LSP) is stable and has a negligible coupling with the SM particles making it a candidate for DM.

Since the discovery of the Higgs boson, it is usual to interpret either of the CP-even neutral scalars (h or H) of the theory to be the SM Higgs. One method to do this is by working in the decoupling limit, where all the SUSY particles and non-standard Higgs bosons are assumed much heavier than the EW scale, making h scalar behave just like the SM Higgs boson. Another method involves comparing the SM Higgs couplings to the different SM particles. The hMSSM model [52] is a simplified version of the MSSM, and the couplings of the new Higgs particles to the SM can be easily written and compared to the SM Higgs couplings,

$$g_{H_{\text{SM}}VV} \quad \rightarrow \quad H_{\text{SM}} = H\cos(\beta-\alpha) + h\sin(\beta-\alpha) \tag{1.66}$$

$$g_{H_{\text{SM}}u\bar{u}} \quad \rightarrow \quad H_{\text{SM}} = H\frac{\sin\alpha}{\sin\beta} + h\frac{\cos\alpha}{\sin\beta} \tag{1.67}$$

$$g_{H_{\text{SM}}d\bar{d}} \quad \rightarrow \quad H_{\text{SM}} = H\frac{\cos\alpha}{\cos\beta} - h\frac{\sin\alpha}{\cos\beta} \tag{1.68}$$

with V being the massive gauge bosons. Taking the so-called alignment limit, $\cos(\beta-\alpha) \rightarrow 0$, the h behaves like the SM Higgs, while H becomes gauge-phobic. The couplings to gauge bosons is particularly important, as they arise from the gauge invariance and do not depend on the particular MSSM model.

In this thesis, hMSSM model predictions are used as it is a very simplified model focused on the Higgs sector, making it easy to study. This is primarily due to the presence of only two free parameters in the Higgs sector: M_A and $\tan\beta$. Asides from the alignment limit, the model has different assumptions that lead to the h mass set to the SM Higgs mass, the Higgs couplings to depend only on the angles, and with the phenomenology to not depend on the usual SUSY parameters, like the SUSY scale (M_S). However, even if the $\tan\beta$ and M_A can have a wide range of possible values, the implication of reaching very low values of $\tan\beta$ ($<< 1$) is to consider a large M_S scale or other fine-tuned scenarios. On the other hand, high values of $\tan\beta$ ($>> 50$) push the M_S towards EW scale, which has been ruled out for many years. Although it is convenient to obtain predictions from the hMSSM model, the underlying SUSY parameters have important phenomenology implications and their elusion in the model is not always appropriate to define benchmark scenarios.

Five additional benchmark models [53] designed for MSSM Higgs searches are contemplated in this thesis. In contrast with the hMSSM, they are updated with current LHC results and fix the different underlying SUSY parameters. The $\text{M}_{\text{h}}^{125}$, $\text{M}_{\text{h}}^{125}(\tilde{\chi})$, $\text{M}_{\text{h}_1}^{125}(\tilde{\tau})$, $\text{M}_{\text{h}}^{125}$(alignment) and $\text{M}_{\text{h}}^{125}$(CPV) have two free parameters $\tan\beta$

and M_A, and are designed to accommodate one of the CP-even Higgs bosons close to 125 GeV, while preserving the key features of the MSSM Higgs sector. The $M^{125}h$ model, also known as the 'vanilla' scenario, focuses on the decoupling limit where the heavy Higgs states are decoupled from the light ones, providing a Higgs boson similar to the SM. The $M^{125}h(\tilde{\chi})$ model incorporates light neutralinos as the lightest SUSY particles (LSPs), accounting for potential dark matter candidates in the MSSM. The $M_{h1}^{125}(\tilde{\tau})$ scenario explores the possibility of enhanced third-generation couplings, particularly through the involvement of stau (the SUSY partner of the tau lepton) co-annihilation processes. This model helps to probe the impact of the SUSY sector on the Higgs sector. The $M^{125}h$(alignment) scenario focuses on alignment limit. Lastly, the M_h^{125}(CPV) scenario investigates the explicit CP violation in the Higgs sector, which can result from complex phases in the MSSM parameters. This can lead to a mixing of the CP-even and CP-odd Higgs states, affecting their masses and couplings.

The ATLAS experiment at the LHC 2

The study of particle physics is performed at the TeV scale in energy, equivalent to distances in the order of 10^{-15} m, which requires large and complex machines only possible within international collaborations. CERN is one of the biggest and renowned laboratories and, since its origin in the 1950s, has hosted many ground-breaking experiments. The Large Hadron Collider (LHC) [54] is the current world's largest particle accelerator, situated underground in the France-Swiss border and in operation since September 2008. The ATLAS detector [55] (A Toroidal LHC ApparatuS) is one of the experiments hosted within the LHC and records its particle collisions for further data analysis. The work in this thesis is based on the recorded proton-proton collision data at a center-of-mass energy, $\sqrt{s}$, of 13 TeV between 2015 and 2018.

This chapter starts with an overview of the LHC, describes how protons are made to collide and summarises of the operational parameters of the accelerator. Then, the ATLAS detector is presented and a description of the different sub-detectors is given.

2.1 The LHC

The LHC is a circular particle accelerator with a circumference of 27 km, situated on average 100 m underground. The primary activity is colliding protons. However, proton-Pb and Pb-Pb collisions are also performed typically for one month per year. Particles are steered, collimated and boosted by different types of superconducting magnets and structures along the accelerator ring.

Proton beams circulate through different accelerators before reaching the LHC and the designed energy. Figure 2.1 shows a schematic view of the CERN accelerator complex. First, protons are extracted from ionised hydrogen and accelerated up to 50 MeV in the LINAC2, a linear accelerator. Then, protons are injected into the Proton Synchrotron Booster (PSB), an accelerator made of four synchrotron rings of 157 m in circumference, increasing the energy up to 1.4 GeV. After, the protons are accelerated in sequence to 26 GeV and 450 GeV by the Proton Synchrotron (PS), a circular accelerator of 628 m in circumference, and the Super Proton Synchrotron (SPS), of 6.9 km in circumference. Finally, the protons are injected to the two beam pipes of the LHC and boosted up to 6.5 TeV, during the 2015-2018 period, before colliding. For the Pb operations, the extraction and accelerators prior to the SPS are performed using the LINAC3 and the Low Energy Ion Ring (LEIR) instead.
Inside the LHC, two particle beams travel close to the speed of light before they are made to collide. The two separated particle beam pipes are designed to operate at 7 TeV in opposite directions and kept at ultra-high vacuum, below 10^{-13} atmospheres in pressure. Surrounding the pipes, superconducting magnets built from niobium-titanium alloy coils generate strong magnetic fields of the order of 8 T through an electric current of 11.8 kA. The magnet coils are surrounded by the magnet

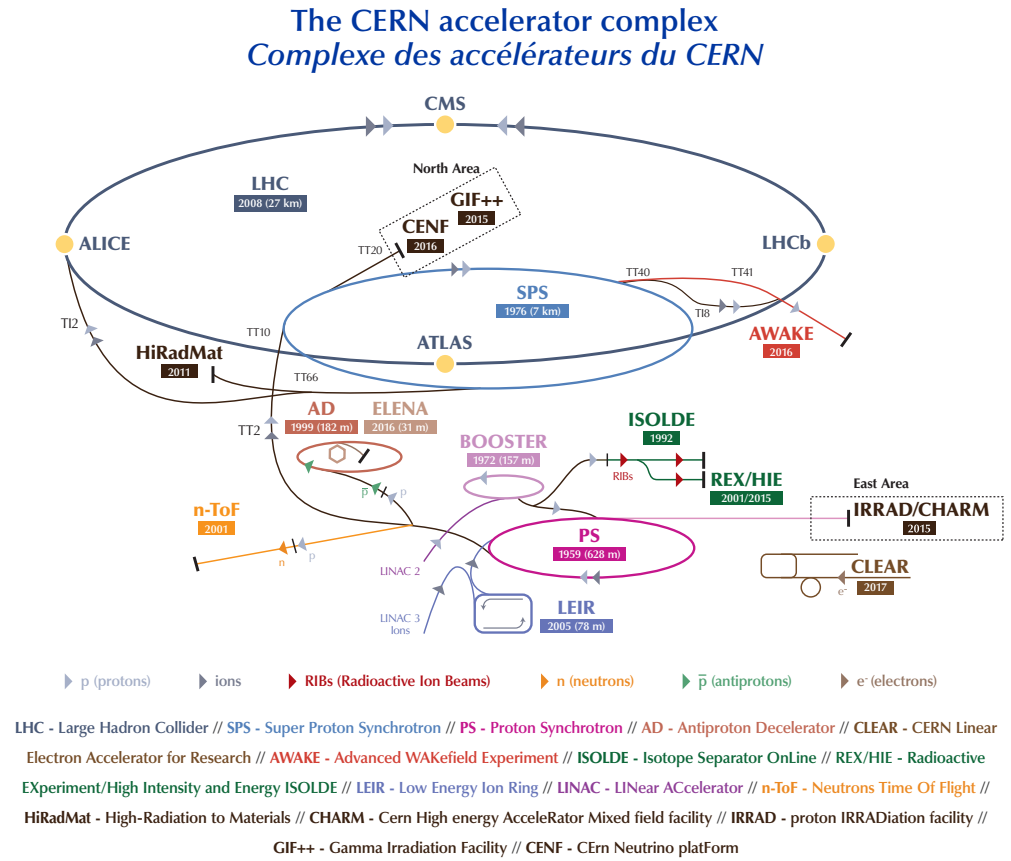

Figure 2.1: Schematics of the CERN accelerator complex, with the different accelerators and detectors [56].

yoke, tones of solid steel sheets designed to keep the wiring firmly in place and stabilise the temperature of the magnets. The magnets are cooled down to 1.9 K with superfluid helium provided by a cryogenic system requiring 120 tonnes of helium. The rest of external layers is dedicated to shield the particle radiation, insulate the magnet or maintain the vacuum and the whole structure. Different types of magnets constitute the accelerator: mainly 1232 dipole magnets of 15 m in length and up to 28 tonnes in weight that bend the particle beams to follow the circular trajectory, and 392 quadrupole magnets, each 5-7 m long, which focus the beams. Other types of magnets are used to correct the beam shape or to align the beams for collision. Figure 2.2 shows the cross-section of a dipole magnet of the LHC, and its different components.
Particles in each beam pipe are accelerated by 8 superconducting radiofrequency (RF) cavities, metallic chambers with alternating electric fields housed in cryogenic chambers, which also space the particles into compact groups named bunches. When protons are accelerated, the bunches contain more than 10^{11} protons spaced every 25 ns (around 7 meters).

The particles are brought to collision at interaction points (IPs) by multiple superconducting magnets focusing the beams. Four detectors are situated at the different

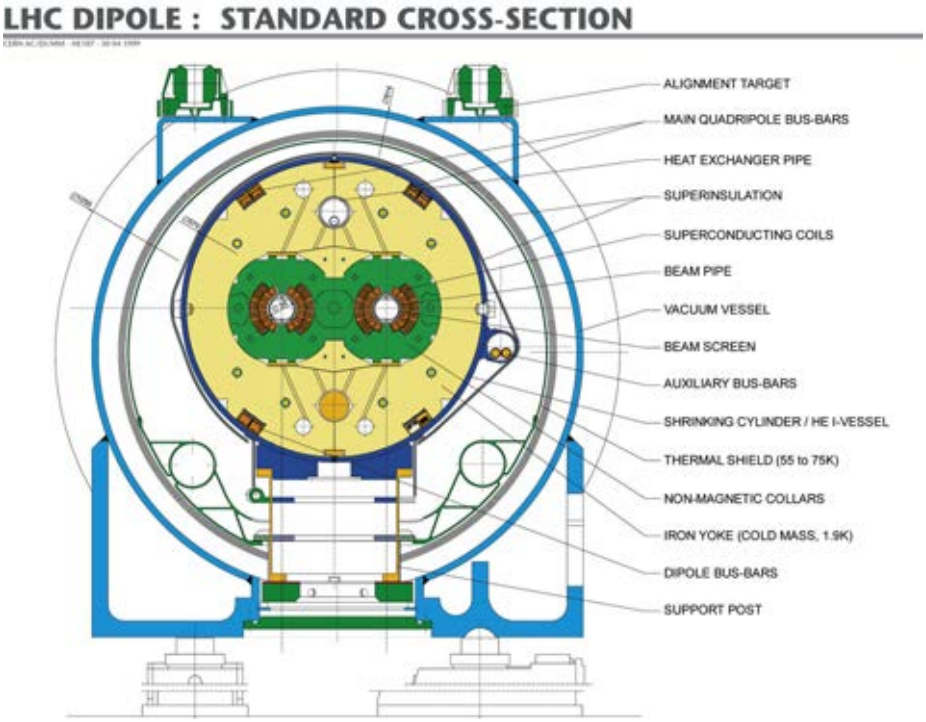

Figure 2.2: Diagram showing the cross-section of an LHC dipole magnet [57].

IPs: ATLAS, CMS [58], LHCb [59] and ALICE [60]. The first two are multi-purpose experiments that study a wide range of physics, comprising precision measurements of the SM as well as searches for beyond the SM such as Supersymmetry, exotic particles or dark matter. Both collaborations are formed by around 3000 scientists each, the two largest at CERN. The LHCb experiment is dedicated to explore hadrons containing $b-$ or $c-$quarks, especially investigating CP-violating processes. The ALICE experiment is the only experiment fully focused on heavy-ion collisions and therefore specialised on QCD physics.

The Large Electron-Positron Collider (LEP) [61] was the previous main experiment at CERN and its operations finished in 2000 to start the installation of the LHC in the same tunnel, replacing the predecessor. LEP was designed to collide e^+ and e^- beams and operated at a maximum of $\sqrt{s} = 209$ GeV. Instead, the LHC was designed to accelerate protons or lead ions, which are easier to accelerate to higher energies than eletrons and positrons and provides more collision data, although it is more challenging to study. LEP explored the EW scale and provided precision measurements of the SM setting a lower bound for the mass of the Higgs boson, later discovered using LHC data in 2012. In September 2008, the first LHC operations started and in November 2009 the first collisions were produced.

2.1.1 Performance in Run 2

The number of events of a certain process is key for its study and can be written as

$$N = \sigma\mathscr{L} = \sigma \int \mathcal{L}\mathrm{d}t, \tag{2.1}$$

where σ is the event cross-section for the given process, $\mathscr{L}$ the integrated luminosity and $\mathcal{L}$ the instantaneous luminosity. The cross-section highly depends on the center-of-mass energy $\sqrt{s}$, one of the main characteristics of a particle collider. As a general rule, σ increases with $\sqrt{s}$, which is important for SM precision measurements or searches for new massive particles.

The instantaneous luminosity is another of the main characteristics of a particle collider, and for the LHC can be approximated [62] to

$$\mathcal{L} = f\frac{n_1 n_2}{4\pi\sigma_x\sigma_y}F, \tag{2.2}$$

with f the revolution frequency, $n_{1,2}$ the total number of protons in each beam and F a reducing factor accounting for the beams not colliding exactly head-on as well as other geometric and beam effects. The first parameter can be approximated to $f = c/27\,\mathrm{km} = 11\,\mathrm{kHz}$ and the total number of protons can be inferred from the nominal number of bunches, 2808, which can contain up to 10^{11} protons. Finally, the denominator is the approximated transverse beam area with transverse beam size $\sigma_{x,y} = 16.6\,\mu\mathrm{m}$. With these assumptions, the instantaneous luminosity is of $\mathcal{O}(10^{34}\,\mathrm{cm}^{-2}\mathrm{s}^{-1})$.

During 2010 and 2011, the LHC delivered proton collisions at $\sqrt{s} = 7$ TeV, and in 2012 at $\sqrt{s} = 8$ TeV. The first proton physics run, namely Run 1, ended in February 2013, and were used for the discovery of the Higgs boson. The evolution of the integrated luminosity delivered during Run 2 to the ATLAS experiment is shown in Figure 2.3(a) for a total of $\mathscr{L} = 139\,\mathrm{fb}^{-1}$ to be used in physics analysis.

Another parameter of interest is the *pile-up*, which is the name given to the additional expected inelastic collisions that occur when crossing bunches of protons. The main source of pile-up interactions are the collisions that appear within a single bunch crossing, called in-time pile-up. In addition, out-of-time pile-up is referred to interactions from neighbouring bunch crossings not resolved fast enough by the detectors. Pile-up effects are a challenge for physics analysis and are inherent to the increase of instantaneous luminosity.

The mean number of interactions per crossing, $\langle\mu\rangle$, is a measure to quantify the pile-up and has changed throughout Run 2, as shown in Figure 2.3(b). Table 2.1 summarises of some LHC operation parameters during Run 1 and Run 2.

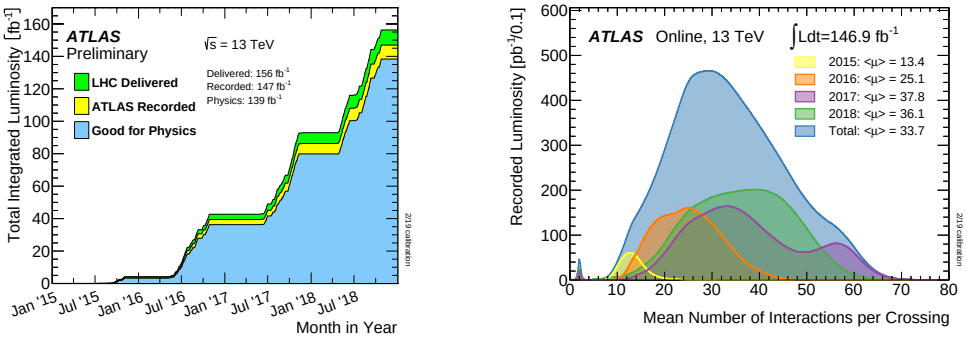

(a) **(b)**

Figure 2.3: The total integrated luminosity delivered by the LHC, recorded by ATLAS and labelled good for physics during Run 2 (a) and the mean number of interactions per bunch crossing split into the different data taking periods in Run 2 and weighted by the corresponding luminosity (b) [63].

Table 2.1: Overview of of the main LHC operational parameters for Run 1 and Run 2 in ATLAS [63, 64].

Parameter	2010	2011	2012	2015	2016	2017	2018
Center-of-mass energy [TeV]	7	7	8	13	13	13	13
Integrated luminosity (fb^{-1})	0.47	5.5	23	4.0	38.5	50.2	63.4
Peak luminosity [10^{33} $cm^{-2}s^{-1}$]	0.2	3.6	7.7	5.0	13.8	20.9	21.0
<Interactions/crossing>	~2	9.1	20.7	13.4	25.1	37.8	36.1
Bunch spacing [ns]	150	50	50	25	25	25	25

2.2 The ATLAS experiment

The ATLAS detector is a multi-purpose particle detector used to study a wide range of physics topics. It is installed 100 m underground at IP-1 of the LHC. Being 25 m in diameter, 44 m in length and 7000 tonnes in weight, ATLAS is the largest particle detector ever built and installed at a collider. The detector is illustrated in Figure 2.4. It has a cylindrical shape and is composed of several detector layers built around the collision point of the particles, with an almost full solid angle coverage.

The data recorded by the detector is used by the collaboration in an extensive physics programme. The luminosity provided by the LHC is large enough to perform both SM precision measurements and searches for new physics phenomena. The data collected during Run 2 are used to study the Higgs boson and its properties, which has been heavily scrutinised since the first observation of the particle. In addition, measurements of the interactions and processes involving the top-quark are particularly interesting to probe the SM and BSM theories. A large portion of the programme is dedicated to a wide range of BSM theories, which include searches for supersymmetry, dark matter or additional resonances among others. Finally, the physics programme also includes the study of the physics involving $b-/c-$quarks as well as heavy ions.

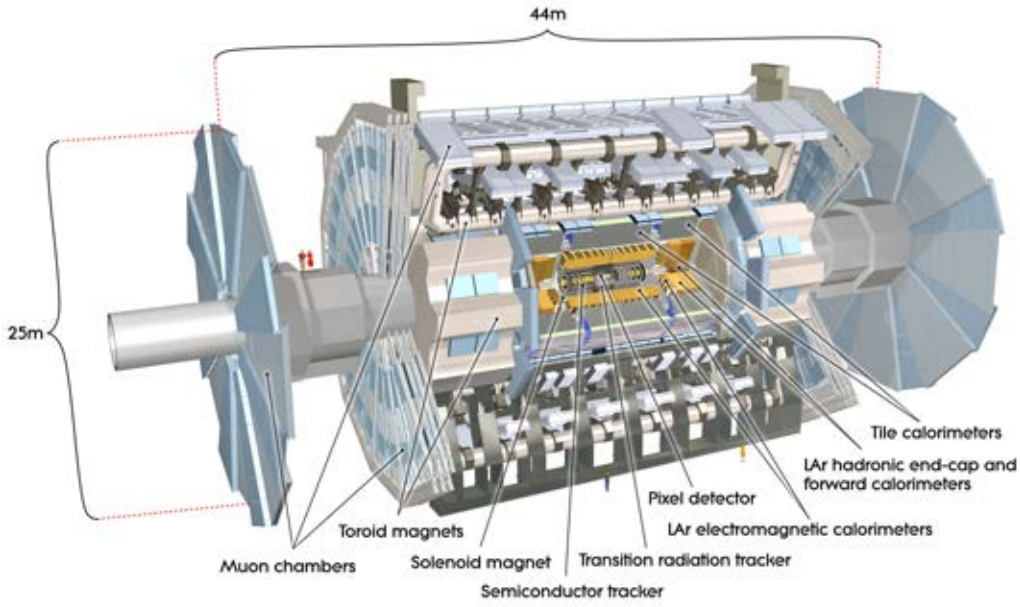

Figure 2.4: Schematic overview of the ATLAS detector [65].

All detector systems are designed such that they provide optimal performance to fulfil the physics programme. For that, it is important that the detector can identify particles ranging from few GeV to several TeV with high efficiency and resolution, providing accurate measurements of position and momentum. On the other hand, the electronics have to be highly resistant to radiation and fast to readout to withstand the high energy collisions provided by the LHC.

2.2.1 Coordinate System

The convention to describe the particles recorded with the ATLAS detector is a right-handed coordinate system as illustrated in Figure 2.5, with the origin at the center of the detector which is also the interaction point. The z-axis is defined in the counter-clockwise direction along the LHC beam line, the y-axis pointing towards the surface and the x-axis towards the center of the ring defined by the accelerator. To describe the physics objects within the detector, spherical coordinates are used instead, with the polar angle, θ, measured from the z-axis while the azimuthal angle, ϕ, measured from the x-axis in the $x-y$ plane. The pseudorapidity, η, is usually used instead of the polar angle, as it transforms easily under relativistic boosts along the z-axis. For particles with energy E and forward momentum p_z, the expression of η can be found from the rapidity, y, in the high-energy approximation,

$$y \equiv \frac{1}{2}\ln\left(\frac{E+p_z}{E-p_z}\right) \xrightarrow[\frac{m}{E}\to 0]{} -\ln\left(\tan\frac{\theta}{2}\right) \equiv \eta \tag{2.3}$$

ATLAS covers the pseudorapidity region up to $|\eta| < 4.9$, although physics analyses

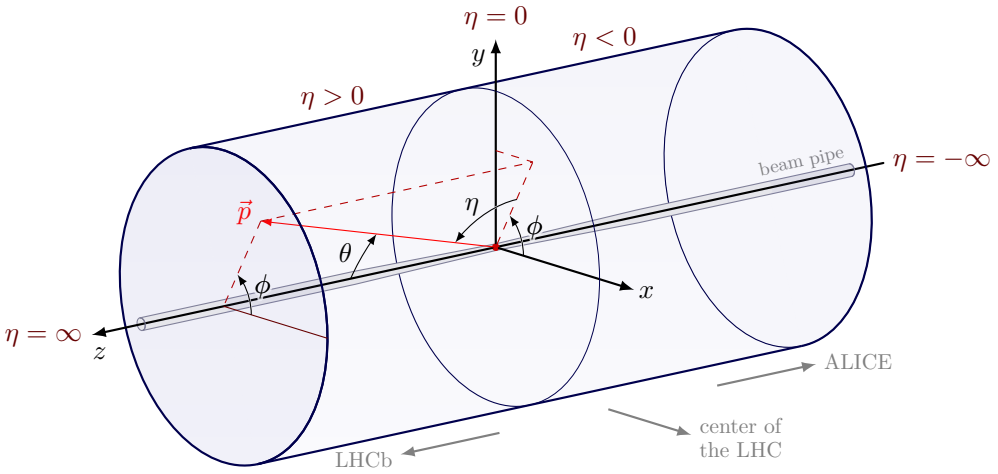

Figure 2.5: Schematic overview of the ATLAS coordinate system.

typically consider objects restricted to $|\eta| < 2.5$. In addition, the difference in η between two points, $\Delta\eta$, is invariant under Lorentz transformation, thus angular distances (ΔR) can be described in the $\eta - \phi$ plane as

$$\Delta R = \sqrt{(\Delta\eta)^2 + (\Delta\phi)^2}, \tag{2.4}$$

with $\Delta\phi$ the difference in ϕ.
Another useful expression is the momentum in the $x - y$ plane,

$$\vec{p_T} = \begin{pmatrix} p_x \\ p_y \end{pmatrix}, p_T = \sqrt{(p_x)^2 + (p_y)^2}. \tag{2.5}$$

As at the time of the collision the particles are made to collide along the z-axis, the initial momentum of the transverse plane is known to be zero due to energy conservation.

2.2.2 The Inner Detector

The Inner Detector (ID) [66–68] is the innermost detector system, which encloses the beam pipe. This detector system provides precise tracking information of charged particles with momentum as low as 100 MeV with a $|\eta| < 2.5$ coverage. Figure 2.6 shows an overview of the system, which is structured into three sub-detectors: the pixel detector, the semiconductor tracker (SCT) and the transition radiation tracker (TRT).

Pixel Detector

The innermost part of the ID is the silicon pixel detector comprising 4 cylindrical layers and 2 end-caps with 3 disc layers each. The layers are located between 33.25 mm to 122.5 mm around the beam pipe with a coverage of $|\eta| < 2.5$. A single 3D pixel is a radiation-hard silicon detector that produces a small measurable current when a charged particle passes through.

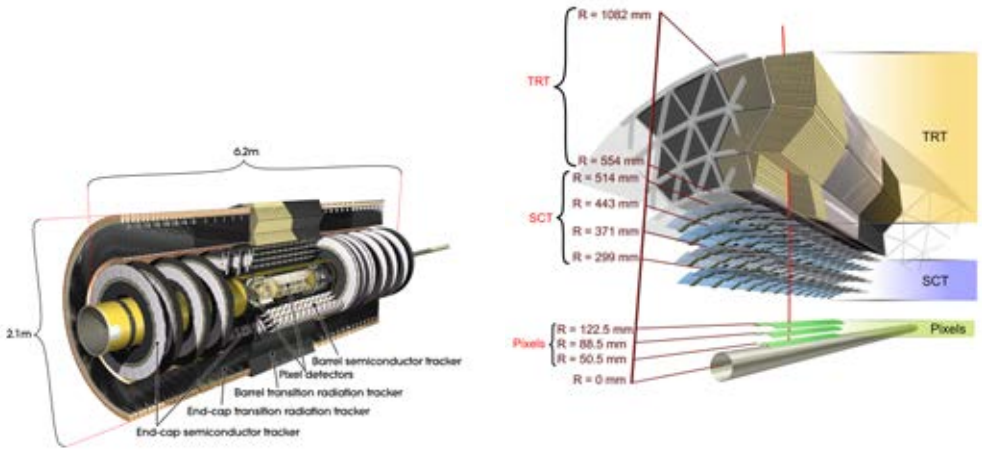

(a) **(b)**

Figure 2.6: Schematic view of the ATLAS Inner Detector (a) and details of its barrel section (b) [65].

The detector is especially important for the reconstruction of tracks, the path followed by charged particles; for the reconstruction of the primary vertex, the position of the main energetic collision; as well as for secondary vertex finding, the position of other concurrent collisions. The insertable b-layer (IBL) [69] is the innermost layer, installed in-between Run 1 and Run 2, having the highest granularity with a pixel size of 50×250 μm^2 (50 μm in the ϕ-direction and 250 μm in the z-direction) for a total of 12 M pixels. In particular, the IBL is very efficient to reconstruct secondary vertices, which are key signatures of long-lived particles decays and crucial for the identification of $b-$hadrons. Furthermore, the three remaining layers have a pixel size of 50×400 μm^2.

Overall, the pixel detector contains 86 M pixels with an expected hit resolution of 8×40 μm^2 for the IBL and 10×115 μm^2 for the rest of pixel layers. In addition, the system makes up around 50% of all ATLAS readout channels. For the next upgrade, the High Luminosity LHC (HL-LHC), a new fully silicon-based Inner Tracker Pixel detector (ITk) [70] will replace the ID.

Semiconductor tracker

The semiconductor tracker (SCT) [71, 72] is a silicon strip detector comprising 4 double layers in the barrel region and nine planar end-cap discs on each side, installed around the pixel detector. The planar strips technology is simpler compared to the silicon pixels, for lower resolution covering a larger area. The strips have a size of 80 μm×12 cm and cover a region up to $|\eta| < 2.5$. The two layers within one layer-module are tilted by 40 mrad.

Overall, the SCT has a resolution of 17×580 μm^2 with a total of 6.3 M readout channels. In general, the semiconductor-based detectors in ATLAS operate at a

temperature between -10 °C and -5 °C to suppress different types of electronic noise.

Transition Radiation Tracker

The outermost part of the ID is the transition radiation tracker (TRT) [73, 74]. In contrast to the others, the TRT is not based on silicon but is a gaseous detector system. It consists of around 300 k straw tubes with a diameter of 4 mm filled with a gas mixture[1] of Xe (70%), CO_2 (27 %) and O_2 (3 %) and with a gold-plated tungsten wire in the tube center with a potential different to the tube surface of 1.5 kV. When a charged particle hits the tube, the ionisation of the gas is detected as the signal. The straws have a length of 144 cm in the barrel region and 37 cm in the end cap, while the single hit resolution is 120 μm and 130 μm, respectively.

The TRT only provides tracking information in the ϕ direction, as the tubes are parallel to the beam line. Besides, the TRT provides particle identification from emitted transition radiation at the material boundaries, since the straws are interleaved with polypropylene. Especially, electrons can be distinguished from charged pions due to larger transition radiation.

2.2.3 The Calorimeter System

The calorimeter system is responsible for the precise measurement of the energy carried by both charged and neutral particles as well as measuring shower properties to allow for particle identification. Showers are cascades of secondary particles which are formed when a highly energetic particle interacts with dense material. ATLAS uses sampling calorimeters which consist of alternating layers of active material (liquid argon and plastic scintillators) and passive detector material (copper, iron, tungsten and lead). While the active material measures the energy deposit of the particles going through, the passive material is designed to interact and absorb particles, thus induces the showering.

The calorimeter system covers the region $|\eta| < 4.9$ and is placed between the central solenoid and the muon spectrometer. Figure 2.7 shows an overview of the system, which is composed of two sub-detectors: the electromagnetic [75, 76] and the hadronic calorimeters [77].

Electromagnetic Calorimeter

The electromagnetic (EM) calorimeter encloses the ID and is a high granularity calorimeter based on liquid argon (LAr) technology with absorber plates made out of lead.

To provide full coverage in ϕ, the EM calorimeter has an accordion-shaped structure where the active material is placed in the gaps between the lead absorber plates and the Kapton electrodes. The detector operates at -183 °C with a total of 170 k readout channels. The barrel region of the EM calorimeter covers the region $|\eta| < 1.475$ and consists of three layers with a 4 mm gap between them and a length of

[1] In Run 2, a mixture of Ar (80%) and CO_2 (20%) was used instead in modules with gas leaks

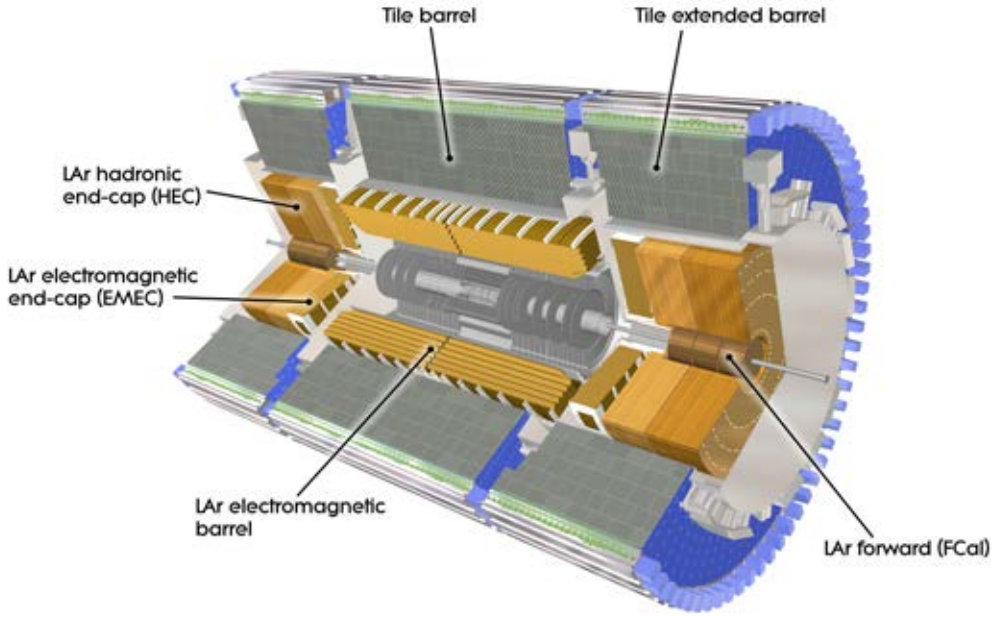

Figure 2.7: Schematic overview of the ATLAS calorimeter system [65].

3.2 m each, with decreasing granularity. The layer closest to the ID has a granularity of $\Delta\eta \times \Delta\phi = 0.0031 \times 0.098$, while the second layer $\Delta\eta \times \Delta\phi = 0.025 \times 0.025$ and the outermost $\Delta\eta \times \Delta\phi = 0.05 \times 0.025$. In addition, the two end-caps cover the region $|\eta| < 3.2$ with a slightly coarser granularity.

In general, the absorption power at high energies of a calorimeter is quantified by means of the radiation length X_0 of its medium. It is defined as the distance over which the particle energy is reduced via radiation losses by a factor $1/e$. Given in terms of the radiation length, the thickness of the barrel region is 22 X_0 while it is 24 X_0 for the end-caps. Moreover, the designed energy resolution [65] of the EM calorimeter is

$$\frac{\sigma_E}{E} = \frac{10\%}{\sqrt{E}} \oplus \frac{17\%}{E} \oplus 0.7\%. \tag{2.6}$$

Hadronic Calorimeter

The second calorimeter system in ATLAS is the hadronic calorimeter. The system is located around the EM calorimeter and consists of three components providing around 19 k readout channels. First, the tile calorimeter is made out of alternating layers of steel as absorber material and scintillator plastic tiles as active material, being read out via photomultiplier tubes. The first two layers have the highest granularity with $\Delta\eta \times \Delta\phi = 0.1 \times 0.1$. The barrel part of the tile calorimeter covers a region of $|\eta| < 1.0$ and the two extended barrels the range of $0.8 < |\eta| < 1.7$.

Next, the end-cap calorimeters are directly outside the EM calorimeter and are

based on the LAr technology. The end-caps use copper as passive material and cover a region of $1.5 < |\eta| < 3.2$ with their highest granularity of also 0.1×0.1 within $|\eta| < 2.5$. Finally, the forward calorimeter is also LAr based [78], and its first layer uses copper as absorber, which provides information for both electromagnetic and hadronic particles. The other two layers make use of tungsten as absorber, which is better suited for hadronic measurements. In total, the forward calorimeter covers a region of $3.2 < |\eta| < 4.9$. The designed resolution [65] of the tile calorimeter is

$$\frac{\sigma_E}{E} = \frac{50\%}{\sqrt{E}} \oplus 3\%. \tag{2.7}$$

2.2.4 Muon Spectrometer

The muon spectrometer (MS) is the outermost detector system of ATLAS, designed to identify muons and measure their energy. Figure 2.8 shows an overview of the system, which is composed of four detector systems grouped into trigger and precision muon tracking chambers [79, 80].

In total, the MS has more than one million readout channels and is embedded in three superconducting toroidal magnets, that provide a magnetic field in the ϕ-direction. Muons mostly reach the MS without losing energy, and the strong magnetic fields are designed for their precise measurement. The p_{T} resolution is around 3% for 10-200 GeV and 10% for 1 TeV muons.

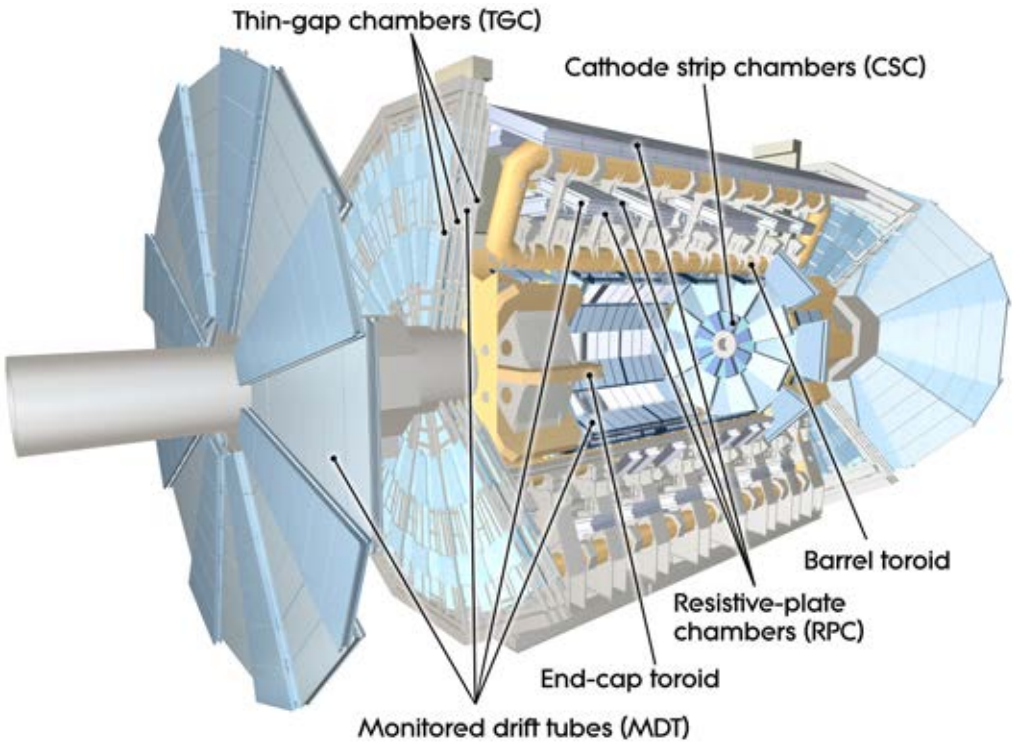

Figure 2.8: Schematic overview of the ATLAS muon spectrometer [65].

Muon Trigger Chambers

The muon trigger chambers are designed for a fast readout to provide energetic muon identification in a timescale compatible with every bunch crossing. In the barrel region, $|\eta| < 1.05$, three layers of resistive plate chambers (RPCs) consistsing of two parallel plates with high resistivity and filled with a gas mixture (94.7% $C_2H_2F_4$, 5% Iso-C_4H_{10}, 0.3% SF_6) are installed.

The RPCs provide an $\eta - \phi$ measurement with a spatial resolution of 10 mm and time resolution of 1.5 ns. Thin gap chambers (TGCs) are installed in the end-caps, $1.05 < |\eta| < 2.4$, and consist of multi-wire chambers filled with a gas mixture (55% CO_2 and 45% n-C_5H_{12}) with the wires separated by 1.8 mm. Besides trigger information, the TGCs provide ϕ information with a resolution of 5 mm.

Precision Muon Tracking Chambers

The precision muon tracking chambers are designed to provide high resolution and precision tracking information. The system is mainly composed of monitored drift tubes (MDTs), installed in the barrel and end-cap region covering $|\eta| < 2.7$. MDTs are aluminium drift tubes with 3 cm of diameter filled with a gas mixture (95% Ar and 7% CO_2). Each chamber contains 3-8 layers of drift tubes with a spatial resolution of 35 μm.

The forward region of the system, $2.0 < |\eta| < 2.7$, is covered by cathod strip chambers (CSCs) and provide a resolution of 40 μm in the radial direction and 5 mm in the ϕ direction [65]. These chambers are proportional multi-wire chambers, similar to the TGCs, with lower response time.

2.2.5 Magnet System

The magnet system is of major importance to allow momenta and charge measurements, bending the trajectory of charged particles depending on these properties. Figure 2.9 shows an overview of the system, which consists of two sub-systems: the central solenoid magnet, located between the ID and the calorimeters, and the toroidal magnet system, embedded within the MS.

The solenoid generates a constant magnetic field of 2 T, with a superconducting magnet made out of NbTi cooled via liquid helium to a temperature of 1.8 K. There is one barrel toroid magnet and two end-cap toroid magnets with eight coils each, each delivering an inhomogeneous magnetic field of roughly 0.5 T and 1 T, respectively.

2.2.6 Trigger System and Data Acquisition

With bunches crossing every 25 ns, the LHC produces collisions at a frequency of 40 MHz at nominal operation conditions. For ATLAS, this is translated to an unmanageable rate of more than 60 TB/s of data. The Trigger and Data Acquisition (TDAQ) system is designed to select and record the events considered interesting for analysis for an average storage rate of 1 kHz.

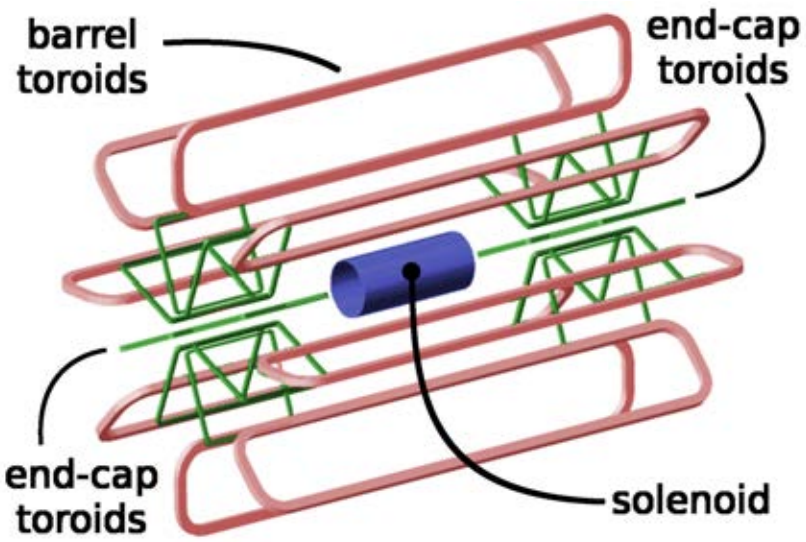

Figure 2.9: Schematic overview of the ATLAS magnet system [81].

The trigger system is structured into two parts since Run II [82, 83]: the Level-1 (L1) hardware-based trigger system and the software-based high level trigger (HLT). The L1 trigger uses reduced granularity information from the calorimeters and from the muon RPCs and TGCs to select events with interesting signatures (normally corresponding to high p_{T} electrons, muons, photons, jets or high missing transverse momentum). The L1 system reduces the rate from 40 MHz to about 100 kHz with a computing time (or latency) of 2.5 μs. The information of the collisions is stored in buffers and the Central Trigger Processor (CTP) performs the decision based on the inputs of the various L1 sub-systems. The L1 trigger output consists of regions of interest (RoIs) in η and ϕ, and are sent to the HLT. The HLT uses the full detector information within the RoIs to reduce the event rate down to approximately 1 kHz with a latency of 200 ms. A schematic of the ATLAS trigger system is presented in Figure 2.10.

After, the data is transferred to a computing center for further processing and storage. An offline data quality monitoring system performs checks on fully reconstructed events, to ensure their quality for use in physics analyses. Validation criteria include requirements on the condition and performance of the beams and different ATLAS sub-detectors at the time of operation. As displayed in Figure 2.3(b), from the 156 fb^{-1} of integrated luminosity delivered by the LHC during Run 2, 147 fb^{-1} were recorded by the detector and 139 fb^{-1} catalogued as good-quality data.

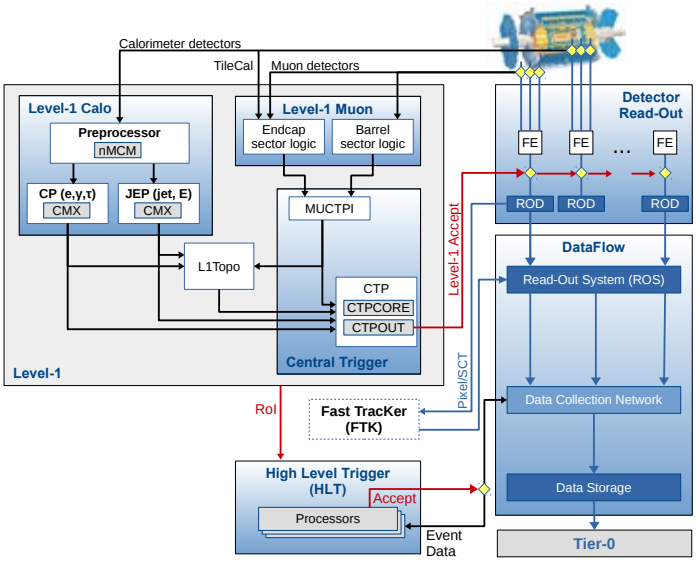

Figure 2.10: Schematic overview of the ATLAS Trigger and Data Acquisition system in Run 2 [84].

Physics simulation of proton collisions 3

Proton collisions are complex processes and their understanding is essential to interpret the experimental data from the LHC. Normally, physics analyses rely on the ability to accurately simulate the various processes of proton-proton collisions and the interactions with the detector in order to perform comparisons with the recorded data and quantify the level of agreement with the SM. The simulation is usually performed with Monte Carlo (MC) generators, which are stochastic tools that incorporate both theoretical predictions and empirical results to describe the statistical processes.

The simulation of proton-proton interactions is summarised in this chapter, with an overview of each of the steps, starting from the theoretical foundations, computational methods, MC generators and finalizing with the simulation of the ATLAS detector.

3.1 Event simulation

The typical proton-proton collision at the LHC is depicted in Figure 3.1. The inelastic scattering is the main interesting process, where the energy of the system is large enough and a constituent of each proton (parton) interacts, generating new particles. The interaction that involves any of the other partons, normally at lower energies, is referred to as underlying event.

A key phenomenon is the parton shower, a process where, due to the strong interaction, particles lose energy due to the radiation of gluons, which further generate quark-antiquark pairs, which in turn radiate gluons again in a chain reaction. These generated particles lose energy progressively down to the point where QCD leaves the perturbative regime (~1 GeV) and the hadronisation occurs, when quarks and gluons form hadrons, colourless bound states.

To complete the simulation of the collision, the pile-up is included, which adds the effects from the other proton collisions that originate from the same or previous bunch-crossing.

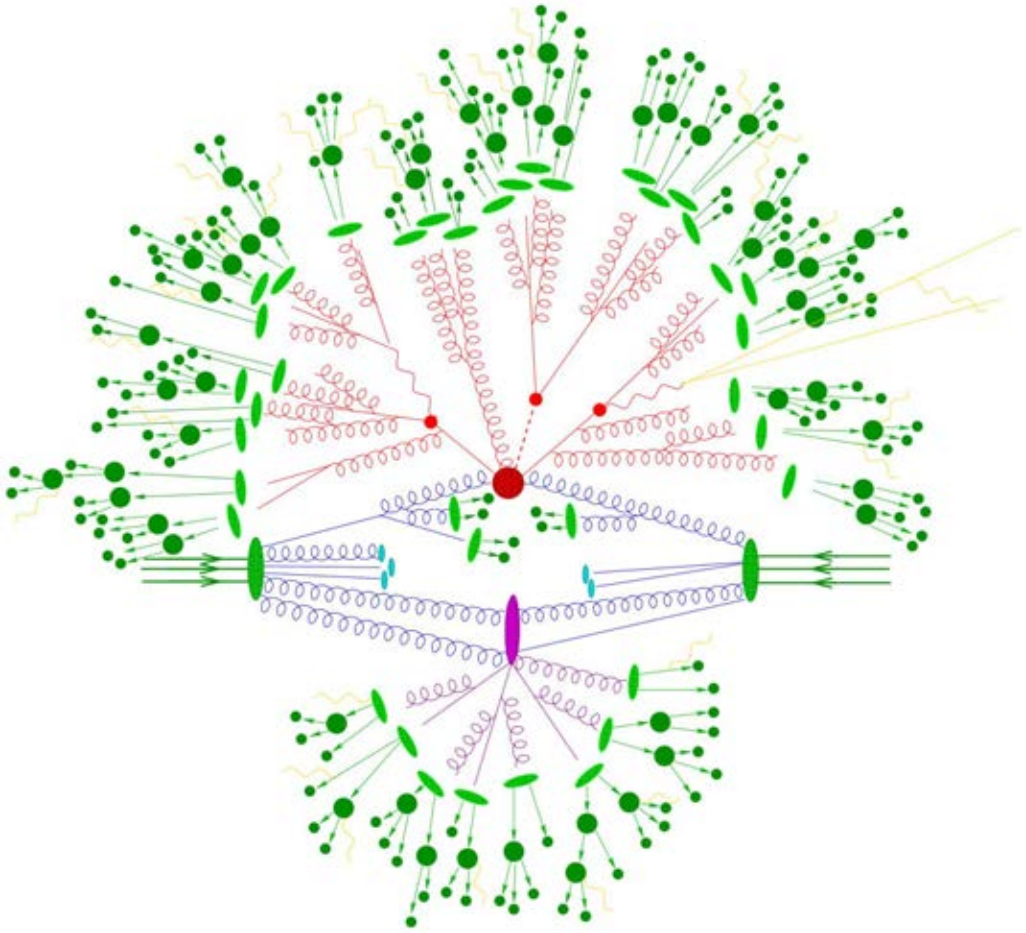

Figure 3.1: Illustration of a proton-proton collision as simulated by a Monte-Carlo event generator. The hard interaction (red blob in the center) is followed by the decay of two top-quarks and a Higgs boson (small red blobs). Additional QCD radiation is produced (red) before the final-state partons hadronise (light green) following hadron decays (dark green). Also, a secondary interaction (purple) and photon radiation (yellow) are represented. No pile-up effects are illustrated [85].

3.1.1 Factorisation theorem

The cross-section to produce a final state X from the hard scattering of two protons, $\sigma_{pp\to X}$ can be factorised into two components in perturbation theory, as the strong coupling constant, α_s, is small at high energy kinematic regimes. Using the factorisation theorem [86],

$$\sigma_{pp\to X} = \sum_{a,b} \int \mathrm{d}x_a \mathrm{d}x_b f_a(x_a, \mu_F^2) f_b(x_b, \mu_F^2) \cdot \hat{\sigma}_{ab\to X}(x_a p_a, x_b p_b, \mu_F^2, \mu_R^2), \quad (3.1)$$

where $f_i(x_i, \mu_F^2)$ are the parton distribution functions (PDF) for partons $i = a, b \in \{g, u, \bar{u}, d, ...\}$ and encode the probability of finding a parton of type i within the proton carrying a fraction of the proton's momentum x_i at the factorisation scale μ_F. The dependence of the scale appears from performing only fixed-order calculations and the value is typically set comparable to the energy of the process, for example, to the total transverse mass of the final-state particles. The partonic cross-section, $\hat{\sigma}_{ab\to X}(x_a p_a, x_b p_b, \mu_F^2, \mu_R^2)$, is calculated at finite perturbative order, hence the additional dependence on the renormalisation scale, μ_R, at which to evaluate α_s.

3.1.2 Parton density function

The PDFs are crucial for the accurate description of the partons that form the protons. The first type of partons are the valence quarks which determine the quantum numbers of the proton. In addition, gluons and virtual quark-antiquark pairs (sea-quarks) are also part of the proton and come from vacuum fluctuations. A PDF, $f_i^A(x_i, Q^2)$ describes the probability density of a parton of a certain type, i, inside a given hadron, A, to carry a certain momentum fraction, $x_i = p_i/p_A$ evaluated at a specific momentum transfer Q^2.

In general, the PDFs are extracted from empirical measurements performed at a specific scale. Then, the Dokshitzer-Gribov-Lipatov-Altarelli-Parisi (DGLAP) equations [87–89] are used to extrapolate the PDF to different scales. Other alternatives to extract the functions like using lattice QCD are possible, but very computationally challenging [90].

There are dedicated collaborations such as the *NNPDF*, *CTEQ* and *MSTW* that provide [91–93] PDFs for physics analyses. Figure 3.2 shows the *NNPDF3.0NLO* PDF set for the different proton partons and two different factorisation scales.

There are two main factorisation schemes that describe processes involving b-quarks: the four-flavour scheme (4FS) and the five-flavour scheme (5FS). The 4FS treats the b-quarks massive ($m_b > \mu_R$) and since $m_b > m_p$, they are not included in the sea of quarks and do not have an associated PDF. In the context of QCD perturbative evolution, one of the consequences is that calculations at lower scales $\mu_R < m_b$ are especially impacted as the α_s running depends on the number of quark flavours in the initial state, $n_f = 4$ (Equation 1.24). On the other hand, at high scales the mass effects are negligible and usually described by the 5FS, in which the b-quark is

considered massless, included in the initial state and treated as the other quarks, $n_f = 5$.

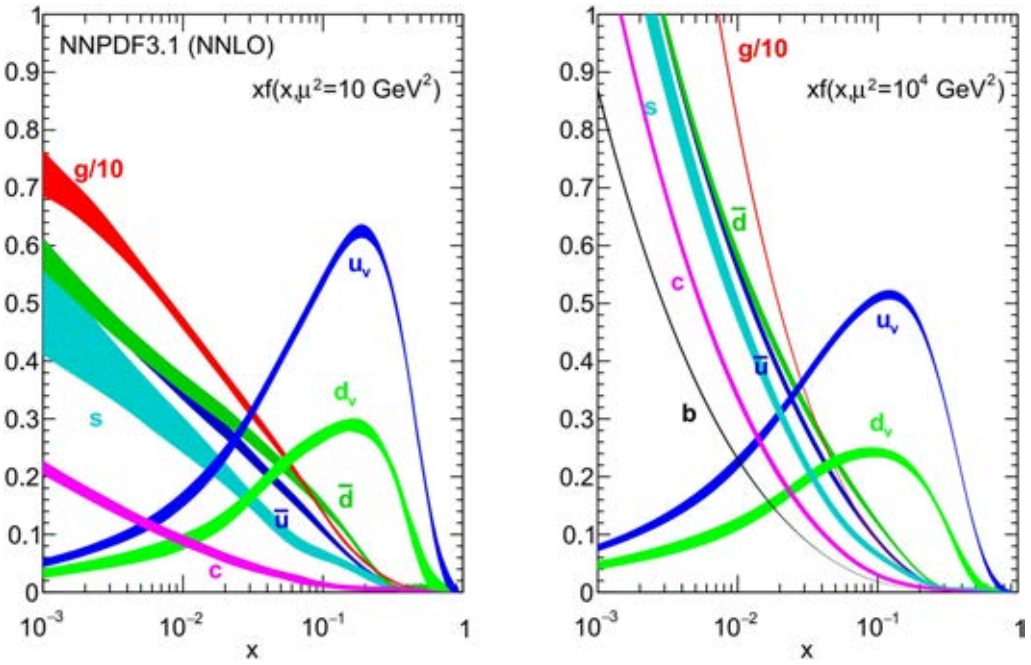

Figure 3.2: The parton distribution functions are shown for the factorisation scales $\mu_F^2 = 10$ GeV^2 (left) and $\mu_F^2 = 10$ TeV^2 (right) obtained with the *NNPDF3.1NNLO* global analysis [94].

3.1.3 Matrix element

The computation of the partonic cross-section of partons i, j into an arbitrary final state X, is related to the matrix element (ME) amplitude as,

$$\hat{\sigma}_{ij\to X} \sim \sum_{k=0}^{\infty} \int \mathrm{d}\Phi_{X+k} \left| \sum_{l=0}^{\infty} M_{X+k}^{l} \right|^2 (\Phi_F, \mu_F, \mu_R) \tag{3.2}$$

were PDFs and other normalisation factors are removed for compactness. M_{X+k}^{l} is the ME amplitude for the production of X in association with k additional final-state partons, or legs, and with l additional loop corrections. The quantity depends on the phase space Φ of the final state, μ_F and μ_R.

In a perturbative regime, the ME amplitudes for increasingly complex processes (diagrams with additional legs and loops) tend to decrease. As a result, the cross-section is generally computed at a perturbative order, without the sum computed to infinity and for a choice of μ_F and μ_R. The Leading Order (LO) is the lowest possible order for the calculation, with $k = l = 0$. Next, $l = 0, k = n$ provides the LO computation for the production of $X + n$ jets. Finally, $k + l \leq n$ corresponds to a N^{n}LO prediction for the production of X, while also to a N^{n-k}LO prediction for the production of $X + k$ jets.

3.1.4 Parton shower

One problem that arises in the fixed order computations of the differential cross-section is the appearance of logarithmic divergences from collinear splitting that originate from the integration of the phase space of the additional partons. For an inclusive cross-section computation, these divergences cancel out with virtual corrections order by order, following the KLN theorem [95, 96].

In this case, the base event is simulated at fixed order while the QCD emission process (splitting) is computed with the PS algorithm [97], which generates a sequence of emissions with decreasing angle or energy. The algorithm recursively produces the typical splitting processes ($g \to q\bar{q}$, $g \to gg$ and $q \to qg$) for each parton until the energy of the shower reaches ~1 GeV, the hadronisation scale. This showering process that is applied to the final products after the hard-scattering is referred to as final state radiation (FSR), while the simulation of the initial state radiation (ISR) is performed to the incoming partons. In the case of ISR, the subsequent emissions grow on energy and are modelled with a backwards-evolution algorithm [98].

There is an incompatibility with ME and PS for a full cross-section computation at order $n > 1$, as there is a potential overlap in the phase space of the extra partons that are considered for the ME at order n with the ones considered in the splitting at order $n - 1$. There are different approaches to solve the double counting, known as ME-PS matching. The most common strategy is known as slicing, which defines a matching scale where the higher energy region is covered only by the ME while any additional parton with energy below that scale is vetoed and only covered with the PS algorithm. With this strategy, both energy regions are described with the corresponding optimal algorithm.

3.1.5 Hadronisation

The hadronisation process starts when the energy of the PS emissions is low enough to reach the hadronisation scale (~1 GeV), where the perturbative regime of QCD is not valid. At that point, the partons from the PS have defined momentum, flavour and colour and further description of the emissions has to rely on phenomenological models. The process consists on a reconstruction algorithm that groups together the partons into different hadrons, that can further split, until all partons are confined into stable hadrons.

The two most widely used models are the Lund string model [99] and the cluster model [100]. In the first, the quark-antiquark pair colour interaction is described as a string with a potential assumed to be linearly increasing with the distance, emulating the QCD potential. The string then splits forming new quark-antiquark pairs when the energy stored passes the quark-antiquark total mass, forming hadrons whose momenta is determined from the initial momentum by a fragmentation function. On the other hand, the second model is based on forcing the final state gluons to split into quark-antiquark pairs and then grouping all quarks in colour-singlet clusters, allowed to decay and split into smaller clusters or hadrons. For both models, the process is repeated iteratively until only stable hadrons remain.

3.1.6 Pile-up and underlying event

Other interactions apart from the hard-scattering event have to be included in the MC simulations to properly model the LHC collisions, the pile-up and the underlying event. Both types of interactions mainly consist of soft QCD interactions, the first arising from other protons colliding in the same or previous bunch-crossing while the second being the interaction of the other partons that do not originate the hard-scattering process. Both mainly consist of soft QCD interactions in the forward region, close to the beam axis, and the simulation is based on the combination of phenomenological models and the configuration of the LHC beam. In the special case of out-of-time pileup (interactions from previous bunch-crossings), the simulation has to take into account the time response of the detector.

3.1.7 Monte Carlo simulation and generators

Monte Carlo (MC) generators are dedicated software tools to perform the MC simulations, based on pseudorandom numbers to generate the events with the predicted distributions. They are generally classified according to the steps the simulation can perform, with general purpose generators being capable of simulating the whole event process, while dedicated generators target specific parts of the simulation chain, such as the ME or the PS computation.

The full process involving ME generation, PS, underlying event and hadronisation can be simulated by MC generators like Pythia 8 [101] , Herwig 7 [102, 103] or Sherpa [104]. However, Pythia 8 provides leading order cross-section calculations which are often not sufficient and hence, the generator is typically used to compute the PS process, which is based on the Lund string model. On the other hand, Herwig 7 provides many ME calculations at NLO, however since the fraction of negative event weights can be quite large (up to $\sim 40\%$ for certain generator setups), the generator is also typically used for PS computation, based on the cluster model. PowhegBox [105–109] and MadGraph5_aMC@NLO [110] are examples of other generators that are especially designed to provide accurate high-order ME calculations, which are typically interfaced with Pythia 8 or Herwig 7 for the simulation of PS and hadronisation.

More in detail, these tools have parameters to describe the non-perturbative processes that can be tuned using collision data. The most common tunes used by the ATLAS collaboration are the A14 [111] parameters combined with *NNPDF3.0LO* PDFs set [112] for Pythia 8 and the H7UE set [103] with the *MMHT2014LO* PDFs sets [113] for Herwig 7. Throughout this thesis different combinations of MC generators and settings are used, they are detailed in the corresponding chapters. If not stated otherwise, the same parameters are shared. The mass of the top quark is set to $m_t = 172.5$ GeV, the mass of the Higgs boson to $m_H = 125$ GeV and the mass of the b-quark to $m_b = 4.8$ GeV for Pythia 8, to $m_b = 4.5$ GeV for Herwig 7 and to $m_b = 4.75$ GeV for Sherpa. The simulation involving b- and c-hadron decays for Pythia and Herwig is interfaced with EvtGen [114].

3.2 Detector simulation

With the proton-proton collisions simulated and the final-state stable particles defined, the remaining step is to simulate the interactions with the detector. The full ATLAS detector simulation is performed in two steps: first, the ATLAS detector response of the MC output is simulated, and then the signals are reconstructed using the same algorithms used in real data. Figure 3.3 depicts the different steps both for data and simulated MC events.

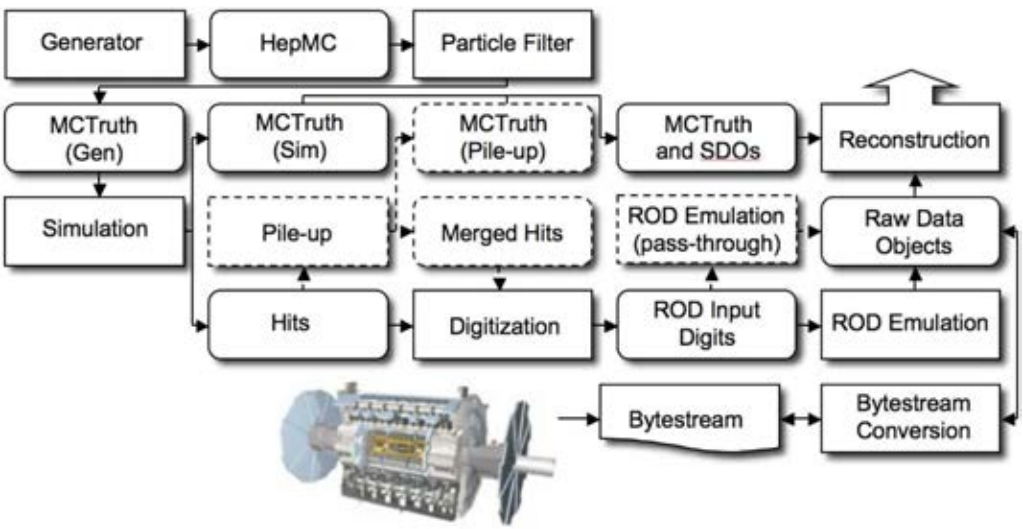

Figure 3.3: Schematic of the different steps for the full reconstruction procedure of data and MC events. Data events start next to the ATLAS detector, while MC events start at the "Generator", both ending at the "Reconstruction" block [115].

The GEANT 4 package [116] is widely used in physics to simulate the propagation and interaction of particles with matter. The simulation that includes all the geometry of the ATLAS sub-detector systems with GEANT 4 is referred to *Full Simulation* (Full-Sim), which is computationally expensive (several minutes per event) but gives the most accurate result. As more than 90% of the dedicated CPU time is spent on the calorimeter simulations, fast alternatives are used in practice. The *AtlFast-II* (AF-II) simulation is performed with faster simulation algorithms for the calorimeter simulation, ATLAS Fast Calorimeter Simulation (FASTCALOSIM) [117], and for the ID simulation, Fast ATLAS Tracking Simulation (FATRAS) [118]. The rest of the systems is simulated with GEANT 4 adding significantly less CPU time than the calorimeter or ID simulation while maintaining an adequate level of accuracy.

Finally, the normalisation of a SM process is normally chosen according to the cross-section at the highest-order available calculation and other corrections are applied in the form of scale factors (SFs), derived from the ratio between data and MC in specific calibration regions.

Object reconstruction 4

The concept of *reconstruction* refers to the use of algorithms for the identification of physics objects from the signals recorded in the different sub-systems of the detector. The physics processes described in this thesis produce electrons, muons, taus, photons, neutrinos and quarks in the final state. However, not all of these listed particles can be directly observed, as neutrinos leave the detector without interacting, tau leptons may decay before reaching ATLAS and quarks form jets. Therefore, it is necessary to define the physics objects measured in the detector.

The reconstruction of the different physics objects used in this thesis analyses is described in this chapter. It starts with the definition of basic detector objects, continues with the description of jets and their flavour tagging, and end with the reconstruction of leptons and missing transverse energy.

Figure 4.1 illustrates the interaction of different particles with the ATLAS detector. Charged particles produce a track in the ID, electrons and photons shower in the EM calorimeter, hadrons shower in the hadronic calorimeter and muons leave signals in the muon spectrometer.

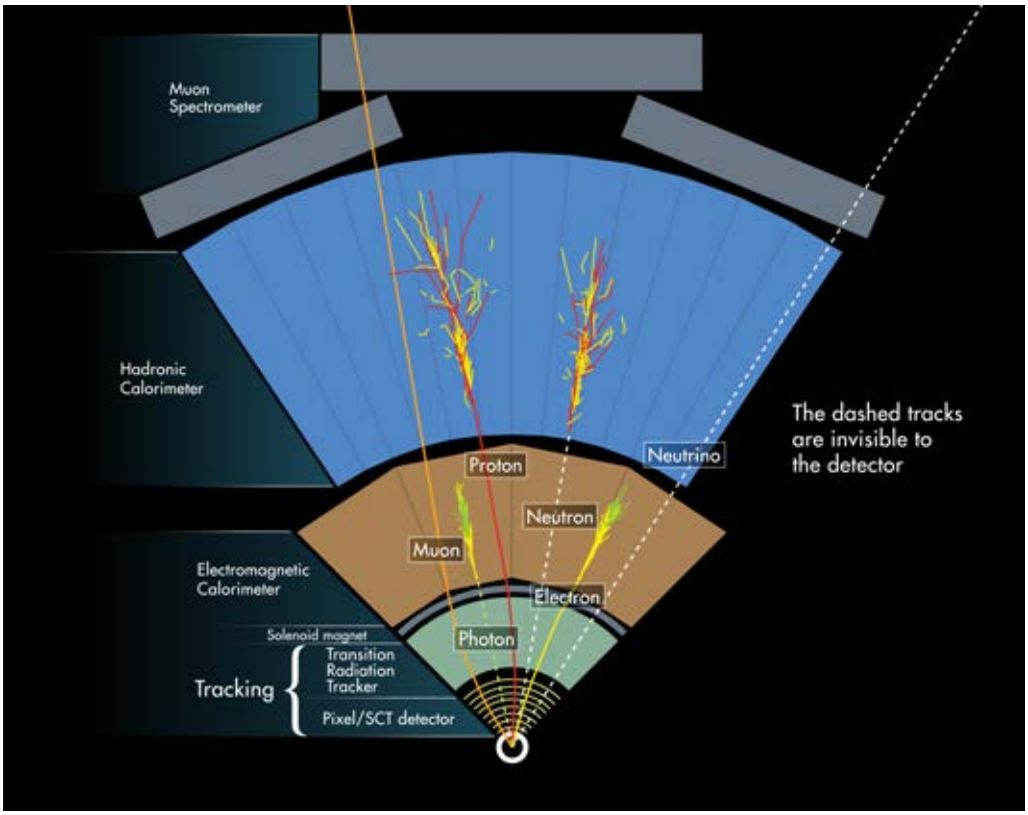

Figure 4.1: Illustration of a section of the ATLAS detector showing the interaction of particles with the different sub-detectors [119].

4.1 Basic objects

The fundamental blocks used in the reconstruction algorithms are tracks, vertices and topo-clusters (or calorimeter energy clusters). All physics objects are composed by these blocks and introduced in the following section.

4.1.1 Tracks and vertices

Tracks are reconstructed objects produced by charged particles interacting in the ID and MS and used to identify their trajectory. The reconstruction consists in grouping hits from the different tracking sub-systems and requiring different criteria to ensure the quality of the tracks. The tracks that originate from the hard-scattering are referred to as primary tracks, and the origin of the track (vertex) is referred to as the primary vertex (PV).

As a first step, hits are built from groups of pixels and strips that reach a threshold energy deposit. Starting from the inner ID layers, the seed to reconstruct a track consists of three hits in the silicon detector, and then hits from the outer layers of the tracker are added iteratively if compatible with the trajectory. When adding hits, a score is assigned to the track to quantify the correctness of the track trajectory and suppresses the contribution of random collections of hits (or fake tracks). Then, a dedicated algorithm evaluates the different seeds to limit shared hits, which typically indicate wrong assignments. In addition, quality criteria are applied: tracks are required to have $p_{\mathrm{T}} > 500$ MeV, $|\eta| < 2.5$, a minimum of seven pixel and SCT clusters, a maximum of either one shared pixel or two SCT clusters on the same layer, no more than one missing expected hit (or hole) in the pixel detector and a maximum of two holes in both pixel and SCT clusters. Also, the transverse impact parameter calculated with respect to the beam position, $|d_0|$, is required to be smaller than 2 mm. In addition, the longitudinal difference between the PV and d_0 along the beam, $|z_0 \sin\theta|$, is requiered to be smaller than 3 mm. As a last step, TRT hits are added to the tracks after extrapolation.

Vertices are of particular interest as they are the origin of the charged particles or interactions. The PV is the most important one, as it denotes the origin of the hard-scattering interaction, but secondary vertices are also characteristic of the origin of heavy-quarks or long-lived particles.

For a given event, the PVs are reconstructed iteratively from tracks using a dedicated vertex finding algorithm. From a set of quality tracks, a candidate position is defined and the compatibility with the set of tracks in terms of weights is evaluated in order to recompute the vertex position. In each step then, the tracks that are less compatible are given smaller weights and, after the convergence of the optimal vertex position, are left unassigned and remain as input for the following vertex. The PV is defined as the vertex with the largest p_{T}^2 sum.

4.1.2 Topological clusters

Topological cell clusters, or topo-clusters, are objects reconstructed iteratively from calorimeter information. The signal is from the energy deposited in the different calorimeter cells by particle showers. The seed of a topo-cluster consists of calorimeter cells whose readout signal is four times higher than the background noise, and neighbouring cells are added if the ratio is higher than two. As a last step, an extra layer is added regardless of the signal-to-background ratio. This clustering takes advantage of the high granularity of the calorimeters and the resulting objects are used for the reconstruction of electrons, photons and hadrons.

4.2 Jets

Jets are cone-shaped collimated showers formed by the hadronic cascades that originate from the complex interactions of quarks and gluons when travelling through the detector. These objects are essential for physics analyses with partons in the final state, especially b-quarks, whose jets have particular properties that can be used to characterise them with great efficiency. Nevertheless, the kinematic properties of the cascades are challenging to define, as they can contain information from one or multiple final state partons and from the hard-scattering or other radiation processes.

There are different possible definitions that depend of dedicated algorithms which group calorimeter information and do not depend on common QCD effects. Jet algorithms are collinear safe, referred to the jet configuration not changing if two constituents are merged forming one with double the momentum (or vice-versa), and infrared safe, meaning that the reconstruction is not affected by adding low p_{T} particles.

4.2.1 Reconstruction

The jet reconstruction is typically performed combining four-vector objects using the anti-k$_t$ algorithm [120]. The algorithm merges clusters based on a relative distance defined as,

$$d_{i,j} = \min(p_{\mathrm{T},i}^{2n}, p_{\mathrm{T},j}^{2n}) \frac{\Delta R_{i,j}}{R^2} \tag{4.1}$$

with $p_{\mathrm{T},i/j}$ being the p_{T} of the cluster i and j, $\Delta R_{i,j}$ the angle separation between them, R the chosen radius parameter that sets the size of the jet and n the chosen integer that defines the p_{T} dependence of $d_{i,j}$. The decision to combine clusters or to define a cluster as a jet comes from comparing the $d_{i,j}$ value with the beam spot distance, $d_{i,B} = p_{\mathrm{T},i}^{2n}$. Clusters are grouped if $d_{i,j} < d_{i,B}$, otherwise the cluster i is defined as a jet, in an iterative process until all input clusters are used. The anti-k$_t$ algorithm is defined by setting $n = -1$, which groups with higher priority the high energy clusters, and leads to a cone-shape around the highest object. This feature can be observed in Figure 4.2.

Various definitions of jets are used in ATLAS. In this thesis, EMTopo jets and PFlow jets are used and described in the following.

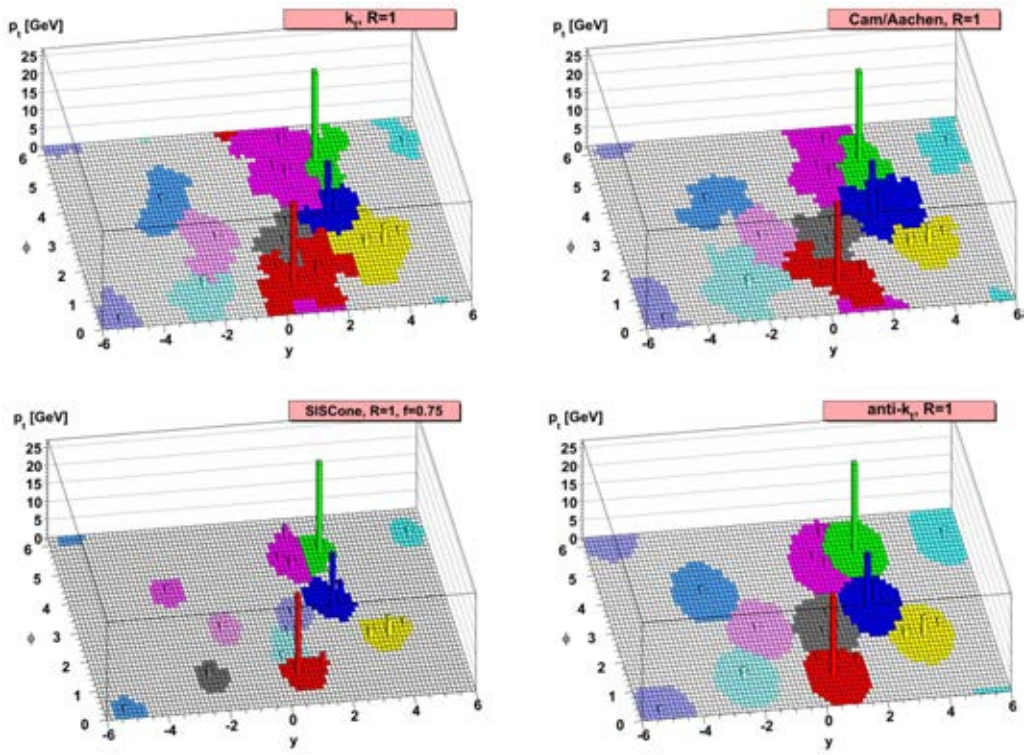

Figure 4.2: Illustration of different clustering algorithms. The anti-k$_t$ (bottom right) shows cone-like structure around the track with the highest momentum [120].

EMTopo jets

The so-called EMTopo jets are the primary jet definition used in physics analyses in ATLAS before the end of Run 2. The reconstruction is performed at the EM energy scale only using topo-clusters [121] with the anti-k$_t$ algorithm implemented in the *FASTJET* software package [122]. The jets used in this thesis are reconstructed with the radius parameter $R = 0.4$ with requirements in $p_{\mathrm{T}} > 25$ GeV and $|\eta| < 2.5$. The EMTopo jets are calibrated in several steps, summarised in Figure 4.3 and described below.

After the jet reconstruction, the jet direction is modified such that the jet originates from the primary vertex. Then, energy corrections based on pile-up are applied subtracting the average energy due to in-time pile-up and other residual corrections that depend on the number of PV; and bunch crossings. After, absolute calibrations are applied to the jet energy scale (JES) and η derived from dedicated dijet MC events. Then, a global sequential calibration is applied to improve the p_{T} resolution and the associated uncertainties from the jet fluctuations that can arise from various initial factors, like the flavour or energy of the original parton. The final step is the in-situ calibration, which is only applied to data and is extracted from jets p_{T} and η comparisons of data to known well-modelled MC that include central jets in dijet events, $\gamma/Z + jets$ or multijet events.

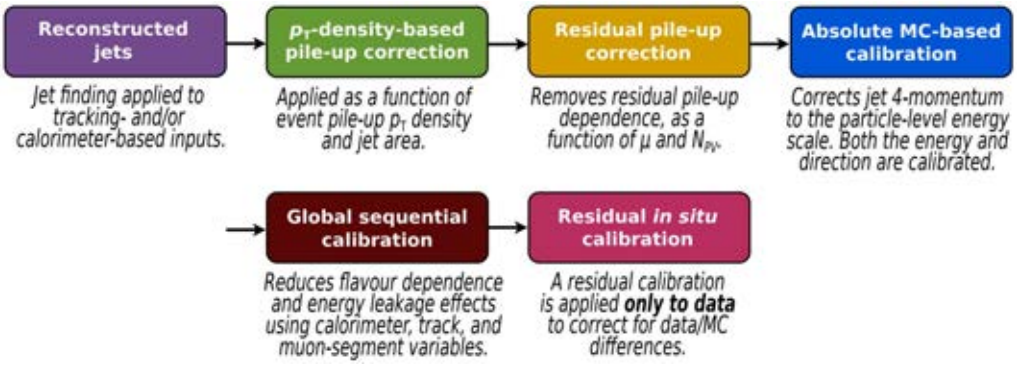

Figure 4.3: Stages of jet energy scale calibrations, all applied to the four-momentum of the jet [123].

PFlow jets

Particle Flow jets, known as PFlow jets, were introduced during Run 2 and combine tracking and calorimeter information. This type of jets has improved energy and angular resolution compared to EMTopo jets and enhanced reconstruction and stability against pile-up.

The reconstruction [124] is also based on the anti-k$_t$ algorithm with $R = 0.4$, and the first step consists in matching the tracks (from the ID) from charged particles to the topo-clusters. The energy deposits of the matched topo-clusters are replaced by the corresponding track momentum. Then, the resulting topo-clusters and the tracks matched to the PV are used as input to the anti-k$_t$ algorithm. The jets are calibrated like the EMTopo jets in the range 20 GeV $< p_{\mathrm{T}} <$ 1500 GeV [125].

4.2.2 Jet tagging

Jet or flavour tagging consists in identifying the parton flavour that generated the signal reconstructed as a jet. Efficient tagging is essential for analyses studying processes with b- or c-quarks in their final state (knows as heavy flavour quarks), as the jet tagging is additional information that can be used to select events with various jets and improves the signal efficiency.

Jets originating from the hadronisation of b-quarks, or b-tagged jets, leave a distinct signal due to the properties of b-hadrons: lifetime of $\sim 10^{-12}$ s (b's with $p_{\mathrm{T}} > 30$ GeV decay after 2.5 mm), mass of ~5 GeV and high decay multiplicity (including semi-leptonic decays). Figure 4.4 shows a scheme of a typical signal, that includes displaced tracks with large d_0.

The signal of the c-hadrons is similar but not identical as the lifetime, mass and decay multiplicity are lower, which makes the distinction between these two kinds of jets difficult. The last type of jet is referred to light-flavour jets, whose signal originates directly from quark fragmentation and can be easily separated from b-jets. However, other phenomena like long-lived particles, photon conversions or low quality tracks can also prompt displaced vertices and tracks.

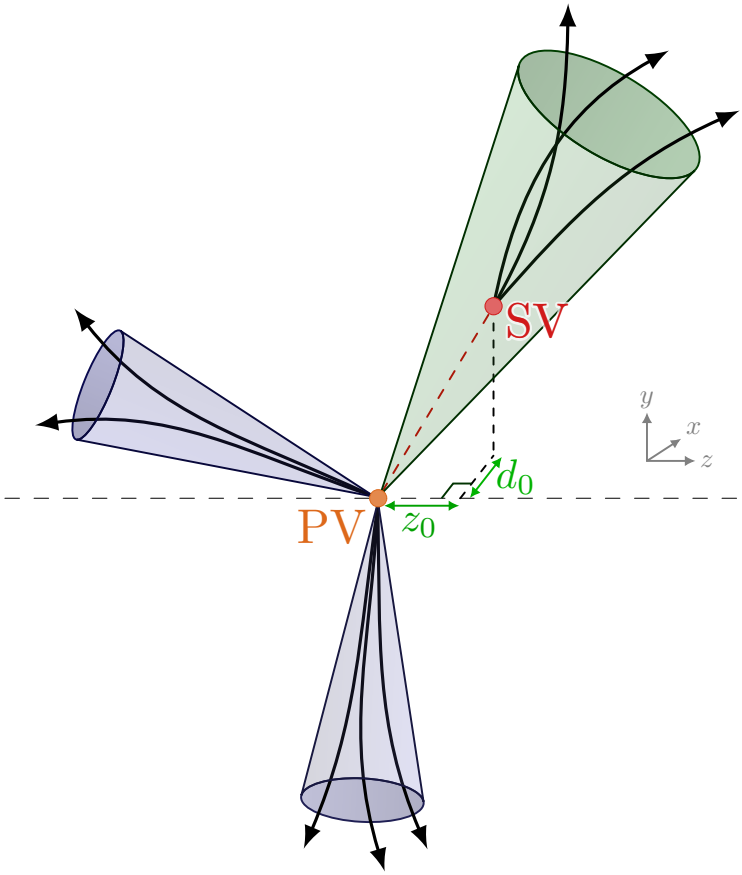

Figure 4.4: Schematic view of the typical topology of an event with a b-jet, including the PV, a secondary vertex (SV) with displaced tracks and the characteristic impact parameters, d_0 and z_0.

Algorithms

Flavour tagging algorithms use the properties of a given jet and return a score, referred to as output discriminant, which indicates how likely the input jet is considered to be a b-, c- or light-jet. Two algorithms are used in this thesis: the MV2c10 tagger which was the default option for EMTopo jets, and the DL1r tagger that is used for PFlow jets.

The MV2c10 tagger [126] is based on the MV2 algorithm, which relies on boosted decision trees (BDTs) trained using several kinematic variables of the jets, properties of the secondary vertices and other taggers as inputs. The MV2c10 tagger was trained with $t\bar{t}$ and Z' events, to cover a large p_{T} spectrum, and b-jets defined as signal while the background consisted of 7% c-jets and 93% light-jets.

The DL1r tagger [127] is a multi-class Deep Neural Network (DNN) model, with three output nodes corresponding to the classification of the input jet to be a b-, c- or light jet. The final discriminant is given as a function of the three probabilities. The input to the training consists in the same inputs used for the MV2c10 tagger,

additional variables for c-jet identification used in a jet vertex finder algorithm and flavour probabilities provided by a recursive NN designed to exploit the correlations between the tracks originating from the same b-hadron. The training set consists of the same $t\bar{t}$ and Z' events, weighted to have an equal mix of quark flavour jets.

The b-jet efficiency as a function of the jet p_{T} and the c- and light-jets rejection as a function of the jet b-jet efficiency for both MV2c10 and DL1r algorithms are shown in Figure 4.5. The DL1r tagger relies on more advanced machine learning techniques than the MV2c10 tagger. The multi-class output together with the possibility of tuning the final discriminant computation makes the DL1r tagger more flexible than the binary classification of MV2c10. Regarding performance, the efficiency of both algorithms to tag true b-jets is comparable, while the rejection rates of c- and light jets is larger for the DL1r tagger. The improvement in rejection for the 60% working point, detailed below, is by up to 70% for c-jets and 120% for light jets.

Working points

The full spectrum of the final b-tagging discriminant is not directly used in physics analyses due to the complexity of the calibration. Instead, four different b-tagging working points (WP) are defined based on the b-jet acceptance efficiency evaluated on a $t\bar{t}$ sample: 60%, 70%, 77% and 85%, which are often referred to as *Very Tight*, *Tight*, *Medium* and *Loose* operating points, respectively. Some c- and light-jets pass the 85% WP, ending up with a b-tagging efficiency between 85% and 100%. Meanwhile, the jets that pass the 60% WP mainly consists in b-jets.

The criteria are important when defining the b-jets for event selection, as the $b-$jets misidentification, so c- and $light$-jet acceptance inefficiency, improves for lower b-jet efficiency working points, therefore rejecting more background but with lower signal statistics. On the other hand, the pseudo-continuous b-tagging WP, so the WP that a jet passes, is additional information that can be used to further refine the selection or in multivariate methods.

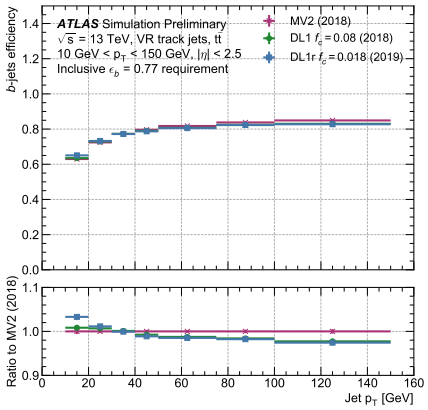

(a)

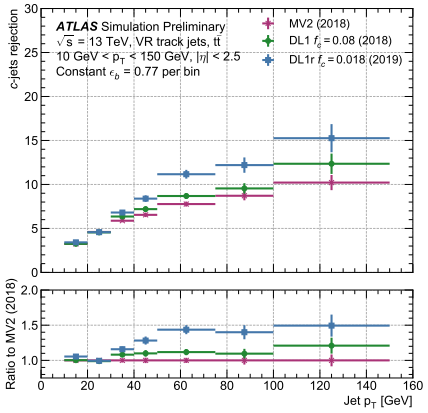

(b)

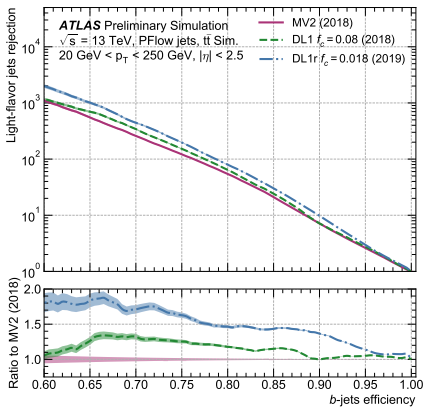

(c)

Figure 4.5: Identification efficiency for b-jets as a function of p_{T} (a), and rejection rate for c-jets (b) and light-jets (c) as a function of the b-tagging efficiency for the MV2c10 and DL1 taggers in a simulated $t\bar{t}$ sample [127].

4.3 Leptons

4.3.1 Electrons

Electrons interact with the ID and the EM calorimeter system. The typical signature is a track in the ID and electromagnetic shower in the EM calorimeter. Overall, the performance in terms of identification and reconstruction of electrons is high.

First, topo-clusters are selected and matched to ID tracks in the region $|\eta| < 2.47$ excluding the transition region of the barrel and end-cap ($1.37 < |\eta| < 1.52$). Next, the matched clusters are grouped to form superclusters, which are variable-size clusters, using a dynamic clustering algorithm. After a first energy and position calibration, tracks are matched to the electron superclusters. The calibration of the energy scale and resolution of electrons is computed from $Z \to ee$ decays and validated in $Z \to \ell\ell\gamma$ [128]. In addition, the energy resolution of the reconstructed electron is optimised using a multivariate algorithm based on the properties of showers in the EM calorimeter.

Further identification criteria are required for an electron candidate, passing a selection to increase the purity. The prompt electrons are evaluated with a likelihood discriminant to define three operating points with different purities: *Tight*, *Medium* and *Loose*. The discriminant is computed using variables measured in the ID and the EM calorimeter, chosen such that they discriminate prompt isolated electrons from other signal deposits (jets, converted photons or other electrons from heavy-flavoured hadron decays). The most important quantities are based on the track quality, the lateral and longitudinal development of the electromagnetic shower as well as the particle identification in the TRT. The probability density function to build the likelihood are derived from $Z \to ee$ ($E^{\mathrm{T}} > 15$ GeV) and $J/\psi \to ee$ ($E^{\mathrm{T}} < 15$ GeV) events.

Another requirement is the isolation criteria, to require the electron signal to be separated from other particles. Electrons are typically required to be spatially separated from other particles based on two quantities: a maximum value for the sum of transverse energy of topo-clusters in a $\Delta R = 0.2$ cone surrounding the electron and of the sum of transverse momentum of tracks around the electron, with a ΔR cone that decreases with p_{T}. Effects of leakage and pile-up are taken into account and also tracks are required to satisfy $p_{\mathrm{T}} > 1$ GeV, $|\eta| < 2.5$ and quality criteria. In this thesis, the criteria used is the Gradient isolation which has an efficiency of 90% at $p_{\mathrm{T}} = 25$ GeV and 99% at $p_{\mathrm{T}} = 60$ GeV.

4.3.2 Muons

Muons leave the ATLAS detector without significant energy loss. The typical signal consists on a track in the ID and MS sub-detectors. There are different types of muons depending on which ID, MS or calorimeter information is available [129].

As a summary, the muon reconstruction has two stages: tracks are reconstructed independently in the ID and MS, and then are combined to form the muon tracks.

The muon track candidates are built from track segments found in the different MS sub-systems. In the muon trigger chambers and MDTss, segments are reconstructed with a straight line to fit the hits of each detector layer after an alignment to the trajectory in the bending plane of the detector. The RPCs, TGCs and CSCs hits provide measurements in the orthogonal direction and the forward region of the detector to build additional track segments. The muon track candidates are then built from the track segments fit together using a global χ^2 fit. With that information, different types of muons can be defined.

The combined (CB) muons are the muon candidates obtained from using combined information from MS tracks that are extrapolated to the tracks of ID (an inside-out approach is also used). The segment-tagged (ST) muons are reconstructed from tracks in the ID extrapolated to typically one track segment in the MDTss and CSCs. ST muons are normally low in p_{T} and in regions with low acceptance. Calorimeter-tagged (CT) muons are built from an ID track that is instead matched to an energy deposit in the calorimeter compatible with a minimal ionising particle. The CT muon strategy outputs the lowest purity, although proves useful for detector regions not fully covered by the MS, and is optimised for 15 GeV $< p_{\mathrm{T}} <$ 100 GeV and $|\eta| < 0.1$. The fourth type, extrapolated (ME) muons, are only reconstructed using the MS with an acceptance of $2.5 < |\eta| < 2.7$.

The muon identification criteria (similar to the electron identification) is performed applying quality criteria to increase the purity of the selection. In order to identify prompt muons with high efficiency and a good momentum resolution, a requirement is done for the amount of hits in the ID and the MS systems. Four different muon operating points are defined: *Tight*, *Medium*, *Loose*, *high* p_T and *low* p_T. The Medium and Loose working points are used in this thesis. The first one is widely used in physics analyses and is designed to minimise muon reconstruction and calibration systematic uncertainties. It consists of combined and extrapolated muons with three or more hits in at least two of the MDTs layers, or just one hit for $|\eta| < 0.1$ with no more than one hole in the MS. On the other hand, the Loose working point maximises the reconstruction efficiency and accounts all types of muons, adding the segmented- and calorimeter-tagged muons for $|\eta| < 0.1$. The reconstruction efficiency for muons with $p_{\mathrm{T}} > 20$ GeV at the Medium and Loose working points is 96.1% and 98.1%, respectively.

The isolation criteria is based on track and calorimeter variables, similar to the electron case. The criteria improve the efficiency removing non-prompt muons, the ones not generated in the hard-scattering but in other parton shower processes for example, which are usually close to jets and other objects. The track related variable, $p_{\mathrm{T}}{}^{\mathrm{varcone30}}$ is the scalar p_{T} sum of the additional tracks in a cone $\Delta R = 10\,\mathrm{GeV}/p_{\mathrm{T}}^{\mu}$ (maximum of 0.3), that depends on the muon transverse momentum p_{T}^{μ}. The calorimeter related variable is the same as for electrons, built from the sum of energies around the muon track. In this thesis, the *FixedCutTightTrackOnly* working point is used, which is defined only with track isolation: $p_{\mathrm{T}}^{\mathrm{varcone30}}/p_{\mathrm{T}}^{\mu} < 0.06$.

4.3.3 Taus

The τ leptons typically decay before reaching active electronics of the ATLAS detector and have to be identified via their decay products. The decay can be either leptonically (into electrons or muons) or hadronically. The leptonic decay represents the 35% of the cases and is covered by the reconstruction of the produced electron or muon. The hadronic decays represent 65%, which contain one or three charged pions in 72% and 22% of the cases, respectively. In addition, at least one associated neutral pion is also produced in 68% of the hadronic decays. The dedicated τ reconstruction and identification algorithms in ATLAS target the hadronic decay, with the main background being jets from energetic hadrons produced in the fragmentation of quarks and gluons, known as the QCD background. Therefore, the τ objects in ATLAS mentioned in this thesis refer to hadronically decaying τ leptons.

The candidates are seeded by jets which are required to have $p_{\mathrm{T}} > 10$ GeV and $|\eta| < 2.5$ excluding the barrel-end-cap transition region [130]. The tau identification is based on a machine learning classifier which is trained using the calorimeter information and the tracks associated to the jet candidate. A trained BDT is used for EMTopo jets while a recurrent NN is used for PFlow jets. Three different efficiency working points are defined: *Loose* , *Medium* and *Tight*. The τ leptons used in this thesis are defined with the medium working point, required to have $p_{\mathrm{T}} > 25$ GeV and isolation criteria of $\Delta R < 0.2$ between the τ and any selected electron or muon.

4.4 Missing transverse energy

The missing transverse momentum, also denoted as $\mathrm{E}_{\mathrm{T}}^{\mathrm{miss}}$ is the transverse component of the negative vector sum of the fully calibrated objects (electrons, muons, photons, τ leptons and jets) as well as soft objects associated to the PV. In an ideal detector, the the sum of four-momenta of all particles produced is equal to the net momentum of the initial collision, implying that the net momentum in the transverse plane of the collision has to be zero, $E_{\mathrm{T}}^{\mathrm{miss}} = 0$. Nevertheless, the net momentum is not null as particles like neutrinos leave the detector without depositing energy or others can interact with the detector in regions not covered by electronics. For analyses with neutrinos in the final state, it is typical to consider that the transverse energy carried by the neutrinos is the $E_{\mathrm{T}}^{\mathrm{miss}}$, which allows their reconstruction.

Machine learning and statistical methods 5

This Chapter introduces the Machine Learning (ML) methods used in the different analysis to enhance the separation between the signal and the background, and also the statistical methods used to extract the measurements of the signal.

Machine Learning (MC) is one of the core developing fields in computer science allowing the analysis of large and complex datasets, offering sophisticated techniques with a broad range of possible applications. Regarding high energy physics, the large amount of MC simulations or data that is being recorded is well suited for the application of ML techniques. In this chapter, different multi-variate techniques used in this thesis are introduced, focusing on the classification methods used to improve signal and background separation.

In order to test the predictions of a given model, experimental data and MC simulations are compared using statistical methods. This chapter describes the tools used to extract a measurement of the production of the target signal, in addition to upper limits.

5.1 Machine Learning

The deployment of ML methods is already reaching crucial tasks in ATLAS as online data recording, from neural networks in calorimetry FPGAs [131] to particle reconstruction in trigger algorithms [132], which benefit from faster and more efficient response than previous filters.

For those cases, a neural network is trained to reduce background–signal ratio, to offer a high-level discriminating variable for a classification problem or to provide a prediction of a certain quantity. These methods can outperform conventional algorithms as the inference is performed from multi-dimensional inputs, providing large amounts of information to the machine learning algorithm. Regular algorithms rely on kinematic variables and although multiple can be combined, ML methods can use a greater amount of inputs and reach higher performance, given enough data.

Regarding detector simulation, it is one of the most computational intensive tasks within ATLAS, especially from the calorimeter simulation, and solutions involving adversarial networks and auto-encoders are being studied to output faster but reliable output.

Regarding particle reconstruction and identification, examples of implementations can be found within the τ identification [132] or b-tagging algorithms [133]. In physics analyses, the use of ML is already standardised to typically reconstruct signal processes or to discriminate them from the background. Then, the output is a high discriminating variable that can be used to define high-purity signal analysis regions, for example.

Machine Learning is a very broad umbrella term for algorithms which are not per se optimised for a specific task but are can adapt to different problem sets by tuning their parameter set using data (training). ML requires, besides the model itself, preparation and follow-up processing steps. In which extent they are necessary depends on the available data, the model and its application.

Generally, two types of machine learning are distinguished: Supervised learning and Unsupervised learning. The main difference is that the first requires fully labelled training data while the latter does not. In the context of this thesis, supervised approaches are used based on Neural Networks (NNs) and Boosted Decision Trees (BDTs).

The statistical model is denoted as $\mathrm{P}_{\mathrm{model}}(\mathbf{x_i}; \boldsymbol{\theta})$ parameterised with the set of parameters $\boldsymbol{\theta}$ while $\mathbf{x_i} = (x_i^1, x_i^2, ..., x_i^M)$ is the feature set of a single input data point i of the $\mathbf{X} = (\mathbf{x_1}, \mathbf{x_2}, ..., \mathbf{x_N})$ dataset consisting of N data points. $\mathrm{P}_{\mathrm{data}}$ is the true distribution that generates the data but is unknown. In the case of supervised learning, every data point has a label which categorizes the event, $\mathbf{y} = (y_1, y_2, ..., y_N)$.

5.1.1 Pre-processing

The selection of the dataset and its size depends on the problem that the ML is intended to solve. The datasets used in ML methods to discriminate between signal and background processes usually consist on simulated events. If the aim is to reconstruct a specific quantity, only the events of the target signal are used. Aside, the dataset can also consist of just objects, like b-jets, instead of events. The dataset and the amount of input depends mostly then on the problem at hand, its complexity and the target performance, as more complex setups will need advanced algorithms with higher number of input variables and large datasets.

The input variables can be categorised as low- or high-level variables. The low-level variables are usually available quantities that have not been combined or designed to directly help to the problem, like the kinematics of the objects of an event. Then, high-level variables are referred to those obtained with low-level variables and designed to offer discrimination, as reconstructed kinematics or the output of other classifiers, like b-tagging. Although high-level variables offer a lot of discrimination, a complete set of low-level variables have the necessary information to reach or even surpass the same level of discrimination, as low correlations between variables can be exploited in advanced setups.

It is important to ensure an unbiased training process. For this purpose, the full dataset is split at least in two orthogonal samples. The training sample is used for the actual algorithm training, while the validation set is evaluated and monitored to choose between different models. While a loss function is used to find the best parameter set for the training itself, the performance on the validation set is evaluated in terms of sensitivity, selection efficiency, stability... in order to fine-tune the model, such as the choice of input variables or hyperparameters. Ideally, a third dataset referred to as testing set is only used to evaluate the final algorithm and

is not involved in the training process. Some trainings performed in this thesis are not performed with the testing set although no significant bias is introduced, as the difference in performance between the validation and testing set is below statistical effects. In order to evaluate the full dataset, cross-validation (also named k-folding [134]) setups are used where k trainings are performed where the train/validation/test sets are labelled accordingly so every set can be evaluated appropriately.

In this thesis and typically in ATLAS analyses, every simulated event has an associated unique integer not correlated with any physical variable. Hence, it is ideal to split the full dataset into the different sets. Another detail is that every simulated event has an event weight, so the full simulated process has the appropriate cross-section and kinematic distributions, which value can also be negative in some cases. This is almost exclusive of high energy physics datasets and although the user level tools accept event weights as input, the absolute value of the even weights has to be used as negative values are not properly defined in the training.

5.1.2 Performance

The model performance is usually the decisive measure of an ML method and depending on the objective, different metrics are used to better evaluate the performance. The most common variables are discussed in the following.

5.1.3 Loss function

The loss function E or cost function is the quantity optimised during the model training and represent the deviation of a model from the desired behaviour. To be suitable for minimisation, the function has to be differentiable. The choice of the loss function depends on the problem and requires optimisation. For supervised learning, the loss function depend on the labels and the worse the prediction is, the higher the loss function.

It is standard to express the loss of the full dataset $\mathbf{X}$ as the average of loss of the single data points $\mathbf{x_i}$,

$$E(\mathbf{X}, \boldsymbol{\theta}) = \frac{1}{N} \sum_{i=1}^{N} E(y_i, \mathrm{P}_{\mathrm{model}}(\mathbf{X}, \boldsymbol{\theta})) \tag{5.1}$$

For regression problems the typical expression is the mean square error [134],

$$E_{MSE}(\mathbf{X}, \boldsymbol{\theta}) = \frac{1}{N} \sum_{i=1}^{N} (y_i \mathrm{P}_{\mathrm{model}})^2 \tag{5.2}$$

simply an average of the deviation from the true labels. For binary classification, the so-called *binary cross-entropy* [135] is frequently used,

$$E_{BSE}(\mathbf{X}, \boldsymbol{\theta}) = -\frac{1}{N} \sum_{i=1}^{N} y_i \cdot \log(\mathrm{P}_{\mathrm{model}}(\mathbf{X}, \boldsymbol{\theta})) + (1 - y_i) \cdot \log(1 - \mathrm{P}_{\mathrm{model}}(\mathbf{X}, \mathbf{X})) \tag{5.3}$$

which is the negative log-likelihood of a Bernouilly distribution, and a modified

version is used in multi-classification problems.

AUC

In the analyses presented in this thesis, the output distribution of the NN is used as a high-level variable and in the multi-variate fit to data. Hence, the loss function is not the only important criteria as both the shapes and the separation between the signal and background output distributions are essential for the performance of the analyses. The quantity to evaluate the separation from signal and background for a given variable is the *Area Under the ROC Curve* (AUC), and is the main decisive variable for a training in this thesis.

Given two variable distributions from a signal and a background sample, the *ROC* curve (Receiver Operating Characteristic) is defined as the signal efficiency against the background rejection.The shape of the curve already provides a lot of the information regarding the overlap of the distributions, but the characteristic quantity is the integral of the curve, the AUC. The AUC minimum value is 0.5, when the overlap between two distributions is total, while the maximum value is 1, when the distributions are totally separated. In the maximum value case, there is a cut in the discriminating variable can distinguish completely between signal and background.

5.1.4 Neural networks

Neural Networks (NNs) were introduced in the 1940s [136] but became feasible in the last decades as large computing power and GPUs are widely available. The concept of a NN are nodes (neurons) connected to each other via weights, and the most basic network is referred as feed-forward NN.

An example is illustrated in Figure 5.1, with in one input layer, one hidden layer and one output node. The result of node has the form of a linear system $b + w \cdot x$, with bias b, weight w and the input of the neuron x. More technically, the result of every node (except the input layer) is given by the sum of its inputs, the output of the different neurons connected to the given node multiplied by the weights w_i which represent said connection. More generally, a bias b_i is added to the sum and then used as input to an activation function f_i, which introduces non-linearity. The final output of the depicted feed-forward NN can be expressed as

$$\mathrm{P}_{\mathrm{model}}(\mathbf{X}, \boldsymbol{\theta}) = f_2(\mathbf{b_2} + \mathbf{W_2} f_1(\mathbf{b_1} + \mathbf{W_1 x})) \tag{5.4}$$

with the inputs of a given data-point $\mathbf{x}$; the parameter set $\boldsymbol{\theta}$ including weight matrices W_i and bias terms b_i. Fully expanding in matrix notation,

$$\mathrm{P}_{\mathrm{model}}(\mathbf{X}, \boldsymbol{\theta}) = f_2\left(\begin{bmatrix} b^2_{11} \end{bmatrix} + \begin{bmatrix} w^2_{11} & w^2_{12} \end{bmatrix} f_1\left(\begin{bmatrix} b^1_{11} \\ b^1_{21} \end{bmatrix} + \begin{bmatrix} w^1_{11} & w^1_{12} \\ w^1_{21} & w^1_{22} \end{bmatrix} \begin{bmatrix} x_{11} \\ x_{21} \end{bmatrix}\right)\right) \tag{5.5}$$

This simple example has nine free parameters $\boldsymbol{\theta}$ which are optimised during the training; more complex networks easily reach several ten-thousands of free parameters. Due to the non-linearity introduced by f_i, a NN can approximate any

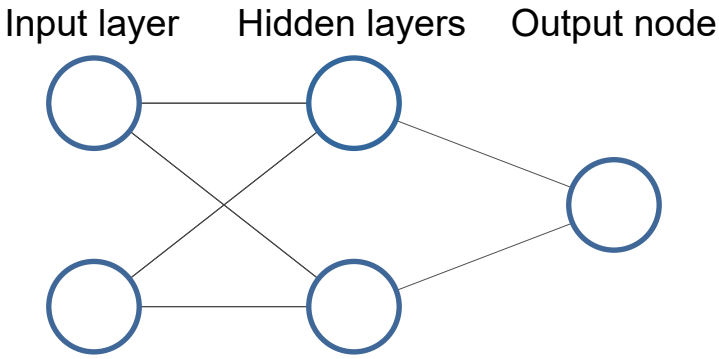

Figure 5.1: Fully connected feed-forward neural network with two input nodes, one hidden layer with two nodes and one output node.

arbitrary function by giving the network enough freedom (amount of hidden layers and nodes). When a NN consists of multiple hidden layers, it is referred as a deep learning [137] algorithm.

The main NN structure used in this thesis are feed-forward networks, but there are a vast number of different architectures available developed for very different applications [138]. Several software packages are available and accessible to the public, mainly in Python, with popular examples as Pytorch [139], Tensorflow [140] and Keras [141]. The main package used in this thesis is the latter, which models are deployed in ATLAS using the C++ based package lwtnn [142].

The training of a NN is the process consisting on the optimisation of the free parameters $\boldsymbol{\theta}$ using gradient descent. Other parameters that affect the model and are manually set are called hyperparameter, which include for example the number of layers and nodes.

Regarding training, batch training is the typical procedure, where the minimisation of the loss function is done in steps with the training data divided into equally sized segments. The loss function is calculated, and the parameters optimised at every step. When a full iteration over the entire dataset is referred as an epoch. This method enhances the minimisation of the loss function as computing it using the full training dataset leads to profile the very specifics of the training dataset, hence loosing generalisation when evaluating other data not used in the training (overtraining), and can also lead to stop the minimisation process in local minima thus not reaching the true performance.

For batch training approach, the dataset is randomised and then split with an adequate batch size to ensure that every batch is a correct representation of the dataset. Hence, the batch size is a hyperparameter and if too small, the minimisation is faster but the loss function will vary too much at every step, leading to a lower resolution and lower performance, as the model will be too general.

Optimiser

After a first random initialisation of the free parameters $\boldsymbol{\theta}$, they are updated iteratively at each step of the training following,

$$\theta' = \theta - l\nabla_\theta E(\theta; \mathbf{X}) \tag{5.6}$$

where l is the learning rate, also a hyperparameter, that tunes the rate of the update on the weights, the gradient of the loss function with respect the given free parameter. A large value of l prevents the optimal convergence as the loss value might change enough between steps and the minimisation becomes random before reaching the minimum. On the other side, a very low learning rate slows the optimisation and the minimisation can get stuck in a local minimum. Methods that vary the learning rate or the batch size at every step can prevent the extremes and gradually shift to a precise approach with the number of steps or epochs [143]. In this thesis, the Adam optimiser [144] is used which estimates of the first and second moment of the gradient.

Backpropagation

For the gradient-descend method, the computation of the gradient of the loss function with respect to all trainable parameters is needed. However, it is not feasible to calculate it analytically for NNs as the gradient includes lots of nested gradients. Backpropagation [145] is used to calculate the gradient, which computes the nested gradients applying the chain rule gradually to fully compute the network. The gradient computation is optimised by reusing sub-expressions and parameter dependencies.

Activation Functions

The introduction of activation functions $f(z)$ is essential to allow the NNs to act as a non-linear function. Many candidates of activation functions exist, from simple step functions to monotonically increasing functions (as tanh) or logistic functions (as the *sigmoid* function). Although these activation functions are simple and manage to harmonise the inputs of a node, the resulting NN suffers from vanishing gradient issues which significantly slow the training. The *Rectified Linear Unit* (ReLU) [146] activation function is widely used, defined as

$$f_{\text{ReLU}}(z) = \begin{cases} 0 & \text{for} z < 0 \\ z & \text{for} z \geq 0 \end{cases} \qquad f'_{\text{ReLU}}(z) = \begin{cases} 0 & \text{for} z < 0 \\ 1 & \text{for} z \geq 0 \end{cases} \tag{5.7}$$

which is not affected by vanishing effects and the gradient is fast to compute, as the derivative function $f'(z)$ is very simple. Other popular activation functions are the Leaky ReLU [147] and *Softplus* [148].

In general, the output nodes have different activation functions depending on the desired shape of the result. For the classification problems, like the NN used in the thesis, the output node can be interpreted as a probability with the sigmoid

function,

$$f_{\text{sigmoid}}(z) = \frac{1}{1 + e^{-z}} \tag{5.8}$$

Regularisation

Besides the training performance, the ML model should be resilient to fluctuations in the training data or by the randomness of the training process itself. If performing the training with two equivalent data-sets results in very different models and performance, it might be a strong indication of overfitting or other instabilities, difficult to study as a NN has many free parameters.

To protect the model and its ability to be generalisable, the training is made robust with regularisation techniques. Most popular stochastic methods [149–151] are introducing dropout, batch normalisation or early stopping. The first, randomly removes an adjustable percentage (hyperparameter) of weights between neighbouring layers avoiding strong correlations between neurons. The batch renormalisation consists on scaling the input of the layers and the early stopping halts the training process after a criterion to avoid overtraining, like that the loss in the validation set is not improving after a certain amount of epochs.

Another popular method, the L2 regularisation, consists in adding a term in the loss function that includes the sum of the squared weight values, penalising large weight values. In this thesis, the dropout and early stopping are applied as textbook, while no effects were seen when introducing other methods like L2 regularisation. The batch normalisation is not applied, although an equivalent approach is applied to the input layer. The different input variables are scaled to have a mean value of 0 and a variance of 1, which avoids large differences in weights due to the difference of units. One consideration is that distributions like p_{T} are not bounded like η and outliers at the tail of the distributions can introduce instabilities in the model.

Neural network parameterisation

The analyses presented in this thesis use a NN technique referred as parameterisation, usually applied to NN with signal or background events generated with different parameters. The parameterised NN [152] appears as a structure that simplifies trainings setups as it can replace sets of classifiers trained at individual values of given parameters, thus also increasing the statistics of the training dataset.

The NN has in the input layer these parameters that distinguish different classes of interest, like the training label set, a generator parameter or a source of uncertainty [153]. Consequently, the response depends on the introduced parameters as depicted in Figure 5.2.

In the different searches presented in the thesis, the true mass of the targeted new BSM particle is used as a parameter. As the parameter can be used to directly classify the events, the training should be setup appropriately. For signal events the parameter corresponds to the mass of the corresponding sample, while for

background it is not well-defined and a random value is assigned to each event, taken from the distribution of signal masses. This makes the NN not to directly use the parameter to perfectly classify the events, while the classification is optimised for each signal.

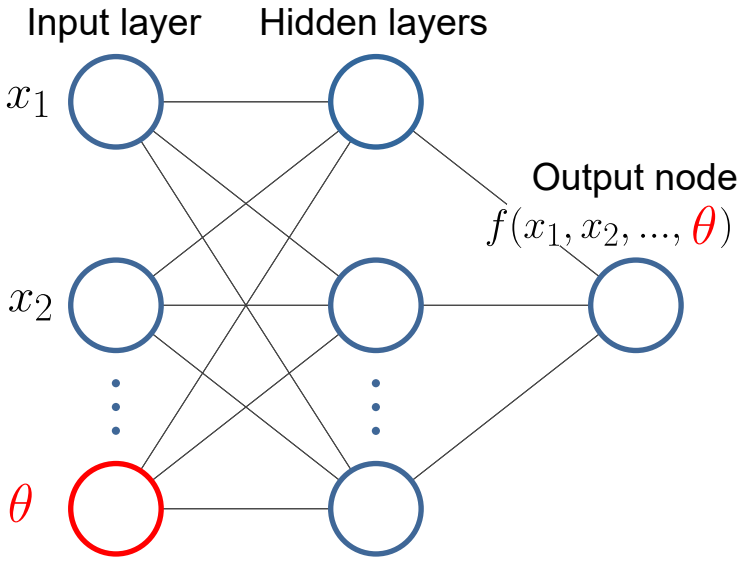

Figure 5.2: Simple schematic of a fully connected feed-forward Neural network with input features $x_1, x_2, ...$ as well as an input parameter θ, such as response f depends on the parameter.

5.1.5 Boosted decision trees

Boosted decision trees (BDTs) were one of the most commonly used multivariate technique in the last decade of high energy physics, before NNs became more accessible and popular.

BDTs are used for various problem sets like NNs, as object identification or signal/background discrimination. Implementation are in typical ATLAS software, ROOT [154] via the TMVA [155] package and more widely in python via scikit-learn [156] or xgboost [157].

The unit of a BDT is a decision tree, depicted in Figure 5.3. The structure is like a tree, as the name suggests, with branches connected via nodes. A cut on a specific input is made at each node, repeated until a stop criterion is met. The most usual criteria are that the minimum events in a leaf is reached or that the maximum amount of cuts is reaches (maximal tree depth). The decision tree alone is a weak learner and very sensitive to small changes in the training data, while an ensemble of weak learning leads to a powerful and robust model.
Boosting is one technique to ensemble trees, which combines the response of the single decision trees into a single discriminant,

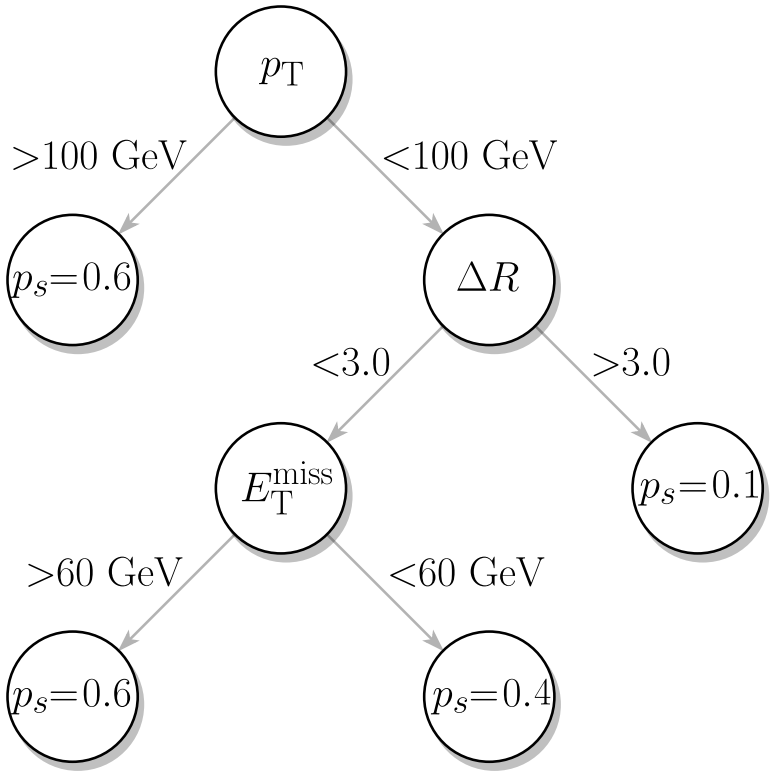

Figure 5.3: Schematic representation of a decision tree trained on a dataset composed of signal and background events with example training variables and cuts. The output of the tree is the probability that each event has of being generated by signal, values above (below) 0.5 correspond to signal-like (background-like) events.

$$\mathrm{P}_{\mathrm{model}} = \sum_{n=1}^{N} \alpha_n \mathrm{P}_{\mathrm{tree}}^{(n)}(\mathbf{x_i}) \tag{5.9}$$

Different boosting methods are widely available and the most popular for classification are Gradient Boosting (GradBoost) and Adaptive Boosting (AdaBoost) [158]. A GradBoost BDT [157] consists on training individual trees sequentially computing the loss function, typically E_{MSE}, and the contribution of the next tree is added to the ensemble weighted such as the loss function is minimised,

$$E_n = E\left(\mathrm{P}_{\mathrm{model}}^{(}n-1)(\mathbf{x_i}) + \gamma_n \mathrm{P}_{\mathrm{tree}}^{(n)}(\mathbf{x_i})\right) \tag{5.10}$$

AdaBoost is a specific case in which the weight of the events wrongly classified for a given tree is increased to have an impact in the loss function minimisation, hence increasing the learning in challenging phase-spaces. Nevertheless, this can yield to a model sensitive to statistical deviations of the dataset or outlier events.

5.2 Profile likelihood fit

In order to test the compatibility between data and the MC simulations, statistical methods in the context of hypothesis testing need to be introduced. The profile

likelihood fit is a statistical tool used in this thesis to extract a measurement for the amount of the signal targeted in the analysis. When the presence of signal is not significant, upper limits are extracted based on the asymptotic formulation [159]. In this section, the profile likelihood fit method is presented with the necessary concepts in the context of a BSM search. The technical implementation is provided by the RooStat framework [160].

The fundamental idea behind hypothesis testing is to compare the agreement of the experimental data between two hypotheses and quantify which hypothesis can be discarded with a certain level of confidence. The two hypotheses to be compared are: the null-hypothesis H_0, the SM without new physics; and the alternative hypothesis H_μ, which accounts for BSM interactions. The μ refers to the signal strength, commonly referred as parameter of interest (POI), which is a normalisation factor for the targeted signal that can be expressed as,

$$\mu = \frac{\sigma}{\sigma_{ref}} \tag{5.11}$$

where σ is arbitrary and σ_{ref} a reference value, typically a benchmark value from a theory or an expected sensitivity, like 1 pb. Hence, H_μ can be evaluated with a continuos spectrum of signal strengths, and will approach the SM hypothesis (H_0) for $\mu \to 0$, the agreement is checked for H_μ with a continuous spectrum of signal strengths, which will approach the SM, H_0, for $\mu = 0$.

Given a binned data distribution with n_i events for a bin i, the expected value of n_i can be expressed as,

$$E[n_i(\mu, \mathbf{b}, \boldsymbol{\theta})] = \mu \cdot s_i(\boldsymbol{\theta}) + \sum_{k_\alpha \in \mathbf{k}} k_\alpha \cdot b_{\alpha,i}(\boldsymbol{\theta}) \tag{5.12}$$

with s_i the predicted signal events, $b_{\alpha,i}$ the predicted background events of the process α. The normalisation factor k_α affects the background process α, analogous to μ. Typically, k_α is introduced only for the most relevant backgrounds. The rest of the processes are normalised to their predicted cross-sections and the corresponding k_α is fixed to one. The nuisance parameters $\boldsymbol{\theta}$ are additional degrees of freedom which correspond to the systematic uncertainties acting both on the shape and normalisation of all processes. Their central value is defined to be zero and the deviation with respect to the original value is referred to as pull, where a deviation of ±1 corresponds to a variation of one standard deviation.

The fit procedure allows the reduction of the impact of systematic uncertainties, especially by taking advantage of the highly populated background-dominated bins included in the fit. This requires a good understanding of the background and the systematic effects. To verify the improved background prediction, fits under the background-only hypothesis are typically performed, and differences between the data and the post-fit background prediction are checked using selections and physical variables other than the ones used in the fit.

The binned likelihood function is given as

$$\mathscr{L}(\mu, \mathbf{k}, \boldsymbol{\theta}) = \prod_{i}^{N} \frac{(E[n_i(\mu, \mathbf{b}, \boldsymbol{\theta})])^{n_i}}{n_i!} e^{E[n_i(\mu, \mathbf{b}, \boldsymbol{\theta})]} \prod_{\theta_j \in \boldsymbol{\theta}} P(\theta_j) \tag{5.13}$$

which corresponds to a product of Poisson probabilities for all N bins and the penalty terms of all nuisance parameters. The form $P(\theta_j)$ are generally Gaussian distributions for each systematic uncertainties and Poisson distributions for the statistical uncertanty of each bin, that are introduced in the likelihood to penalise large deviations.

The optimal μ, $\mathbf{k}$ and $\boldsymbol{\theta}$ are obtained from the fit to data that maximises the agreement between data and the prediction.
The optimal test statistic to perform the fit is the likelihood ratio,

$$\lambda_\mu = \frac{\mathscr{L}(\mu, \hat{\hat{\mathbf{k}}}, \hat{\hat{\boldsymbol{\theta}}})}{\mathscr{L}(\hat{\mu}, \hat{\mathbf{k}}, \hat{\boldsymbol{\theta}})} \tag{5.14}$$

with the single-hat parameters that maximise likelihood while $\hat{\hat{\mathbf{k}}}$, $\hat{hat}\boldsymbol{\theta}$ those that maximise the likelihood for a given μ. As the likelihoods are products of several terms smaller than one, a more stable test statistic is the negative log-likelihood,

$$q_\mu = -2 \ln \lambda_\mu \tag{5.15}$$

For the purpose of setting upper limits on the signal production, some special cases are defined depending on μ and $\hat{\mu}$. If $\hat{\mu}$ is negative, i.e. the fitted signal has a negative normalisation, the modified test statistic assumes signal to be only positive: $\tilde{q}(\mu) = -2 \ln \frac{\mathscr{L}(\mu, \hat{\hat{\mathbf{k}}}, \hat{\hat{\boldsymbol{\theta}}})}{\mathscr{L}(0, \hat{\hat{\mathbf{k}}}, \hat{\hat{\boldsymbol{\theta}}})}$, where the parameters in the denominator optimise the likelihood for $\mu = 0$. Another exception is to set the modified test statistic to 0 for $\hat{\mu} > \mu$, as signal below the observed measurement is in complete agreement with the hypothesis.

The level of agreement between data and predictions for a given signal strength is quantified by computing the p-value p_μ, which is the probability of the measured data being a deviation from the assumed H_μ,

$$p_\mu = \int_{q_{\mu,obs}}^{\infty} f(q_\mu | H_\mu) dq_\mu \tag{5.16}$$

where $f(q_\mu | H_\mu)$ is the probability density function of q_μ under the assumption of H_μ. The significance $Z = \Phi^{-1}(1 - p_\mu)$ (being Φ the cumulative Gaussian distribution) is often preferred to quantify the level of disagreement in terms of sigma deviations. Typically, an alternative hypothesis is rejected at 1.64σ ($p_\mu = 0.05$) and the background-only at 5σ ($p_0 = 2.87 \cdot 10^{-7}$).

Normally, searches are dedicated to very small signals and poorly separated from the background. Rejecting the null hypothesis at a fixed probability as mentioned, leads to exclude signals with very low statistics not really targeted by the analysis [161]. The CL_s method solves this issue, which defines,

$$\mathrm{CL}_s = \frac{p_\mu}{1 - p_0} \tag{5.17}$$

which is the previous p-value, which any bad compatibility benefits the background-only hypothesis; normalised to the confidence level of the background-only hypothesis, which is closer to 1 when the measurement is not compatible with the background. In general, the exclusion limits obtained with this method are conservative.

Search for charged Higgs bosons decaying into a top and bottom quarks

$H^+ \to tb$ analysis overview

6

The discovered scalar particle in 2012 raises whether it is the Higgs boson of the SM or part of an extended scalar sector. Charged Higgs bosons[1] are predicted in several extensions of the SM that add a second doublet or triplets to the scalar sector, as discussed in Section 1.3.

The ATLAS and CMS collaborations have searched for charged Higgs bosons in pp collisions at $\sqrt{s}$= 7, 8 and 13 TeV with data samples ranging from 2.9 to 36 fb^{-1}, probing the mass range below the top-quark mass in the $\tau\nu$ [162–167], cs [168, 169], cb [170, 171],WA (A pseudo-scalar) decay modes, as well as above the top-quark mass in the $\tau\nu$ and tb decay modes [3, 162–165, 167, 172–174]. In addition, $H^+ \to WZ$ decays were searched for in the vector-boson-fusion production mode [175, 176]. ATLAS has also set limits on the H^+ production in a search for di-jet resonances in events with an isolated lepton using the Run 2 dataset [177]. No evidence of charged Higgs bosons was found in any of these searches.

The analysis presented in this thesis is performed with the full Run 2 proton-proton collision data of 139 fb^{-1} at $\sqrt{s}$=13 TeV. The results of this search are public [178], and were later interpreted to be used in an ATLAS effort to combine dark matter results [179]:

- ATLAS Collaboration, *Search for charged Higgs bosons decaying into a top quark and a bottom quark at $\sqrt{s}$=13 TeV with the ATLAS detector*, JHEP 06 (2021) 145
- ATLAS Collaboration, *Combination and summary of ATLAS dark matter searches using 139 fb^{-1} of $\sqrt{s}$=13 TeV pp collision data and interpreted in a two-Higgs-doublet model with a pseudoscalar mediator*, ATLAS-CONF-2021-036

This chapter describes the $H^+ \to tb$ analysis motivation, challenges and strategy. After a short introduction, the event selection is presented followed by the description of the modelling of the signal and background processes. Then, the analysis strategy and a summary of the systematic uncertainties are given.

6.1 Introduction

The analysis searches for charged Higgs bosons heavier than the top quark and decaying into a top and bottom quark. At the LHC, charged Higgs bosons in this mass range are expected to be produced primarily in association with a top quark and a bottom quark [180], illustrated in Figure 6.1.

The signal consists in two top quarks and two bottom quarks, once of each produced in association with the H^+ and the other from its decay. For convenience, the typical classification for $t\bar{t}$ events is used, based in the decay of the involved top quarks. The

[1] In the following, charged Higgs bosons are denoted H^+, with the charge-conjugate H^- always implied. Similarly, the difference between quarks and antiquarks q and $\bar{q}$ is generally understood from the context, so that $H^+ \to tb$ means both $H^+ \to t\bar{b}$ and $H^- \to \bar{t}b$.

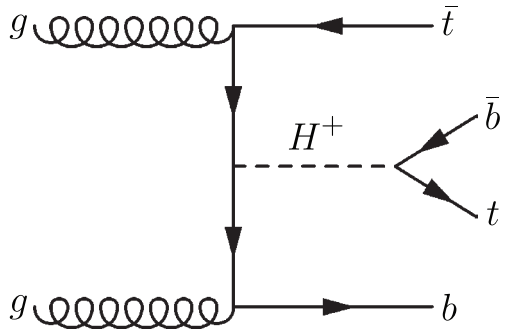

Figure 6.1: Leading-order Feynman diagram for the production of a heavy charged Higgs boson in association with a top antiquark and a bottom quark, as well as its decay into a top quark and a bottom antiquark.

main decay mode for top quarks is to a W and a b-quark, with the former decaying either leptonically (to leptons) or hydronically (to a pair of quarks). This yields to four possible diagrams depending on the decay of each top but three different types of final states with different decay rates [14]: the all-hadronic final state where both W-bosons decay hadronically (45.7%), the dileptonic mode where both W-bosons decay leptonically[2] (10.5%) and the lepton+jets (semi-leptonic) final state, in which one W-boson decays hadronically and one leptonically (43.8%).

In the scope of the analysis, the lepton+jets channel is studied as offers large statistics with a relatively clean topology, as the lepton in the final state allows to suppress the multi-jet background. In addition, the full event can be kinematically reconstructed, since only one neutrino is present and can be determined with E_T^{miss}. The dilepton channel was studied in the past ATLAS searches, with low impact in the final result. Aside, the lepton+jets channel could be further split into a resolved (low p_T) regime and a boosted regime, in order to optimise high p_T regimes that lead to collimated partons that cannot be resolved with the standard jet collections. The final state is depicted in Figure 6.2

The detector signature is chosen to include exactly one isolated lepton ℓ, considering only electrons and muons. Nonetheless, the τ leptons decaying into electrons or muons are included. As six quarks are present in the final state, six jets are expected to be present in the final state with at least four of them originating from a b-quark. Although the recommendations available at the time were based on EMTopo jets, the performance improvements with PFlow jets would have benefited the analysis, as the b-tagging is one important part of the selection.

The targeted final state complexity originates from the dominant $t\bar{t}$ production with additional jets ($t\bar{t}$+jets). In particular, $t\bar{t}$+$\geq$1b is the main irreducible background for which an example diagram is shown in Figure 6.3. Hence, the correct modelling of this process is key for the analysis and unfortunately, it is poorly constrained by data measurements and has large theory uncertainties.

[2] Hadronically decaying τ leptons are included in the numbers.

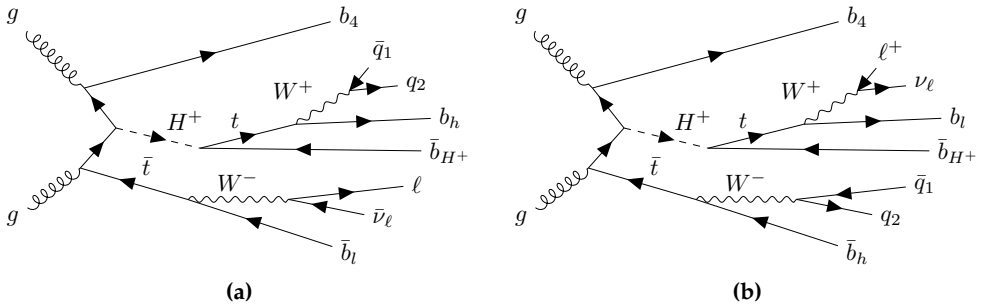

Figure 6.2: Leading-order Feynman diagrams for the production and decay of a heavy charged Higgs boson into a top and a bottom quark, with the former decaying hadronically (a) or leptonically (b), in the signal-lepton final state.

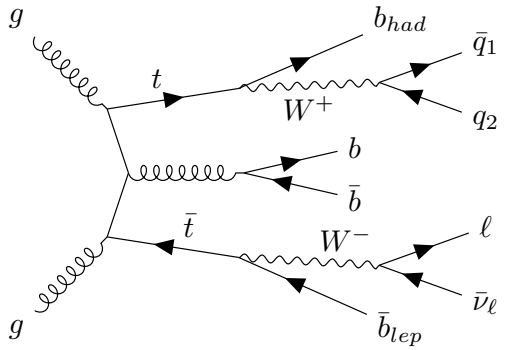

Figure 6.3: Leading-order Feynman diagram for the $t\bar{t}$ production with a radiated $b\bar{b}$ in the single-lepton final state.

As a summary of the analysis strategy, the first step is the event selection, where a first phase space is chosen to enhance the H^+ signal contribution but also includes events to study the SM background. Events are then split into signal-enriched categories (signal region, SR) and signal-depleted categories (control region, CR). The control regions are used to extract data-driven corrections for the $t\bar{t}$ modelling while for the signal regions, a NN is used to separate signal and background. The signal regions are used in a combined profile-likelihood fit on the NN output distribution, different for each signal hypothesis. In the fit, a large set of nuisance parameters is used to cover the systematic uncertainties.

6.2 Event selection

This section details the selection of the events used in the analysis, applied to recorded and simulated events. The physics objects mentioned are described in more detail in Chapter 4.

The events for this analysis are extracted from the Run 2 data, recorded with

the ATLAS detector at the LHC from $\sqrt{s}$=13 TeV pp collisions for a total integrated luminosity of 139 fb^{-1}. As trigger requirements, the events had to be recorded using single-lepton triggers which are summarised in Table 6.1. Multiple triggers were used in order to maximise the selection efficiency, either with low p_{T} thresholds and lepton identification and isolation requirements, or with higher thresholds but looser identification criteria and no isolation requirements. Slightly different sets of triggers were used for 2015 and 2016-2018 data due to the increase in pile-up. The minimum p_{T} required by the triggers was increased to keep both trigger rate and data storage within their limits. For muons, the lowest p_{T} threshold was 20 (26) GeV in 2015 (2016-2018), while for electrons, triggers with a minimum p_{T} threshold of 24 (26) GeV are. Furthermore, at least one primary vertex is required.

Table 6.1: Single-lepton triggers and quality criteria used for the $H^+ \to tb$ analysis.

Object	p_{T} threshold [GeV]		Identification		Isolation	
	2015	2016-2018	2015	2016-2018	2015	2016-2018
Electron	24	26	medium	tight	-	loose
	60	60	medium	medium	-	-
	120	140	loose	loose	-	-
Muons	20	26	medium	medium	loose	medium
	50	50	medium	medium	-	-

The working points for leptons include the *tight* identification for electrons and *medium* for muons. In addition, electrons are required to satisfy the *Gradient* isolation criteria while muons are required to pass the *FixedCutTightTrackOnly* criteria. Hadronically decaying τ leptons are required to have $p_{\mathrm{T}} > 25$ GeV and pass the *mediumBDT* identification working point. However, these selected τ leptons are not used directly in the analysis, just for the overlap removal.

EMTopo jets are used with a radius parameter $R = 0.4$. To reduce pile-up effects, the *medium* working point of the jet vertex tagger (JVT) is applied. b-jets are identified and selected using the 70% working point of the MV2c10 tagger, although the pseudo-continuous score of the different jets is also used in the analysis.

In order to avoid counting a single detector signal as more than one lepton or jet, an overlap removal procedure is applied. First, the closest jet within[3] ΔR_y =0.2 of a selected electron is removed. If any jet passes the selection but is within ΔR_y =0.4, the electron is rejected. Muons are discarded if a jet is within ΔR_y =0.4, which suppress semi-leptonic decays of heavy-flavour hadrons. If the jet has less than three tracks however, the jet is discarded instead of the muon.
Events are required to have at least five jets, from which at least two have to be tagged with the 70% b-tagging working point. In addition, exactly one lepton with $p_{\mathrm{T}} > 27$ GeV and no additional lepton with $p_{\mathrm{T}} > 10$ GeV passing the *medium* (*loose*) identification working point for electrons (muons) is allowed.

[3] ΔR_y is ΔR using rapidity instead of the pseudorapidity for its calculation

6.3 Signal and background modelling

The Monte Carlo modelling of signal and background samples is described in this section.

The final state of the signal includes four b-jets, two light-jets, one lepton and one neutrino. Such final state is shared fully or partially by a large number of background processes, the main one being $t\bar{t}$+jets. Additional contributions to the background are from the production of W- and Z- bosons with jets (V+jets), single-top-quark production, diboson processes (VV) and the associated production of bosons and top quarks ($t\bar{t}V$, $t\bar{t}H$). Non-prompt leptons and misidentified jets form what is known as multi-jet background, which contribution is negligible due to the trigger and lepton quality requirements.
Various MC generators have been used for the production of the samples. Table 6.2 lists all simulated samples used in the analysis, both nominal which are use for the baseline SM background prediction and the alternative samples, used primarily to estimate systematic uncertainties. In general, the settings described in Section 3.1.7 apply for the generated samples. Also, the detector response is simulated either with Geant 4 or AF-II for the full detector or the fast simulation. The pile-up interactions are simulated with Pythia 8 and events are weighted to match the respective pile-up profiles observed in data during Run 2 (average of 34 interactions).

6.3.1 Signal modelling

The signal of this analysis is the associated production of a charged Higgs boson, $pp \to tbH^+$, followed by the $H^+ \to tb$ decay. The samples are generated with MadGraph5_aMC@NLO, which is a 4FS NLO generator with the *NNPDF2.3NLO* PDF set. The parton shower and hadronisation are modelled with Pythia 8.212. The width of the H^+ has been set to zero, which is an assumption with negligible impact on the analysis for the models considered, as the experimental resolution is much larger than the H^+ natural width [184]. Interference with the SM $t\bar{t}bb$ background is neglected and only the H^+ decay into tb is considered. The dynamic QCD factorisation and renormalisation scales, μ_F and μ_R, are set to $\frac{1}{3}\sum_i \sqrt{m(i)^2 + p_{\mathrm{T}}(i)^2}$, where i runs over the final-state particles used in the generation (H^+, t and b).

Eighteen different samples are generated, with H^+ masses ranging between 200 and 2000 GeV with step sizes chosen to match the experimental mass resolution of the H^+ signal. Table 6.3 lists the signal samples used in the analysis, also includes the Santander-matched cross-sections for 2HDM Type-II (MSSM), but without soft QCD corrections [185–188] The sample corresponding to the 1000 GeV H^+ mass has also been fully simulated.

Table 6.2: Summary of all simulated MC samples used in the $H^+ \to tb$ analysis. The nominal sample is the first row for each process. DR and DS stand for the diagram removal scheme [181] and the diagram subtraction scheme [182, 183], respectively.

Process	ME generator	PS generator	Normalisation	PDF set	Simulation
$H^+ \to tb$	MadGraph5_aMC@NLO 2.6.2	Pythia 8.212	NLO	*NNPDF2.3NLO*	Fast
$t\bar{t}$ and single-top					
$t\bar{t}$	PowhegBox v2	Pythia 8.230	NNLO+NNLL	*NNPDF3.0NLO*	Fast
	PowhegBox v2	Herwig 7.04	NNLO+NNLL	*NNPDF3.0NLO*	Fast
$t\bar{t}+b\bar{b}$ (4FS)	PowhegBoxRes	Pythia 8.230	NNLO+NNLL	*NNPDF3.0NLOnf4*	Fast
Wt	PowhegBox v2 (DR)	Pythia 8.230	NNLO+NNLL	*NNPDF3.0NLO*	Full/Fast
	PowhegBox v2 (DS)	Pythia 8.230	NNLO+NNLL	*NNPDF3.0NLO*	Full
	PowhegBox v2 (DR)	Herwig 7.04	NNLO+NNLL	*NNPDF3.0NLO*	Fast
	MadGraph5_aMC@NLO 2.6.2 (DR)	Pythia 8.230	NNLO+NNLL	*CT10NLO*	Fast
t-channel	PowhegBox v2	Pythia 8.230	NLO	*NNPDF3.0NLOnf4*	Full
	PowhegBox v2	Herwig 7.04	NLO	*NNPDF3.0NLOnf4*	Fast?
	MadGraph5_aMC@NLO 2.6.2	Pythia 8.230	NLO	*NNPDF3.0NLOnf4*	Fast?
s-channel	PowhegBox v2	Pythia 8.230	NLO	*NNPDF3.0NLO*	Full
	PowhegBox v2	Herwig 7.04	NLO	*NNPDF3.0NLO*	Fast?
	MadGraph5_aMC@NLO 2.6.2	Pythia 8.230	NLO	*NNPDF3.0NLO*	Fast?
V+jets					
W+jets	Sherpa v2.2.1 (2j@NLO, 4j@LO)	Sherpa	NNLO	*NNPDF3.0NNLO*	Full
Z+jets	Sherpa v2.2.1 (2j@NLO, 4j@LO)	Sherpa	NNLO	*NNPDF3.0NNLO*	Full
Diboson					
VV (had.)	Sherpa v2.2.1	Sherpa	NLO	*NNPDF3.0NNLO*	Full
VV (lep.)	Sherpa v2.2.2	Sherpa	NLO	*NNPDF3.0NNLO*	Full
VV (lep.+jj)	Sherpa v2.2.2 (EW@NLO)	Sherpa	NLO	*NNPDF3.0NNLO*	Full
$t\bar{t}+V$					
$t\bar{t}W$	MadGraph5_aMC@NLO v2.3.3	Pythia 8.210	NLO+NLO (EW)	*NNPDF3.0NLO*	Full
	Sherpa v2.0.0 (2j@LO)	Sherpa	NLO+NLO (EW)	*NNPDF3.0NNLO*	Full
$t\bar{t}\ell\ell$	MadGraph5_aMC@NLO v2.3.3	Pythia 8.210	NLO+NLO (EW)	*NNPDF3.0NLO*	Full
	Sherpa v2.0.0 (1j@LO)	Sherpa	NLO+NLO (EW)	*NNPDF3.0NNLO*	Full
$t\bar{t}Z$ (qq, $\nu\nu$)	MadGraph5_aMC@NLO v2.3.3	Pythia 8.210	NLO+NLO (EW)	*NNPDF3.0NLO*	Full
	Sherpa v2.0.0 (2j@LO)	Sherpa	NLO+NLO (EW)	*NNPDF3.0NNLO*	Full
Others					
$t\bar{t}\,t\bar{t}$	MadGraph5_aMC@NLO v2.3.3	Pythia 8.230	NLO+NLO (EW)	*NNPDF3.1NLO*	Full
tZq	MadGraph5_aMC@NLO v2.3.3	Pythia 8.212	NLO	*CTEQ6L1*	Full
tWZ	MadGraph5_aMC@NLO v2.3.3 (DR)	Pythia 8.212	NLO	*NNPDF3.0NLO*	Full
$t\bar{t}H$	PowhegBox v2	Pythia 8.230	NLO+NLO (EW)	*NNPDF3.0NLO*	Full/Fast
	PowhegBox v2	Herwig 7.04	NLO+NLO (EW)	*NNPDF3.0NLO*	Fast
	MadGraph5_aMC@NLO v2.6.0	PYTHIA8.230	NLO+NLO (EW)	*NNPDF3.0NLO*	Fast
$tHjb$	MadGraph5_aMC@NLO v2.6.2	PYTHIA8.230	NLO	*NNPDF3.0NLOnf4*	Full
tWH	MadGraph5_aMC@NLO v2.6.2 (DR)	PYTHIA8.235	NLO	*NNPDF3.0NLO*	Full

Table 6.3: Summary of the generated events for the different $H^+ \to tb$ signal samples with different H^+ mass. In addition, the expected cross-sections for $\tan\beta$=1, 60 in the hMSSM scenario [189] are presented.

H^+ mass [GeV]	Events	$\sigma(\tan\beta = 1)$ [pb]	$\sigma(\tan\beta = 60)$ [pb]
200	5.0M	3.3642	3.1218
225	1.5M	2.6823	2.4761
250	1.5M	2.4642	1.9838
275	1.0M	1.7517	1.5993
300	1.0M	1.4224	1.2931
350	0.8M	0.9626	0.8697
400	0.8M	0.6626	0.5915
500	0.7M	0.3300	0.2927
600	0.6M	0.1749	0.1534
700	0.6M	0.0969	0.0844
800	0.6M	0.0559	0.0482
900	0.6M	0.0333	0.0286
1000	0.7M	0.0204	0.0175
1200	0.9M	0.0082	0.0069
1400	1.2M	0.0036	0.0030
1600	1.2M	0.0016	0.0014
1800	2.0M	0.0008	0.0006
2000	2.0M	0.0004	0.0003

6.3.2 Background modelling

$t\bar{t}$ + jets

The dominant background for the H^+ signal is the $t\bar{t}$ pair production with additional jets, especially $t\bar{t}$+≥1b processes. Hence, events are categorised depending on the flavour of the additional jets. The labelling is performed with *particle jets*, jets formed only taking into account particles with a mean lifetime over $3 \cdot 10^{-11}$ s not originating directly from top-quarks or W-bosons. Then, the jet flavour label is assigned from ΔR(jet,hadron)<0.4 as follows:

- $t\bar{t}$+≥1b: $t\bar{t}$ + at least one additional jet containing at least one b-hadron.
- $t\bar{t}$+≥1c: not $t\bar{t}$+≥1b and at least one additional jet containing at least one c-hadron.
- $t\bar{t}$+light: all other cases.

The nominal production is modelled with the 5FS and PowhegBox v2 setting the renormalisation and factorisation scales to $\mu_R = \mu_F = m_{\mathrm{T}}(\mathrm{top})$ and $h_{\mathrm{damp}} = 1.5 \cdot m_{\mathrm{top}}$. The parton shower and hadronisation processes are simulated with Pythia 8. All generated $t\bar{t}$ samples assume a diagonal Cabibbo-Kobayashi-Maskawa matrix, thus the $W \to cb$ contribution is not included ($B = 5.72 \times 10^{-4}$. Additional $t\bar{t}$+jets events are produced with one of the W-bosons decaying leptonically and the other to cb, using the SM with non-zero Wolfenstein coefficients and 5FS.

Single-top

t-channel
Single-top t-channel production is modelled with PowhegBox v2, which provides ME at NLO in the 4FS with the *NNPDF3.0NLOnf4* PDF set. The renormalisation and factorisation scales are set to $\sqrt{m_b^2 + p_{\mathrm{T},b}^2}$. The events are showered with Pythia 8.

s-channel
Single-top s-channel production is modelled using the PowhegBox v2, which provides ME at NLO in the 5FS scheme with the *NNPDF3.0NLO* PDF set. The renormalisation and factorisation scales are set to the top-quark mass. The events are showered with Pythia 8.

Wt
Single-top Wt associated production is modelled using PowhegBox v2, which provides ME at NLO in the 5FS with the *NNPDF3.0NLO* PDF set. The renormalisation and factorisation scales are set to the top-quark mass. The diagram removal scheme is employed to handle the interference with $t\bar{t}$ production [181, 183]. The events are showered with Pythia 8.

$t\bar{t} + V$

The production of $t\bar{t} + V$ events is modelled using MadGraph5_aMC@NLO v2.3.3, which provides ME at NLO with the *NNPDF3.0NLO* PDF set. The renormalisation and factorisation scales are set to $\frac{1}{2} \sum_i \sqrt{m(i)^2 + p_{\mathrm{T}}(i)^2}$, where i runs over the final-state particles used in the generation. The events are showered with Pythia 8.

V + jets

Vector bosons plus jets production is simulated with the Sherpa v2.2.1 or v2.2.2 generator. In this setup, NLO-accurate ME for up to two jets, and LO-accurate ME for up to four jets are calculated with the Comix [62] and OpenLoops [190–192] libraries. The default Sherpa PS [193] based on Catani-Seymour dipoles and the cluster hadronisation model are used. They employ the dedicated set of tuned parameters developed by the Sherpa authors for this version, based on the *NNPDF3.0NNLO* PDF set.

Diboson

Diboson samples are simulated with the Sherpa v2.2 generator. In this setup multiple ME are matched and merged with the Sherpa PS based on Catani-Seymour dipole using the MEPS@NLO prescription. For semi-leptonically and fully leptonically decaying diboson samples, as well as loop-induced diboson samples, the virtual QCD correction for ME at NLO accuracy are provided by the OpenLoops library. For electroweak $VVjj$ production, the calculation is performed in the G_μ scheme, ensuring an optimal description of pure electroweak interactions at the electroweak scale. All samples are generated using the *NNPDF3.0NNLO* set, along with the dedicated set of tuned PS parameters.

Other small background

$t\bar{t}H$

The production of $t\bar{t}H$ events is modelled with the PowhegBox generator at NLO in the 5FS with the *NNPDF3.0NLO* PDF set. The h_{damp} parameter is set to $\frac{3}{4} \cdot (m_t + m_{tbar} + m_H) = 352.5$ GeV. The events are showered with Pythia 8.

tH

The production of $tHjb$ events is modelled using the MadGraph5_aMC@NLO v2.6.0 generator in the 4FS with the *NNPDF3.0NLOnf4* PDF set. The renormalisation and factorisation scales are set to $\frac{1}{2}\sum_i \sqrt{m(i)^2 + p_{\text{T}}(i)^2}$, where i runs over the final-state particles used in the generation. The shower starting scale is set to $\mu_q = H_{\text{T}}/2$, where H_{T} is defined as the scalar sum of the p_{T} of all outgoing partons. The events are showered with Pythia 8.230.

The production of tHW events is modelled instead using the MadGraph5_aMC@NLO v2.6.2 generator in the 5FS with the *NNPDF3.0NLO* PDF set. The different scales are set to the same forms as for tH. The events are showered with Pythia 8.235.

$t\bar{t}t\bar{t}$

The production of four tops events is modelled with MadGraph5_aMC@NLO v2.3.3, which provides ME at NLO with the *NNPDF3.1NLO* PDF set. The renormalisation and factorisation scales are set to $\frac{1}{2}\sum_i \sqrt{m(i)^2 + p_{\text{T}}(i)^2}$, where i runs over the final-state particles used in the generation. The events are showered with Pythia 8.230.

tZq and tZW
The tZq events are generated using the MadGraph5_aMC@NLO v2.3.3 generator at LO in the 4FS with the *CTEQ6L1* LO PDF set. The renormalisation and factorisation scales are set to $4\sqrt{m(b)^2 + p_{\mathrm{T}}(b)^2}$, where the b-quark comes from the gluon splitting.

The tZW sample is simulated using the MadGraph5_aMC@NLO v2.3.3 generator but at NLO in the 5FS with the *NNPDF3.0NLO* PDF set. The top quark is decayed inclusively while the Z boson decays to a pair of leptons. The renormalisation and factorisation scales are set instead to the top quark mass. The DR scheme is applied to handle the interference with ttZ.

Both tZq and tZW are showered with Pythia 8.212.

6.4 Analysis strategy

The search targets the H^+ production decaying into tb in the single-lepton channel. The events that pass the selection described in Section 6.2 are further divided into two types of disjointed analysis regions: signal regions and control regions. The control regions are used to improve the modelling of the $t\bar{t}$+jets background, while several multi-variate techniques are used in the signal regions to improve the separation between signal and background events.

6.4.1 Region definition

The analysis regions are categorised as a function of the number of reconstructed jets and b-tagged jets at the 70% b-tagging operating point. The signal regions are 5j3b, 5j≥4b, ≥6j3b and ≥6j≥4b.

Figure 6.4 illustrates the background composition, which clearly shows the dominance of the $t\bar{t}$ background, especially the $t\bar{t}$+≥1b component in the ≥4b regions. The 3b categories consist of a mixture of the three $t\bar{t}$ components: 52% of the 5j3b background are $t\bar{t}$+light events, while the 70% of the ≥6j3b events is split equal by $t\bar{t}$+≥1b and $t\bar{t}$+light events.

Table 6.4 shows the number of expected and selected events in the different regions, including the ≥5j2b selection which is used to derive weights to improve the $t\bar{t}$ modelling, as shown in the next section. The number of expected H^+ signal events for the 600 GeV mass hypothesis is also shown, which contribution is less than 0.5% for the ≥5j2b and thus considered negligible. Another observation, is that the region with the higher sensitivity in terms of $n_S/\sqrt{n_B}$ is the ≥ 6j≥ 4b region.

Figure 6.5 shows the acceptance times efficiency of the ≥5j≥3b inclusive selection per signal mass sample. It can be observed the decrease in acceptance starting from 1000 GeV, due to the loss of jets and characteristic of boosted regimes.

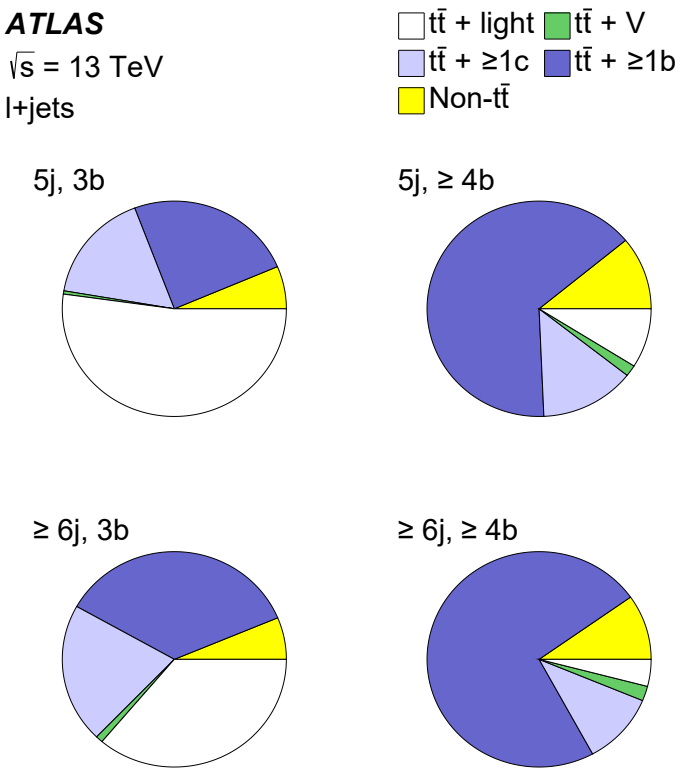

Figure 6.4: Background composition in the various analysis signal regions.

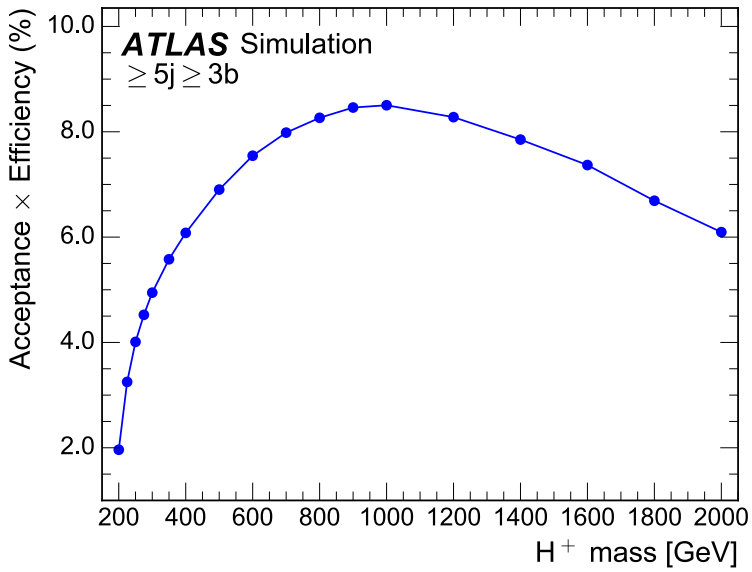

Figure 6.5: Total event acceptance of every H^+ signal sample in the analysis signal regions. Statistical uncertainties are included but hidden within the markers.

Table 6.4: Number of expected and selected events split according to the analysis regions. The ≥ 5j2b region is used to derive weights to improve the agreement between data and background. The quoted uncertainties include both statistical and systematic uncertainties except for the first column (≥ 5j2b) which only includes statistical uncertainties. The predicted number of H^+ signal events for the 600 GeV mass hypothesis is also shown, assuming a cross-section times branching fraction of 0.32 pb.

	≥ 5j2b	5j3b	5j≥4b	≥6j3b	≥6j≥4b
$t\bar{t}$ + light	1365450 ± 420	44000 ± 8000	290 ± 130	31000 ± 6000	340 ± 180
$t\bar{t}$ + ≥1b	92380 ± 44	20500 ± 2400	2080 ± 240	30000 ± 4000	6100 ± 1500
$t\bar{t}$ + ≥1c	217830 ± 120	14000 ± 1600	440 ± 90	17800 ± 2400	910 ± 180
$t\bar{t}$ + W	3181 ± 5	109 ± 16	3.2 ± 0.6	230 ± 40	15.7 ± 2.8
$t\bar{t}$ + Z	3976 ± 12	300 ± 40	51 ± 7	650 ± 90	169 ± 24
Wt channel	46190 ± 110	2300 ± 600	80 ± 50	1800 ± 800	150 ± 90
t channel	19505 ± 74	790 ± 310	55 ± 21	600 ± 500	70 ± 50
Other top	1898 ± 8	125 ± 17	17.7 ± 3.3	190 ± 70	60 ± 24
VV & V + jets	49830 ± 140	1700 ± 700	68 ± 25	1600 ± 600	120 ± 50
$t\bar{t}H$	2918 ± 2	530 ± 60	129 ± 20	1110 ± 130	420 ± 60
Total	1803170 ± 480	84000 ± 10000	3200± 400	85000 ± 12000	8400 ± 1700
Data	1830756	95852	4109	98929	10552
600 GeV	1911 ± 24	520 ± 40	73 ± 8	960 ± 80	279 ± 25

6.4.2 Reweighting technique

The main background for the search is $t\bar{t}$+jets, and its correct modelling is essential for the correct description of the data. It is observed that the simulation does not properly model high jet multiplicities nor the hardness of additional jet emissions [194, 195].

To improve the data/MC agreement of this essential background, data-based corrections are applied to the $t\bar{t}$ samples. Since the mismodelling is assumed to be mainly due to the additional radiation in the parton shower, hence independent on the flavour of the associated jets, the corrections derived in the ≥5j2b regions are expected to improve the agreement in the 3b and ≥4b regions. The remaining discrepancies can still be covered by the systematic model.

The corrections are derived for each jet multiplicity and as a function of $H_{\mathrm{T}}^{\mathrm{all}}$, defined as the scalar p_{T} sum of jets and the lepton, i.e. all the selected objects. The reweighting factors for each jet multiplicity is expressed as:

$$R(H_{\mathrm{T}}^{\mathrm{all}}) = \frac{\mathrm{Data}(H_{\mathrm{T}}^{\mathrm{all}}) - \mathrm{MC}^{\text{non-}t\bar{t}(H_{\mathrm{T}}^{\mathrm{all}})}}{\mathrm{MC}^{t\bar{t}(H_{\mathrm{T}}^{\mathrm{all}})}} \tag{6.1}$$

and, by construction, assumes that any disagreement between data and MC is from $t\bar{t}$. In this context, $t\bar{t}$ includes $t\bar{t}$+≥1b, $t\bar{t}$+≥1c and $t\bar{t}$+light as well as single top Wt contributions.

Figure 6.6 includes all the derived corrections, showing higher weights for increased jet multiplicities and, in general, the $H_{\mathrm{T}}^{\mathrm{all}}$ corrections have a hyperbolic behaviour: converging $H_{\mathrm{T}}^{\mathrm{all}} > 800$ GeV and rapidly increasing towards lower values. Among various functions, the hyperbola plus a sigmoid functional form was found to best fit the $H_{\mathrm{T}}^{\mathrm{all}}$ weight distributions: $w = a + \frac{b}{(H_{\mathrm{T}}^{\mathrm{all}})^c} - \frac{d}{1+\exp\left(e-f\cdot H_{\mathrm{T}}^{\mathrm{all}}\right)}$. Systematic uncertainties are included in the analysis extracted from the eigenvalues of the fitted parameters' error matrix.

The agreement between simulation and data in the analysis region improves, as an example, Figure 6.7 shows the improvement in the leading jet p_{T} distribution before and after the reweighting. The remaining disagreement is especially from normalisation effects, which are obtained in the combined likelihood fit. All figures of this analysis are shown after the reweighting corrections are applied, unless stated otherwise.

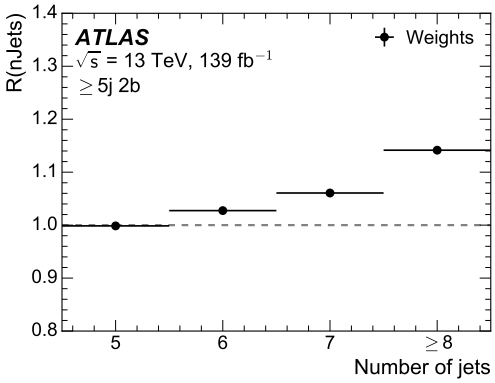

(a) ≥5j2b

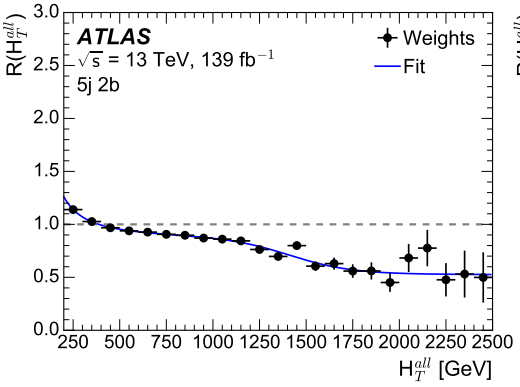

(b) 5j2b

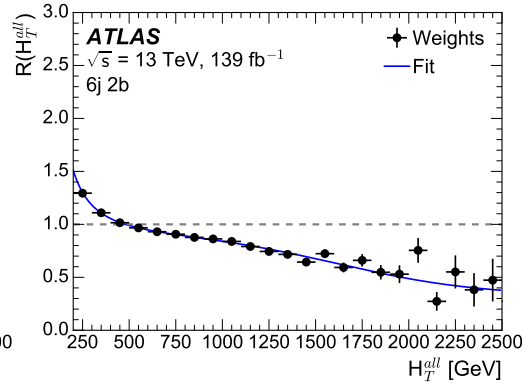

(c) 6j2b

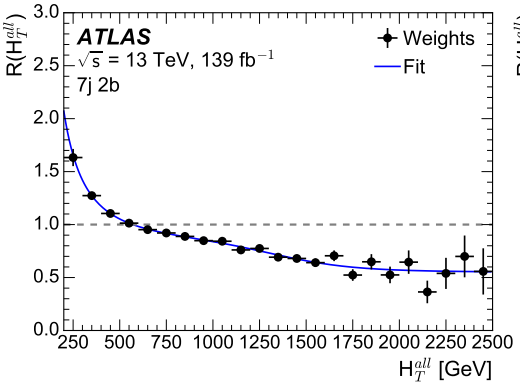

(d) 7j2b

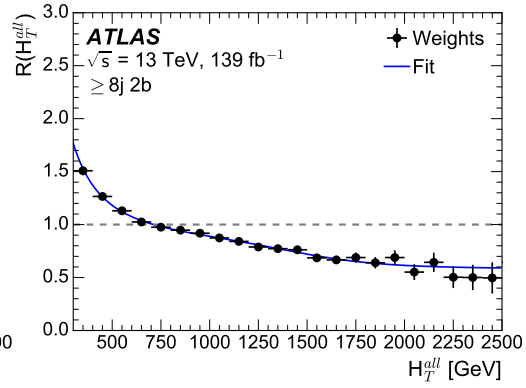

(e) ≥8j2b

Figure 6.6: Reweighting factors (weights) obtained from the comparison between data and simulation of the number of jets (a) and $H_{\mathrm{T}}^{\mathrm{all}}$ for various jet multiplicity selections (b) to (e). The errors in the data points include the statistical uncertainties in data and MC predictions.

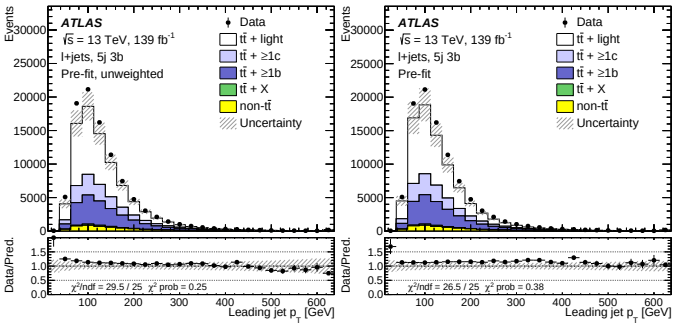

(a) 5j3b, unweighted

(b) 5j3b, reweighted

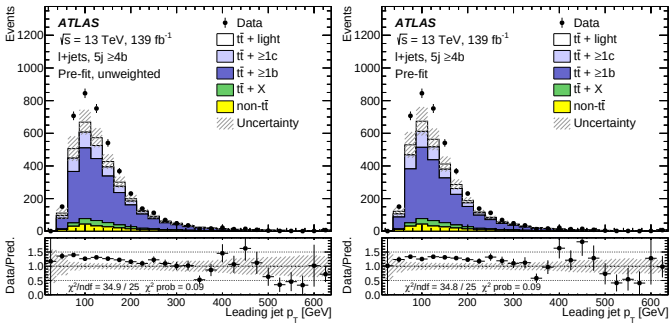

(c) 5j≥4b, unweighted

(d) 5j≥4b, reweighted

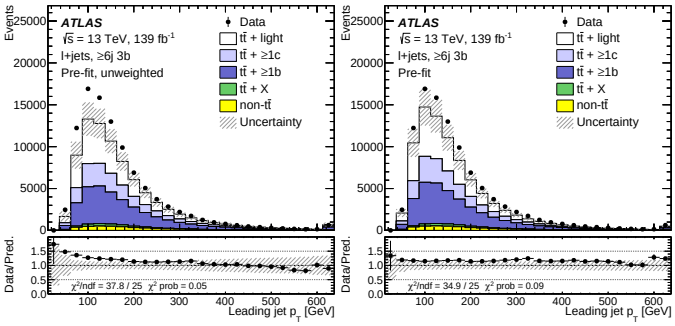

(e) ≥6j3b, unweighted

(f) ≥6j3b, reweighted

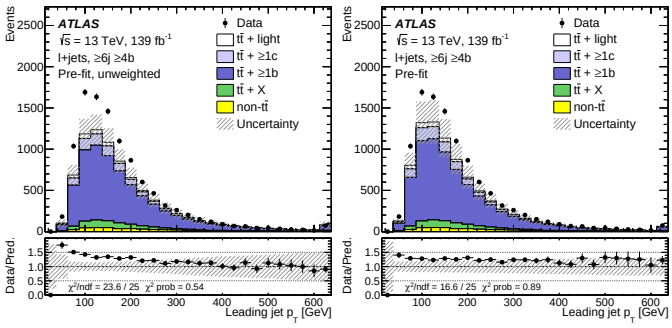

(g) ≥6j≥4b, unweighted

(h) ≥6j≥4b, reweighted

Figure 6.7: Comparison of the predicted leading jet p_{T} and data before the fit in the four analysis signal regions before (left) and after (right) the reweighting was applied. The uncertainty bands include both the statistical and systematic uncertainties, except for the cross-sections of the $t\bar{t}$+≥1b and $t\bar{t}$+≥1c backgrounds. The lower panels display the ratio of the data to the total prediction. The hatched bands show the uncertainties before the fit to the data, which are dominated by systematic uncertainties. The χ^2/ndf and the χ^2 probability are also shown. Statistical uncertainties on MC predictions and data are uncorrelated across bins, while systematic uncertainties on the predictions are correlated.

6.4.3 Multivariate techniques

Multivariate techniques are used in this analysis to enhance the separation between signal and background. The kinematics of $t\bar{t}$+≥1b and signal events are very similar, and these methods can use different distributions as inputs to obtain a powerful discriminating variable.

The main classificator is a parameterised NN trained over all signal and background, as described in Section 5.1.4. In the set of input variables, a kinematic discriminant is included to enhance the separation between a given H^+ sample and $t\bar{t}$+jets.

H^+ parameterised NN

A set of NNs is trained for each of the signal regions: 5j3b, 5j≥4b, ≥6j3b and ≥6j≥4b separately. The NN uses high-level variables as input, hence a simple and small architecture is enough to extract all the discrimination power.

The architecture is sequential with two fully connected layers of 64 nodes and a single output node, implemented with the Python deep learning library, Keras [141]. The activation function used is the commonly employed ReLU, the loss is the *binary cross-entropy* function and the optimiser is the Adam algorithm. Batch normalisation is performed to speed up the learning process and dropout is applied during training at a 10% rate. To further regularise the training, inputs are transformed to the same scale (same mean and variance) as the training set, event weights of each label add up to the same value and a two-fold cross-validation setup is used. All signal samples are used in the training against all background samples, which are weighted according to their cross-sections. Table 6.5 shows the 15 variables used as input for the NN, which includes the H^+ mass. A NN using this technique, normally referred as parameterised NN [152], is being provided with an input that distinguishes the different signals and has the output as a function of the H^+ value. For signal events the parameter corresponds to the mass of the H^+, while for background events a random value of the H^+ is assigned to each event, taken from the distribution of signal masses. This makes the NN not to directly use the parameter to perfectly classify the events, while the classification is optimised for each signal.

The kinematic discriminant, $H_{\mathrm{T}}^{\mathrm{jets}}$, the centrality and the leading jet p_{T} are consistently among the most important variables in the four trained regions. The NN output is obtained evaluating the NN with the H^+ mass set at the desired hypothesis. The obtained distributions for signal and background in the analysis regions for the 200 and 800 GeV H^+ masses are shown in Figure 6.8.

The shapes are significantly different between the two mass-points, although the shape of the distributions transforms gradually from one mass to the next. Notice that the shape of the background changes, since the same NN is being evaluated but with a different H^+ mass value. The separation of the H^+ signal from the background is most difficult for low H^+ masses as the two processes have very similar kinematics and topology.

Table 6.5: List of variables included in the training of the NN.

Variable	Description
m_{H^+}	Parameter of the NN. H^+ mass hypothesis.
D	Kinematic discriminant of the H^+ mass hypothesis.
$H_{\mathrm{T}}^{\mathrm{jets}}$	Scalar sum of the transverse energy of all jets. Sensible to events with massive H^+
Centrality	Centrality calculated using all jets and leptons.
p_{T}^{0}	Leading jet p_{T}. Similar to $H_{\mathrm{T}}^{\mathrm{jets}}$.
$m_{bb}^{\mathrm{min}\Delta R}$	Invariant mass of the closest b-jet pair. The bb pair aims to partially reconstruct the H^+ invariant mass, very different from the $t\bar{t}$ background.
p_{T}^{4}	p_{T} of fifth leading jet. Characterises the low energy scale of the event.
H_{1}^{all}	Second Fox-Wolfram moment calculated using all jets and leptons.
$\Delta R_{bb}^{\mathrm{avg}}$	Average ΔR between all b-jet pairs in the event.
$\mathrm{min}\Delta R_{lep,bb}$	ΔR between the lepton and the pair of b-jets with smallest ΔR.
$m_{uu}^{\mathrm{min}\Delta R}$	Invariant mass of the untagged jet-pair with minimum ΔR. Aims to reconstruct the W-boson that decays hadronically.
$m_{bb}^{\mathrm{max}p_{\mathrm{T}}}$	Invariant mass of the b-jet pair with maximum p_{T}.
$m_{bb}^{\mathrm{max}m}$	Maximal invariant mass of b-jets.
$m_{jjj}^{\mathrm{max}p_{\mathrm{T}}}$	Invariant mass of the jet triplet with maximum p_{T}.
N_{jets} and $N_{b\text{-jets}}$	jet and b-jet multiplicity.

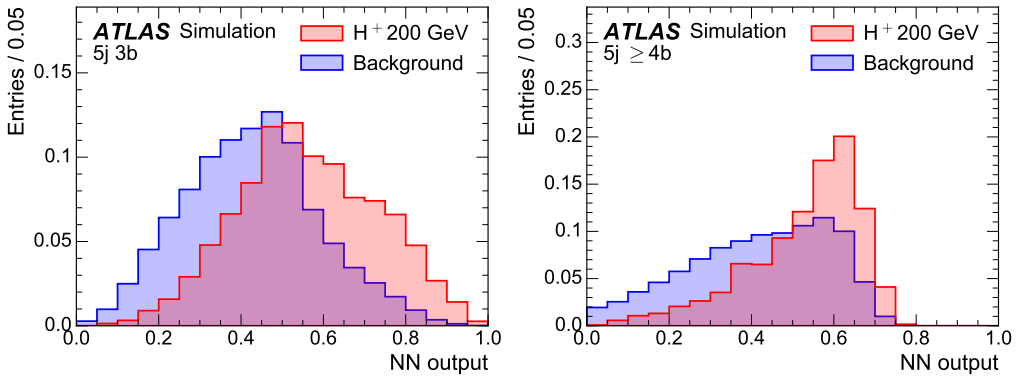

(a) 5j3b

(b) 5j≥4b

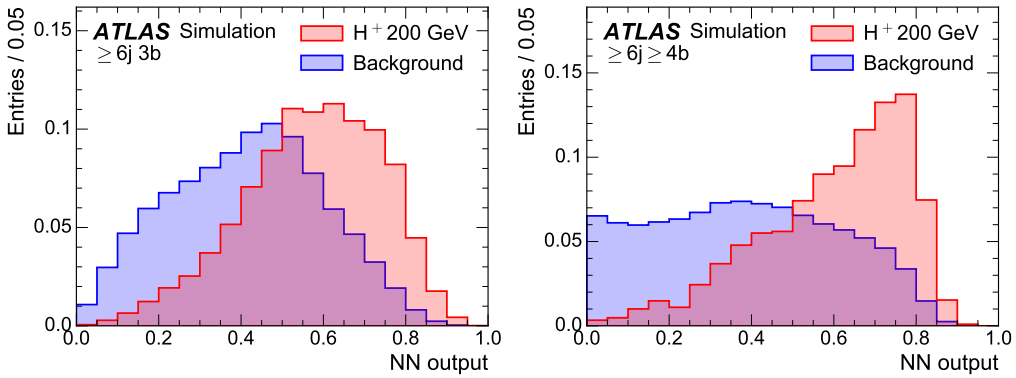

(c) ≥6j3b

(d) ≥6j≥4b

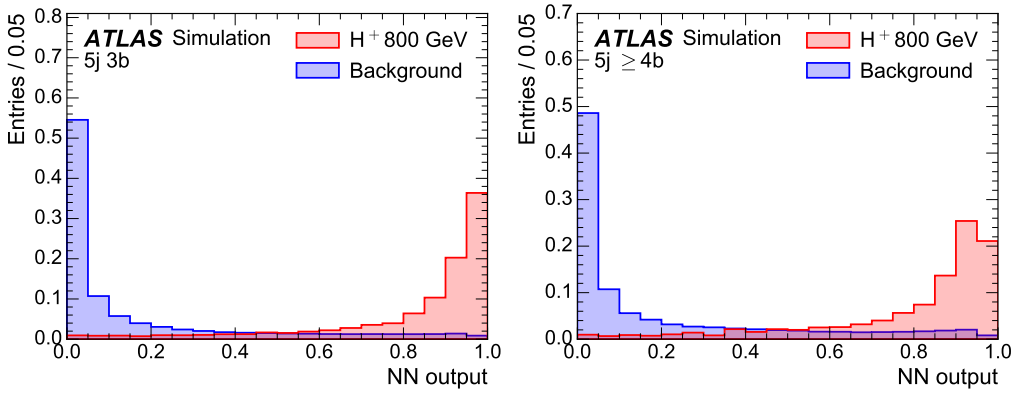

(e) 5j3b

(f) 5j≥4b

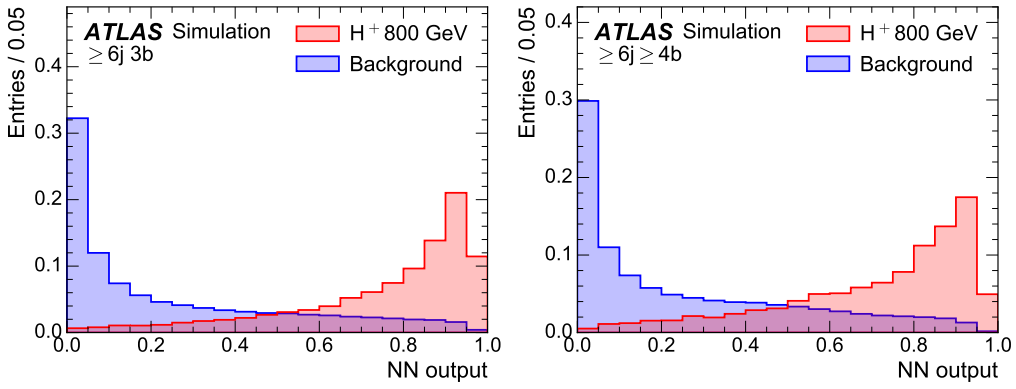

(g) ≥6j3b

(h) ≥6j≥4b

Figure 6.8: Expected distributions of the NN output for H^+ masses of 200 GeV (a-d) and 800 GeV (d-g) for SM backgrounds and H^+ signal in the four trained regions. All distributions are normalised to unity.

Kinematic discriminant

The discriminant is a variable that reflects the compatibility of an event to be signal or $t\bar{t}$ background. This discriminant value is obtained by evaluating the probability density function (pdf) of a given event under both the signal and background hypotheses. It can be defined in general as,

$$D(\mathbf{x}) = \frac{P^{\text{sig}}(\mathbf{x})}{P^{\text{sig}}(\mathbf{x}) + P^{\text{bkg}}(\mathbf{x})} \tag{6.2}$$

where $P^{\text{sig}}(\mathbf{x})$ and $P^{\text{bkg}}(\mathbf{x})$ are the normalised pdf of the corresponding hypothesis, used below more generally as $P^{\text{hyp}}(\mathbf{x})$. The value D is computed for every signal mass and approaches to 1 if an event is identified as signal and to 0 if an event is identified as background.

The pdfs are based on kinematic information, from templates built from distributions using the four-momentum of the different objects of the given event. The jets are first matched to the final state partons identified at generator level. A quark is matched to a jet if $\Delta R \leq 0.3$ and then, two categories are defined: when the full set of partons is successfully matched, the event is referred to as *All Parton Matched* (APM), while the event is called *Missing Jet* (MJ) if any of the partons fail to be matched. The MJ category consists mainly of events that are missing the matching of a quark produced by the W-boson, which are typically low in p_{T} and the associated jet is not reconstructed. Event kinematics are built using up to six jets even if the total number of reconstructed jets in events is sometimes larger than six. Concerning neutrinos, they are reconstructed solving the quadratic equation: $m_W^2 = (p_\ell + p_\nu)^2$, which assumes that all $\text{E}_{\text{T}}^{\text{miss}}$ is produced by the $W \to \ell\nu$ decay. In general, two solutions are obtained and the solution with lower $p_{z,\nu}$ is taken. It is often the case that the equation does not return a real solution, and the $\text{E}_{\text{T}}^{\text{miss}}$ is lowered until a single solution is possible.

Given that jets are used to reconstruct kinematics and the information of parton-jet truth associations is not available in real events, averaging the pdfs over all possible parton-jet combinations is needed to evaluate the discriminant. By construction, the individual pdf corresponding to the permutation of the correct set of jet-parton combination will have the biggest contribution in the discriminant. To reduce execution time, only up to the leading eight jets are used to build kinematics. A flavour weight is assigned for each jet using the PCBT score in order to lower the contribution of the combination in the discriminant when a light jet is wrongly used as a b-parton in the kinematic reconstruction or vice versa, thus reducing the impact on the discriminant of the incorrect combinations. The pdf of each hypothesis, signal and background, can be expressed as:

$$P^{\text{hyp}}(\mathbf{x}) = \frac{\sum_{i=0}^{N} P_{b\text{tag}}^{\text{hyp}}(\mathbf{x}_i) P_{\text{kin}}^{\text{hyp}}(\mathbf{x}_i)}{\sum_{i=0}^{N} P_{b\text{tag}}^{\text{hyp}}(\mathbf{x}_i)}, \tag{6.3}$$

where N is the total number of jet-parton combinations and $P_{\text{kin}}^{\text{hyp}}(\mathbf{x})$ and $P_{\text{btag}}^{\text{hyp}}(\mathbf{x}_i)$

are the kinematic pdf and the flavour weight for the given hypothesis, respectively. The kinematic variables and the b-tagging used to build the expressions for $P^{\text{hyp}}_{\text{kin}}$ and $P^{\text{hyp}}_{b\text{tag}}$ is described in detail below. The tagging weights can be expressed (for a single permutation) as,

$$P^{\text{hyp}}_{b\text{tag}} = P_b(j1)P_l(j2)P_l(j3)P_b(j4)P_b(j5)\begin{cases} 1 & \text{5jet} \\ P_l(j6)P_l(j7)P_l(j8) & \geq \text{6jet}, 3b \\ P_b(j6)P_l(j7)P_l(j8) & \geq \text{6jet}, \geq 4b \end{cases} \tag{6.4}$$

As the H^+ can decay either leptonically or hadronically, the kinematics involving the H^+ are a weighted combination of the two, according to the ratio of events. Concerning neutrinos the same principle is applied only in the case of two neutrino solutions. To address the APM and MJ categories, $P^{\text{hyp}}_{\text{APM}}$ and $P^{\text{hyp}}_{\text{MJ}}$ are calculated individually following the previous equation. Similarly, the final pdf in the discriminant is a weighted combination of the two, where the weight is the ratio between APM and MJ events.

Signal probability
The signal kinematic probability $P^{\text{sig}}_{\text{kin}}$ is the product of the normalised kinematic probabilities extracted from the templates describing the phase space of the partonic final state. Templates are built for each signal mass sample by reconstructing the invariant masses from every truth-matched event for the signal, and subdivided by region and the categories already defined.

The invariant masses considered are the mass of the H^+, the mass of the hadronic W ($M_{q\bar{q}}$) and the masses of the leptonic and hadronic top-quarks ($m_{b_{lep}\ell\nu}$ and $m_{b_{had}q\bar{q}}$). To minimise correlations between quantities, differences of masses are used:

$$\begin{cases} \chi_{t_{had}} = m_{b_{had}q\bar{q}} - m_{q\bar{q}} \\ \chi_{H^+_{had}} = m_{b_h b_{had}q\bar{q}} - m_{b_{had}q\bar{q}} \\ \chi_{H^+_{lep}} = m_{b_h b_{lep}\ell\nu} - m_{b_{lep}\ell\nu} \\ \chi_{t_{had}b_4} = m_{t_{had}b_4} - m_{t_{had}} = m_{b_{had}q\bar{q}b_4} - m_{b_{had}q\bar{q}} \\ \chi_{t_{lep}b_4} = m_{t_{lep}b_4} - m_{t_{lep}} = m_{b_{lep}\ell\nu b_4} - m_{b_{lep}\ell\nu} \end{cases} \tag{6.5}$$

where b_h denotes the b-quark from the $H^+ \to tb$ decay and $b_{had/lep}$ the one from the top quark with the hadronically/leptonically decaying W-boson, $t_{had/lep}$. $\chi_{t_{lep/had}b_4}$ refers to the recoil system of the H^+, from the t- and $b-$quarks generated in association with the boson. Introducing the mixing between the two possible H^+ decays, the probability reads:

$$\begin{aligned} P^{\text{sig}}(\chi_{H^+})P^{\text{sig}}(\chi_{tb}) = &\omega_{had}P^{\text{sig}}(\chi_{H^+_{had}})P^{\text{sig}}(\chi_{t_{lep}b_4}) + \\ &\omega_{lep}P^{\text{sig}}(\chi_{H^+_{lep}})P^{\text{sig}}(\chi_{t_{had}b_4}), \end{aligned} \tag{6.6}$$

The full kinematic signal probability results,

$$P^{\text{sig}}_{\text{kin}} = P^{\text{sig}}(m_{W_h})P^{\text{sig}}(\chi_{t_{had}})P^{\text{sig}}(m_{t_{lep}})P^{\text{sig}}(\chi_{H^+}) \begin{cases} 1 & \text{5jet} \\ P^{\text{sig}}(\chi_{tj}) & \geq \text{6jet}, 3b \\ P^{\text{sig}}(\chi_{tb}) & \geq \text{6jet}, \geq 4b \end{cases} \tag{6.7}$$

$$P^{\text{bkg}}_{\text{kin}} = P^{\text{bkg}}(m_{W_h})P^{\text{bkg}}(\chi_{t_{had}})P^{\text{bkg}}(m_{t_{lep}}) \begin{cases} P^{\text{bkg}}(\chi_{H^+}) & \text{5jet} \\ P^{\text{bkg}}(m_{jj})P^{\text{bkg}}(\chi_{t\bar{t}}) & \geq \text{6jet}, 3b \\ P^{\text{bkg}}(m_{bb})P^{\text{bkg}}(\chi_{t\bar{t}}) & \geq \text{6jet}, \geq 4b \end{cases} \tag{6.8}$$

which specifically shows the exceptions when using the H^+ recoil system: it is not used for 5j regions and a light jet is used instead for ≥6j3b. In the case of an event with two neutrino solutions, the leptonic quantities should be averaged with the analogous $\omega_{1\nu}/\omega_{2\nu}$.

Background probability

The background kinematic pdf $P^{\text{bkg}}_{\text{kin}}$, follows a similar formula to the signal kinematic pdf. Apart from the H^+ boson mass and its recoil system, all other masses can be reconstructed: the mass of the hadronic W ($m_{q\bar{q}}$) and the mass of the leptonic and hadronic top-quark ($m_{b_{lep}\ell\nu}$ and $m_{b_{had}q\bar{q}}$), for a total of three masses. To replace the other two, the $m_{b\bar{b}}$ and the $\chi_{t\bar{t}} = m_{t\bar{t}} - m_{t_{had}} - m_{t_{lep}}$ systems are used.

In the 5jet regions the $m_{b\bar{b}}$ system cannot be reconstructed, hence the fourth kinematic variable is replaced with a pseudo-H^+ reconstructed with a light jet. Concerning the ≥6j3b region, two light jets are used instead $m_{j_h j_4}$ as the soft b-quark is typically tagged as a light jet and outputs a better performance than mixing jet flavours. Following the description, the background kinematic pdf is expressed as:

$$P^{\text{bkg}}_{\text{kin}} = P^{\text{bkg}}(m_{W_h})P^{\text{bkg}}(\chi_{t_{had}})P^{\text{bkg}}(m_{t_{lep}}) \begin{cases} P^{\text{bkg}}(\chi_{H^+}) & \text{5jet} \\ P^{\text{bkg}}(m_{jj}) & \geq \text{6jet}, 3b \\ P^{\text{bkg}}(m_{bb}) & \geq \text{6jet}, \geq 4b \end{cases} \tag{6.9}$$

The discriminant distributions for signal and background in the analysis regions for the 200 and 800 GeV H^+ masses are shown in Figure 6.9. Similarly to the NN output, the shapes transform gradually from one mass to the next and the separation is most difficult for low H^+ masses.

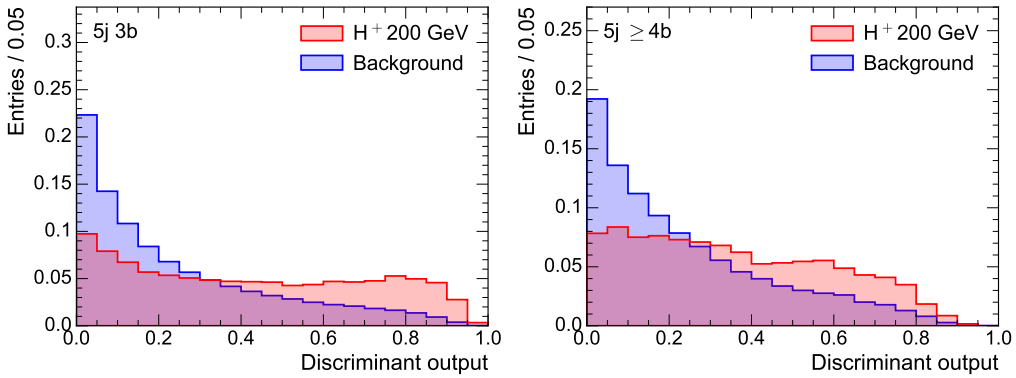

(a) 5j3b

(b) 5j≥4b

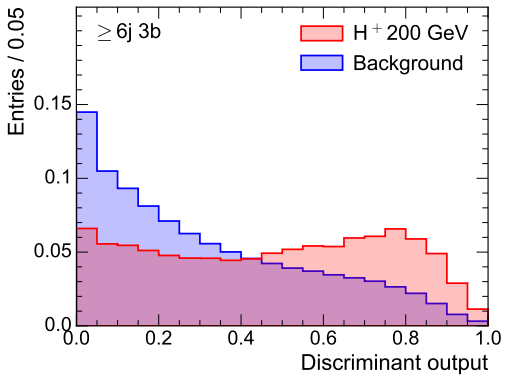

(c) ≥6j3b

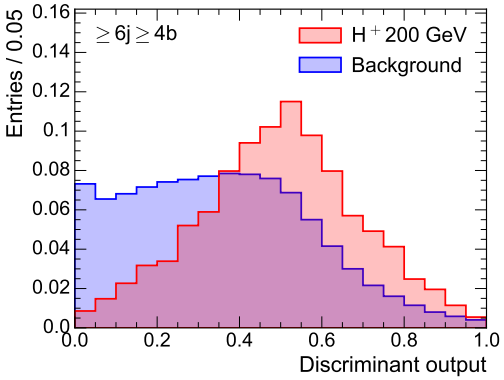

(d) ≥6j≥4b

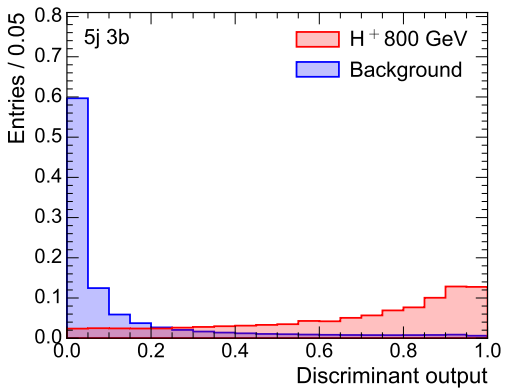

(e) 5j3b

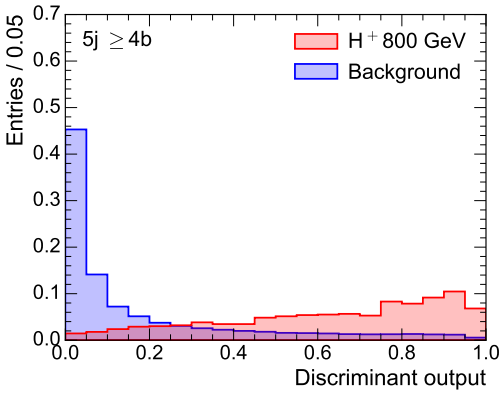

(f) 5j≥4b

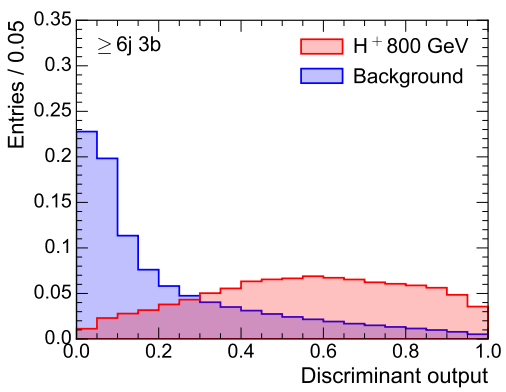

(g) ≥6j3b

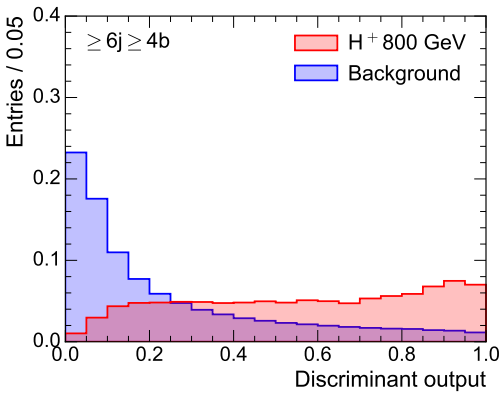

(h) ≥6j≥4b

Figure 6.9: Expected distributions of the kinematic discriminant for H^+ masses of 200 GeV (a-d) and 800 GeV (d-g) for SM backgrounds and H^+ signal in the four signal regions. All distributions are normalised to unity.

6.5 Systematic uncertainties

The presented analysis is heavily affected by systematic uncertainties from different sources, explained in this section. There are two main categories of systematic uncertainties: experimental uncertainties, mainly associated to the reconstruction of the various physics objects, and the modelling uncertainties related to the signal and background process modelling in MC.

In total, 352 nuisance parameters are used and summarised in Table 6.6, corresponding to the systematic components, and the $t\bar{t}$+≥1b and $t\bar{t}$+≥1c normalisation factors included in the fit. The systematic uncertainties can either affect both the shape and the normalisation (SN), only the normalisation (N) or only the shape (S) of a process. Some uncertainty sources might consist of several independent components, e.g. the b-jet efficiency calibrations or the PDF tunings, and one nuisance parameter is associated to each component. In addition, for every bin considered in the analysis one nuisance parameter is assigned to take into account the uncertainties coming from the finite statistics of the background MC samples.

6.5.1 Experimental uncertainties

The experimental uncertainties have in general a low impact on the final fit. Only the uncertainties associated to jets and b-tagging have influence. All experimental nuisance parameters are correlated across all analysis regions and processes.

The total uncertainty on the integrated luminosity of the full Run 2 is the only experimental uncertainty that only affects the normalisation, and is measured to be 1.7% [62]. The pile-up modelling uncertainty, that accounts for the related differences between data and simulation, is also considered [196].

Jets and heavy-flavour tagging

The uncertainties associated to jets are the most relevant experimental sources in this analysis. Although the single components are in the range of 1%-5%, the analysis is most sensitive on events with large number of jets, thus enhancing their effect. The uncertainties on the jet energy scale and resolution add up to 31 and 9 nuisance parameters, respectively [197, 198].

The uncertainties for the jet energy scale are extracted from test-beam and LHC data as well as from simulation, being less than 4% for jets with $p_{\mathrm{T}} = 25$ GeV and less than 2% for central jets with 1.5 TeV $> p_{\mathrm{T}} >$ 100 GeV. Further uncertainty sources are also considered assuming a conservative uncertainty of ±50% on the quark-gluon fraction for the simulation of jets with different flavours. Moreover, pile-up corrections are taken into account as well as uncertainties from jet kinematics as well as differences between the two detector simulations used in the analysis. The jet energy resolution uncertainties are extracted from measured di-jet events using Run 2 data and MC simulation. Finally, the jet vertex tagger uncertainty is extracted from data-MC calibrations measured [199] in $Z \to \mu^+\mu^-$ events.

Table 6.6: Overview of the systematic uncertainties included in the analysis. An "N" means that the uncertainty is taken as normalisation-only for all processes and regions affected, whereas "SN" means that the uncertainty is taken on both shape and normalisation. Some systematic uncertainties are split into several components for a more accurate treatment: the number of such components is indicated in the rightmost column. "Small backgrounds" refers to the tZq, tZW, $tHjb$, and tWH processes. The $t\bar{t}$ reweighting systematic uncertainty is also applied to the Wt single top background.

Systematic uncertainty	Type	Components
Experimental uncertainties		
Luminosity	N	1
Pileup modelling	SN	1
Physics objects		
Electrons	SN	7
Muons	SN	15
Jet energy scale	SN	31
Jet energy resolution	SN	9
Jet vertex tagger	SN	1
$E_{\mathrm{T}}^{\mathrm{miss}}$	SN	3
b-tagging		
Efficiency	SN	45
Mis-tag rate (c)	SN	20
Mis-tag rate (light)	SN	20
Signal and background modelling		
Signal		
PDF variations	SN	30
Scales	SN	2
$t\bar{t}$ background		
$t\bar{t}$ cross-section	N	1
PDF variations	SN	90
$t\bar{t}$ reweighting	SN	28
$t\bar{t}+ \geq 1c$ normalisation	N (free floating)	1
$t\bar{t}+ \geq 1b$ normalisation	N (free floating)	1
$t\bar{t}+$ light modelling	SN	6
$t\bar{t}+ \geq 1c$ modelling	SN	6
$t\bar{t}+ \geq 1b$ modelling	SN	7
Other backgrounds		
$t\bar{t}W$ cross-section	N	2
$t\bar{t}Z$ cross-section	N	2
$t\bar{t}W$ modelling	SN	1
$t\bar{t}Z$ modelling	SN	1
Single top cross-section	N	3
Single top modelling	SN	7
W+jets normalisation	N	3
Z+jets normalisation	N	3
Diboson normalisation	N	1
$t\bar{t}t\bar{t}$ cross-section	N	1
Small backgrounds cross-sections	N	3

Uncertainties related to b-tagging are relevant in this analysis due the use of b-jets for the selection and the use of their kinematics in the multi-variate techniques. The b-tagging calibrations are derived separately for jets containing b-hadrons, c-hadrons or neither as a function of p_{T} and the different b-tagging working points in dedicated calibration analyses targetting different topologies. The different uncorrelated sources are obtained from a principal component analysis (eigenvalue decomposition) and are in the range of 2%-10% for the b-jet efficiency calibration and between 10% to 25% and 15% to 50% for the c-jets and light-flavour jets mis-tag rate calibration, respectively. In total, the flavour-tagging uncertainties consists of 85 components.

Leptons

Even though the systematic uncertainties related to leptons have a small effect, 22 different uncertainty sources are taken into account [200, 201] The components are related to the trigger, reconstruction, identification and isolation efficiencies for electrons (four components) and muons (ten components), together with components related to the lepton p_{T} scale and resolution of electrons (three components) and muons (five components).

Missing transverse momentum

The systematic uncertainties associated to the $\mathrm{E}_{\mathrm{T}}^{\mathrm{miss}}$ have minor impact as it is only used to reconstruct the neutrino of the event. Since the $\mathrm{E}_{\mathrm{T}}^{\mathrm{miss}}$ is calculated from the reconstructed physics objects and a soft term, the energy scale and resolution uncertainties from the physics objects are propagated to the $\mathrm{E}_{\mathrm{T}}^{\mathrm{miss}}$ together with an additional component for the soft term.

6.5.2 Modelling Uncertainties

In contrast to the experimental uncertainties, the modelling uncertainties are not correlated across all background and signal processes, but typically they are still correlated across analysis regions with some exceptions. The uncertainties are split into several components depending on the signal and background processes as well as into different physics effects in MC generators. While the cross-section, branching fraction and normalisation uncertainties only affect the normalisation of the physics processes, all other modelling uncertainties are also sensitive to shape effects.

Signal modelling

The sources of uncertainty considered for the signal are associated to the energy scales to generate the MC and the PDF tunings. First, the impact of ISR in the ME is estimated with the independent variation of the renormalisation μ_R and factorisation μ_F scales by a factor 0.5 (higher parton radiation) and by 2 (lower parton radiation). The PDF uncertainty is estimated using a symmetrised Hessian PDF set, following the PDF4LHC recommendations for Run 2 [202].

$t\bar{t}$ modelling

The $t\bar{t}$ process is the most important background in the analysis and numerous uncertainties are considered for an appropriate modelling. Since the composition of the $t\bar{t}$ subcategories are different in the signal regions, different effects are expected. The $t\bar{t}$+≥1b and $t\bar{t}$+≥1c processes are fairly sensitive to differences in the precision of the ME calculation or the flavour scheme, while $t\bar{t}$+light profits from precise measurements. Hence, all systematic uncertainties associated to $t\bar{t}$ are uncorrelated across the $t\bar{t}$+≥1b, $t\bar{t}$+≥1c and $t\bar{t}$+light categories, having separate nuisance parameters. Unless stated otherwise, the nuisance parameters are correlated among bins and regions.

Table 6.7 summarises the uncertainties applied to the $t\bar{t}$ background.

Table 6.7: Summary of the sources of systematic uncertainty for the $t\bar{t}$ background modelling. The last column of the table indicates the subcomponents for the corresponding systematic uncertainty. All systematic uncertainty sources, except those associated to the $t\bar{t}$ reweighting, are treated as uncorrelated across the three components.

Uncertainty source	Description		Components
$t\bar{t}$ cross-section	Up or down by 6%		$t\bar{t}$+light
$t\bar{t}$+≥1b normalisation	Free-floating		$t\bar{t}$+≥1b
$t\bar{t}$+≥1c normalisation	Free-floating		$t\bar{t}$+≥1c
$t\bar{t}$ reweighting	Uncertainties of fitted function parameters		$t\bar{t}$ and Wt
μ_R	Scaling by 0.5 (2.0)	in PowhegBox +Pythia	$t\bar{t}$
μ_F	Scaling by 0.5 (2.0)	in PowhegBox +Pythia	$t\bar{t}$
ISR	Varying α_S^{ISR}	in PowhegBox +Pythia	$t\bar{t}$
FSR	Varying α_S^{FSR}	in PowhegBox +Pythia	$t\bar{t}$
NLO matching	MadGraph5_aMC@NLO +Pythia	vs. PowhegBox +Pythia	$t\bar{t}$
PS & hadronisation	PowhegBox +Herwig	vs. PowhegBox +Pythia	$t\bar{t}$
$t\bar{t}$+≥1b modelling	4FS vs. 5FS		$t\bar{t}$+≥1b

The inclusive $t\bar{t}$ cross-section (NNLO+NNLL) has an uncertainty of ±6%, which is only applied to $t\bar{t}$+light as it is dominant in the inclusive phase space [203–209]. This uncertainty covers several effects from varying the factorisation and normalisation scales, the PDF set, α_S as well as the top-quark mass. The normalisations for $t\bar{t}$+≥1b and $t\bar{t}$+≥1c are allowed to vary freely and are obtained with the fit.

The uncertainties related to initial and final state radiation are split in different components. The μ_R and μ_F are varied independently by a factor 0.5 (2.0) for the up (down) variation. Then, ISR and FSR components are obtained setting accordingly α_S^{ISR} to 0.140 (0.115) and α_S^{FSR} to 0.140 (0.115), where the nominal values are 0.127 for both.

Two-point systematics are derived for the rest of modelling uncertainties. For a given distribution, this type of uncertainties are obtained from the difference in the prediction when comparing two different samples generated with different MC setups. The systematic uncertainty related to PS are retrieved by comparing the nominal setup, Powheg+Pythia 8 to the prediction of the sample generated with Powheg+Herwig 7, where the PS has been modelled with a different generator.

Similarly, the uncertainty related to the NLO matching is retrieved from a sample generated with MadGraph5_aMC@NLO+PYTHIA 8.

To cover the differences between the choice of the four or five flavour schemes, the nominal (5FS) sample is compared to a PowhegBoxRes+Pythia 8 (4FS) $t\bar{t}$+≥1b sample. This uncertainty is only applied to the $t\bar{t}$+≥1b component and only the shape effects are extracted.

The weights derived in Section 6.4.2 that are applied to improve the modelling of the $t\bar{t}$ background are also subject to uncertainties. The associated statistical uncertainties are varied obtaining 28 nuisance parameters, which are correlated between the different $t\bar{t}$ components and Wt. Aside, the $t\bar{t}$ samples with alternative MC setups do not have the same composition of $t\bar{t}$ subcomponents as the nominal sample, especially PowhegBox +Herwig 7. This difference can change significantly the fractions in the fit however, the normalisation of the sub-processes in the analysis regions are measured with the fit. To avoid the propagation of the normalisation effect from the comparison, the alternative samples are scaled to ensure the same flavour composition as the nominal sample in the signal regions. In addition, the same modelling issues that motivate the $t\bar{t}$ weights can be found in the alternative samples, hence different sets of reweighting are also derived using the alternative samples.

Other background modelling

The systematic uncertainties associated to background processes other than $t\bar{t}$+jets are summarised in Table 6.8 with their respective sources and the corresponding descriptions. These uncertainties play a subordinate role compared to the $t\bar{t}$ uncertainties.

A 5% uncertainty is considered for the cross-sections of the three single-top production modes [93, 210–213]. Uncertainties associated with the PS model, and with the NLO matching scheme are evaluated by comparing, for each process individually, the nominal Powheg+Pythia 8 sample with a sample produced using Powheg+Herwig 7 and MadGraph5_aMC@NLO+PYTHIA 8, respectively. As mentioned before, the Wt single-top process is included in the reweighting procedure, and thus the same related uncertainties used for $t\bar{t}$ are applied. The uncertainty associated to the interference between Wt and $t\bar{t}$ production at NLO scheme [183] and the diagram subtraction scheme is assessed by comparing the nominal Powheg+Pythia 8 sample produced using the "diagram removal" scheme with an alternative sample produced with the same generator but using the "diagram subtraction" scheme.

The predicted $t\bar{t}H$ signal cross-section uncertainty used is $^{+5.8\%}_{-9.2\%}$ (QCD scale) ±3.6% (PDF + α_S) [180, 183, 214–218]. Uncertainties of the Higgs boson branching ratios amount to 2.2% for the $b\bar{b}$ decay mode [180]. For the ISR and FSR, the amount of radiation is varied following the same procedure as for $t\bar{t}$, except that the ISR is made of one component varying the different parameters at the same time. Also, the assessment of the PS and the NLO matching uncertainties is similarly performed

comparing the nominal with the same type of alternative MC.

The uncertainty of the $t\bar{t}V$ NLO cross-section prediction is 15%, split into PDF and scale uncertainties as for $t\bar{t}H$ [180, 219]. An additional $t\bar{t}V$ modelling uncertainty, related to the choice of both PS model and matching scheme, is assessed by comparing the nominal MadGraph5_aMC@NLO+PYTHIA 8 samples with the alternative samples generated with Sherpa.

An uncertainty of 40% is assumed for the W+jets normalisation, with an additional 30% for W+ heavy-flavour jets, taken as uncorrelated between events with two and more than two heavy-flavour jets. These uncertainties are based on variations of the μ_R and μ_F scales and of the matching parameters in the Sherpa samples. An uncertainty of 35% is applied to the Z+jets normalisation, uncorrelated across jet bins, to account for both the variations of the scales and matching parameters in the Sherpa samples and the uncertainty in the extraction from data of the correction factor for the heavy-flavour component [91, 219]. For the diboson background, a 50% normalisation uncertainty is assumed, which includes uncertainties in the inclusive cross-section and additional jet production [220].

An overall 50% normalisation uncertainty is considered for the $t\bar{t}t\bar{t}$ background, covering effects from varying μ_R, μ_R, PDF set and α_S [221, 222]. The small background tZq is assigned a 7.9% uncertainty accounting for the μ_R and μ_F variations, and a 0.9% uncertainty for the PDF variations. Finally, a single 50% uncertainty is set for tZW [221].

Table 6.8: Summary of the systematic uncertainties associated to the modelling of the background processes other than $t\bar{t}$. DR denotes the diagram removal scheme (nominal), DS stands for diagram subtraction scheme and HF for heavy flavour.

Process	Uncertainty source	Description
single-top	Cross-section	Up or down by 5%
	PS model	MadGraph5_aMC@NLO +Pythia vs. PowhegBox +Pythia
	NLO matching	PowhegBox +Herwig vs. PowhegBox +Pythia
	$Wt/t\bar{t}$ interference	DR vs. DS scheme in PowhegBox +Pythia
$t\bar{t}H$	Cross-section	$^{+5.8\%}_{-9.2\%}$ ±3.6%
	B($H \to b\bar{b}$)	Up or down by 2.2%
	ISR	Varying α_S^{ISR}, μ_R and μ_F in PowhegBox +Pythia
	FSR	Varying α_S^{FSR} in PowhegBox +Pythia
	PS model	MadGraph5_aMC@NLO +Pythia vs. PowhegBox +Pythia
	NLO matching	PowhegBox +Herwig vs. PowhegBox +Pythia
$t\bar{t}V$	Cross-section	Up or down by 15% (split into PDF and scale)
	PS model NLO matching	Sherpa vs. MadGraph5_aMC@NLO +Pythia
W+jets	Cross-section	Up or down by 40%
W+HF-jets	Normalisation	Up or down by 30%
Z+jets	Normalisation	Up or down by 35%
Diboson	Normalisation	Up or down by 50%
$t\bar{t}t\bar{t}$	Cross-section	Up or down by 50%
tZq	Cross-section	Up or down by 7.9% and 0.9%
tZW	Cross-section	Up or down by 50%

$H^+ \to tb$ analysis results

7

In order to test for the presence of $H^+ \to tb$ signal, a binned maximum-likelihood fit to the data is performed as described in Section 5.2. In total 18 fits are performed, one for each mass hypothesis fitting the NN output evaluated at the corresponding mass values as explained in Section 6.4.3. Four regions are used in the fit: 5j3b, 5j≥4b, ≥6j3b and ≥6j≥4b. The distributions have ten bins, except 5j≥4b which have eight, and the irregular binning of each region is optimised to increase sensitivity. Two initially unconstrained fit parameters are used to model the normalisation of the $t\bar{t}$+≥1b and $t\bar{t}$+≥1c backgrounds. The parameter of interest is the product of the production cross-section $\sigma(pp \to tbH^+)$ and the branching fraction B($H^+ \to tb$).

A total of 350 nuisance parameters are introduced in the fit. To speed up the fit and ease the convergence, the shape or normalisation components of the different systematic uncertainties are pruned if their effect is below a threshold of 1%. In addition, smoothing techniques are applied to reduce the impact of statistical fluctuations when computing the templates of systematic uncertainties.

This section provides the expected and observed results on the fitted signal strength, CL_s exclusion limits, a brief review of the performance and the interpretation and combination of the results in the 2HDM+a model.

7.1 Fit results

The analysis optimisation is performed on MC simulation and the performance is evaluated via *Asimov* data instead of experimental data. The dataset is built from the nominal background and the chosen signal, thus the normalisation factors and nuisance parameters extracted from the fit are the default ones by construction. Nevertheless, the profile likelihood fit provides uncertainties on the signal strength and the expected upper limits. It is the standard procedure to optimise the analysis without using the experimental data to avoid introducing any bias, especially in sensitive regions. Once the desired expected sensitivity is obtained and the background modelling reproduces the experimental data in signal-depleted regions, experimental data is added to the fit. Multiple studies were performed to validate the fits studying the effect of pulls and constraints of the nuisance parameters, evaluate possible biases in the signal modelling or evaluating the data/MC agreement in the post-fit distributions among them.

The agreement between the observed and expected event yields in all regions is shown in Figure 7.1 before and after performing the 800 GeV hypothesis fit. The pre-fit shows the background with an overlay of the signal, while the post-fit includes the signal, although fitted to a negative value and is not visible. The data and MC compatibility improves significantly with the fit. This is general for all the mass hypotheses. Table 7.1 shows the event yields after the corresponding fit under the 200 GeV and 800 GeV H^+ mass hypotheses.

Pre-fit and post-fit distributions of the NN output in the signal regions are shown in Figure 6.9 to Figure 6.12 for the different regions and for the 200 GeV and 800 GeV hypothesis fits. The agreement between the observed and expected bins improves drastically after the fit.

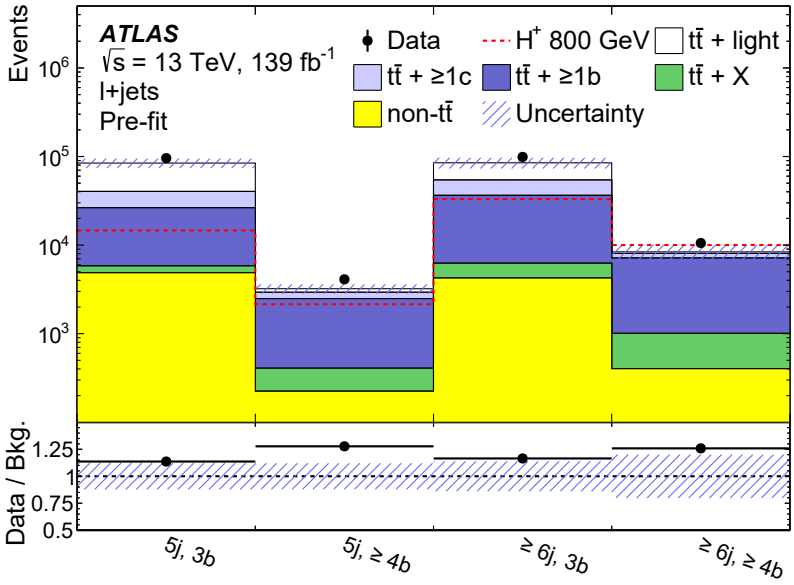

(a) Pre-fit

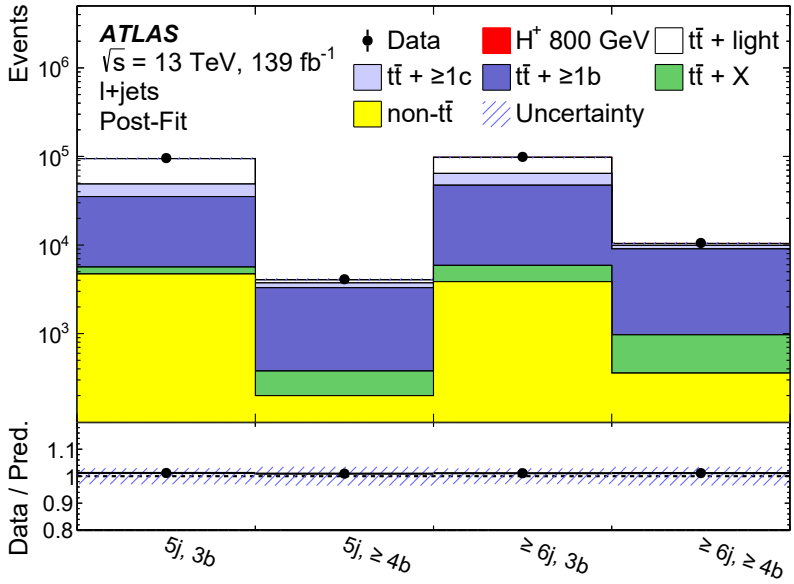

(b) Post-fit

Figure 7.1: Comparison of predicted and observed event yields before (a) and after (b) the fit in each of the signal regions for the 800 GeV hypothesis. The lower panel displays the ratio of the data to the total prediction and the hatched band shows the uncertainties. The pre-fit yields of a charged Higgs boson with a mass of 800 GeV corresponding to a cross-section of 10 pb are overlaid in red.

Table 7.1: Event yields of the $H^{\to}tb$ signal and background processes in the four signal regions after the fit to the data under the H^+ hypotheses of 200 (top) and 800 GeV (bottom). The quoted uncertainties take into account correlations and constraints of the nuisance parameters and include both the statistical and systematic uncertainties. Negative correlations among $t\bar{t}$+≥1b, $t\bar{t}$+≥1c and $t\bar{t}$+light modelling uncertainties can cause the uncertainty on the total yields to be smaller than on individual components.

200 GeV H^+ hypothesis				
	5j3b	5j≥4b	≥ 6j3b	≥ 6j≥4b
$t\bar{t}$+light	45000 ± 4000	310 ± 110	32000 ± 4000	340 ± 140
$t\bar{t}$+≥1b	29600 ± 2900	2940 ± 220	40200 ± 3300	8000 ± 500
$t\bar{t}$+≥1c	14000 ± 4000	440 ± 140	19000 ± 6000	1010 ± 290
$t\bar{t}+W$	110 ± 15	3.2 ± 0.6	236 ± 35	16.2 ± 2.7
$t\bar{t}+Z$	300 ± 40	51 ± 6	670 ± 90	174 ± 23
Single-top Wt-channel	2300 ± 600	80 ± 50	1900 ± 800	150 ± 90
Single-top t-channel	740 ± 300	51 ± 20	500 ± 400	60 ± 50
Other top-quark sources	128 ± 16	17.5 ± 3.2	180 ± 70	58 ± 24
VV & V + jets	1600 ± 600	65 ± 23	1600 ± 600	120 ± 40
$t\bar{t}H$	530 ± 60	127 ± 19	1140 ± 120	430 ± 60
$H^+ \to tb$	600 ± 900	70 ± 90	700 ± 1000	160 ± 230
Total	95700 ± 2900	4150 ± 140	98400 ± 2900	10500 ± 400
Data	95852	4109	98929	10552

800 GeV H^+ hypothesis				
	5j3b	5j≥4b	≥ 6j3b	≥ 6j≥4b
$t\bar{t}$+light	46000 ± 4000	330 ± 120	33000 ± 4000	500 ± 200
$t\bar{t}$+≥1b	29600 ± 3100	2920 ± 210	41000 ± 4000	8100 ± 400
$t\bar{t}$+≥1c	14000 ± 6000	440 ± 190	17000 ± 7000	870 ± 330
$t\bar{t}+W$	108 ± 15	3.3 ± 0.6	233 ± 35	16.0 ± 2.7
$t\bar{t}+Z$	300 ± 40	50 ± 7	660 ± 90	171 ± 23
Single-top Wt-channel	2000 ± 500	56 ± 33	1400 ± 500	100 ± 60
Single-top t-channel	740 ± 300	53 ± 21	600 ± 500	70 ± 50
Other top-quark sources	130 ± 16	17.7 ± 3.2	190 ± 70	61 ± 24
VV & V + jets	1900 ± 700	73 ± 25	1700 ± 600	130 ± 50
$t\bar{t}H$	520 ± 60	125 ± 19	1130 ± 120	420 ± 60
$H^+ \to tb$	30 ± 80	4 ± 10	70 ± 180	20 ± 50
Total	94700 ± 2800	4070 ± 140	97800 ± 2800	10400 ± 400
Data	95852	4109	98929	10552

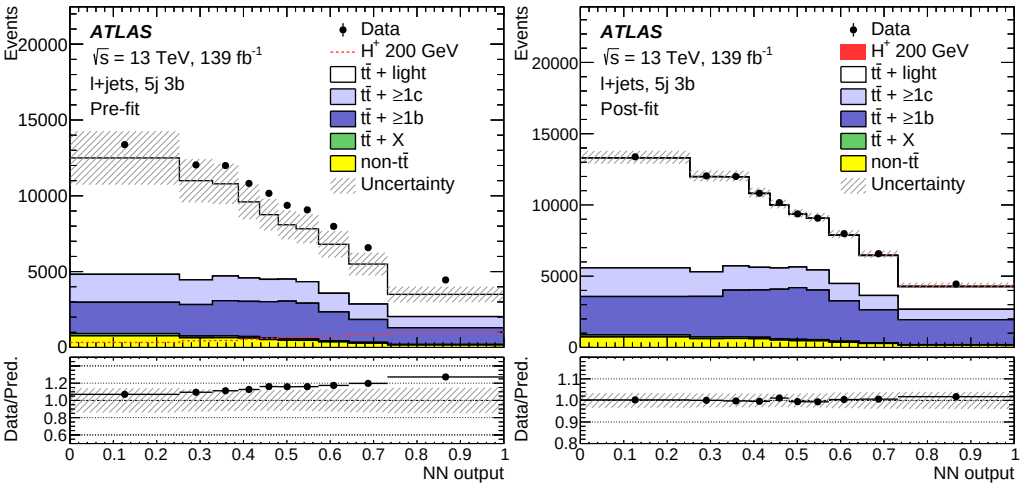

(a) 5j3b pre-fit

(b) 5j3b post-fit

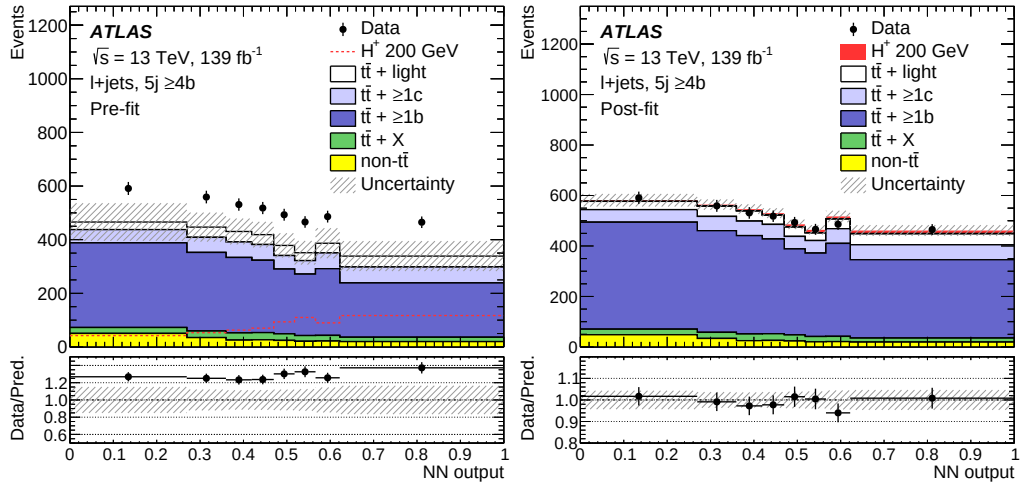

(c) 5j≥4b pre-fit

(d) 5j≥4b post-fit

Figure 7.2: Distributions of the NN output in the 5j signal regions before (left) and after (right) the fit for the 200 GeV H^+ mass hypothesis. The lower panels display the ratio of the data to the total prediction. The hatched bands show the corresponding uncertainties.

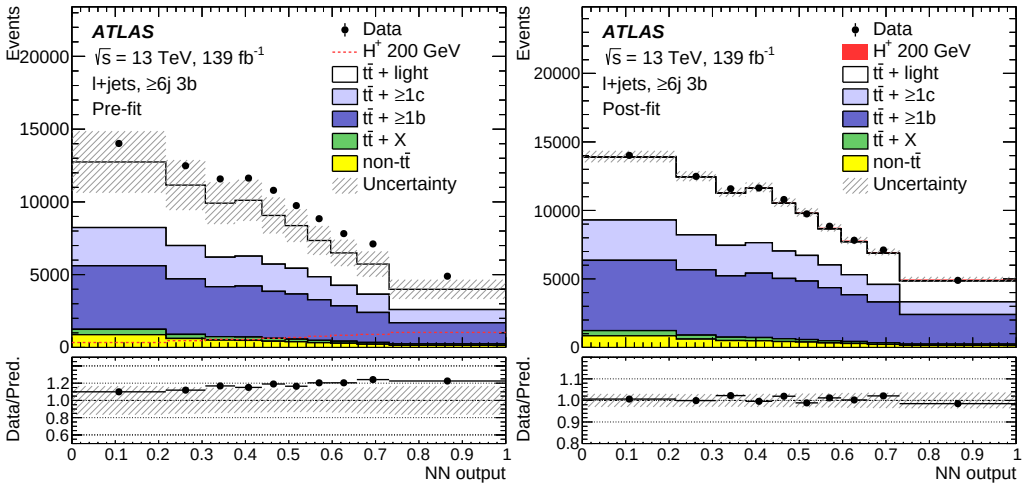

(a) ≥6j3b pre-fit **(b)** ≥6j3b post-fit

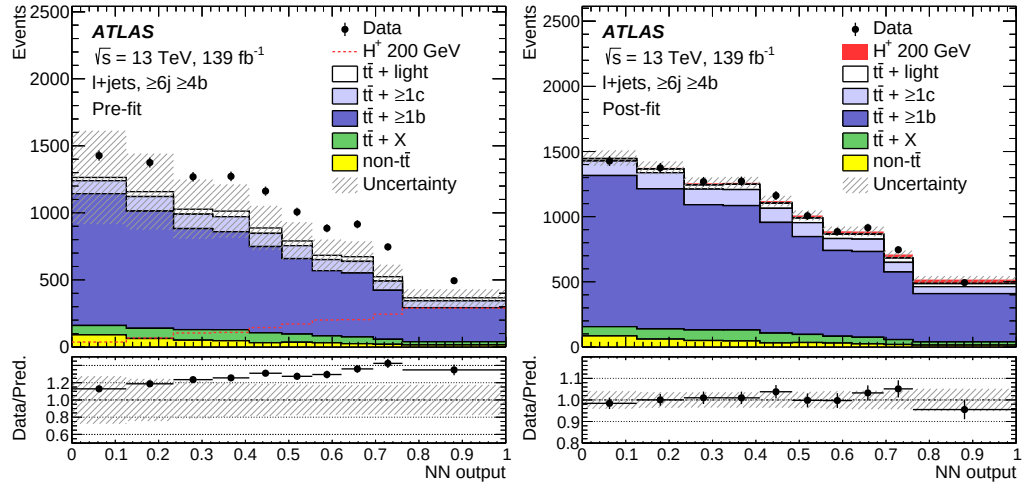

(c) ≥6j≥4b pre-fit **(d)** ≥6j≥4b post-fit

Figure 7.3: Distributions of the NN output in the ≥6j signal regions before (left) and after (right) the fit for the 200 GeV H^+ mass hypothesis. The lower panels display the ratio of the data to the total prediction. The hatched bands show the corresponding uncertainties.

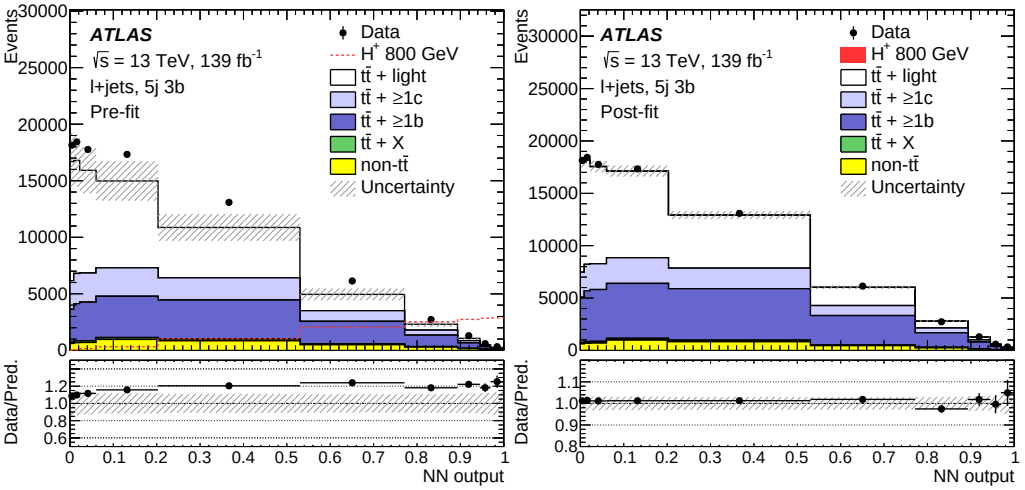

(a) 5j3b pre-fit

(b) 5j3b post-fit

(c) 5j≥4b pre-fit

(d) 5j≥4b post-fit

Figure 7.4: Distributions of the NN output in the 5j signal regions before (left) and after (right) the fit for the 800 GeV H^+ mass hypothesis. The lower panels display the ratio of the data to the total prediction. The hatched bands show the corresponding uncertainties.

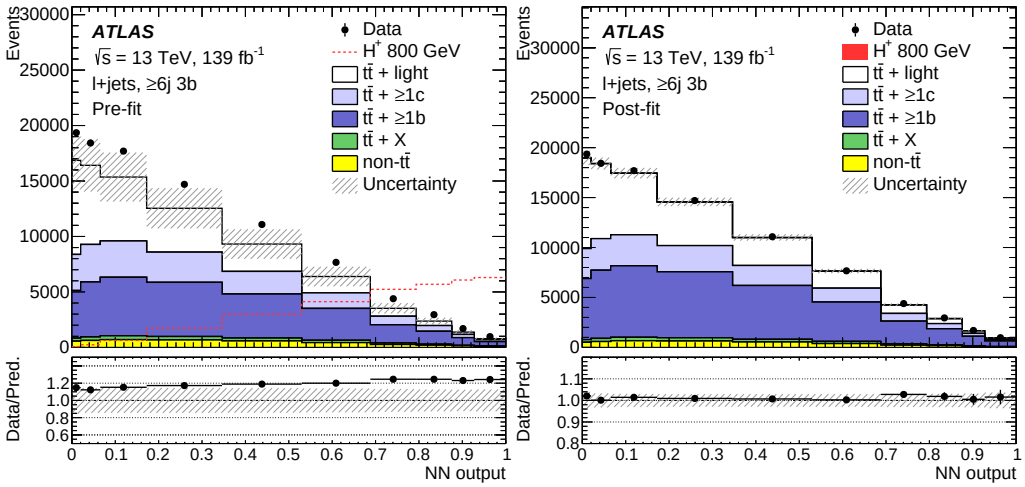

(a) ≥6j3b pre-fit **(b)** ≥6j3b post-fit

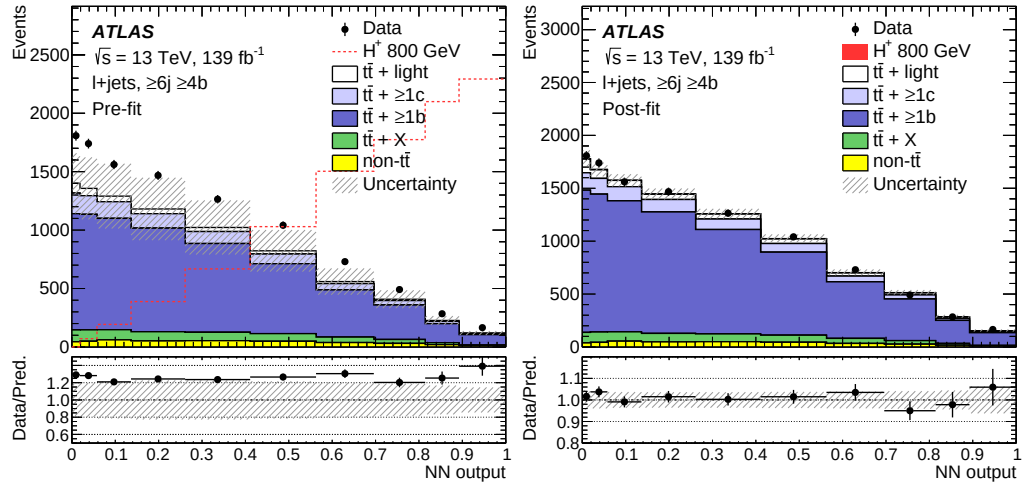

(c) ≥6j≥4b pre-fit **(d)** ≥6j≥4b post-fit

Figure 7.5: Distributions of the NN output in the ≥6j signal regions before (left) and after (right) the fit for the 800 GeV H^+ mass hypothesis. The lower panels display the ratio of the data to the total prediction. The hatched bands show the corresponding uncertainties.

The nuisance parameters and normalisation factors are different to the original values, as the fit accommodates for normalisation and shape differences between the observed and predicted distributions.

The normalisation factors are summarised in Figure 7.6, and range from 1.33 to 1.36 (0.94 to 1.1) with a typical uncertainty of 0.23 (0.48) for the $t\bar{t}$+≥1b ($t\bar{t}$+≥1c) background, depending on the H^+ mass hypothesis fit. Regarding the signal strength, the largest deviation with respect to the SM hypothesis is observed in the low-mass region, between 225–275 GeV. The deviation is negative and does not represent evidence of the signal, it is understood as the signal is the most similar to the $t\bar{t}$+HF and results in high anti-correlations in the fit.

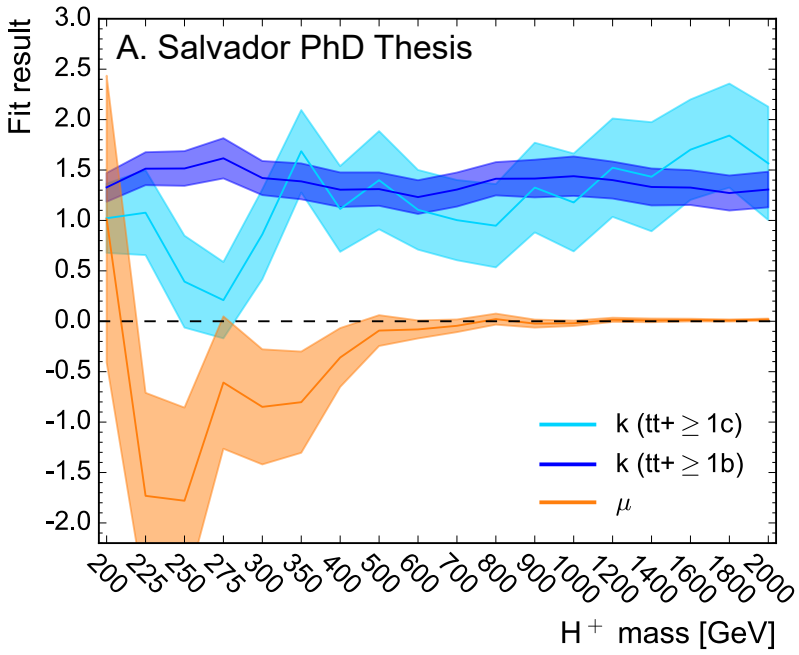

Figure 7.6: Evolution of the obtained signal strength and the $t\bar{t}$+HF normalisation factors as a function of the H^+ mass with the corresponding uncertainties. The signal strength is normalised to 1 pb.

7.1.1 Dominant uncertainties

The uncertainty associated to the fit result is mainly driven by systematic uncertainties. The different sources are ranked by the impact on the signal strength in terms of its shift from the default result $\Delta\mu$, evaluated in separate fits where the associated nuisance parameters are fixed to $\hat{\theta} \pm \Delta\hat{\theta}$. $\hat{\theta}$ is the best fit value of the given nuisance parameter while $\Delta\hat{\theta}$ is the corresponding one standard deviation.

Figure 7.7 lists the 20 top ranked nuisance parameters of the 200 and 800 GeV signal hypothesis fits. The upper axis represents the scale for the pre-fit and post-fit impact on μ. The pre-fit (post-fit) impact is given as $\hat{\theta} \pm \Delta\theta(\hat{\theta} \pm \Delta\hat{\theta})$, with $\Delta\theta$ ($\Delta\hat{\theta}$) the pre-fit (post-fit) uncertainties. The post-fit value of $\Delta\hat{\theta}$ is typically smaller than the

one standard deviation prior $\Delta\theta$, due to constraints from the fit to data. The pre-fit and post-fit impacts are shown as empty and filled rectangles, respectively. The lower axis indicates the scale of the pull of the nuisance parameter defined as $\frac{\hat{\theta}-\theta_0}{\Delta\theta}$ with θ_0 the nominal pre-fit value. The pulls are indicated as black points with their respective error bar while the background normalisations (k) and the single-bin statistical uncertainties (γ) are drawn directly, with $\theta_0 = 0$ and without the pre-fit impact as it is not properly defined.

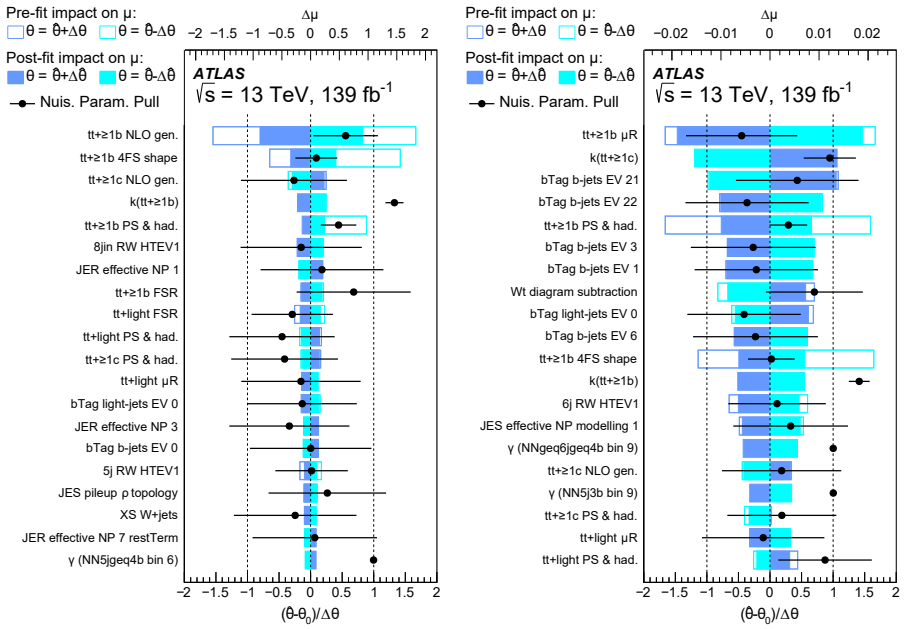

(a) 200 GeV hypothesis fit **(b)** 800 GeV hypothesis fit

Figure 7.7: Ranking of the 20 systematic uncertainties with the largest impact on μ for the fit performed with the 200 GeV (a) and 800 GeV (b) signal hypotheses. The empty (filled) rectangles correspond to the pre-fit (post-fit) impact on μ. The black points represent the post-fit pulls of the nuisance parameters relative to the nominal values, θ_0. Normalisation factors (k) and statistical uncertainties (γ) are shown pulled with respect 1.

The five highest-ranked nuisance parameters of the 200 GeV signal hypothesis fit are all associated to the $t\bar{t}$+≥1b/c, where the two dominant systematic uncertainties are from the $t\bar{t}$+≥1b NLO matching (retrieved from the comparison of MadGraph5_aMC@NLO+Pythia 8 and Powheg+Pythia 8) and the 4FS $t\bar{t}$+≥1b (from the comparison of 4FS and 5FS). Besides the $t\bar{t}$ modelling, jet energy resolution and b-tagging nuisance parameters appear in the ranking, which have a very small impact in comparison. For the 800 GeV signal hypothesis fit, six b-tagging uncertainty components show up in the first 10, and the two top uncertainties are from the $t\bar{t}$+≥1b renormalisation scale (retrieved varying μ_R) and $k(t\bar{t}+\geq 1c)$.

Table 7.2 shows the impact on the signal strength evaluated in groups of systematic uncertainty sources for the 200 and 800 GeV signal hypothesis fits. The total uncertainty is dominated by the systematic uncertainties, where $t\bar{t}$+≥1b modelling dominates for both masses. For the 800 GeV fit, the b-tagging related uncertainties play also a leading role. Meanwhile, the sub-leading uncertainties for the 200 GeV fit are related to the modelling of $t\bar{t}$+≥1c, $t\bar{t}$+light or jets.

Table 7.2: Summary of the statistical and systematic uncertainties on μ for the 200 and 800 GeV signal hypothesis fits. Due to correlations between the different sources of uncertainty, the total systematic uncertainty can be different from the sum in quadrature of the individual sources. The normalisation factors for both $t\bar{t}$+≥1b and $t\bar{t}$+≥1c are included in the statistical component.

Uncertainty source	$\Delta\mu(H^+_{200})$ [pb]	$\Delta\mu(H^+_{800})$ [pb]
$t\bar{t}$+≥1b modelling	1.01	0.025
Jet energy scale and resolution	0.35	0.009
$t\bar{t}$+≥1c modelling	0.32	0.006
Jet flavour tagging	0.20	0.025
Reweighting	0.22	0.007
$t\bar{t}$+light modelling	0.33	0.009
Other background modelling	0.19	0.011
MC statistics	0.11	0.008
JVT, pile-up modelling	<0.01	0.001
Luminosity	<0.01	0.002
Lepton ID, isolation, trigger, E_T^{miss}	<0.01	<0.001
H^+ modelling	0.05	0.002
Total systematic uncertainty	1.35	0.049
$t\bar{t}$+≥1b normalisation	0.23	0.007
$t\bar{t}$+≥1c normalisation	0.045	0.015
Total statistical uncertainty	0.43	0.025
Total uncertainty	1.42	0.055

7.2 Exclusion limits

No significant excess above the expected MC background is observed in all regions and mass intervals, hence upper limits on the signal production are derived as function of the H^+ mass.

Figure 7.8 shows the 95% confidence level (CL) upper limits on $\sigma(pp \to tbH^+)\times B(H^+ \to tb)$ obtained using the CL_S method. Different predictions for the H^+ yields are shown without uncertainties. The observed (expected) limits range from $\sigma \times B = 3.6$ (2.6) pb at $m_{H^+} = 200$ GeV to $\sigma\times B = 0.036$ (0.019) pb at $m_{H^+} = 2$ TeV. Compared to the previous ATLAS search for with 36 fb^{-1} [3], the observed $\sigma\times B$ limits improved by 5% to 70%, depending on the H^+ mass, apart from the lowest one.

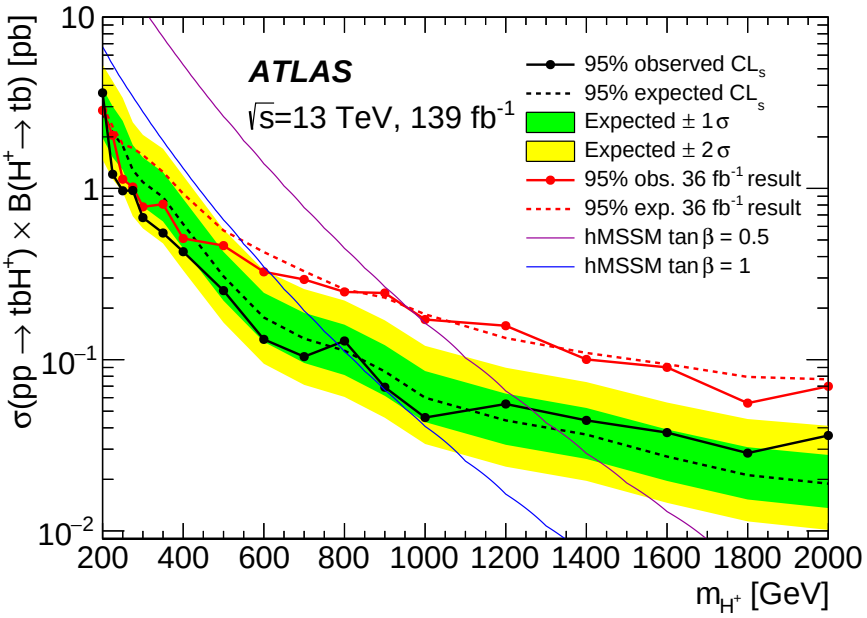

Figure 7.8: Observed and expected upper limits for the production of $H^+ \to tb$ in association with a top quark and a bottom quark. The bands surrounding the expected limit show the 68% and 95% confidence intervals. The red lines show the observed and expected 95% CL exclusion limits obtained with the 36 fb^{-1} data sample [3]. Theory predictions are shown for two representative values of $\tan\beta$ in the hMSSM benchmark scenario. Uncertainties in the predicted H^+ cross-sections or branching ratios are not considered.

The obtained $H^+ \to tb$ production upper limits results are model independent, and therefore can be interpreted in the context of various BSM theories as long as the topology and kinematics of the targeted channel remains equivalent. Figure 7.9 shows 95% CL exclusion limits set on the $\tan\beta$ parameter as a function of m_{H^+} for various benchmark scenarios in the MSSM. It is the first time that they are shown for all M_h^{125} available scenarios using the $H^+ \to tb$ channel.

In the hMSSM framework, effective couplings of the lighter Higgs boson to the top quark, bottom quark and vector bosons are derived from fits to LHC data on the production and decay rates of the observed Higgs boson, including the limits from the search for heavier neutral and charged Higgs boson states. The M_h^{125} scenario is

the first, with relatively heavy superparticles so the couplings , $M_h^{125}(\tilde{\chi})$, $M_{h_1}^{125}(\tilde{\tau})$, M_h^{125}(alignment) and M_h^{125}(CPV) scenarios also feature a scalar particle with mass and couplings compatible with those of the observed Higgs boson, and force a significant portion of their parameter space to be compatible with the limits from searches for supersymmetric particles. In the M_h^{125} scenario, all supersymmetric particles are relatively heavy and the decays of the MSSM Higgs bosons are essentially unaffected, whereas the $M_h^{125}(\tilde{\chi})$ and $M_{h_1}^{125}(\tilde{\tau})$ models include either light charginos and neutralinos or light staus, respectively. In both cases a charged Higgs boson of sufficiently high mass is allowed to decay into the supersymmetric particles. Finally, the value of $\tan\beta$ in both the M_h^{125}(alignment) scenario, characterised by one of the two neutral CP-even scalars having couplings like those of the SM Higgs boson, and the M_h^{125}(CPV) scenario, which includes CP violation in the Higgs sector, is already constrained to be in the 1–20 range by previous searches at the LHC [186].

Uncertainties in the predicted H^+ cross-sections or branching ratios are not included in the limits. For all scenarios except the hMSSM, Higgs boson masses and mixing (and effective Yukawa couplings) have been calculated with the code FeynHiggs [223–229]. Whereas in the hMSSM the branching ratios are computed solely with HDECAY [230, 231], all other scenarios combine the most precise results of FeynHiggs, HDECAY and PROPHECY4f [232, 233].

In the context of these scenarios, $\tan\beta$ values below 1 are observed to be excluded at 95% CL for H^+ masses between 200 and ~790 GeV. High values of $\tan\beta$ between 34 and 60 are excluded in a similar mass range in the hMSSM and $M_h^{125}(\tilde{\chi})$ models. The most stringent limit, $\tan\beta < 2.1$ excluded at 95% CL, is set for the H^+ mass hypothesis of 225 GeV in the hMSSM and for the 250 GeV H^+ mass hypothesis in the different M_h^{125} models. The low $\tan\beta$ and high H^+ mass parameter space was not excluded by any other analysis before, while the high $\tan\beta$ was already excluded by the ATLAS $H^+ \to \tau\nu$ search [234].

Compared to previous results of the same search channel [3], this analysis excludes a broader region of large $\tan\beta$. Additionally, an extended region of low $\tan\beta$ and low and high H^+ masses is also excluded.

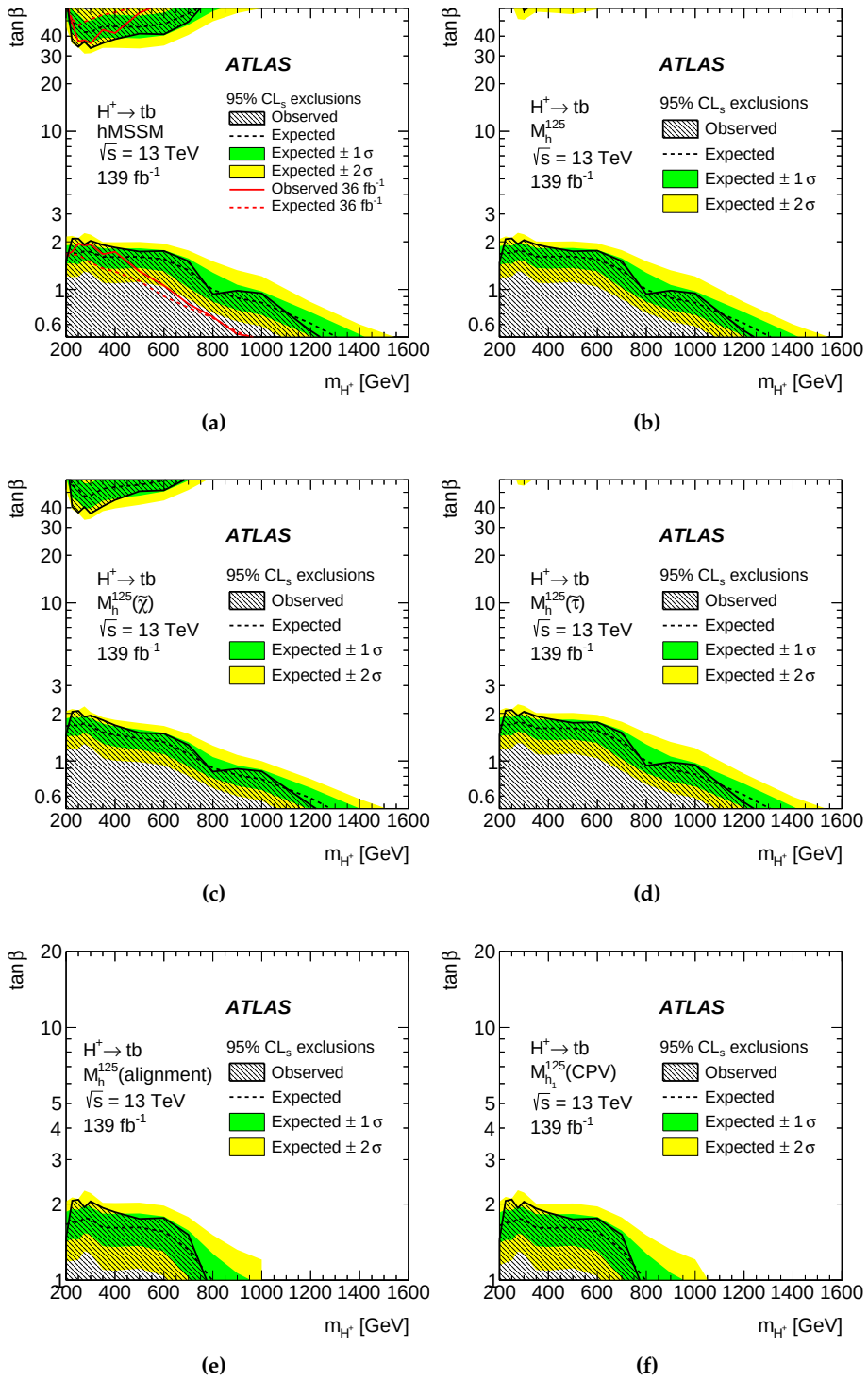

Figure 7.9: Observed and expected limits on $\tan\beta$ as a function of the H^+ mass in various scenarios: (a) hMSSM, (b) M_h^{125}, (c) $M_h^{125}(\tilde{\chi})$, (d) $M_h^{125}(\tilde{\tau})$, (e) M_h^{125}(alignment) and (f) $M_{h_1}^{125}$(CPV). Limits are shown for $\tan\beta$ values in the range of 0.5–60 or 1–20 depending on the availability of model predictions. The bands surrounding the expected limits show the 68% and 95% confidence intervals. Uncertainties in the predicted H^+ cross-sections or branching ratios are not considered.

7.3 2HDM+a interpretation

The H^+ upper limits results can be straightforwardly interpreted in addition in the context of the 2HDM+a, as the production and decay modes, cross-sections and branching ratios of the charged Higgs bosons are identical in both models. The interpretation of $H^\pm \longrightarrow tb$ results in this model is performed for the first time in literature.

The 2HDM+a model [235, 236] is built upon simplified Dark Matter (DM) models, postulating a DM sector composed of a single fermionic DM particle and a pseudo-scalar mediator on top of the 2HDM assumption of building the Higgs sector with two complex Higgs doublets. In this particular model, the interactions between the SM and DM sectors is mediated by a pseudo-scalar a, although other models contemplate axial-vectors or scalars [237–239]. The choice is motivated by the potential in collider searches, as direct-detection of pseudo-scalars is suppressed [240] and does not provide strong constrains.

The phenomenology of the model has the five Higgs bosons from the 2HDM sector: a light CP even boson h, a heavy CP-even boson H, a CP-odd boson A and the charged bosons H^+. As in the previous models, the Type-II structure is considered together with the alignment limit [241], to identify the h state with the SM Higgs boson. The mediator a couples the SM fermions and the Dirac DM particle χ. In addition, a couples to SM fermions proportionally to the Yukawa couplings and mixes with A with mixing angle θ. Figure 7.10 shows a Feynman diagram with an interaction involving H^+, a and χ. A total of 14 parameters are needed to fully determine the model: the masses of the five 2HDM Higgs bosons; the mass of the mediator a; the mass of the DM χ; the coupling between a and χ, g_χ; the EW VEV, v; the VEVs 2HDM ratio, $\tan\beta$; the mixing angles of the CP-even and CP-odd states, α and θ, respectively; and three quartic couplings between the scalar doublets and the mediator.

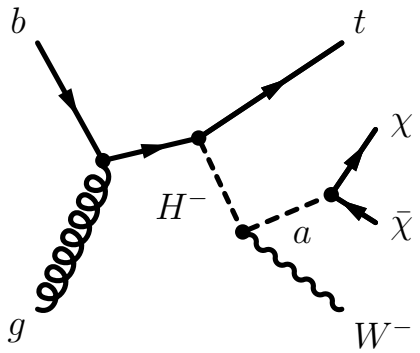

Figure 7.10: Representative Feynman diagram for the dominant gluon-induced production and decay mode in the 2HDM+a involving a charged Higgs boson, the DM particle and the pseudo-scalar mediator.

This model predicts a wide variety of signatures and ATLAS has summary results which consist in a variety of dark matter searches using 139 fb^{-1} [179]. The most prominent signatures, the production of DM in association with a Higgs boson

$E_T^{miss} + h(b\bar{b})$ [242] and with a Z boson $E_T^{miss} + Z(\ell^+\ell^-)$ are used in a combined likelihood fit for the statistical combination. Further signatures are related to DM production in association with a top quark and a W boson ($E_T^{miss} + Wt$), visible decays of the additional heavy Higgs bosons, and invisible decays of the SM Higgs boson to DM.

The nominal H^+ samples are compared to samples generated with different 4FS 2HDM+a models for a range of relevant kinematic variables to verify that the signal signatures are the same, and hence the interpretation is possible. Figure 7.11 shows the compatibility of the truth jet multiplicity for various models in two H^+ example masses.

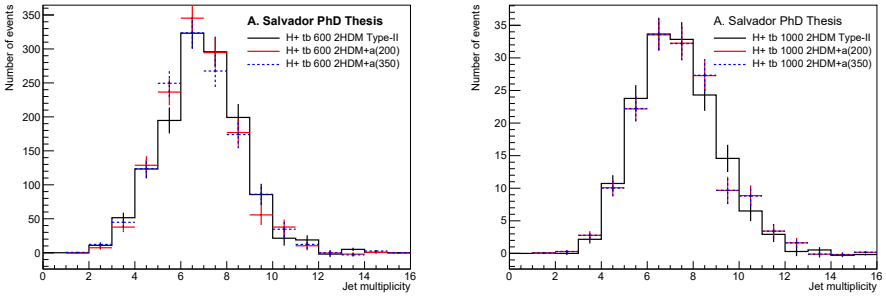

Figure 7.11: Multiplicity of truth jets with $p_T > 25$ GeV corresponding to the 600 GeV (left) and 1000 GeV (right) H^+ samples. The black line corresponds to the 4FS 2HDM Type-II NLO model while the red and blue lines correspond to the 4FS 2HDM+a NLO generated with a masses of 200 and 350 GeV

To generate the exclusion figures, predictions for the $pp \to tbH^+$ cross-section and B($H^+ \to tb$) have been computed for the 4FS 2HDM+a NLO model for different values: $\sin\theta \in [0.1, 0.9]$, $\tan\beta \in [0.3, 50]$, $m_a \in [100\,\text{GeV}, 800\,\text{GeV}]$, $m_{H^+} \in [200\,\text{GeV}, 1000\,\text{GeV}]$. In addition, different predictions were computed for m_χ in the 20–500 GeV range without any relevant change.

Figure 7.12 shows the dependence of B($H^+ \to tb$), the production of the signal and the exclusion result as a function of m_{H^+} and m_a, for $\sin\theta = 0.35, 0.7$ and $\tan\beta = 1$. As expected, the branching fraction depends on both masses and decreases from ~100% at $m_{H^+} \sim m_a + 80$ GeV, when the unrelated $H^+ \to aW$ and $H^+ \to WH$ decays are allowed. The dependence is small as a is not directly targeted by the H^+ analysis. The corresponding cross-section does not change with $\sin\theta$. The exclusion contour is extracted in the m_{H^+}–m_a plane from the analysis limits and the predicted production in the 2HDM+a.

Figure 7.13 shows the exclusion contours including other ATLAS DM searches. The $E_T^{miss} + Z(\ell^+\ell^-)$ and $E_T^{miss} + h(b\bar{b})$ searches dominate the sensitivity across the two parameter planes, expected from the resonant production of the pseudo-scalars. The H^+ results provide complementary sensitivity to the $E_T^{miss} + X$ searches. The corresponding exclusion contour shows only a moderate dependence on m_a.

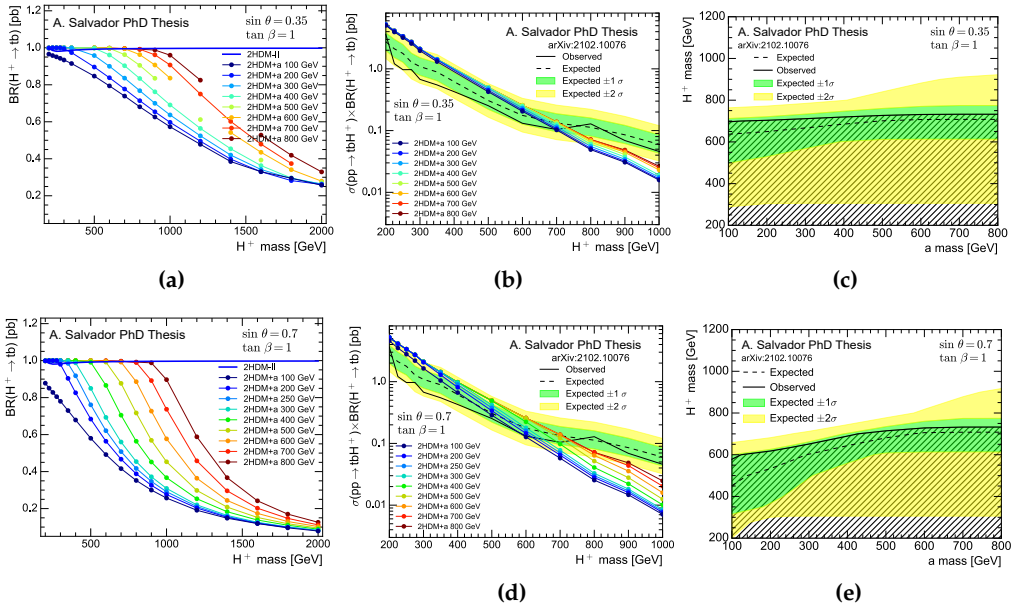

Figure 7.12: (a) and (d) Branching ratio of $H^+ \to tb$ as a function of the H^+ mass for $\sin\theta = 0.35(0.7)$ at the top(bottom). Predictions are compared between the 2HDM Type-II (2HDM-II) and 2HDM+a for various a masses. (b) and (e) Expected and observed cross-section times branching ratio limits of the H^+ process, with various 2HDM+a predictions overlaid. (c) and (f) Observed and expected exclusion plots in the H^+–a mass plane.

Figure 7.14 shows the exclusion contours as a function of m_A and $\tan\beta$, for $\sin\theta = 0.35, 0.7$ and $m_a = 250$ GeV. Similarly, the parameter space is almost fully excluded by the $E_{\mathrm{T}}^{\mathrm{miss}} + Z(\ell^+\ell^-)$ search, except that $E_{\mathrm{T}}^{\mathrm{miss}} + Wt$ search also excludes low $\tan\beta$ region for large values. In addition, the $H^+ \to tb$ search provides complementary sensitivity to the other searches, although with a moderate dependence in the lower parameter region.

Figure 7.15 shows a similar scan to the one in Figure 8 but varying the m_a and setting $m_A = 600$ GeV. Again, the strongest exclusion is observed from the $E_{\mathrm{T}}^{\mathrm{miss}} + Z(\ell^+\ell^-)$ and $E_{\mathrm{T}}^{\mathrm{miss}} + h(b\bar{b})$ searches. An increase in the exclusion range is found for large values of $\tan\beta$, related to the contributions from $b\bar{b}$-initiated signal production, dominant at large values of $\tan\beta$. The $H^+ \to tb$ search provides complementary sensitivity at low $\tan\beta$ values with very small dependence on m_a.

Figure 7.16 shows the exclusion limits as a function of $\sin\theta$ for the 2HDM+a model for two pairs of masses $m_a, m_A = 200, 600$ GeV and $m_a, m_A = 350, 1000$ GeV. The strongest exclusion in the medium $\sin\theta$ range is provided by the $E_{\mathrm{T}}^{\mathrm{miss}} + Z(\ell^+\ell^-)$ and $E_{\mathrm{T}}^{\mathrm{miss}} + h(b\bar{b})$ searches. The $H^+ \to tb$ signature shows a different $\sin\theta$ dependence compared to the other signatures as it is not directly sensitive to the neutral boson production. However, it is particularly sensitive at very small mixing angles.

Finally, the experimental reach of the different searches to the DM mass m_χ is in Figure 7.17, which is the parameter with the strongest impact on the relic density predicted by the 2HDM+a. The searches are compared in terms of the observed

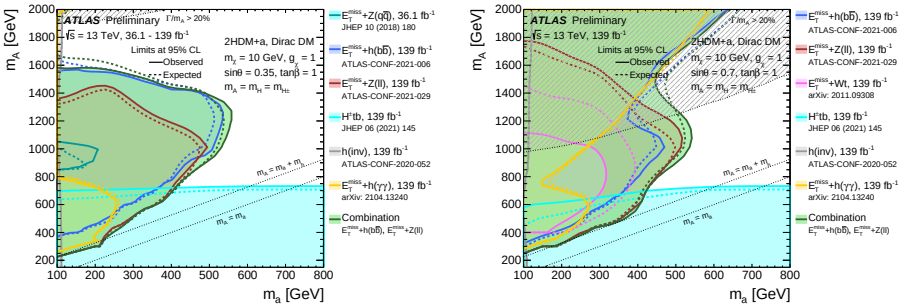

Figure 7.13: Observed (solid lines) and expected (dashed lines) exclusion regions at 95% CL in the m_a–m_A plane with $\sin\theta = 0.35$ (left) and $\sin\theta = 0.7$ (right). The results are shown for several individual searches as well as the combination of the $E_{\mathrm{T}}^{\mathrm{miss}} + Z(\ell^+\ell^-)$ and $E_{\mathrm{T}}^{\mathrm{miss}} + h(b\bar{b})$ searches. The dashed grey regions indicate the region where the width of the Higgs bosons exceeds 20% of its mass.

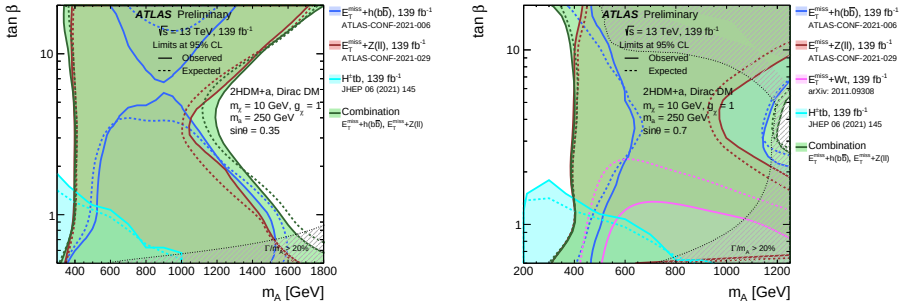

Figure 7.14: Observed (solid lines) and expected (dashed lines) exclusion regions at 95% CL in the m_A–$\tan\beta$ plane with $\sin\theta = 0.35$ (left) and $\sin\theta = 0.7$ (right). The results are shown for several individual searches as well as the combination of the $E_{\mathrm{T}}^{\mathrm{miss}} + Z(\ell^+\ell^-)$ and $E_{\mathrm{T}}^{\mathrm{miss}} + h(b\bar{b})$ searches. The dashed grey regions indicate the region where the width of the Higgs bosons exceeds 20% of its mass.

exclusion limits on the ratio of the excluded cross-section to the nominal cross-section of the model as a function of m_χ. For all signatures shown, the sensitivity is independent of m_χ as long as m_a is allowed to decay into $\chi\bar{\chi}$. The strongest constraints are provided by the $E_{\mathrm{T}}^{\mathrm{miss}} + Z(\ell^+\ell^-)$ search. For higher DM masses, the sensitivity of the $E_{\mathrm{T}}^{\mathrm{miss}} + X$ searches quickly decreases. For $m_\chi > m_a/2$, the strongest constraints are obtained from the H^+ search, which excludes the 2HDM+a for the chosen parameter values for all values m_χ, as the production of the H^+ signal does not depend on this parameter.

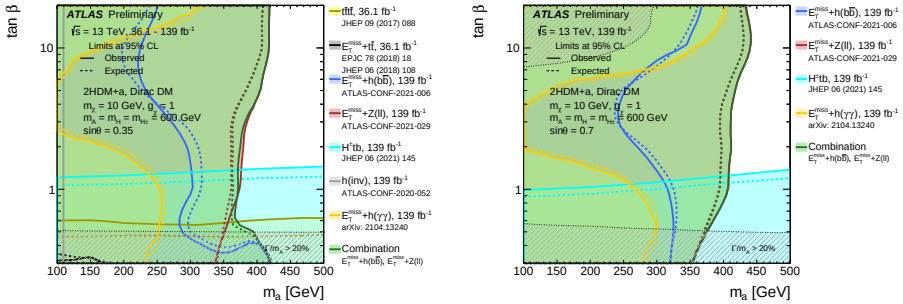

Figure 7.15: Observed (solid lines) and expected (dashed lines) exclusion regions at 95% CL in the m_a–$\tan\beta$ plane with $\sin\theta = 0.35$ (left) and $\sin\theta = 0.7$ (right). The results are shown for several individual searches as well as the combination of the $E_{\mathrm{T}}^{\mathrm{miss}} + Z(\ell^+\ell^-)$ and $E_{\mathrm{T}}^{\mathrm{miss}} + h(b\bar{b})$ searches. The dashed grey regions indicate the region where the width of the Higgs bosons exceeds 20% of its mass.

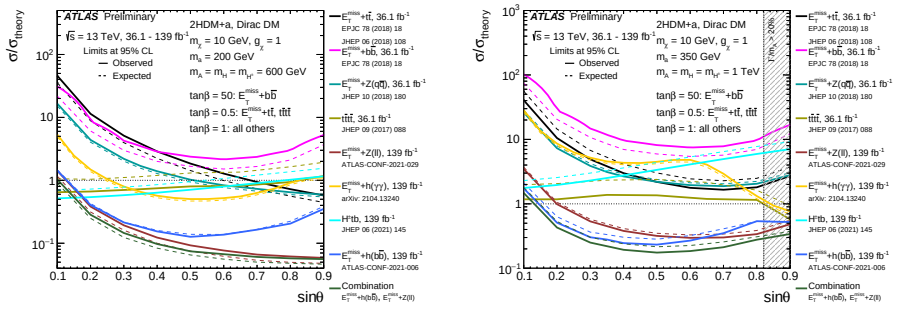

Figure 7.16: Observed (solid lines) and expected (dashed lines) exclusion limits at 95% CL for the 2HDM+a model as a function of $\sin\theta$ with $m_A = 600$ GeV, $m_a = 200$ GeV (left) and $m_A = 1$ TeV, $m_a = 350$ GeV (right). The results are shown for several individual searches as well as the combination of the $E_{\mathrm{T}}^{\mathrm{miss}} + Z(\ell^+\ell^-)$ and $E_{\mathrm{T}}^{\mathrm{miss}} + h(b\bar{b})$ searches.

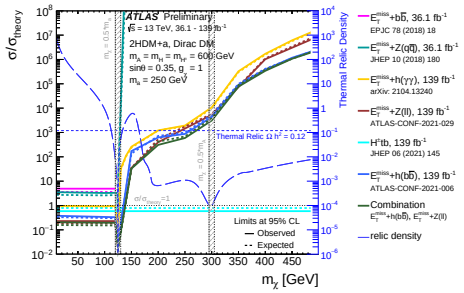

Figure 7.17: Observed (solid lines) and expected (dashed lines) exclusion limits for the 2HDM+a model as a function of m_χ, following the parameter choices of $m_A = 600$ TeV, $m_a = 250$ GeV, $\tan\beta = 1.0$ and $\sin\theta = 0.35$. The limits are calculated at 95% CL and are expressed in terms of the ratio of the excluded cross-section to the nominal cross-section of the model. The results are shown for several individual searches as well as the combination of the $E_{\mathrm{T}}^{\mathrm{miss}} + Z(\ell^+\ell^-)$ and $E_{\mathrm{T}}^{\mathrm{miss}} + h(b\bar{b})$ searches. The relic density for each m_χ assumption is superimposed (long-dashed line) and described by the right vertical axis. For dark matter mass values where the relic density line is below $\Omega h^2 = 0.12$, the model depletes the relic density to below the thermal value. The shaded region around 125 GeV indicates a ±5 GeV band around the kinematic thresholds $m_\chi = 0.5 \cdot m_a$ and $m_\chi = 0.5 \cdot m_A$ where the generator results are deemed unreliable.

Search for neutral scalars in FCNC top processes decaying into bottom quarks

$t \to qX$ analysis overview

8

Flavour-changing neutral-currents (FCNC) interactions are not present at three level in the Standard Model (SM) and are also strongly suppressed at higher orders. Within the SM, the FCNC decay branching fraction of the top-quark into a Higgs boson is below 10^{-15}, well out of reach of sensitivity of the LHC. Hence, any observation of such FCNC decays would be a direct sign of new physics.

The ATLAS and CMS collaborations have searched for various FCNC processes involving the top-quark and light-quarks, $q = u, c$ in pp collisions at $\sqrt{s}$=7, 8 and 13 TeV with data samples ranging from 5.0 to 139 fb^{-1}, probing the top-quark decaying into photons $t \to q\gamma$ [35, 37, 243, 244], into the Z boson $t \to qZ$ [39, 245–247], into the Higgs boson $t \to qH$ [4, 5, 248, 249], and also in single top-quark production $q + g \to t$ [250–252]. Searches for similar signatures involving a FCNC decay of the top-quark into a beyond-the-SM particle lighter than the top-quark are uncovered in literature.

The analysis presented in this thesis is a search for a light scalar X ($m_X < m_{\text{top}}$) in the $t \to qX$ decay[1], with $X \to b\bar{b}$, performed with the full Run 2 proton-proton collision data of 139 fb^{-1} at $\sqrt{s}$=13 TeV. The results of this search are public [253]:

- ATLAS Collaboration, *Search for a new scalar resonance in flavour-changing neutral-current top-quark decays $t \to qX$ ($q = u, c$), with $X \to b\bar{b}$, in proton-proton collisions at $\sqrt{s}$=13 TeV with the ATLAS detector*, arXiv:2301.03902

This chapter describes the $t \to qX$ analysis motivation, challenges and strategy. After a short introduction, the event selection is presented followed by the description of the modelling of the signal and background processes. Then, the analysis strategy and a summary of the systematic uncertainties are given. The analysis shares methodology with the $H^+ \to tb$ search presented in the previous part of the thesis and for the sake of brevity, shared technical details will be referenced as appropriate.

8.1 Introduction

The analysis searches for a neutral scalar produced in a FCNC decay of top quark. At the LHC, the signal is expected to be produced primarily in $t\bar{t}$ events, where one of the top quarks decays in the target decay mode. The process is possible also in single-top production, although it is not considered in this analysis. The decision is motivated by the negligible $t \to cX$ contribution and the particular challenges analysing single-top events, distinct from the $t\bar{t}$ topology. For $m_X < m_{\text{top}}$, the predicted primarily decay is X to $b\bar{b}$.

The signal consists in two top quarks, with one decaying into $t \to qX$ with $X \to b\bar{b}$. For convenience, the typical classification for $t\bar{t}$ events is used, based in the decay of

[1] The process is denoted as $t \to qX$, with the charge-conjugate process $\bar{t} \to \bar{q}X$ implied.

the involved top quarks. The main decay mode for top quarks is to a W-boson and a b-quark, with the former decaying either leptonically (to leptons) or hadronically (to a pair of quarks). This yields different diagrams depending on which top-quark decays into the BSM process and which SM decay follows the second top quark. Four final states are then possible: the signal process being $t \to uX$ or $t \to cX$, and the hadronic or leptonic final state where the W-boson of the witness top decays hadronically or leptonically.

In the scope of the thesis, the leptonic channel is studied as it is the dominant process and offers large statistics with a relatively clean topology. Also, the full event can be kinematically reconstructed, since only one neutrino is present and can be determined with E_T^{miss}. The $t \to uX$ and the $t \to cX$ process are only different on the final quark. Aside, the leptonic channel could be further split as distinct topologies arise depending on m_X. The quark from the $t \to qX$ decay tends to be low in p_T and hard to reconstruct for large m_X, while the b-quarks from the $X \to b\bar{b}$ decay tend to be collimated and reconstructed as a single jet for low m_X. The final state is depicted in Figure 8.1.

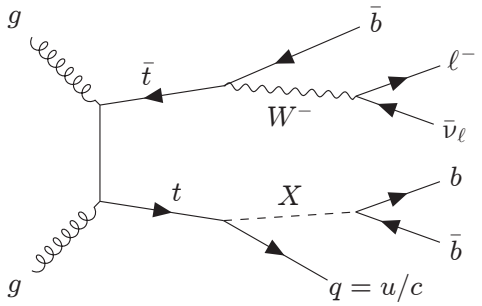

Figure 8.1: Leading-order Feynman diagram for the production and decay of a neutral scalar X in a $t\bar{t}$ event.

The detector signature is chosen to include exactly one isolated lepton ℓ, considering only electrons and muons. Nonetheless, the τ leptons decaying into electrons or muons are included. As four quarks are present in the final state, four jets are expected to be present in the final state with at least three of them originating from a b-quark, and one c- or u-quark depending on the type of signal. The b-tagging is one important piece of the strategy as the selection of $t \to uX$ and $t \to cX$ will be affected by the different efficiencies of rejecting or accepting c- and u-quarks.

The complexity of the targeted final state originates from the dominant $t\bar{t}$ production with additional jets ($t\bar{t}$+jets). In particular, $t\bar{t}$+$\geq$1b is the main irreducible background while the $t\bar{t}$+light background is reducible and can be suppressed tightening the b-tagging selection[2]. The correct modelling of $t\bar{t}$ events is key for the analysis and unfortunately, the process is poorly constrained by data measurements and has large theory uncertainties.

[2] The rejection of light-quarks is threefold from the 70% to the 60% working point with the DL1r algorithm.

As a summary of the analysis strategy, the first step is the event selection, where a first phase space is chosen to enhance the $t \to qX$ signal contribution, but also includes events to study $t\bar{t}$+jets background. Events are then split into signal-enriched categories (signal regions, SRs), and signal-depleted categories which are used to constrain the $t\bar{t}$+≥1b background (control regions, CRs) or to derive corrections for the $t\bar{t}$+jets background (reweighting regions). The reweighting regions are used to extract data-driven corrections for the $t\bar{t}$ modelling while for the signal regions, a NN is used to separate signal and background. The signal regions are used in a combined profile-likelihood fit on the NN output distribution, different for each signal type and mass. On the other side, the yields of the control regions are mainly used in the fit to constrain the $t\bar{t}$+≥1b background. In the fit a large set of nuisance parameters is used to cover the systematic uncertainties.

8.2 Event selection

This section details the selection of the events used in the analysis, applied to recorded and simulated events. The mentioned physics objects are described in more detail in Chapter 4.

The events for this analysis are extracted from the Run 2 data, recorded with the ATLAS detector at the LHC from $\sqrt{s}$=13 TeV pp collisions for a total integrated luminosity of 139 fb^{-1}. As trigger requirements, the events had to be recorded using single-lepton triggers, which are shared with the $H^+ \to tb$ analysis (Section 6.2).

Multiple triggers were used in order to maximise the selection efficiency, either with low p_{T} thresholds and lepton identification and isolation requirements, or with higher thresholds but looser identification criteria and no isolation requirements. Slightly different sets of triggers were used for 2015 and 2016-2018 data due to the increase in pile-up. Furthermore, at least one primary vertex is required.

The working points for leptons include the *tight* identification for electrons and *medium* for muons. In addition, electrons are required to satisfy the *tight* isolation criteria while muons are required the *TightTrackOnly FixedRad* criteria. Hadronically decaying τ leptons are required to have $p_{\mathrm{T}} > 25$ GeV and pass the *mediumRNN* identification working point and used for the object overlap removal.

PFlow jets are used with a radius parameter $R = 0.4$. To reduce pile-up effects, the JVT algorithm is applied for jets with $|\eta| < 2.4$ and $p_{\mathrm{T}} < 60$ GeV.b-jets are identified and selected using the 70% working point of the DL1r tagger. In addition, jets that pass the 70% working point but not the 60%, are referred as bl-jets (from $looser\ b$-tagging). The pseudo-continuous score of the different jets is also used in the analysis.

Events are required to have at least four jets, from which at least two have to be tagged with the 60% b-tagging working point and an additional one fulfilling the 70% (bl). In addition, exactly one lepton with $p_{\mathrm{T}} > 27$ GeV and no additional

lepton with $p_{\mathrm{T}} > 10$ GeV passing the *medium* (*loose*) identification working point for electrons (muons) is allowed. Further requirements on $\mathrm{E}_{\mathrm{T}}^{\mathrm{miss}}$ and the transverse mass of the lepton and $\mathrm{E}_{\mathrm{T}}^{\mathrm{miss}}$ (m_{T}^{W}) are applied for both muon and electron channels to further reject multi-jet background: $E_{\mathrm{T}}^{\mathrm{miss}} \geq 20$ GeV and $E_{\mathrm{T}}^{\mathrm{miss}} + m_{\mathrm{T}}^{W} \geq 60$ GeV.

8.3 Signal and background modelling

The final state of the signal includes three b-jets, a light-jets from either a c- or u-quark, one lepton and one neutrino. Such final state is shared fully or partially by a large number of background processes, the main one $t\bar{t}$+jets. Additional contributions to the background are from the production of W and Z bosons with jets (V+jets), single-top-quark production, diboson processes (VV) and the associated production of bosons and top quarks ($t\bar{t}V$, $t\bar{t}H$). Non-prompt leptons and misidentified jets form what is known as multi-jet background, which contribution is negligible due to the trigger and lepton quality requirements.

Compared to the $H^{+} \to tb$ search, the final state is very similar and the same simulated background can be used, detailed in Section 6.3. The main difference is the treatment of the small background, as the selection is tighter; and the increased relevance of the $t\bar{t}$ events with the $W \to cb$ decay allowed, due to the presence of a c-quark in the $t \to cX$ signal.

8.3.1 Signal modelling

The signal of this analysis is a $t\bar{t}$ event with one top decaying $t \to qX$ with $X \to b\bar{b}$ and $q = u, c$. The samples are generated with PowhegBox v2 interfaced with MadSpin and Pythia 8.2. The $t\bar{t}$ production is modelled at NLO with the *NNPDF2.3NLO* PDF set. The top-quark decays are modelled in MadSpin both the $t \to Wb$ and $t \to qX$ decays, assuming a neutral spin-0 scalar X based on the LO *NNPDF2.3* model with $\mathrm{B}(X \to b\bar{b}) = 100\%$ and the decay width set to 0.4 MeV (same as the SM Higgs). The events are showered with Pythia 8.244.

A total of fifty-two samples are generated corresponding to thirteen different values of m_X ranging from 20 to 160 GeV and four different decays: $t \to uX$, $\bar{t} \to \bar{u}X$, $t \to cX$ and $\bar{t} \to \bar{c}X$. Table 8.1 lists the different mass-points and the number of events generated across the different decays.

Table 8.1: Summary of the generated events for the different $t \to qX$ signal samples with different mass hypotheses, m_X. *A total of 10k events of the 160 GeV sample were generated with a wrong Monte Carlo weight (very large) and are therefore not used in the analysis.

m_X [GeV]	Generated
20	1.50M
30	1.49M
40	1.50M
50	1.50M
60	1.50M
70	1.49M
80	1.50M
90	1.50M
100	1.50M
120	1.50M
140	1.50M
150	1.50M
160	1.50M*

8.4 Analysis strategy

The events that pass the selection described in Section 8.2 are categorised into three types of regions depending on their role: signal regions, control regions and reweighting regions.

The signal regions are signal enhanced and used in a profile likelihood fit with NN methods to distinguish between signal and the SM background. The control regions are also used in the fit, especially to constrain the $t\bar{t}$+≥1b background. Finally, the reweighting regions are used to derive data-driven factors to improve the $t\bar{t}$ modelling.

8.4.1 Region definition

The analysis regions are categorised as a function of the number of reconstructed jets and b-tagged jets. The signal regions are 4j3b, 5j3b and 6j3b, with the b-jets defined at the 60% working point. Additionally, the control regions are defined in ≥4b also with the 60% b-tagging working point: 4j4b, 5j≥4b and 6j≥4b. Finally, three additional regions are used to extract corrections for the $t\bar{t}$ MC, requiring two b-jets fulfilling the 60% working point and a third b-jet identified with the 70%: 4j2b+1bl, 5j2b+1bl and 6j2b+1bl.

Figure 8.2 illustrates the background composition for the different regions, which clearly shows the dominance of the $t\bar{t}$ background, especially the $t\bar{t}$+≥1b component in the 5j3b, 6j3b and ≥4b regions. The 80% of the 4j3b events is split almost equally by $t\bar{t}$+≥1b and $t\bar{t}$+light events. The 2b+1bl categories consist of a mixture of the three $t\bar{t}$ components, dominated by $t\bar{t}$+light events and with increasing $t\bar{t}$+≥1c and $t\bar{t}$+≥1b with the number of jets.

Tables 8.2, 8.3 and 8.4 shows the number of expected and selected events in the different regions. The number of expected $t \to uX$ and $t \to cX$ signal events for the 60 GeV mass hypothesis is also shown, assuming a branching fraction B($t \to qX$)=0.1%.

Figure 8.3 shows the different signal yields and $S/\sqrt{B}$ for different analysis regions. The sensitivity for the 3b regions is larger than for the ≥4b, and increases with m_X up to 140 GeV. The 20 GeV mass has significantly fewer yields, as the jets from the $X \to b\bar{b}$ decay are mostly merged, thus often not selected. In addition, yields and sensitivity are higher for $t \to cX$ than for $t \to uX$, especially in the ≥4b regions, as expected.

Figure 8.4 shows the acceptance times efficiency of the [4-6]j≥3b inclusive selection per signal mass sample and for $t \to uX$ and $t \to cuX$, ranging from 0.2% to 1.7%. The acceptance and jet selection efficiency increase with the scalar mass as a consequence of the phase space dependence on the mass: the jets of the b-quark pair of the $X \to b\bar{b}$ decay become merged at low m_X because of the X boost, reducing the jet multiplicity, while for high masses the jet from the q is lost because of its smaller p_T.

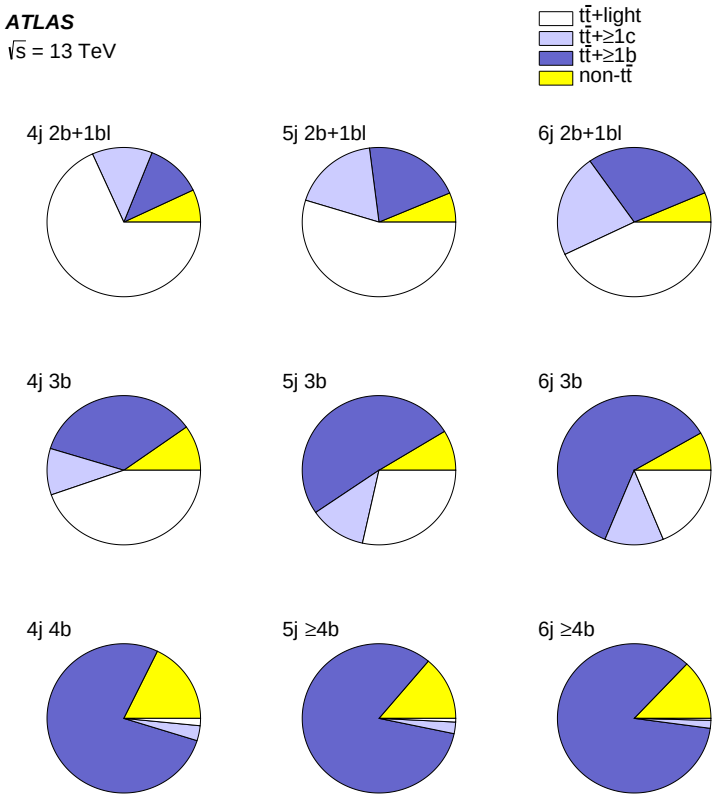

Figure 8.2: Background composition in the various analysis regions.

Table 8.2: Number of expected and selected events split according to the regions used to extract the reweighting factors for the $t\bar{t}$ background and the signal, namely 4j2b+1bl, 5j2b+1bl and 6j2b+1bl. The quoted uncertainties include statistical and systematic uncertainties. The predicted number of $t \to uX$ and $t \to cX$ signal events for the 60 GeV mass hypothesis, assuming a branching fraction of 0.1%, are also shown.

	4j, 2b+1bl	5j, 2b+1bl	6j, 2b+1bl
$t\bar{t}$ + light	26100 ± 2700	17900 ± 2000	8000 ± 1800
$t\bar{t}$ + ≥1b	4600 ± 2500	6800 ± 3500	5400 ± 2800
$t\bar{t}$ + ≥1c	4900 ± 2500	6000 ± 3100	4200 ± 2200
$W \to cb$	210 ± 110	150 ± 80	70 ± 40
Single-top	1700 ± 500	1200 ± 400	620 ± 270
$t\bar{t} + V$	90 ± 60	160 ± 100	160 ± 100
VV & V + jets	870 ± 350	620 ± 70	350 ± 50
$t\bar{t}H + tH$	53 ± 6	133 ± 16	153 ± 18
Total	38000 ± 5000	33000 ± 5000	19000 ± 4000
Data	40889	35995	21210
$t \to uX$ m_X=60 GeV	380 ± 40	293 ± 25	154 ± 32
$t \to cX$ m_X=60 GeV	540 ± 50	372 ± 31	192 ± 35

Table 8.3: Number of expected and selected events after applying reweighting split according to the signal regions, namely 4j3b, 5j3b and 6j3b. The quoted uncertainties include both statistical and systematic uncertainties. The predicted number of $t \to uX$ and $t \to cX$ signal events for the 60 GeV mass hypothesis, assuming a branching fraction of 0.1%, are also shown.

	4j, 3b	5j, 3b	6j, 3b
$t\bar{t}$ + light	11100 ± 1600	7800 ± 1500	3600 ± 900
$t\bar{t}$ + ≥1b	9000 ± 5000	14000 ± 7000	12000 ± 6000
$t\bar{t}$ + ≥1c	2500 ± 1300	3300 ± 1700	2400 ± 1300
$W \to cb$	380 ± 60	290 ± 50	143 ± 27
Single-top	1100 ± 400	1000 ± 400	570 ± 260
$t\bar{t} + V$	130 ± 80	200 ± 120	210 ± 130
VV & V + jets	690 ± 270	590 ± 50	350 ± 40
$t\bar{t}H + tH$	99 ± 15	266 ± 33	310 ± 40
Total	25000 ± 4000	27000 ± 6000	19000 ± 5000
Data	26614	28394	19302
$t \to uX$ m_X=60 GeV	860 ± 90	690 ± 60	350 ± 40
$t \to cX$ m_X=60 GeV	880 ± 90	690 ± 70	350 ± 40

Table 8.4: Number of expected and selected events after applying reweighting split according to the control regions, namely 4j4b, 5j≥4b and 6j≥4b. The quoted uncertainties include both statistical and systematic uncertainties. The predicted number of $t \to uX$ and $t \to cX$ signal events for the 60 GeV mass hypothesis, assuming a branching fraction of 0.1%, are also shown.

	4j, 4b	5j, ≥4b	6j, ≥4b
$t\bar{t}$ + light	5.1 ± 3.5	8 ± 6	6 ± 6
$t\bar{t}$ + ≥1b	250 ± 140	900 ± 500	1200 ± 700
$t\bar{t}$ + ≥1c	10 ± 7	26 ± 14	25 ± 14
$W \to cb$	8.3 ± 1.3	11.9 ± 2.1	8.3 ± 2.8
Single-top	22 ± 14	42 ± 19	50 ± 32
$t\bar{t} + V$	7 ± 5	26 ± 16	36 ± 22
VV & V + jets	13 ± 5	22.7 ± 3.0	20.2 ± 2.7
$t\bar{t}H$	6.2 ± 1.1	44 ± 7	76 ± 11
Total	320 ± 140	1100 ± 500	1500 ± 700
Data	374	1179	1492
$t \to uX$ m_X=60 GeV	2.8 ± 1.3	8.6 ± 3	14 ± 7
$t \to cX$ m_X=60 GeV	17 ± 6	27 ± 8	24 ± 12

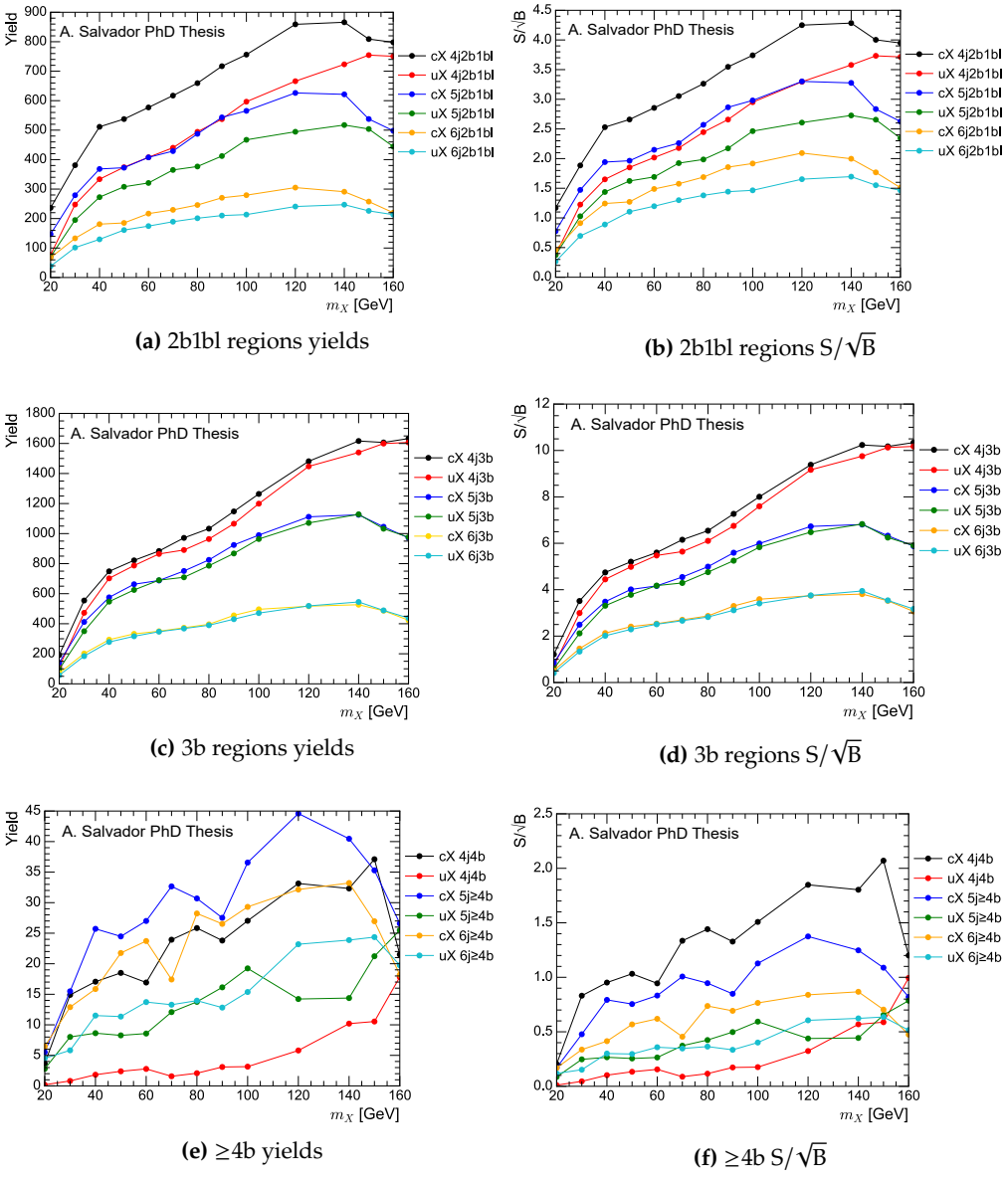

(a) 2b1bl regions yields

(b) 2b1bl regions $S/\sqrt{B}$

(c) 3b regions yields

(d) 3b regions $S/\sqrt{B}$

(e) ≥4b yields

(f) ≥4b $S/\sqrt{B}$

Figure 8.3: Signal yields (left) and $S/\sqrt{B}$ (right) for the 2b+1bl (top), 3b (middle) and ≥4b (bottom) regions after applying reweighting as a function of the mass of X for both $t \to qX$ processes, assuming a branching fraction of 0.1% and an integrated luminosity of 139 fb^{-1}.

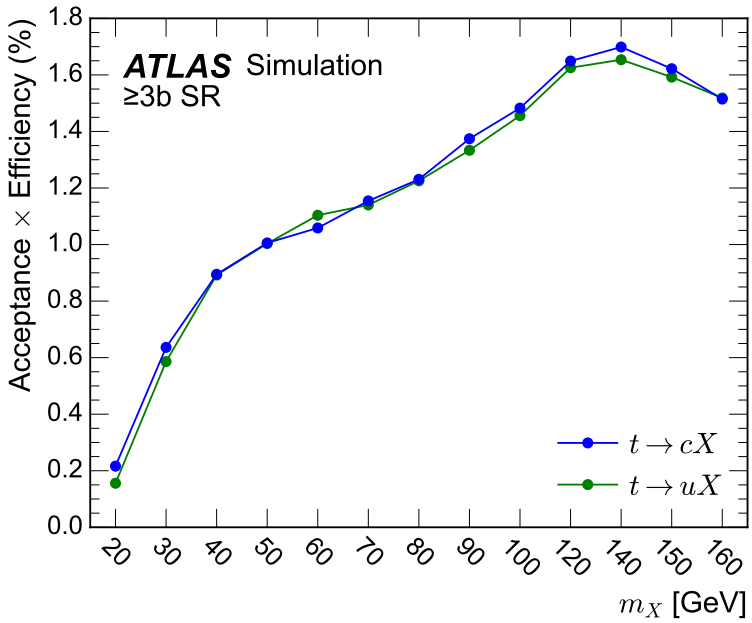

Figure 8.4: Acceptance times efficiency of the signal regions as a function of the scalar signal mass corresponding to the $t \to uX$ and $t \to cX$ channels.

8.4.2 Reweighting technique

The main background for the search is $t\bar{t}$+jets, and its correct modelling is essential for the correct description of the data. As mentioned for the $H^{\rightarrow}tb$ analysis (Section 6.4.2), the simulation does not properly model high jet multiplicities nor the hardness of additional jet emissions and data-based corrections are applied to improve the data/MC agreement.

The correction factors are applied to the $t\bar{t}$ samples as well as the signal samples, as they are modelled as using the same MC generator. The corrections derived in the 2b+1bl regions are expected to improve the agreement in the 3b and ≥4b regions. The remaining discrepancies can be covered by the systematic model.

The corrections are derived for each jet multiplicity and as a function of $H_{\mathrm{T}}^{\mathrm{all}}$, defined as the scalar p_{T} sum of jets, the lepton and $\mathrm{E}_{\mathrm{T}}^{\mathrm{miss}}$. The reweighting factors for each jet multiplicity is expressed as:

$$R(H_{\mathrm{T}}^{\mathrm{all}}) = \frac{\mathrm{Data}(H_{\mathrm{T}}^{\mathrm{all}}) - \mathrm{MC}^{\text{non-}t\bar{t}(H_{\mathrm{T}}^{\mathrm{all}})}}{\mathrm{MC}^{t\bar{t}(H_{\mathrm{T}}^{\mathrm{all}})}} \tag{8.1}$$

and, by construction, assumes that any disagreement between data and MC is from $t\bar{t}$.

Figure 8.5 includes all the derived corrections, showing higher weights for increased jet multiplicities and, in general, the $H_{\mathrm{T}}^{\mathrm{all}}$ corrections have a hyperbolic behaviour: close to one for $H_{\mathrm{T}}^{\mathrm{all}} > 800$ GeV and rapidly increasing towards lower values of $H_{\mathrm{T}}^{\mathrm{all}}$. Among various functions, the hyperbolic function was found to best fit the $H_{\mathrm{T}}^{\mathrm{all}}$ weight distributions: $w = A + \frac{B}{(H_{\mathrm{T}}^{\mathrm{all}})^C}$. The eigenvalues of the error matrix of fitted parameters are included as systematic uncertainties.

The agreement between simulation and data in the analysis region improves, as an example, Figure 8.6 shows the leading jet p_{T} distribution before and after the reweighting, which improves especially at low values. All studies included in this thesis are shown after the reweighting corrections are applied, unless stated otherwise.

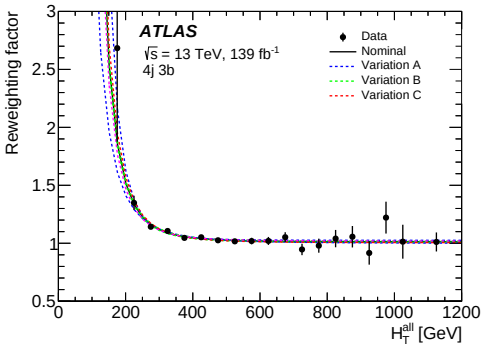

(a) 4j2b+1bl

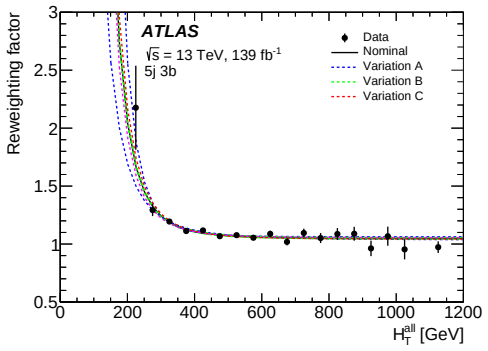

(b) 5j2b+1bl

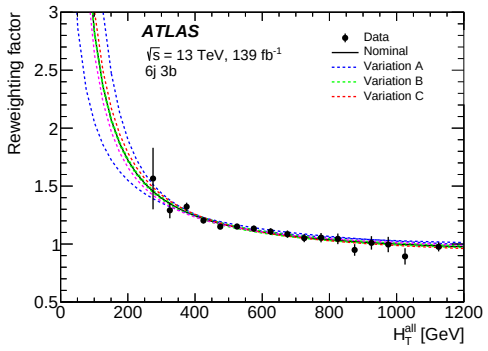

(c) 6j2b+1bl

Figure 8.5: Reweighting factors (weights) obtained from the comparison between data and simulation of the number of $H_{\mathrm{T}}^{\mathrm{all}}$ for the 2b+1bl regions and three different jet multiplicities, with the uncertainty bands associated to the variations of the eigenvalues of the matrix error of the fit function, namely A, B and C. The errors in the data points include the statistical uncertainties in data and MC predictions.

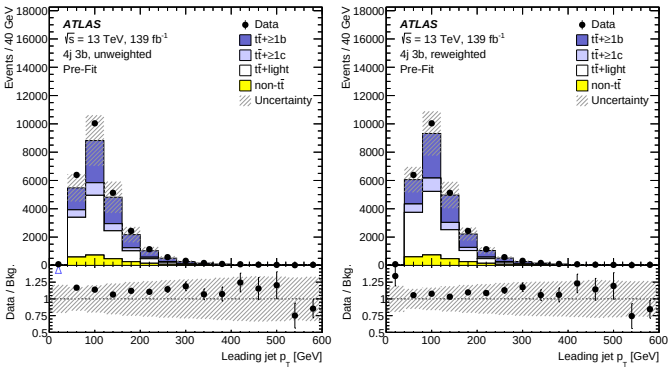

(a) 4j3b, unweighted

(b) 4j3b, reweighted

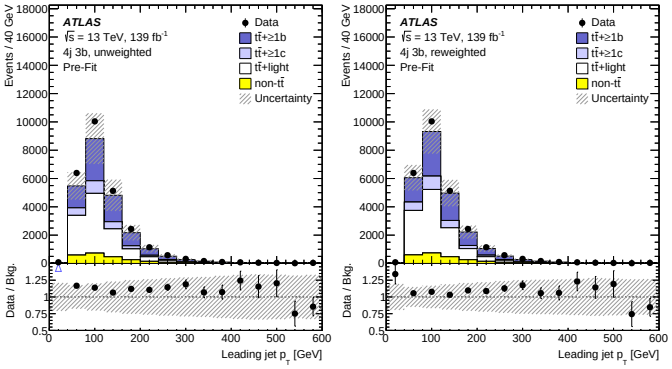

(c) 5j3b, unweighted

(d) 5j3b, reweighted

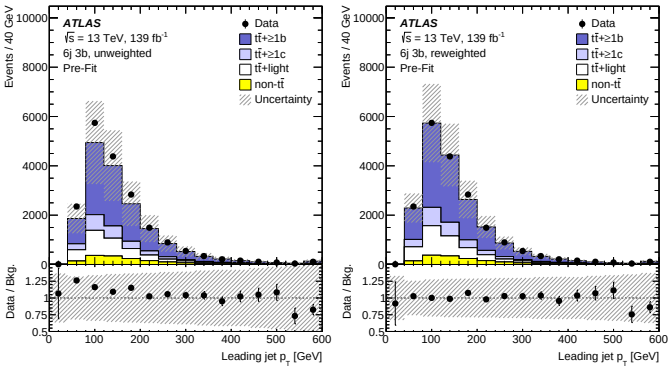

(e) 6j3b, unweighted

(f) 6j3b, reweighted

Figure 8.6: Distributions of the leading jet p_{T} before the fit to the data in the different 3b analysis regions before (left) and after (right) applying the $H_{\mathrm{T}}^{\mathrm{all}}$-based reweighting. The last bin includes the overflows. The lower panels display the ratio of the data to the total prediction. The hatched bands show the uncertainties before the fit to the data and include the correlated systematic uncertainties in the prediction and the statistical uncertainties uncorrelated across bins. When the reweighting is applied, the uncertainty bands are computed accordingly and include the associated uncertainties.

8.4.3 Multivariate techniques

Multivariate techniques are used in this analysis to enhance the separation between signal and background. The kinematics of $t\bar{t}+\geq 1b$ and signal events are very similar, and these methods can use different distributions as inputs to obtain a powerful discriminating variable.

The main classifier is a parameterised NN trained over all masses for each $t \to qX$ signal process and background, implemented with the same software tools as the $H^+ \to tb$ NN (Section 6.4.3). As input variables, low-level observables of the reconstructed objects are used achieving comparable discrimination than other refined techniques used in previous $t \to qH$ searches [248], similar to the $H^+ \to tb$ kinematic discriminant (Section 6.4.3).

$t \to qX$ parameterised NN

A set of NNs is trained separately for $t \to uX$ and $t \to cX$ including the [4-6]j≥3b regions and $m_X \geq 30$ GeV. The NN uses mainly low-level variables as input, hence the architecture and training set has to be large enough to extract all the discrimination power.

The architecture is sequential with five fully connected layers of 250 nodes and a single output node. Batch normalisation is performed to speed up the learning process with a size of 3000 events, learning rate $10^{-0.75}$ and dropout is applied during training at a 25% rate. To further regularise the training, inputs are transformed to the same scale (same mean and variance) as the training set, event weights of each label add up to the same value and a five-fold cross-validation setup is used.

All signal samples of the corresponding process are used in the training against all background samples, which are weighted according to their cross-sections. The inputs of the NN are described below:

- m_X,the X scalar mass hypothesis: Parameter of the NN.
- p_{T}, η and ϕ of the first six leading jets (ordered by pseudo-continuous b-tagging score and p_{T}). In order to reduce the event symmetries and the variable set, the η and ϕ coordinates of all reconstructed objects are transformed with respect to a reference frame define as $\eta_\ell > 0$ and $\phi_\ell = 0$.
- Pseudo-continous b-tagging score for the forth, fifth and sixth jets (ordered by b-tagging score).
- Lepton p_{T} and η.
- $\mathrm{E}_{\mathrm{T}}^{\mathrm{miss}}$ and $\phi_{E_{\mathrm{T}}^{\mathrm{miss}}}$.
- Three invariant masses and three ΔR of two b-tagged jets from pairs of the three most b-tagged jets.

m_X is the parameter that distinguishes the different signals, consequently the parameterised NN (Section 5.2) output is a function of m_X. For signal events, the parameter corresponds to the mass of the generated X while for background events a random value of m_X is assigned to each event, taken from the m_X distribution of signal masses. This makes the NN not to directly use the parameter to perfectly

classify the events.

The presented setup has been scrutinised and is the result of exploring different sets of parameters, architectures, variables and setups. Efforts joining the two $t \to qX$ signals in a single training resulted in less discrimination for the $t \to uX$ process. Also, the 20 GeV signal sample is not included in the training as it introduced disagreement in data/MC in all NN outputs. Other more advanced setups, as a Graph NN, were not substantially improving the performance.

Table 8.5: List of variables included in the training of the $t \to qX$ NN.

Variable	Description
m_{H^+}	Parameter of the NN. H^+ mass hypothesis.
D	Kinematic discriminant of the H^+ mass hypothesis.
$H_{\mathrm{T}}^{\mathrm{jets}}$	Scalar sum of the transverse energy of all jets. Sensible to events with massive H^+
Centrality	Centrality calculated using all jets and leptons.
p_{T}^{0}	Leading jet p_{T}. Similar to $H_{\mathrm{T}}^{\mathrm{jets}}$.
$m_{bb}^{\mathrm{min}\Delta R}$	Invariant mass of the closest b-jet pair. The bb pair aims to partially reconstruct the H^+ invariant mass, very different from the $t\bar{t}$ background.
p_{T}^{4}	p_{T} of fifth leading jet. Characterises the low energy scale of the event.
H_{1}^{all}	Second Fox-Wolfram moment calculated using all jets and leptons.
$\Delta R_{bb}^{\mathrm{avg}}$	Average ΔR between all b-jet pairs in the event.
$\mathrm{min}\Delta R_{lep,bb}$	ΔR between the lepton and the pair of b-jets with smallest ΔR.
$m_{uu}^{\mathrm{min}\Delta R}$	Invariant mass of the untagged jet-pair with minimum ΔR. Aims to reconstruct the W-boson that decays hadronically.
$m_{bb}^{\mathrm{max}p_{\mathrm{T}}}$	Invariant mass of the b-jet pair with maximum p_{T}.
$m_{bb}^{\mathrm{max}m}$	Maximal invariant mass of b-jets.
$m_{jjj}^{\mathrm{max}p_{\mathrm{T}}}$	Invariant mass of the jet triplet with maximum p_{T}.
N_{jets} and $N_{b\text{-jets}}$	jet and b-jet multiplicity.

The importance of the variables in the NN training depends on the mass of the scalar and in a lesser extent on the channel but, in general, the most important ones are the various combinations of both di-jet invariant masses and angular distances between the two jets. Less important, and only in a small range of masses, are the b-tagging score of the fourth jet and the transverse momentum of the third jet.

The NN output is obtained evaluating the $t \to uX$ or the $t \to cX$ NN setting the m_X at the desired hypothesis. The obtained distributions for signal and background in the analysis regions for various representative values of m_X and the two signal decays are shown in Figure 8.8 and Figure 8.7. The shapes are significantly different between the presented mass-points, although the shape of the distributions transforms gradually from one mass to the next. Notice that the shape of the background changes, since the same NN is being evaluated but with different m_X values.

Figure 8.9 summarises the performance in terms of AUC. The performance is best at a mass of 30 GeV, given that this is the mass for which the input variables show the best discrimination, on the contrary the 120 GeV outputs the lowest performance.

For 20 GeV, the performance is low because is not included in the training and due to the kinematics and statistics being too different from the rest of masses. The performance of $t \to uX$ and $t \to cX$ follow the same structure, with the $t \to uX$ training performance being slightly better in the lower range of masses.

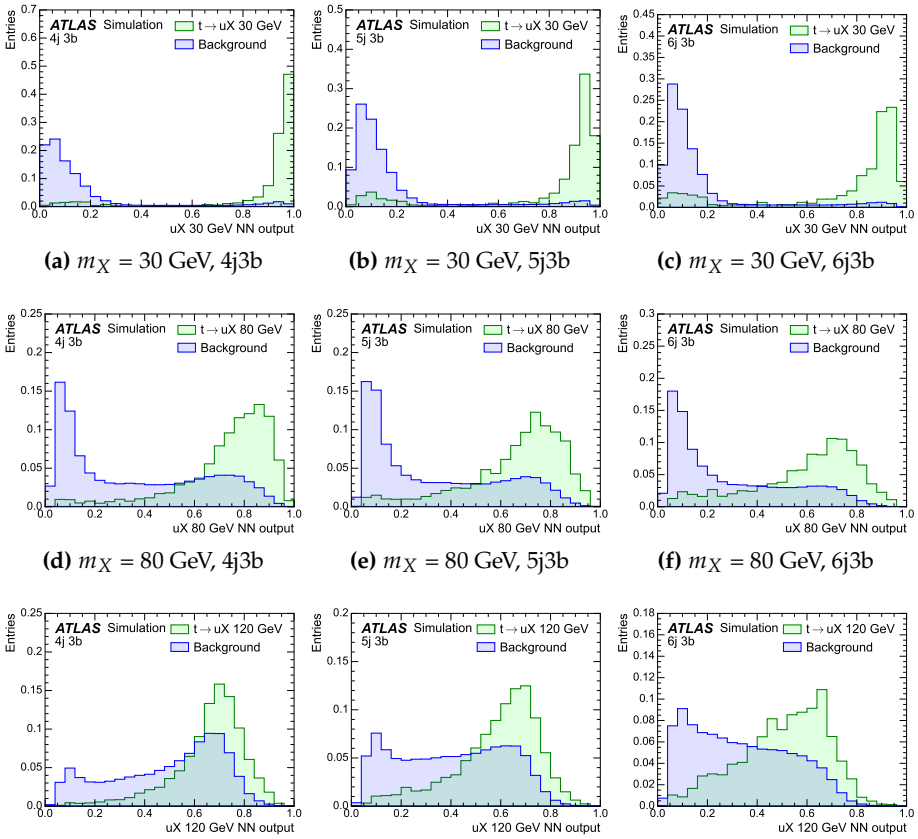

(a) $m_X = 30$ GeV, 4j3b **(b)** $m_X = 30$ GeV, 5j3b **(c)** $m_X = 30$ GeV, 6j3b

(d) $m_X = 80$ GeV, 4j3b **(e)** $m_X = 80$ GeV, 5j3b **(f)** $m_X = 80$ GeV, 6j3b

(g) $m_X = 120$ GeV, 4j3b **(h)** $m_X = 120$ GeV, 5j3b **(i)** $m_X = 120$ GeV, 6j3b

Figure 8.7: Expected NN output distributions in the three signal regions for top-quark decays to uX under the 30, 80 and 120 GeV X scalar mass hypotheses.

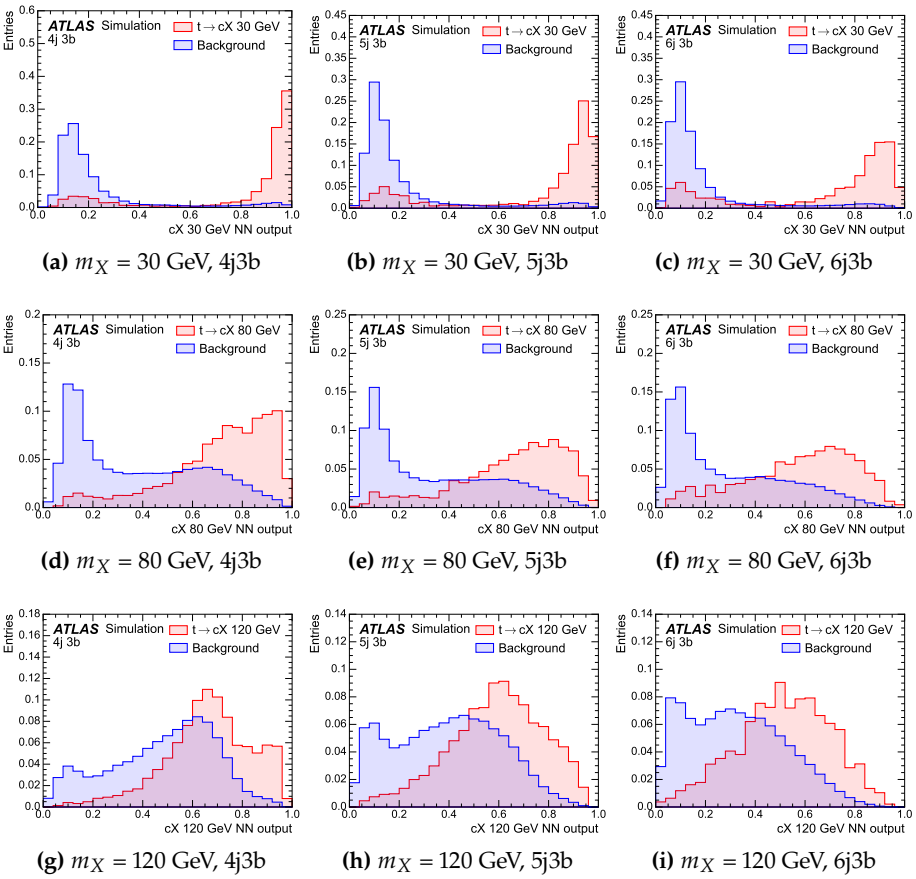

(a) $m_X = 30$ GeV, 4j3b **(b)** $m_X = 30$ GeV, 5j3b **(c)** $m_X = 30$ GeV, 6j3b

(d) $m_X = 80$ GeV, 4j3b **(e)** $m_X = 80$ GeV, 5j3b **(f)** $m_X = 80$ GeV, 6j3b

(g) $m_X = 120$ GeV, 4j3b **(h)** $m_X = 120$ GeV, 5j3b **(i)** $m_X = 120$ GeV, 6j3b

Figure 8.8: Expected NN output distributions in the three signal regions for top-quark decays to cX under the 30, 80 and 120 GeV X scalar mass hypotheses.

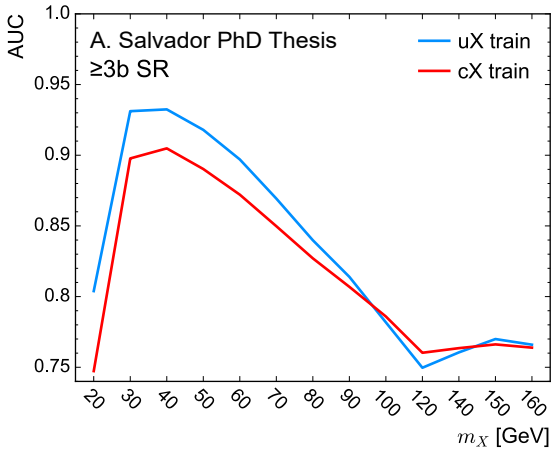

Figure 8.9: Comparison of the performance, measured as the area of the ROC curve as a function of the mass of the scalar X for the ≥3b regions. The NNs are trained using either the $t \to uX$ (blue) or $t \to cX$ (red) samples, and evaluated accordingly.

8.5 Systematic uncertainties

The presented analysis is heavily affected by systematic uncertainties from different sources, explained in this section. There are two main categories of systematic uncertainties: experimental uncertainties, mainly associated to the reconstruction of the various physics objects, and the modelling uncertainties related to the signal and background process modelling in MC.

In total, 282 nuisance parameters are used and summarised in Table 8.6, corresponding to the systematic components. The systematic uncertainties can either affect both the shape and the normalisation (SN), only the normalisation (N) or only the shape (S) of a process. Some uncertainty sources might consist of several independent components, e.g. the b-jet efficiency calibrations, and one nuisance parameter is associated to each component. In addition, for every bin considered in the analysis two nuisance parameters are assigned, one for signal and one for background, to take into account the uncertainties coming from the finite statistics of the MC samples.

8.5.1 Experimental uncertainties

The experimental uncertainties have in general a low impact on the final fit. Only the uncertainties associated to jets and b-tagging have influence. All experimental nuisance parameters are correlated across all analysis regions and processes. These uncertainties are similar to the $H^+ \to tb$ experimental uncertainties detailed in Section 6.5.1. The main differences arise from the updated recommendations on objects, especially the use of PFlow jets and the DL1r b-tagger.

8.5.2 Modelling Uncertainties

In contrast to the experimental uncertainties, the modelling uncertainties are not correlated across all background and signal processes, but typically they are still correlated across analysis regions with some exceptions. The uncertainties are split into several components depending on the signal and background processes as well as into different physics effects in MC generators. While the cross-section, branching fraction and normalisation uncertainties only affect the normalisation of the physics processes, all other modelling uncertainties are also sensitive to shape effects.

Signal modelling

Several normalisation and shape uncertainties are taken into account for the $t \to qX$ process. Since no alternative signal samples are used in the analysis, the uncertainties from the choice of NLO generator, PS and hadronisation, and reweighting of the $t\bar{t}$+light background are assigned to the signal. These uncertainties are chosen to be correlated with the $t\bar{t}$+light background, motivated by the fact that the $t\bar{t}$ pair generated in the signal sample should be modelled as the $t\bar{t}$+light background process.

Table 8.6: Overview of the systematic uncertainties included in the analysis. An "N" means that the uncertainty is taken as normalisation-only for all processes and regions affected, whereas "SN" means that the uncertainty is taken on both shape and normalisation. Some of the systematic uncertainties are split into several components for a more accurate treatment: the number of such components is indicated in the rightmost column. There is one component for each jet multiplicity for the $t\bar{t}$ modelling uncertainties, explicitly indicated as "x 3".

Systematic uncertainty	**Type**	**Components**
Experimental uncertainties		
Luminosity	N	1
Pileup modelling	SN	1
Physics objects		
Electrons	SN	4
Muons	SN	10
Jet energy scale	SN	29
Jet energy resolution	SN	9
Jet vertex tagger	SN	1
$E_{\mathrm{T}}^{\mathrm{miss}}$	SN	3
b-tagging		
Efficiency	SN	45
Mis-tag rate (c)	SN	15
Mis-tag rate (light)	SN	20
Signal modelling		
Signal		
$t\bar{t}$+light PS & hadronisation	SN	3
$t\bar{t}$+light NLO	SN	3
$t\bar{t}$+light radiation	SN	5
$t\bar{t}$+light reweighting	SN	4 x 3
$t\bar{t}$ background		
$t\bar{t}+ \geq 1c$ normalisation	N	1
$t\bar{t}+ \geq 1b$ normalisation	N	1
$t\bar{t}$ reweighting	SN	4 x 3
$t\bar{t}+$ light modelling	SN	7 x 3
$t\bar{t}+ \geq 1c$ modelling	SN	7 x 3
$t\bar{t}+ \geq 1b$ modelling	SN	8 x 3
$t\bar{t}$: $W \rightarrow cb$ normalisation	N	1
$t\bar{t}$: $W \rightarrow cb$ modelling	SN	2 x 3
Other backgrounds		
Single top cross-section	N	1
Single top modelling	SN	22
Diboson normalisation	N	3
V+jets	N	3
$t\bar{t}V$ cross-section	N	1
$t\bar{t}H$ cross-section	N	1
$t\bar{t}H$ modelling	SN	2
tH cross-section	N	1

$t\bar{t}$ modelling

The $t\bar{t}$ process is the most important background in the analysis and a large number of uncertainties are considered for an appropriate modelling. Since the composition of the $t\bar{t}$ subcategories are different in the analysis' regions, different effects are expected. Similar to the $H^+ \to tb$ search (Section 6.5.2) all systematic uncertainties associated to $t\bar{t}$ are uncorrelated across the $t\bar{t}$+≥1b, $t\bar{t}$+≥1c and $t\bar{t}$+light categories, having separate nuisance parameters. Furthermore, the components are also uncorrelated among jet multiplicities to better model differences between jet multiplicities arising from the tight b-tagging and reweighting factors. The $W \to cb$ category is also included but in its own category and also uncorrelated among jet multiplicities. Unless stated otherwise, the nuisance parameters are correlated among bins and among regions with the same jet multiplicity. Table 8.7 summarises the uncertainties applied to the $t\bar{t}$ background.

Table 8.7: Summary of the sources of systematic uncertainty for the $t\bar{t}$ background modelling. The last column of the table indicates the subcomponents for the corresponding systematic uncertainty. All systematic uncertainty sources, except those associated to the $t\bar{t}$ reweighting, are treated as uncorrelated across the three components.

Uncertainty source	Description		Components
$t\bar{t}$+≥1b normalisation	±50%		$t\bar{t}$+≥1b
$t\bar{t}$+≥1c normalisation	±50%		$t\bar{t}$+≥1c
$t\bar{t}$ reweighting	Uncertainties of fitted function parameters		$t\bar{t}$
μ_R	Scaling by 0.5 (2.0)	in PowhegBox +Pythia	$t\bar{t}$
μ_F	Scaling by 0.5 (2.0)	in PowhegBox +Pythia	$t\bar{t}$
$\mu_R \times \mu_F$	Scaling both by 0.5 (2.0)	in PowhegBox +Pythia	$t\bar{t}$
ISR	Varying α_S^{ISR}	in PowhegBox +Pythia	$t\bar{t}$
FSR	Varying α_S^{FSR}	in PowhegBox +Pythia	$t\bar{t}$
NLO matching	MadGraph5_aMC@NLO +Pythia	vs. PowhegBox +Pythia	$t\bar{t}$
PS & hadronisation	PowhegBox +Herwig	vs. PowhegBox +Pythia	$t\bar{t}$
$t\bar{t}$+≥1b modelling	4FS vs. 5FS		$t\bar{t}$+≥1b

A normalisation uncertainty of 50% is assumed separately for $t\bar{t}$+≥1b and $t\bar{t}$+≥1c. The choice is motivated by the level of agreement between data and prediction in the control regions for this background before the fit. The $t\bar{t}$+≥1b normalisation uncertainty is constrained from the fit, while the $t\bar{t}$+≥1c normalisation uncertainty is not due the lack of sensitivity to this process.

For the uncertainties related to the renormalisation and factorisation scales, μ_R and μ_F are varied independently by a factor 0.5 (2.0) for the up (down) variation, with an extra nuisance parameter for the simultaneous variation of μ_R and μ_F. The ISR and FSR components are obtained setting accordingly α_S^{ISR} to 0.140 (0.115) and α_S^{FSR} to 0.140 (0.115), where the nominal values are both 0.127.

Two-point systematics are derived for the rest of modelling uncertainties, including $W \to cb$. For a given distribution, this type of uncertainties are obtained from the difference in the prediction when comparing two different samples generated with different MC setups. The systematic uncertainty related to PS are retrieved by comparing the nominal setup, PowhegBox +Pythia 8 to the prediction of the

sample generated with PowhegBox +Herwig 7, where the PS has been modelled with a different generator. Similarly, the uncertainty related to the NLO matching is retrieved from a sample generated with MadGraph5_aMC@NLO +Pythia 8.

To cover the differences between the choice of flavour scheme, the nominal is compared to a PowhegBoxRes+Pythia 8 (4FS) $t\bar{t}$+≥1b sample. This uncertainty is only applied to the $t\bar{t}$+≥1b component.

The weights derived in Section 8.4.2 that are applied to improve the modelling of the $t\bar{t}$ background are also subject to uncertainties. The associated statistical uncertainties are varied obtaining 12 nuisance parameters, which are correlated between the different $t\bar{t}$ components[3]. Aside, the $t\bar{t}$ samples with alternative MC setups do not have the same composition of $t\bar{t}$ subcomponents as the nominal sample, especially PowhegBox +Herwig 7. This difference can change significantly the fractions in the fit however, the normalisation of the sub-processes in the analysis regions are obtained with the fit.

To avoid the propagation of the normalisation effect from the comparison, the alternative samples are scaled to ensure the same flavour composition as the nominal sample in the analysis regions. In addition, the discussed uncertainties are also scaled by the yield ratio between nominal and corresponding alternative $t\bar{t}$. The 50% normalisation effects of $t\bar{t}$+≥1b and $t\bar{t}$+≥1c have an effect on the reweighing, which is estimated by applying a dedicated reweighting computed with the normalisation effects. These propagation effects are correlated with the corresponding 50% prior and assigned to the rest of individual $t\bar{t}$ components.

Other background modelling

The systematic uncertainties associated to background processes other than $t\bar{t}$+jets play a subordinate role.

A +5%/-4% uncertainty is considered for the cross-sections of the three single-top production modes, estimated from averaging the theoretical uncertainties in t-, s- and Wt-channel productions [254, 255]. Uncertainties associated with the PS model, and with the NLO matching scheme are evaluated by comparing, for each process individually, the nominal PowhegBox +Pythia 8 sample with a sample produced using PowhegBox +Herwig 7 and MadGraph5_aMC@NLO +Pythia 8, respectively. Similarly to the $t\bar{t}$ background, the multiple ISR and FSR modelling uncertainties included and all the modelling uncertainties are decorrelated among jet multiplicity. The uncertainty associated to the interference between Wt and $t\bar{t}$ production at NLO [183] is assessed by comparing the nominal PowhegBox +Pythia 8 sample produced using the "diagram removal" scheme with an alternative sample produced with the same generator but using the "diagram subtraction" scheme.

Uncertainties affecting the normalisation of the V+jets background are estimated for the sum of W+jets and Z+jets. The agreement between data and the total back-

[3] as mentioned above, the $t\bar{t}$+light components are correlated with the signal.

ground prediction is found to be within approximately 40%, taken to be the total normalisation uncertainty correlated across all V+jets processes. An additional 25% uncertainty is added in quadrature for each additional jet multiplicity beyond four, resulting in 47% and 52% in regions with five and six jets, respectively [256].

Uncertainties in the diboson background normalisation include 5% from the NLO theory cross-sections [257], as well as an additional 24% normalisation uncertainty added in quadrature for each additional inclusive jet-multiplicity bin, based on a comparison among different algorithms for merging LO matrix elements and parton showers [256]. Therefore, the total uncertainty is 34%, 42% and 48% for events with four, five and six jets, respectively. Recent comparisons between data and Sherpa 2.1.1 for $WZ \to \ell'\nu\ell\ell+ \geq 4$ jets show agreement within the experimental uncertainty of approximately 40% [258], which further motivates the uncertainties above. Uncertainties in the $t\bar{t}V$, tZ, $t\bar{t}H$ and tH cross-sections are 60%, 60%, +9/-12% and 50%, respectively, arising from the uncertainties in their respective NLO theoretical cross-sections [180, 259]. In addition, $t\bar{t}H$ uncertainties related to the PS and the NLO matching is similarly implemented comparing the nominal with the same type of alternative MC.

9 $t \to qX$ analysis results

In order to test for the presence of a $t \to qX$ signal, a binned maximum-likelihood fit to the data is performed as described in Section 5.2. In total 26 fits are performed, one for each mass hypothesis, fitting in the signal regions the NN output evaluated at the corresponding mass, and the yields in the control regions. The control regions are 4j4b, 5j≥4b and 6j≥4b consist then in one bin, while the three signal regions (4j3b, 5j3b and 6j3b) distributions have ten bins, with irregular binning optimised to increase sensitivity. The parameter of interest is the production of the signal, $\mathrm{B}(t \to qX)$.

A total of 282 nuisance parameters are introduced in the fit. To speed up the fit and ease the convergence, the shape or normalisation components of the different systematic uncertainties are pruned if their effect is below a threshold of 0.2%. In addition, smoothing techniques are applied to reduce the impact of statistical fluctuations when computing the templates of systematic uncertainties.

This section provides the expected and observed results on the fitted signal strength, $\mathrm{CL_s}$ exclusion limits, a brief review of the $t \to qH$ measurement.

9.1 Fit results

The analysis optimisation is performed on MC simulation and the performance is evaluated via *Asimov* data instead of experimental data. The dataset is built from the nominal background and the chosen signal, thus the normalisation factors and nuisance parameters extracted from the fit are the default ones by construction. Nevertheless, the profile likelihood fit provides uncertainties on the signal strength and the expected upper limits. It is the standard procedure to optimise the analysis without using the experimental data to avoid introducing any bias, especially in signal regions.

Once the desired expected sensitivity is obtained and the background modelling reproduces the experimental data in signal-depleted regions, experimental data is added to the fit. Multiple studies were performed to validate the fits studying the effect of pulls and constraints of the nuisance parameters, evaluate possible biases in the signal modelling or evaluating the data/MC agreement in the post-fit distributions among them.

Table 9.1 shows the event yields after the $t \to uX$ and $t \to cX$ fits under the 30 GeV X scalar mass fits. Figures 9.1, 9.2 and 9.3 show the post-fit distributions of the NN output in the 3b regions and the yields in the ≥4b regions for two signal processes and the 30, 80 and 120 GeV m_X hypotheses, respectively. Good agreement between the observed and expected bins is observed after the fit, also seen in the rest of masses and in the input variables of the NN.

Table 9.1: Event yields of the $t \to qX$ signal and background processes in the four analysis regions after the fit to the data under the X scalar mass hypothesis of 30 GeV for $t \to uX$ (top) and $t \to cX$ (bottom). The quoted uncertainties take into account correlations and constraints of the nuisance parameters and include both the statistical and systematic uncertainties. Negative correlations among $t\bar{t}$+≥1b, $t\bar{t}$+≥1c and $t\bar{t}$+light modelling uncertainties can cause the uncertainty on the total yields to be smaller than on individual components.

$t \to uX$, $m_X = 30$ GeV fit						
	4j 3b	4j 4b	5j 3b	5j ≥4b	6j 3b	6j ≥4b
$t\bar{t}$+light	9300 ± 900	4.0 ± 2.4	6200 ± 900	7 ± 5	2700 ± 500	5 ± 4
$t\bar{t}$+≥1b	11200 ± 1000	319 ± 22	15400 ± 1200	980 ± 50	12000 ± 900	1250 ± 60
$t\bar{t}$+≥1c	3400 ± 1100	12 ± 7	4200 ± 1300	33 ± 11	2900 ± 900	29 ± 10
$W \to cb$	380 ± 60	8.1 ± 1.2	270 ± 50	11.4 ± 1.9	132 ± 22	7.4 ± 2.4
Single-t	1200 ± 400	19 ± 11	1100 ± 400	49 ± 22	640 ± 280	60 ± 40
$t\bar{t}H$	106 ± 14	6.6 ± 1.0	273 ± 32	45 ± 7	309 ± 35	75 ± 10
$t\bar{t}V$	120 ± 80	7 ± 5	190 ± 120	25 ± 15	190 ± 120	33 ± 21
VV, V+jets	870 ± 290	16 ± 5	770 ± 40	28.9 ± 3.0	459 ± 32	27.5 ± 3.2
Signal	10 ± 40	0.02 ± 0.08	8 ± 33	0.2 ± 0.8	4 ± 16	0.1 ± 0.6
Total	26580 ± 170	392 ± 17	28410 ± 180	1176 ± 33	19300 ± 150	1490 ± 40
Data	26614	374	28394	1179	19302	1492

$t \to cX$, $m_X = 30$ GeV fit						
	4j 3b	4j 4b	5j 3b	5j ≥4b	6j 3b	6j ≥4b
$t\bar{t}$+light	10200 ± 1200	6.4 ± 3.3	6700 ± 1000	10 ± 6	3000 ± 600	7 ± 5
$t\bar{t}$+≥1b	9800 ± 1200	284 ± 25	14500 ± 1300	970 ± 50	11400 ± 1000	1250 ± 60
$t\bar{t}$+≥1c	3900 ± 1300	17 ± 10	4600 ± 1400	41 ± 14	3300 ± 1100	35 ± 12
$W \to cb$	400 ± 60	8.7 ± 1.2	280 ± 50	12.3 ± 2.1	134 ± 23	7.9 ± 2.6
Single-t	1200 ± 400	25 ± 15	1100 ± 400	43 ± 19	550 ± 230	51 ± 31
$t\bar{t}H$	109 ± 14	6.9 ± 1.0	280 ± 33	46 ± 7	316 ± 35	78 ± 11
$t\bar{t}V$	140 ± 80	8 ± 5	220 ± 120	28 ± 16	220 ± 120	38 ± 22
VV, V+jets	810 ± 260	16 ± 5	730 ± 50	27.0 ± 3.0	425 ± 34	25.0 ± 3.0
Signal	20 ± 40	0.5 ± 1.2	14 ± 31	0.5 ± 1.1	7 ± 15	0.4 ± 1.0
Total	26600 ± 180	373 ± 18	28400 ± 190	1183 ± 34	19310 ± 150	1490 ± 40
Data	26614	374	28394	1179	19302	1492

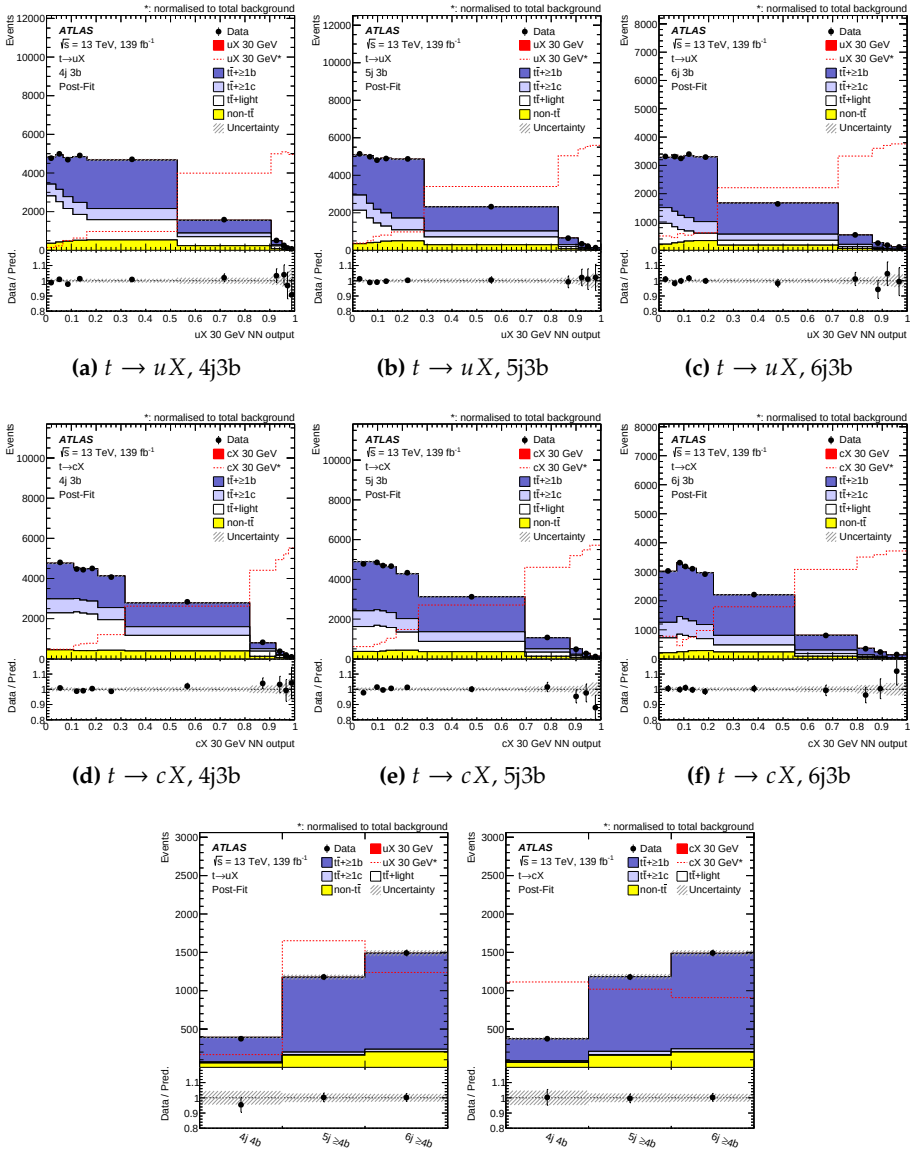

(a) $t \to uX$, 4j3b **(b)** $t \to uX$, 5j3b **(c)** $t \to uX$, 6j3b

(d) $t \to cX$, 4j3b **(e)** $t \to cX$, 5j3b **(f)** $t \to cX$, 6j3b

(g) $t \to uX$, ≥4b **(h)** $t \to cX$, ≥4b

Figure 9.1: Comparison between the data and prediction for the NN output in the 3b regions for the $t \to uX$ ((a) to (c)) and the $t \to cX$ ((d) to (f)) processes, and the yields in the ≥4b regions for the $t \to uX$ (g) and the $t \to cX$ (h) processes after the signal-plus-background fit to data for corresponding fit under the 30 GeV X scalar mass hypothesis.

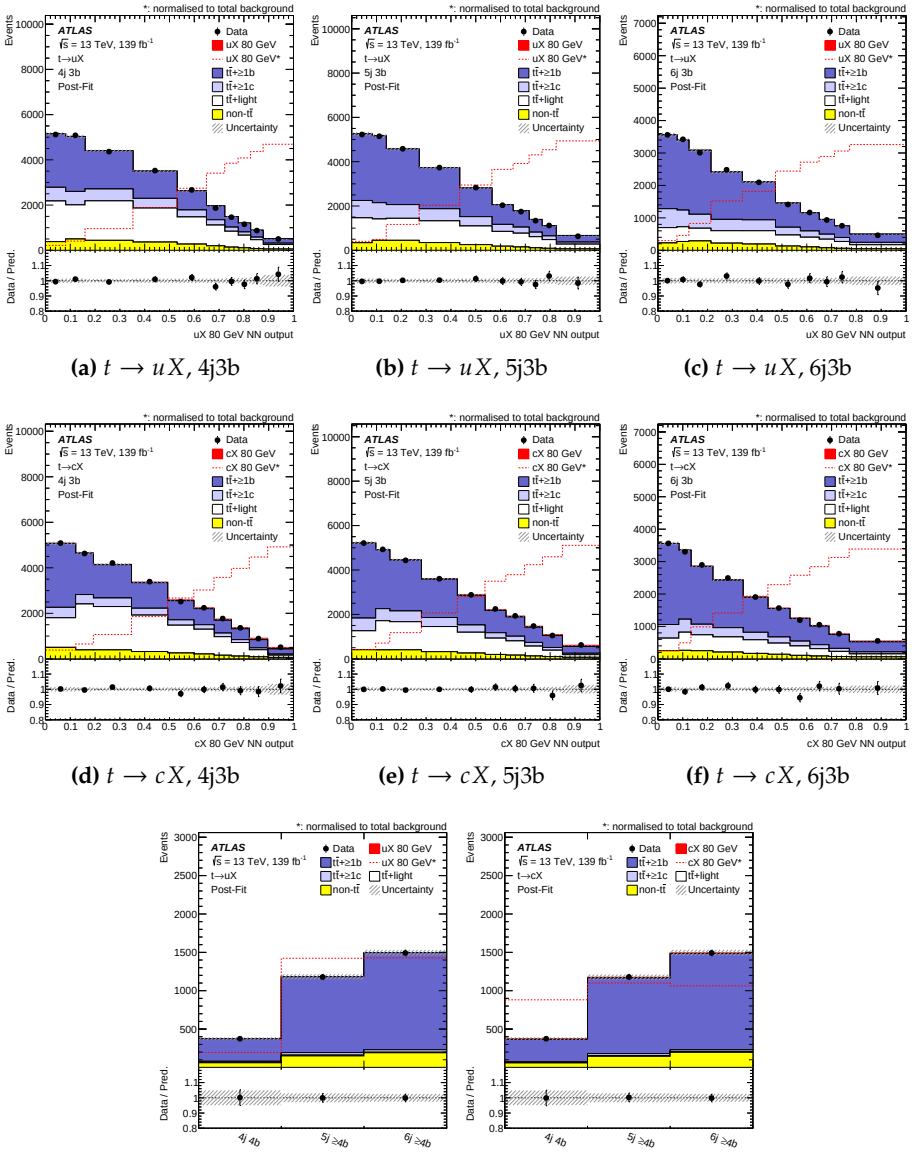

(a) $t \to uX$, 4j3b **(b)** $t \to uX$, 5j3b **(c)** $t \to uX$, 6j3b

(d) $t \to cX$, 4j3b **(e)** $t \to cX$, 5j3b **(f)** $t \to cX$, 6j3b

(g) $t \to uX$, ≥4b **(h)** $t \to cX$, ≥4b

Figure 9.2: Comparison between the data and prediction for the NN output in the 3b regions for the $t \to uX$ ((a) to (c)) and the $t \to cX$ ((d) to (f)) processes, and the yields in the ≥4b regions for the $t \to uX$ (g) and the $t \to cX$ (h) processes after the signal-plus-background fit to data for the corresponding fit under the 80 GeV X scalar mass hypothesis.

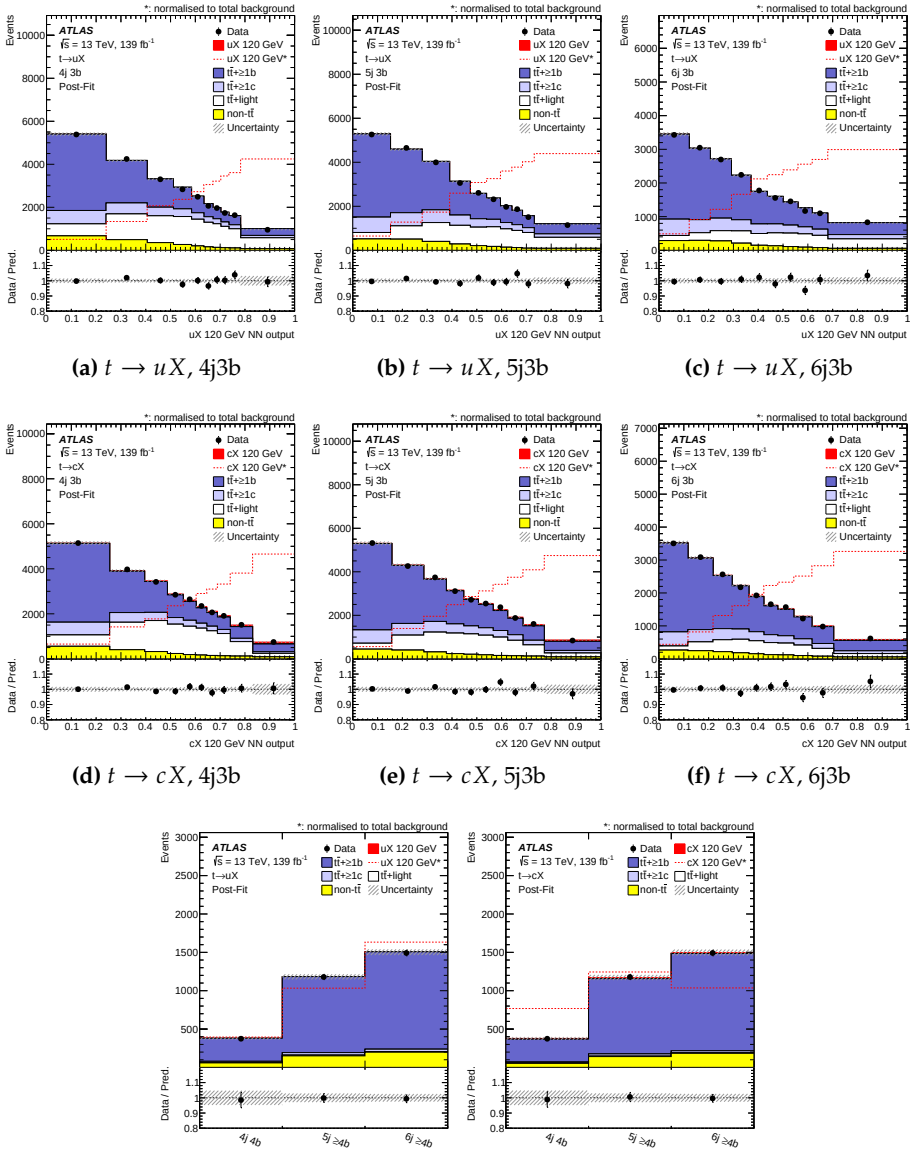

(a) $t \to uX$, 4j3b **(b)** $t \to uX$, 5j3b **(c)** $t \to uX$, 6j3b

(d) $t \to cX$, 4j3b **(e)** $t \to cX$, 5j3b **(f)** $t \to cX$, 6j3b

(g) $t \to uX$, ≥4b **(h)** $t \to cX$, ≥4b

Figure 9.3: Comparison between the data and prediction for the NN output in the 3b regions for the $t \to uX$ ((a) to (c)) and the $t \to cX$ ((d) to (f)) processes, and the yields in the ≥4b regions for the $t \to uX$ (g) and the $t \to cX$ (h) processes after the signal-plus-background fit to data for the corresponding fit under the 120 GeV X scalar mass hypothesis.

The nuisance parameters and normalisation factors are different to the original values, as the fit accommodates for normalisation and shape differences between the observed and predicted distributions.

The signal strength and the $t\bar{t}$+≥1b and $t\bar{t}$+≥1c normalisation nuisance parameters are summarised in Figure 9.4. The $t\bar{t}$+≥1b normalisation nuisance parameter ranges from 0.19 to 0.56 (0.10 to 0.49) with a typical uncertainty of 0.25 (0.24) for the $t \to uX$ ($t \to cX$) fits, while the $t\bar{t}$+≥1c parameter ranges from 0.29 to 1.10 (-0.13 to 1.02) with a typical uncertainty of 0.79 (0.47). Regarding the signal strength, the largest deviations with respect to the SM hypothesis are observed for $m_X = 80$ GeV and $m_X = 40$ GeV hypotheses for the $t \to cX$ and $t \to uX$, respectively. $t \to uX$ shows some negative deviations which does not represent evidence of the signal.

Figure 9.5 shows the p_0 values corresponding to the significance as a function of m_X and for both types of signal. The $t \to cX$ process shows larger but constant ~2σ deviations in the 40–120 GeV range which peaks at $m_X = 80$ GeV with 2.2σ, while the $t \to uX$ has a more defined peak at 40 GeV equivalent to 1.8σ. The difference between the $t \to uX$ and $t \to cX$ results is not only from the difference in statistics, they slightly differ in the fourth jet due to its different flavour. Given the use of b-tagging information in the NN training, the discrimination achieved between background and $t \to uX$ or $t \to cX$ signals slightly differs too and depends on the mass of the scalar.

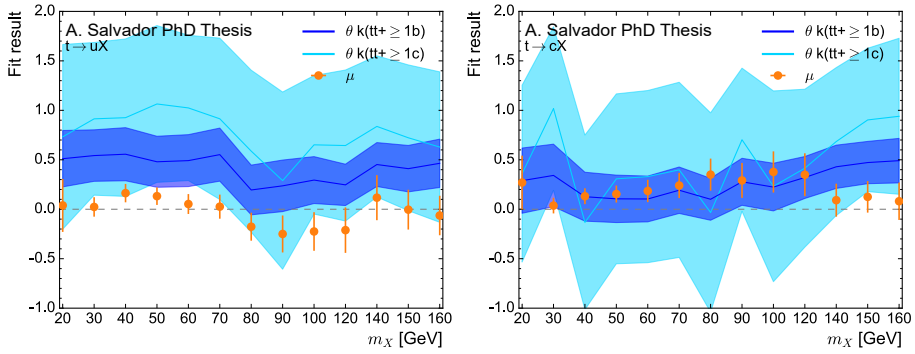

(a) $t \to uX$ **(b)** $t \to cX$

Figure 9.4: Evolution of the obtained signal strength and the nuisance parameters related to the $t\bar{t}$+≥1b and $t\bar{t}$+≥1c normalisation as a function of the X scalar mass with the corresponding uncertainties. The signal strength is normalised to 0.1% branching fraction.

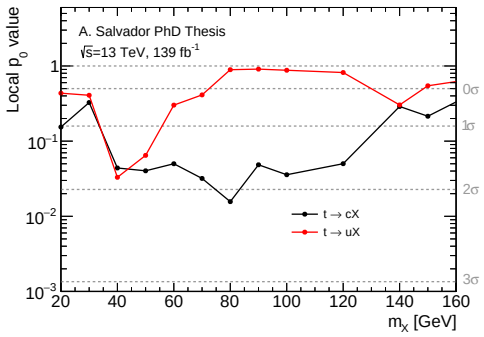

Figure 9.5: p_0 values for the fitted signal strength as a function of the mass of X hypothesis for the $t \to cX$ (black) and $t \to uX$ (red) signal fits.

9.1.1 Dominant uncertainties

The uncertainty associated to the fit result is mainly driven by systematic uncertainties. The different sources are ranked by the impact on the signal strength in terms of its shift from the default result $\Delta\mu$, evaluated in separate fits where the associated nuisance parameters are fixed to $\hat{\theta} \pm \Delta\hat{\theta}$. $\hat{\theta}$ is the best fit value of the given nuisance parameter while $\Delta\hat{\theta}$ is the corresponding one standard deviation.

Figure 9.6 lists the 20 top ranked nuisance parameters of the 30, 80 and 120 GeV m_X hypothesis fits for both types of signal. The upper axis represents the scale for the pre-fit and post-fit impact on μ. The pre-fit (post-fit) impact is given as $\hat{\theta} \pm \Delta\theta(\hat{\theta} \pm \Delta\hat{\theta})$, with $\Delta\theta$ ($\Delta\hat{\theta}$) the pre-fit (post-fit) uncertainties. The post-fit value of $\Delta\hat{\theta}$ is typically smaller than the one standard deviation prior, $\Delta\theta$, due to constraints from the fit to data. The pre-fit and post-fit impacts are shown as empty and filled rectangles, respectively. The lower axis indicates the scale of the pull of the nuisance parameter defined as $\frac{\hat{\theta}-\theta_0}{\Delta\theta}$ with θ_0 the nominal pre-fit value. The pulls are indicated as black points with their respective error bar while the single-bin statistical uncertainties (γ) are drawn with $\theta_0 = 0$ and without the pre-fit impact, as it is not properly defined.

The five highest-ranked nuisance parameters of the presented $t \to uX$ signal hypothesis fit include the 4j component of the different $t\bar{t}$+jets PS or $t\bar{t}$+light NLO matching, the $t\bar{t}$+$\geq$1c normalisation, the statistical component of the last bin of the 4j3b distributions or a component of the c-tagging efficiency. Regarding the $t \to cX$ fits, the five highest-ranked across masses include the $t\bar{t}$+$\geq$1b and $t\bar{t}$+$\geq$1c normalisations, components of the light- and c-tagging, 4j component of $t\bar{t}$+$\geq$1b PS/NLO and $t\bar{t}$+light PS, 5j component of $t\bar{t}$+$\geq$1b 5FS vs 4FS and the statistics of the mentioned bin.

Table 9.2 and Table 9.3 shows, for both $t \to qX$ processes, the impact on the signal strength evaluated in groups of systematic uncertainty sources for the 30, 80 and 120 GeV signal hypothesis fits. The total uncertainty is dominated by the systematic uncertainties, where $t\bar{t}$+$\geq$1b modelling dominates for all masses except $t \to uX$ at $m_X = 120$, where one of the b-tagging components dominates. In general, the $t\bar{t}$+$\geq$1b modelling dominates, followed by the modelling of the other two components or those from b-tagging.

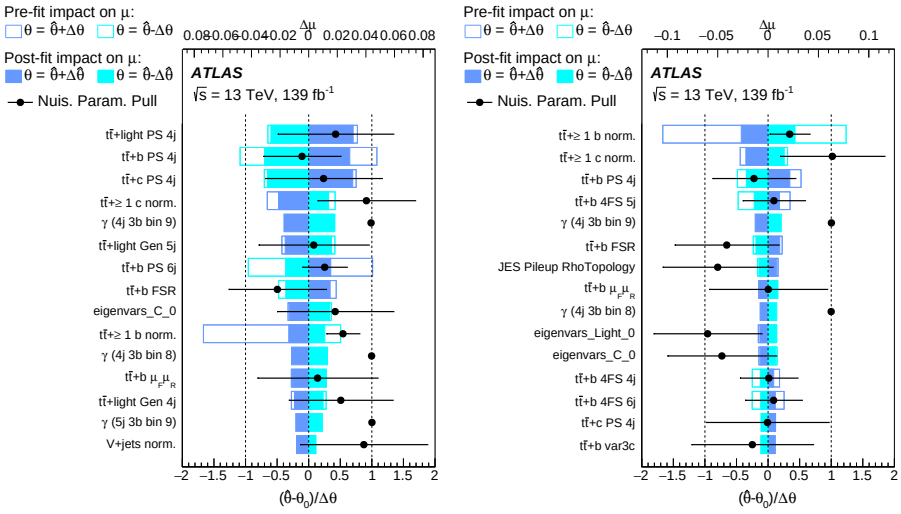

(a) $t \to uX$, $m_X = 30$ GeV **(b)** $t \to cX$, $m_X = 30$ GeV

(c) $t \to uX$, $m_X = 80$ GeV **(d)** $t \to cX$, $m_X = 80$ GeV

(e) $t \to uX$, $m_X = 120$ GeV **(f)** $t \to cX$, $m_X = 120$ GeV

Figure 9.6: Ranking of the 20 systematic uncertainties with the largest impact on μ for the fit performed with the 30 GeV (a, d), 80 GeV (b, e), 120 GeV (c, f) m_X hypothesis and both $t \to qX$ processes. The empty (filled) rectangles correspond to the pre-fit (post-fit) impact on μ. The black points represent the post-fit pulls of the nuisance parameters relative to the nominal values, θ_0. Statistical uncertainties (γ) are shown pulled with respect to 1.

Table 9.2: Summary of the statistical and systematic uncertainties on $\mu = \mathrm{B}(t \to uX)$ for the 30, 80 and 120 GeV X scalar mass hypothesis fits. Due to correlations between the different sources of uncertainty, the total systematic uncertainty can be different from the sum in quadrature of the individual sources.

Uncertainty source	$\Delta\mu(uX_{30})$	$\Delta\mu(uX_{80})$	$\Delta\mu(uX_{120})$
$t\bar{t}$+≥1b modelling	0.040	0.060	0.098
$t\bar{t}$+≥1c modelling	0.033	0.055	0.091
$t\bar{t}$+light modelling	0.034	0.058	0.040
$t\bar{t}$+≥1b normalisation	0.012	0.011	0.039
$t\bar{t}$+≥1c normalisation	0.017	0.036	0.087
$W \to cb$ modelling	0.001	0.010	0.017
Reweighting	0.005	0.013	0.017
Other backgrounds	0.008	0.026	0.023
Luminosity, JVT, pile-up	0.002	0.006	0.012
Lepton trigger, identification, isolation	0.001	0.004	0.007
Jet energy scale and resolution	0.008	0.037	0.040
b-tagging efficiency for b-jets	0.007	0.008	0.041
b-tagging efficiency for c-jets	0.014	0.027	0.079
b-tagging efficiency for light jets	0.007	0.008	0.010
$\mathrm{E}_{\mathrm{T}}^{\mathrm{miss}}$	0.002	0.010	0.011
Total systematic uncertainty	0.077	0.125	0.220
Signal statistical uncertainty	0.014	0.009	0.007
Total statistical uncertainty	0.064	0.070	0.065
Total uncertainty	0.098	0.141	0.230

Table 9.3: Summary of the statistical and systematic uncertainties on $\mu = \mathrm{B}(t \to cX)$ for the 30, 80 and 120 GeV X scalar mass hypothesis fits. Due to correlations between the different sources of uncertainty, the total systematic uncertainty can be different from the sum in quadrature of the individual sources.

Uncertainty source	$\Delta\mu(cX_{30})$	$\Delta\mu(cX_{80})$	$\Delta\mu(cX_{120})$
$t\bar{t}$+≥1b modelling	0.034	0.074	0.079
$t\bar{t}$+≥1c modelling	0.010	0.012	0.040
$t\bar{t}$+light modelling	0.008	0.049	0.038
$t\bar{t}$+≥1b normalisation	0.026	0.038	0.001
$t\bar{t}$+≥1c normalisation	0.019	0.048	0.013
$W \to cb$ modelling	0.001	0.020	0.015
Reweighting	0.005	0.013	0.019
Other backgrounds	0.009	0.057	0.047
Luminosity, JVT, pile-up	0.005	0.005	0.003
Lepton trigger, identification, isolation	0.001	0.004	0.003
Jet energy scale and resolution	0.017	0.049	0.051
b-tagging efficiency for b-jets	0.003	0.016	0.023
b-tagging efficiency for c-jets	0.010	0.038	0.091
b-tagging efficiency for light jets	0.009	0.065	0.125
$\mathrm{E}_{\mathrm{T}}^{\mathrm{miss}}$	0.001	0.003	0.008
Total systematic uncertainty	0.056	0.150	0.208
Signal statistical uncertainty	0.017	0.012	0.008
Total statistical uncertainty	0.064	0.067	0.058
Total uncertainty	0.079	0.162	0.217

9.2 Exclusion limits

No significant excess above the expected MC background is observed in all regions and mass intervals, hence upper limits on the signal production are derived as function of the X scalar mass.

Figure 9.7 shows the 95% confidence level (CL) upper limits on B($t \to uX$)×B($X \to b\bar{b}$) and B($t \to uX$)×B($X \to b\bar{b}$), obtained using the CL_S method. An excess of 1.8σ is seen in the $t \to uX$ channel at $m_X = 40$ GeV. Also, a roughly two-standard deviation excess can be seen in the $t \to cX$ observed limit over almost the entire range of m_X. As mentioned before, this excess is not compatible with the presence of a scalar particle X, which would show up as a narrower, resonance-like, excess in the limit plot.

The observed (expected) limits range from 0.019% (0.017%) to 0.062% (0.056%) for B($t \to uX$)×B($X \to b\bar{b}$) and from 0.018% (0.015%) to 0.078% (0.056%) for B($t \to cX$)×B($X \to b\bar{b}$).

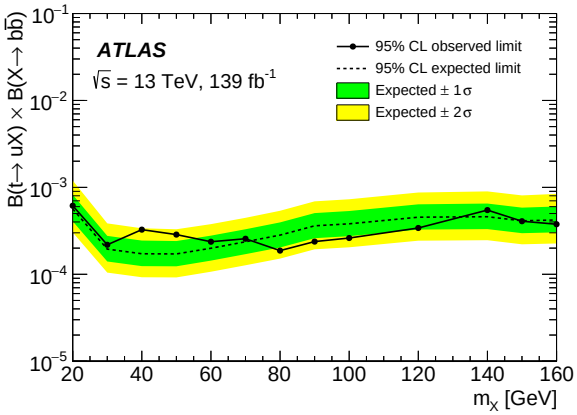

(a) $t \to uX$

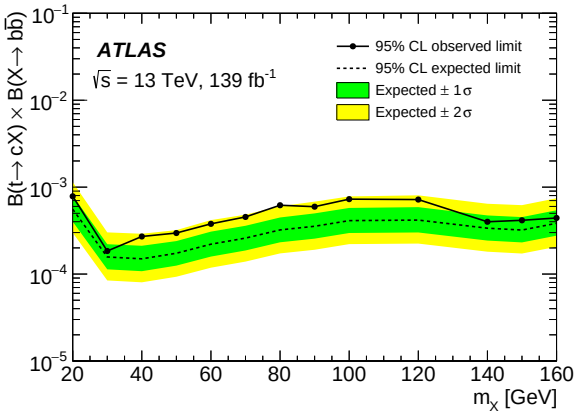

(b) $t \to uX$

Figure 9.7: Observed and expected upper limits for B($t \to uX$)×B($X \to b\bar{b}$) (a) and B($t \to uX$)×B($X \to b\bar{b}$) (b) as a function of the X scalar mass. The bands surrounding the expected limit show the 68% and 95% confidence intervals.

9.3 $t \to qH$ measurement

Two additional fits are performed for the $t \to uH$ and $t \to cH$ processes, involving the SM Higgs boson. The samples are simulated with the same generators as the rest of the signal samples: the $t\bar{t}$ pair is produced using the PowhegBox v2 generator interfaced to MadSpin and Pythia 8.2, with one of the tops decaying leptonically and the second one decaying to a charm or an up quark together with the Higgs boson. The Higgs is left to decay according to the SM branching ratios. Similarly, no sample of single top production in association with the Higgs boson has been included.

Thanks to the use of a parameterised NN, its evaluation using a mass hypothesis different from any of the signal samples used in the training is possible. The NN output scores for the $t \to uH$ and $t \to cH$ signal samples as well as the different background samples are evaluated using the mass hypothesis corresponding to the Higgs mass, $m_H = 125$ GeV. The performance of the NN is close to the evaluation at $m_X = 120$, and has to be close to ideal as the $m_H = 125$ GeV value is not far from the mass used in the training.

Two fits corresponding to the $t \to uH$ and $t \to cH$ hypotheses have been performed using the same method, regions and background modelling as for the rest of the hypotheses. The fitted μ is -0.19 ± 0.44 for $t \to uH$ and 0.51 ± 0.39 for $t \to uH$. Figure 9.8 shows the top ranked nuisance parameter for both the $t \to uH$ and $t \to cH$ fits. As expected, no big differences in pulls are observed when compared with the fits corresponding to the 120 GeV scalar mass hypothesis (Figure 9.6).

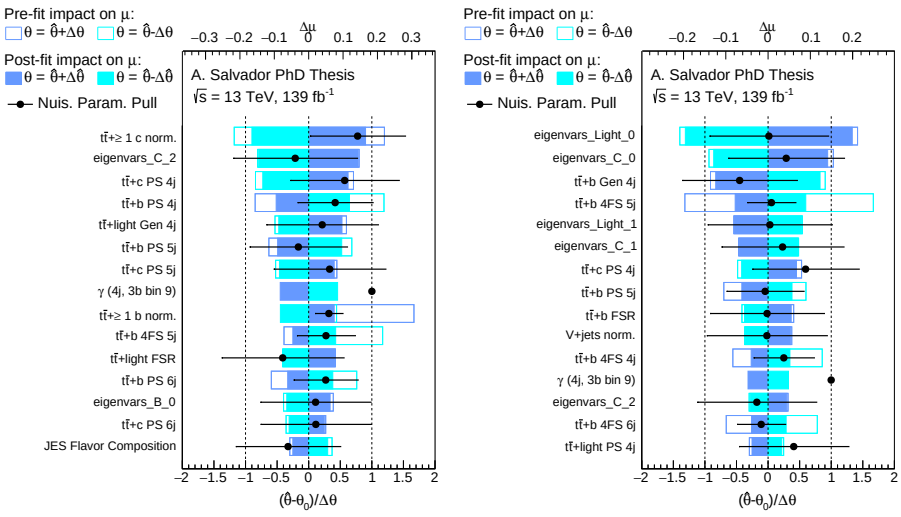

(a) $t \to uH$ **(b)** $t \to cH$

Figure 9.8: Ranking of the 20 systematic uncertainties with the largest impact on μ for the fit performed with the SM Higgs hypothesis and both $t \to qH$ processes. The empty (filled) rectangles correspond to the pre-fit (post-fit) impact on μ. The black points represent the post-fit pulls of the nuisance parameters relative to the nominal values, θ_0. Statistical uncertainties (γ) are shown pulled with respect 1.

Branching ratio upper limits for both $t \to uH$ and $t \to cH$ hypotheses have been extracted. The observed (expected) upper limits are 7.6×10^{-4} (11.8×10^{-4}) and 8.8×10^{-4} (7.7×10^{-4}) for B($t \to uH$) and B($t \to cH$), respectively. Figure 9.9 shows the upper limits for the $t \to uH$ and $t \to cH$ hypotheses including the fit results with the 125 GeV mass, which, only for illustrating the compatibility with the rest of the mass fits, have been scaled assuming a B(H$\to b\bar{b}$) = 100% instead of the SM branching ratio of 58%. A very good compatibility with a poor-man extrapolation from the 120 to 140 GeV mass fit results can be observed.

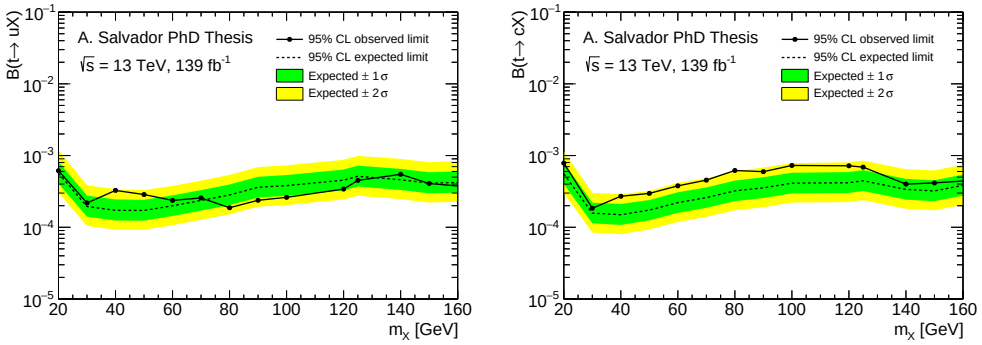

(a) $t \to uX$ **(b)** $t \to uX$

Figure 9.9: Observed and expected upper limits for B($t \to uX$)×B($X \to b\bar{b}$) (a) and B($t \to cX$)×B($X \to b\bar{b}$) (b) as a function of the X scalar mass. The bands surrounding the expected limit show the 68% and 95% confidence intervals. The upper limits corresponding to the Higgs boson mass hypothesis have been scaled down assuming B($H \to b\bar{b}$) = 100%.

Figure 9.10 shows a comparison of different upper limits results: the result of $t \to cX$ for the 120 GeV hypothesis, the $t \to cH$ result presented in this section, the CMS $t \to cH$ result with 137 fb^{-1} data [5], and the $t \to cH$ ATLAS result with 36 fb^{-1} data [248]. It should be noted that the $t \to cX$ upper limit assumes a B(X$\to b\bar{b}$) = 100%, while 58% is assumed for the SM Higgs decay.

Previously published results by ATLAS and CMS include the single-top signal sample in the analyses while, as mentioned above, this sample is not included in this analysis. The comparison is only presented for the decay involving the c-quark as the effect of including the single-top process is negligible. It can be observed that the expected limits obtained are on average a factor of three better than the previous ATLAS, scaled to the same integrated luminosity, and slightly better than the CMS results.

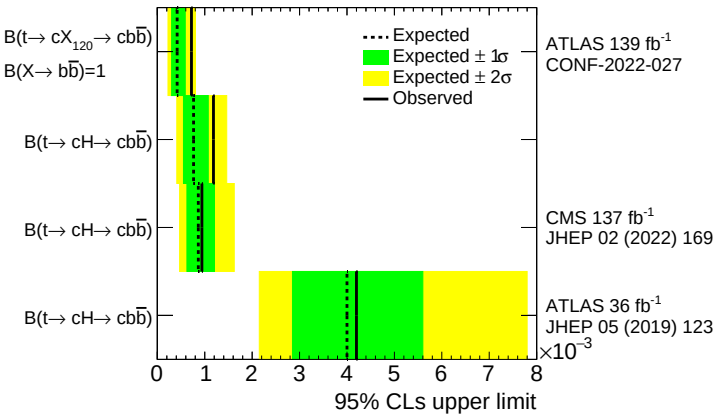

Figure 9.10: Expected and observed upper limits for the branching ratio of different $t \to cX$ results. The results shown include the $t \to cX$ results for the 120 GeV mass hypothesis, the $t \to cX$ result presented in this section and the $t \to cX$ published results from FCNC searches performed by CMS using 137 fb^{-1} and by ATLAS using 36 fb^{-1}. The bands surrounding the expected limits show the 68% and 95% confidence intervals.

10 Summary and conclusions

This dissertation presented two searches of new scalars leading to single-lepton final states with high b-jet multiplicity, using the data collected from proton-proton collisions by the ATLAS experiment at the LHC between 2015 and 2018, at a center-of-mass energy $\sqrt{s} = 13$ TeV for a total of 139 fb^{-1} integrated luminosity. The first analysis searches for a heavy charged Higgs boson decaying to a top and a bottom quarks, produced in association with top and bottom quarks. The second analysis searches for a FCNC decay process of a top to an up-type quark and a new neutral scalar, decaying into a pair of bottom quarks. The two searched processes are very different but share the final state and $t\bar{t}$+jets is a common dominant background. Hence, similar approaches are used for both analyses. Data-based corrections to the $t\bar{t}$ background are applied to improve its modelling, and the signal sensitivity is enhanced with the implementation of parameterised neural networks in regions where the signal is expected to be largest. The neural network output depends on the target neutral or charged scalar mass. A fit to the data is performed simultaneously in the analysis regions, separately for each signal type and mass. No significant excess above the expected Standard Model background is found and 95% confidence level upper limits on the production of the scalars are set.

For the first analysis, observed (expected) upper limits are set for the production cross-section $\sigma(pp \to tbH^+)$ times the branching fraction B($H^+ \to tb$), and range from $\sigma \times \mathrm{B} = 3.6(2.6)$ pb at $m_{H^+} = 200$ GeV to 0.036(0.019) pb at $m_{H^+} = 2$ TeV. The observed $\sigma \times$ B limits improve by 5% to 70%, depending on the H^+ mass, when compared to the previous ATLAS search with 36 fb^{-1}, except for the lowest mass. The improvements are achieved through increased statistics, tighter lepton triggers, improved b-tagging, and the parameterised neural networks. The limits at the low H^+ mass region are dominated by systematic uncertainties. In the context of the hMSSM model and several M_h^{125} scenarios, values of $\tan\beta \in [0.5, 2.1]$ are excluded for $m_{H^+} \in [200, 1200]$ GeV. In addition, values of $\tan\beta > 34$ are excluded for $m_{H^+} \in [200, 750]$ GeV. Compared to previous results, this analysis extends the exclusion at low and high $\tan\beta$ values, especially for high m_{H^+}. For the first time in literature, the analysis is interpreted in the context of a 2HDM+a model. Although the $E_{\mathrm{T}}^{\mathrm{miss}} + Z(\ell^+\ell^-)/h(b\bar{b})$ searches are the most sensitive ones to the model, this analysis contributes to the exclusion of high m_a values for up to intermediate values of m_{H^+} and low values of $\tan\beta$.

The $t \to qX$ analysis sets 95% CL the observed (expected) upper limits between 0.019% (0.017%) and 0.062% (0.056%) for the branching fraction B($t \to uX$)×B($X \to b\bar{b}$), and between 0.018% (0.015%) and 0.078% (0.056%) for the branching fraction B($t \to cX$) × B($X \to b\bar{b}$) in the explored mass range. The same analysis is used to derive limits for the branching fraction involving the SM Higgs boson, resulting in 95% confidence level upper limits of 0.077% (0.088%) for the observed (expected) B($t \to uH$) and 0.12% (0.076%) for the observed (expected) B($t \to cH$).

Bibliography

References in citation order.

[1] ATLAS Collaboration. 'Observation of a new particle in the search for the Standard Model Higgs boson with the ATLAS detector at the LHC'. In: *Physics Letters B* 716.1 (2012), pp. 1–29. DOI: 10.1016/j.physletb.2012.08.020 (cited on pages 1, 5).

[2] CMS Collaboration. 'Observation of a new boson at a mass of 125 GeV with the CMS experiment at the LHC'. In: *Physics Letters B* 716.1 (2012), pp. 30–61. DOI: 10.1016/j.physletb.2012.08.021 (cited on pages 1, 5).

[3] ATLAS Collaboration. 'Search for charged Higgs bosons decaying into top and bottom quarks at $\sqrt{s} = 13$ with the ATLAS detector'. In: *Journal of High Energy Physics* 2018.11 (2018). DOI: 10.1007/jhep11(2018)085 (cited on pages 1, 83, 124, 125).

[4] ATLAS Collaboration. 'Search for flavour-changing neutral current interactions of the top quark and the Higgs boson in events with a pair of τ-leptons in pp collisions at $\sqrt{s} = 13$ TeV with the ATLAS detector'. In: (2022). DOI: 10.48550/ARXIV.2208.11415 (cited on pages 2, 29, 135).

[5] CMS Collaboration. 'Search for flavor-changing neutral current interactions of the top quark and the Higgs boson decaying to a bottom quark-antiquark pair at $\sqrt{s} = 13$ TeV'. In: *JHEP* 02 (2022), p. 169. DOI: 10.1007/JHEP02(2022)169 (cited on pages 2, 135, 170).

[6] Steven Weinberg. 'A Model of Leptons'. In: *Phys. Rev. Lett.* 19 (21 1967), pp. 1264–1266. DOI: 10.1103/PhysRevLett.19.1264 (cited on page 5).

[7] Sheldon L. Glashow. 'Partial-symmetries of weak interactions'. In: *Nuclear Physics* 22.4 (1961), pp. 579–588. DOI: https://doi.org/10.1016/0029-5582(61)90469-2 (cited on page 5).

[8] Abdus Salam. 'Gauge unification of fundamental forces'. In: *Rev. Mod. Phys.* 52 (3 1980), pp. 525–538. DOI: 10.1103/RevModPhys.52.525 (cited on page 5).

[9] S. Abachi et al. 'Search for High Mass Top Quark Production in pp Collisions at s=1.8 TeV'. In: *Physical Review Letters* 74.13 (1995), pp. 2422–2426. DOI: 10.1103/physrevlett.74.2422 (cited on pages 5, 27).

[10] CDF Collaboration. 'Observation of Top Quark Production in $\bar{p}p$ Collisions with the Collider Detector at Fermilab'. In: *Phys. Rev. Lett.* 74 (14 1995), pp. 2626–2631. DOI: 10.1103/PhysRevLett.74.2626 (cited on pages 5, 27).

[11] H. Fritzsch, M. Gell-Mann, and H. Leutwyler. 'Advantages of the color octet gluon picture'. In: *Physics Letters B* 47.4 (1973), pp. 365–368. DOI: https://doi.org/10.1016/0370-2693(73)90625-4 (cited on page 5).

[12] Abdus Salam. 'Weak and Electromagnetic Interactions'. In: *Conf. Proc. C* 680519 (1968), pp. 367–377. DOI: 10.1142/9789812795915_0034 (cited on page 5).

[13] W. Pauli. 'Über den Zusammenhang des Abschlusses der Elektronengruppen im Atom mit der Komplexstruktur der Spektren'. In: *Zeitschrift für Physik* 31.1 (1925), pp. 765–783. DOI: 10.1007/BF02980631 (cited on page 5).

[14] Particle Data Group. 'Review of Particle Physics'. In: *PTEP* 2020.8 (2020), p. 083C01. DOI: 10.1093/ptep/ptaa104 (cited on pages 6, 7, 22, 27, 84).

[15] Emmy Noether. 'Invariant variation problems'. In: *Transport Theory and Statistical Physics* 1.3 (1971), pp. 186–207. DOI: 10.1080/00411457108231446 (cited on page 8).

[16] C. N. Yang and R. L. Mills. 'Conservation of Isotopic Spin and Isotopic Gauge Invariance'. In: *Phys. Rev.* 96 (1 1954), pp. 191–195. DOI: 10.1103/PhysRev.96.191 (cited on page 9).

[17] Murray Gell-Mann. 'Symmetries of Baryons and Mesons'. In: *Phys. Rev.* 125 (3 1962), pp. 1067–1084. DOI: 10.1103/PhysRev.125.1067 (cited on page 10).

[18] C. Abel et al. 'Measurement of the Permanent Electric Dipole Moment of the Neutron'. In: *Phys. Rev. Lett.* 124 (8 2020), p. 081803. DOI: 10.1103/PhysRevLett.124.081803 (cited on pages 11, 31).

[19] H. David Politzer. 'Reliable Perturbative Results for Strong Interactions?' In: *Phys. Rev. Lett.* 30 (26 1973), pp. 1346–1349. DOI: 10.1103/PhysRevLett.30.1346 (cited on page 11).

[20] David J. Gross and Frank Wilczek. 'Ultraviolet Behavior of Non-Abelian Gauge Theories'. In: *Phys. Rev. Lett.* 30 (26 1973), pp. 1343–1346. DOI: 10.1103/PhysRevLett.30.1343 (cited on page 11).

[21] T. D. Lee and C. N. Yang. 'Question of Parity Conservation in Weak Interactions'. In: *Phys. Rev.* 104 (1 1956), pp. 254–258. DOI: 10.1103/PhysRev.104.254 (cited on page 14).

[22] C. S. Wu et al. 'Experimental Test of Parity Conservation in Beta Decay'. In: *Phys. Rev.* 105 (4 1957), pp. 1413–1415. DOI: 10.1103/PhysRev.105.1413 (cited on page 14).

[23] Peter W. Higgs. 'Broken Symmetries and the Masses of Gauge Bosons'. In: *Phys. Rev. Lett.* 13 (16 1964), pp. 508–509. DOI: 10.1103/PhysRevLett.13.508 (cited on page 18).

[24] P.W. Higgs. 'Broken symmetries, massless particles and gauge fields'. In: *Physics Letters* 12.2 (1964), pp. 132–133. DOI: https://doi.org/10.1016/0031-9163(64)91136-9 (cited on page 18).

[25] F. Englert and R. Brout. 'Broken Symmetry and the Mass of Gauge Vector Mesons'. In: *Phys. Rev. Lett.* 13 (9 1964), pp. 321–323. DOI: 10.1103/PhysRevLett.13.321 (cited on page 18).

[26] Hideki Yukawa. 'On the Interaction of Elementary Particles. I'. In: *Progress of Theoretical Physics Supplement* 1 (Jan. 1955), pp. 1–10. DOI: 10.1143/PTPS.1.1 (cited on page 20).

[27] Nicola Cabibbo. 'Unitary Symmetry and Leptonic Decays'. In: *Phys. Rev. Lett.* 10 (12 1963), pp. 531–533. DOI: 10.1103/PhysRevLett.10.531 (cited on page 22).

[28] Makoto Kobayashi and Toshihide Maskawa. 'CP Violation in the Renormalizable Theory of Weak Interaction'. In: *Prog. Theor. Phys.* 49 (1973), pp. 652–657. DOI: 10.1143/PTP.49.652 (cited on page 22).

[29] Ling-Lie Chau and Wai-Yee Keung. 'Comments on the Parametrization of the Kobayashi-Maskawa Matrix'. In: *Phys. Rev. Lett.* 53 (19 1984), pp. 1802–1805. DOI: 10.1103/PhysRevLett.53.1802 (cited on page 22).

[30] S. L. Glashow, J. Iliopoulos, and L. Maiani. 'Weak Interactions with Lepton-Hadron Symmetry'. In: *Phys. Rev. D* 2 (7 1970), pp. 1285–1292. DOI: 10.1103/PhysRevD.2.1285 (cited on page 23).

[31] ATLAS Collaboration. *Standard Model Summary Plots February 2022*. Geneva, 2022. URL: http://cds.cern.ch/record/2804061 (cited on page 26).

[32] ATLAS Collaboration. 'A detailed map of Higgs boson interactions by the ATLAS experiment ten years after the discovery'. In: *Nature* 607.7917 (2022), pp. 52–59. DOI: 10.1038/s41586-022-04893-w (cited on page 26).

[33] ATLAS Collaboration. *Top working group cross-section summary plots June 2022*. Geneva, 2022. URL: http://cds.cern.ch/record/2812502 (cited on page 28).

[34] J. A. Aguilar-Saavedra. 'Top flavour-changing neutral interactions: theoretical expectations and experimental detection'. In: (2004). DOI: 10.48550/ARXIV.HEP-PH/0409342 (cited on page 29).

[35] ATLAS Collaboration. 'Search for flavour-changing neutral-current couplings between the top quark and the photon with the ATLAS detector at 13 TeV'. In: *Physics Letters B* (2022), p. 137379. DOI: 10.1016/j.physletb.2022.137379 (cited on pages 29, 135).

[36] ATLAS Collaboration. 'Search for flavour-changing neutral-current interactions of a top quark and a gluon in pp collisions at 13 TeV with the ATLAS detector'. In: *The European Physical Journal C* 82.4 (2022), p. 334. DOI: 10.1140/epjc/s10052-022-10182-7 (cited on page 29).

[37] CMS Collaboration. 'Search for anomalous single top quark production in association with a photon in pp collisions at $\sqrt{s} = 8$ TeV'. In: *Journal of High Energy Physics* 2016.4 (2016). DOI: 10.1007/jhep04(2016)035 (cited on pages 29, 135).

[38] CMS Collaboration. 'Search for anomalous Wtb couplings and flavour-changing neutral currents in t-channel single top quark production in pp collisions at 7 and 8 TeV'. In: *Journal of High Energy Physics* 2017.2 (2017), p. 28. DOI: 10.1007/JHEP02(2017)028 (cited on page 29).

[39] CMS Collaboration. *Search for flavour changing neutral currents in top quark production and decays with three-lepton final state using the data collected at sqrt(s) = 13 TeV*. Geneva, 2017. URL: https://cds.cern.ch/record/2292045 (cited on pages 29, 135).

[40] CMS Collaboration. 'Search for Flavor-Changing Neutral Current Interactions of the Top Quark and Higgs Boson in Final States with Two Photons in Proton-Proton Collisions at $\sqrt{s} = 13$ TeV'. In: *Phys. Rev. Lett.* 129 (3 2022), p. 032001. DOI: 10.1103/PhysRevLett.129.032001 (cited on page 29).

[41] K. Abe et al. 'Atmospheric neutrino oscillation analysis with external constraints in Super-Kamiokande I-IV'. In: *Physical Review D* 97.7 (2018). DOI: 10.1103/physrevd.97.072001 (cited on page 29).

[42] Ettore Majorana and Luciano Maiani. 'A symmetric theory of electrons and positrons'. In: *Ettore Majorana Scientific Papers: On occasion of the centenary of his birth*. Ed. by Giuseppe Franco Bassani. Berlin, Heidelberg: Springer Berlin Heidelberg, 2006, pp. 201–233. DOI: 10.1007/978-3-540-48095-2_10 (cited on page 29).

[43] Ziro Maki, Masami Nakagawa, and Shoichi Sakata. 'Remarks on the Unified Model of Elementary Particles'. In: *Progress of Theoretical Physics* 28.5 (Nov. 1962), pp. 870–880. DOI: 10.1143/PTP.28.870 (cited on page 29).

[44] B. Pontecorvo. 'Neutrino Experiments and the Problem of Conservation of Leptonic Charge'. In: *Zh. Eksp. Teor. Fiz.* 53 (1967), pp. 1717–1725 (cited on page 29).

[45] Muon g 2 Collaboration. 'Measurement of the Positive Muon Anomalous Magnetic Moment to 0.46 ppm'. In: *Phys. Rev. Lett.* 126 (14 2021), p. 141801. DOI: 10.1103/PhysRevLett.126.141801 (cited on page 30).

[46] F. Zwicky. 'Republication of: The redshift of extragalactic nebulae'. In: *General Relativity and Gravitation* 41.1 (2009), pp. 207–224. DOI: 10.1007/s10714-008-0707-4 (cited on page 30).

[47] A. Bosma. '21-cm line studies of spiral galaxies. II. The distribution and kinematics of neutral hydrogen in spiral galaxies of various morphological types.' In: *The Astronomical Journal* 86 (Dec. 1981), pp. 1825–1846. DOI: 10.1086/113063 (cited on page 30).

[48] Keiichi Umetsu et al. 'CLASH: JOINT ANALYSIS OF STRONG-LENSING, WEAK-LENSING SHEAR, AND MAGNIFICATION DATA FOR 20 GALAXY CLUSTERS*'. In: *The Astrophysical Journal* 821.2 (2016), p. 116. DOI: 10.3847/0004-637X/821/2/116 (cited on page 30).

[49] C. L. Bennett et al. 'NINE-YEAR WILKINSON MICROWAVE ANISOTROPY PROBE (WMAP) OBSERVATIONS: FINAL MAPS AND RESULTS'. In: *The Astrophysical Journal Supplement Series* 208.2 (2013), p. 20. DOI: 10.1088/0067-0049/208/2/20 (cited on page 30).

[50] Planck Collaboration. 'Planck 2018 results'. In: *Astronomy & Astrophysics* 641 (2020), A6. DOI: 10.1051/0004-6361/201833910 (cited on page 30).

[51] Edwin Hubble. 'A Relation between Distance and Radial Velocity among Extra-Galactic Nebulae'. In: *Proceedings of the National Academy of Science* 15.3 (Mar. 1929), pp. 168–173. DOI: 10.1073/pnas.15.3.168 (cited on page 30).

[52] A. Djouadi et al. 'Fully covering the MSSM Higgs sector at the LHC'. In: (2015). DOI: 10.48550/ARXIV.1502.05653 (cited on page 33).

[53] Emanuele Bagnaschi et al. 'MSSM Higgs boson searches at the LHC: benchmark scenarios for Run 2 and beyond'. In: *The European Physical Journal C* 79.7 (2019). DOI: 10.1140/epjc/s10052-019-7114-8 (cited on page 33).

[54] Lyndon Evans and Philip Bryant. 'LHC Machine'. In: *Journal of Instrumentation* 3.08 (2008), S08001–S08001. DOI: 10.1088/1748-0221/3/08/s08001 (cited on page 35).

[55] ATLAS Collaboration. 'The ATLAS Experiment at the CERN Large Hadron Collider'. In: *Journal of Instrumentation* 3.08 (2008), S08003–S08003. DOI: 10.1088/1748-0221/3/08/s08003 (cited on page 35).

[56] Esma Mobs. *The CERN accelerator complex - August 2018. Complexe des accélérateurs du CERN - Août 2018*. General Photo. 2018. URL: http://cds.cern.ch/record/2636343 (cited on page 36).

[57] CERN. *Diagram of an LHC dipole magnet. Schéma d'un aimant dipôle du LHC*. 1999. URL: https://cds.cern.ch/record/40524 (cited on page 37).

[58] CMS Collaboration. 'The CMS experiment at the CERN LHC'. In: *Journal of Instrumentation* 3.08 (2008), S08004–S08004. DOI: 10.1088/1748-0221/3/08/s08004 (cited on page 37).

[59] LHCb Collaboration. 'The LHCb Detector at the LHC'. In: *Journal of Instrumentation* 3.08 (2008), S08005–S08005. DOI: 10.1088/1748-0221/3/08/s08005 (cited on page 37).

[60] ALICE Collaboration. 'The ALICE experiment at the CERN LHC'. In: *Journal of Instrumentation* 3.08 (2008), S08002–S08002. DOI: 10.1088/1748-0221/3/08/s08002 (cited on page 37).

[61] Stephen Myers. 'The LEP Collider, from design to approval and commissioning'. In: John Adams' memorial lecture (1991). Delivered at CERN, 26 Nov 1990. DOI: 10.5170/CERN-1991-008 (cited on page 37).

[62] ATLAS Collaboration. *Luminosity determination in pp collisions at $\sqrt{s} = 13$ TeV using the ATLAS detector at the LHC*. Geneva, 2019. URL: https://cds.cern.ch/record/2677054 (cited on pages 38, 105).

[63] ATLAS Collaboration. *Luminosity Public Results for Run-2*. URL: https://twiki.cern.ch/twiki/bin/view/AtlasPublic/LuminosityPublicResultsRun2 (cited on page 39).

[64] ATLAS Collaboration. *Luminosity Public Results for Run-1*. URL: https://twiki.cern.ch/twiki/bin/view/AtlasPublic/LuminosityPublicResults (cited on page 39).

[65] The ATLAS Collaboration. 'The ATLAS Experiment at the CERN Large Hadron Collider'. In: *Journal of Instrumentation* 3.08 (2008), S08003–S08003. DOI: 10.1088/1748-0221/3/08/s08003 (cited on pages 40, 42, 44–46).

[66] ATLAS Collaboration. *ATLAS inner detector: Technical Design Report, 1*. Geneva, 1997. URL: https://cds.cern.ch/record/331063 (cited on page 41).

[67] ATLAS Collaboration. *ATLAS inner detector: Technical Design Report, 2*. Geneva, 1997. URL: https://cds.cern.ch/record/331064 (cited on page 41).

[68] Karolos Potamianos. 'The upgraded Pixel detector and the commissioning of the Inner Detector tracking of the ATLAS experiment for Run-2 at the Large Hadron Collider'. In: (2016). DOI: 10.48550/ARXIV.1608.07850 (cited on page 41).

[69] ATLAS Collaboration. *ATLAS Insertable B-Layer Technical Design Report*. 2010. URL: https://cds.cern.ch/record/1291633 (cited on page 42).

[70] ATLAS Collaboration. 'Technical Design Report for the ATLAS Inner Tracker Pixel Detector'. In: (2017). DOI: 10.17181/CERN.FOZZ.ZP3Q (cited on page 42).

[71] Carl Haber. 'The ATLAS Semiconductor Tracker'. In: *Nuclear Instruments and Methods in Physics Research Section A: Accelerators, Spectrometers, Detectors and Associated Equipment* 409.1 (1998), pp. 161–166. DOI: https://doi.org/10.1016/S0168-9002(97)01256-4 (cited on page 42).

[72] ATLAS Collaboration. 'Operation and performance of the ATLAS semiconductor tracker in LHC Run 2'. In: (2021). DOI: 10.48550/ARXIV.2109.02591 (cited on page 42).

[73] ATLAS TRT Collaboration. 'The ATLAS Transition Radiation Tracker'. In: *Astroparticle, Particle and Space Physics, Detectors and Medical Physics Applications*. WORLD SCIENTIFIC, 2004. DOI: 10.1142/9789812702708_0073 (cited on page 43).

[74] ATLAS Collaboration. 'Performance of the ATLAS Transition Radiation Tracker in Run 1 of the LHC: tracker properties'. In: *Journal of Instrumentation* 12.05 (2017), P05002–P05002. DOI: 10.1088/1748-0221/12/05/p05002 (cited on page 43).

[75] ATLAS Collaboration. 'ATLAS liquid-argon calorimeter: Technical Design Report'. In: Technical design report. ATLAS (1996). DOI: 10.17181/CERN.FWRW.FOOQ (cited on page 43).

[76] ATLAS Collaboration. 'ATLAS Liquid Argon Calorimeter Phase-II Upgrade: Technical Design Report'. In: (2017). DOI: 10.17181/CERN.6QIO.YGHO (cited on page 43).

[77] ATLAS Collaboration. 'ATLAS tile calorimeter: Technical Design Report'. In: Technical design report. ATLAS (1996). DOI: 10.17181/CERN.JRBJ.7O28 (cited on page 43).

[78] ATLAS Collaboration. 'The ATLAS Forward Calorimeter'. In: *Journal of Instrumentation* 3.02 (2008), P02010–P02010. DOI: 10.1088/1748-0221/3/02/p02010 (cited on page 45).

[79] ATLAS Collaboration. *ATLAS muon spectrometer: Technical Design Report*. Geneva, 1997. URL: https://cds.cern.ch/record/331068 (cited on page 45).

[80] ATLAS muon Collaboration. *ATLAS Muon Detector Commissioning*. 2009. DOI: 10.48550/ARXIV.0910.2767. URL: https://arxiv.org/abs/0910.2767 (cited on page 45).

[81] J.J. Goodson. 'Search for Supersymmetry in States with Large Missing Transverse Momentum and Three Leptons including a Z-Boson'. Presented 17 Apr 2012. PhD thesis. Stony Brook University, 2012 (cited on page 47).

[82] ATLAS Collaboration. *ATLAS high-level trigger, data-acquisition and controls: Technical Design Report*. Geneva, 2003. URL: https://cds.cern.ch/record/616089 (cited on page 47).

[83] ATLAS Collaboration. 'The Run-2 ATLAS Trigger System'. In: (2016). DOI: 10.1088/1742-6596/762/1/012003 (cited on page 47).

[84] ATLAS Collaboration. *Public DAQ/HLT plots for Run-2*. URL: https://twiki.cern.ch/twiki/bin/view/AtlasPublic/ApprovedPlotsDAQ (cited on page 48).

[85] T Gleisberg et al. 'Event generation with SHERPA 1.1'. In: *Journal of High Energy Physics* 2009.02 (2009), pp. 007–007. DOI: 10.1088/1126-6708/2009/02/007 (cited on page 50).

[86] J C Collins and D E Soper. 'The Theorems of Perturbative QCD'. In: *Annual Review of Nuclear and Particle Science* 37.1 (1987), pp. 383–409. DOI: 10.1146/annurev.ns.37.120187.002123 (cited on page 51).

[87] V. N. Gribov and L. N. Lipatov. 'Deep inelastic e p scattering in perturbation theory'. In: *Sov. J. Nucl. Phys.* 15 (1972), pp. 438–450 (cited on page 51).

[88] G. Altarelli and G. Parisi. 'Asymptotic freedom in parton language'. In: *Nuclear Physics B* 126.2 (1977), pp. 298–318. DOI: https://doi.org/10.1016/0550-3213(77)90384-4 (cited on page 51).

[89] Yuri L. Dokshitzer. 'Calculation of the Structure Functions for Deep Inelastic Scattering and e+ e- Annihilation by Perturbation Theory in Quantum Chromodynamics.' In: *Sov. Phys. JETP* 46 (1977), pp. 641–653 (cited on page 51).

[90] Manjunath Bhat et al. 'Flavor nonsinglet parton distribution functions from lattice QCD at physical quark masses via the pseudodistribution approach'. In: *Physical Review D* 103.3 (2021). DOI: 10.1103/physrevd.103.034510 (cited on page 51).

[91] Richard D. Ball et al. 'Parton distributions for the LHC run II'. In: *Journal of High Energy Physics* 2015.4 (2015). DOI: 10.1007/jhep04(2015)040 (cited on pages 51, 110).

[92] M. R. Whalley, D. Bourilkov, and R. C. Group. *The Les Houches Accord PDFs (LHAPDF) and Lhaglue*. 2005. DOI: 10.48550/ARXIV.HEP-PH/0508110. URL: https://arxiv.org/abs/hep-ph/0508110 (cited on page 51).

[93] A. D. Martin et al. 'Parton distributions for the LHC'. In: *The European Physical Journal C* 63.2 (2009), pp. 189–285. DOI: 10.1140/epjc/s10052-009-1072-5 (cited on pages 51, 109).

[94] Richard D. Ball et al. 'Parton distributions from high-precision collider data'. In: *The European Physical Journal C* 77.10 (2017). DOI: 10.1140/epjc/s10052-017-5199-5 (cited on page 52).

[95] Toichiro Kinoshita and Akira Ukawa. 'Mass singularities of Feynman amplitudes'. In: *International Symposium on Mathematical Problems in Theoretical Physics*. Ed. by Huzihiro Araki. Berlin, Heidelberg: Springer Berlin Heidelberg, 1975, pp. 55–58 (cited on page 53).

[96] T. D. Lee and M. Nauenberg. 'Degenerate Systems and Mass Singularities'. In: *Phys. Rev.* 133 (6B 1964), B1549–B1562. DOI: 10.1103/PhysRev.133.B1549 (cited on page 53).

[97] Geoffrey C. Fox and Stephen Wolfram. 'A model for parton showers in QCD'. In: *Nuclear Physics B* 168.2 (1980), pp. 285–295. DOI: https://doi.org/10.1016/0550-3213(80)90111-X (cited on page 53).

[98] Torbjörn Sjöstrand. 'A model for initial state parton showers'. In: *Physics Letters B* 157.4 (1985), pp. 321–325. DOI: https://doi.org/10.1016/0370-2693(85)90674-4 (cited on page 53).

[99] B. Andersson et al. 'Parton fragmentation and string dynamics'. In: *Physics Reports* 97.2 (1983), pp. 31–145. DOI: https://doi.org/10.1016/0370-1573(83)90080-7 (cited on page 53).

[100] J.-C. Winter, F. Krauss, and G. Soff. 'A modified cluster-hadronisation model'. In: *The European Physical Journal C - Particles and Fields* 36.3 (2004), pp. 381–395. DOI: 10.1140/epjc/s2004-01960-8 (cited on page 53).

[101] Torbjörn Sjöstrand et al. 'An introduction to PYTHIA 8.2'. In: *Computer Physics Communications* 191 (2015), pp. 159–177. DOI: https://doi.org/10.1016/j.cpc.2015.01.024 (cited on page 54).

[102] Manuel Bähr et al. 'Herwig++ physics and manual'. In: *The European Physical Journal C* 58.4 (2008), pp. 639–707. DOI: 10.1140/epjc/s10052-008-0798-9 (cited on page 54).

[103] Johannes Bellm et al. 'Herwig 7.0/Herwig++ 3.0 release note'. In: *The European Physical Journal C* 76.4 (2016), p. 196. DOI: 10.1140/epjc/s10052-016-4018-8 (cited on page 54).

[104] Enrico Bothmann et al. 'Event Generation with Sherpa 2.2'. In: *SciPost Phys.* 7 (3 2019), p. 34. DOI: 10.21468/SciPostPhys.7.3.034 (cited on page 54).

[105] Paolo Nason. 'A New Method for Combining NLO QCD with Shower Monte Carlo Algorithms'. In: *Journal of High Energy Physics* 2004.11 (2004), pp. 040–040. DOI: 10.1088/1126-6708/2004/11/040 (cited on page 54).

[106] Stefano Frixione, Paolo Nason, and Carlo Oleari. 'Matching NLO QCD computations with parton shower simulations: the POWHEG method'. In: *Journal of High Energy Physics* 2007.11 (2007), pp. 070–070. DOI: 10.1088/1126-6708/2007/11/070 (cited on page 54).

[107] Simone Alioli et al. 'A general framework for implementing NLO calculations in shower Monte Carlo programs: the POWHEG BOX'. In: *Journal of High Energy Physics* 2010.6 (2010), p. 43. DOI: 10.1007/JHEP06(2010)043 (cited on page 54).

[108] H. B. Hartanto et al. 'Higgs boson production in association with top quarks in the POWHEG BOX'. In: *Phys. Rev. D* 91 (9 2015), p. 094003. DOI: 10.1103/PhysRevD.91.094003 (cited on page 54).

[109] Stefano Frixione, Giovanni Ridolfi, and Paolo Nason. 'A positive-weight next-to-leading-order Monte Carlo for heavy flavour hadroproduction'. In: *Journal of High Energy Physics* 2007.09 (2007), pp. 126–126. DOI: 10.1088/1126-6708/2007/09/126 (cited on page 54).

[110] Johan Alwall et al. 'MadGraph/MadEvent v4: the new web generation'. In: *Journal of High Energy Physics* 2007.09 (2007), pp. 028–028. DOI: 10.1088/1126-6708/2007/09/028 (cited on page 54).

[111] *ATLAS Pythia 8 tunes to 7 TeV data*. Geneva, 2014. URL: https://cds.cern.ch/record/1966419 (cited on page 54).

[112] Richard D. Ball et al. 'Parton distributions with LHC data'. In: *Nuclear Physics B* 867.2 (2013), pp. 244–289. DOI: https://doi.org/10.1016/j.nuclphysb.2012.10.003 (cited on page 54).

[113] L. A. Harland-Lang et al. 'Parton distributions in the LHC era: MMHT 2014 PDFs'. In: *The European Physical Journal C* 75.5 (2015), p. 204. DOI: 10.1140/epjc/s10052-015-3397-6 (cited on page 54).

[114] David J. Lange. 'The EvtGen particle decay simulation package'. In: *Nuclear Instruments and Methods in Physics Research Section A: Accelerators, Spectrometers, Detectors and Associated Equipment* 462.1 (2001). BEAUTY2000, Proceedings of the 7th Int. Conf. on B-Physics at Hadron Machines, pp. 152–155. DOI: https://doi.org/10.1016/S0168-9002(01)00089-4 (cited on page 54).

[115] ATLAS Collaboration. 'The ATLAS Simulation Infrastructure'. In: *The European Physical Journal C* 70.3 (2010), pp. 823–874. DOI: 10.1140/epjc/s10052-010-1429-9 (cited on page 55).

[116] S. Agostinelli et al. 'Geant4—a simulation toolkit'. In: *Nuclear Instruments and Methods in Physics Research Section A: Accelerators, Spectrometers, Detectors and Associated Equipment* 506.3 (2003), pp. 250–303. DOI: https://doi.org/10.1016/S0168-9002(03)01368-8 (cited on page 55).

[117] ATLAS Collaboration. *The simulation principle and performance of the ATLAS fast calorimeter simulation FastCaloSim*. Geneva, 2010. URL: https://cds.cern.ch/record/1300517 (cited on page 55).

[118] K Edmonds et al. *The Fast ATLAS Track Simulation (FATRAS)*. Geneva, 2008. URL: https://cds.cern.ch/record/1091969 (cited on page 55).

[119] Joao Pequenao and Paul Schaffner. 'How ATLAS detects particles: diagram of particle paths in the detector'. 2013 (cited on page 57).

[120] Matteo Cacciari, Gavin P Salam, and Gregory Soyez. 'The anti-kt jet clustering algorithm'. In: *Journal of High Energy Physics* 2008.04 (2008), pp. 063–063. DOI: 10.1088/1126-6708/2008/04/063 (cited on pages 59, 60).

[121] ATLAS Collaboration. 'Jet energy scale measurements and their systematic uncertainties in proton-proton collisions at $\sqrt{s}$ = 13 TeV with the ATLAS detector'. In: *Phys. Rev. D* 96 (7 2017), p. 072002. DOI: 10.1103/PhysRevD.96.072002 (cited on page 60).

[122] Matteo Cacciari, Gavin P. Salam, and Gregory Soyez. 'FastJet user manual'. In: *The European Physical Journal C* 72.3 (2012), p. 1896. DOI: 10.1140/epjc/s10052-012-1896-2 (cited on page 60).

[123] ATLAS Collaboration. 'Jet energy scale and resolution measured in proton-proton collisions at $\sqrt{s}$ = 13 TeV with the ATLAS detector'. In: (2020). DOI: 10.1140/epjc/s10052-021-09402-3 (cited on page 61).

[124] ATLAS Collaboration. 'Jet reconstruction and performance using particle flow with the ATLAS Detector'. In: *The European Physical Journal C* 77.7 (2017), p. 466. DOI: 10.1140/epjc/s10052-017-5031-2 (cited on page 61).

[125] ATLAS Collaboration. 'Jet energy scale and resolution measured in proton-proton collisions at $\sqrt{s}$ = 13 TeV with the ATLAS detector'. In: (July 2020) (cited on page 61).

[126] *Expected performance of the ATLAS b-tagging algorithms in Run-2*. Geneva, 2015. URL: http://cds.cern.ch/record/2037697 (cited on page 62).

[127] ATLAS Collaboration. *Expected performance of the 2019 ATLAS b-taggers*. 2019. URL: http://atlas.web.cern.ch/Atlas/GROUPS/PHYSICS/PLOTS/FTAG-2019-005/ (cited on pages 62, 64).

[128] ATLAS Collaboration. 'Electron and photon performance measurements with the ATLAS detector using the 2015–2017 LHC proton-proton collision data'. In: *Journal of Instrumentation* 14.12 (2019), P12006–P12006. DOI: 10.1088/1748-0221/14/12/p12006 (cited on page 65).

[129] 'Muon reconstruction performance of the ATLAS detector in proton–proton collision data at 13 TeV'. In: *The European Physical Journal C* 76.5 (2016), p. 292. DOI: 10.1140/epjc/s10052-016-4120-y (cited on page 65).

[130] ATLAS Collaboration. *Measurement of the tau lepton reconstruction and identification performance in the ATLAS experiment using pp collisions at 13 TeV*. Geneva, 2017. URL: https://cds.cern.ch/record/2261772 (cited on page 67).

[131] ATLAS Liquid Argon Calorimeter group. 'Machine Learning for Real-Time Processing of ATLAS Liquid Argon Calorimeter Signals with FPGAs'. In: *PoS* EPS-HEP2021 (2022), p. 752. DOI: 10.22323/1.398.0752 (cited on page 69).

[132] ATLAS Collaboration. *Identification of hadronic tau lepton decays using neural networks in the ATLAS experiment*. Geneva, 2019. URL: https://cds.cern.ch/record/2688062 (cited on page 69).

[133] ATLAS Collaboration. *Deep Sets based Neural Networks for Impact Parameter Flavour Tagging in ATLAS*. Geneva, 2020. URL: https://cds.cern.ch/record/2718948 (cited on page 69).

[134] 'Cross-Validation'. In: *Encyclopedia of Machine Learning*. Ed. by Claude Sammut and Geoffrey I. Webb. Boston, MA: Springer US, 2010. DOI: 10.1007/978-0-387-30164-8_190 (cited on page 71).

[135] Shie Mannor, Dori Peleg, and Reuven Rubinstein. 'The cross entropy method for classification'. In: Jan. 2005, pp. 561–568. DOI: 10.1145/1102351.1102422 (cited on page 71).

[136] Warren S. McCulloch and Walter Pitts. 'A logical calculus of the ideas immanent in nervous activity'. In: *The bulletin of mathematical biophysics* 5.4 (1943), pp. 115–133. DOI: 10.1007/BF02478259 (cited on page 72).

[137] Ian Goodfellow, Yoshua Bengio, and Aaron Courville. *Deep Learning*. http://www.deeplearningbook.org. MIT Press, 2016 (cited on page 73).

[138] Matthew Feickert and Benjamin Nachman. *A Living Review of Machine Learning for Particle Physics*. 2021. DOI: 10.48550/ARXIV.2102.02770. URL: https://arxiv.org/abs/2102.02770 (cited on page 73).

[139] Adam Paszke et al. 'PyTorch: An Imperative Style, High-Performance Deep Learning Library'. In: *Advances in Neural Information Processing Systems 32*. Curran Associates, Inc., 2019, pp. 8024–8035 (cited on page 73).

[140] Martín Abadi et al. *TensorFlow: Large-Scale Machine Learning on Heterogeneous Systems*. Software available from tensorflow.org. 2015. URL: https://www.tensorflow.org/ (cited on page 73).

[141] Francois Chollet et al. *Keras*. 2015. URL: https://github.com/fchollet/keras (cited on pages 73, 98).

[142] Daniel Hay Guest et al. 'lwtnn/lwtnn: Version 2.13'. In: (2022). DOI: 10.5281/zenodo.6467676 (cited on page 73).

[143] Samuel L. Smith et al. *Don't Decay the Learning Rate, Increase the Batch Size*. 2017. DOI: 10.48550/ARXIV.1711.00489. URL: https://arxiv.org/abs/1711.00489 (cited on page 74).

[144] Diederik P. Kingma and Jimmy Ba. 'Adam: A Method for Stochastic Optimization'. In: *CoRR* abs/1412.6980 (2015) (cited on page 74).

[145] David E. Rumelhart, Geoffrey E. Hinton, and Ronald J. Williams. 'Learning representations by back-propagating errors'. In: *Nature* 323.6088 (1986), pp. 533–536. DOI: 10.1038/323533a0 (cited on page 74).

[146] Abien Fred Agarap. 'Deep learning using rectified linear units (relu)'. In: *arXiv:1803.08375* (2018) (cited on page 74).

[147] Bing Xu et al. *Empirical Evaluation of Rectified Activations in Convolutional Network*. 2015. DOI: 10.48550/ARXIV.1505.00853. URL: https://arxiv.org/abs/1505.00853 (cited on page 74).

[148] Andrew L. Maas. 'Rectifier Nonlinearities Improve Neural Network Acoustic Models'. In: 2013 (cited on page 74).

[149] Nitish Srivastava et al. 'Dropout: A Simple Way to Prevent Neural Networks from Overfitting'. In: *Journal of Machine Learning Research* 15.56 (2014), pp. 1929–1958 (cited on page 75).

[150] Sergey Ioffe and Christian Szegedy. *Batch Normalization: Accelerating Deep Network Training by Reducing Internal Covariate Shift*. 2015. DOI: 10.48550/ARXIV.1502.03167. URL: https://arxiv.org/abs/1502.03167 (cited on page 75).

[151] Rich Caruana, Steve Lawrence, and C. Giles. 'Overfitting in Neural Nets: Backpropagation, Conjugate Gradient, and Early Stopping.' In: vol. 13. Jan. 2000, pp. 402–408 (cited on page 75).

[152] Pierre Baldi et al. 'Parameterized neural networks for high-energy physics'. In: *The European Physical Journal C* 76.5 (2016). DOI: 10.1140/epjc/s10052-016-4099-4 (cited on pages 75, 98).

[153] Aishik Ghosh, Benjamin Nachman, and Daniel Whiteson. 'Uncertainty-aware machine learning for high energy physics'. In: *Physical Review D* 104.5 (2021). DOI: 10.1103/physrevd.104.056026 (cited on page 75).

[154] Rene Brun and Fons Rademakers. 'ROOT — An object oriented data analysis framework'. In: *Nuclear Instruments and Methods in Physics Research Section A: Accelerators, Spectrometers, Detectors and Associated Equipment* 389.1 (1997). New Computing Techniques in Physics Research V, pp. 81–86. DOI: https://doi.org/10.1016/S0168-9002(97)00048-X (cited on page 76).

[155] A. Hoecker et al. *TMVA - Toolkit for Multivariate Data Analysis*. 2007. DOI: 10.48550/ARXIV.PHYSICS/0703039. URL: https://arxiv.org/abs/physics/0703039 (cited on page 76).

[156] F. Pedregosa et al. 'Scikit-learn: Machine Learning in Python'. In: *Journal of Machine Learning Research* 12 (2011), pp. 2825–2830 (cited on page 76).

[157] Tianqi Chen and Carlos Guestrin. 'XGBoost'. In: *Proceedings of the 22nd ACM SIGKDD International Conference on Knowledge Discovery and Data Mining*. ACM, 2016. DOI: 10.1145/2939672.2939785 (cited on pages 76, 77).

[158] Yoav Freund and Robert E Schapire. 'A Decision-Theoretic Generalization of On-Line Learning and an Application to Boosting'. In: *Journal of Computer and System Sciences* 55.1 (1997), pp. 119–139. DOI: https://doi.org/10.1006/jcss.1997.1504 (cited on page 77).

[159] Glen Cowan et al. 'Asymptotic formulae for likelihood-based tests of new physics'. In: *The European Physical Journal C* 71.2 (2011). DOI: 10.1140/epjc/s10052-011-1554-0 (cited on page 78).

[160] Lorenzo Moneta et al. *The RooStats Project*. 2010. DOI: 10.48550/ARXIV.1009.1003. URL: https://arxiv.org/abs/1009.1003 (cited on page 78).

[161] Thomas Junk. 'Confidence level computation for combining searches with small statistics'. In: *Nuclear Instruments and Methods in Physics Research Section A: Accelerators, Spectrometers, Detectors and Associated Equipment* 434.2 (1999), pp. 435–443. DOI: https://doi.org/10.1016/S0168-9002(99)00498-2 (cited on page 79).

[162] ATLAS Collaboration. 'Search for charged Higgs bosons decaying via $H^{\pm} \to \tau\nu$ in $t\bar{t}$ events using pp collision data at $\sqrt{s} = 7$ TeV with the ATLAS detector'. In: *Journal of High Energy Physics* 2012.6 (2012). DOI: 10.1007/jhep06(2012)039 (cited on page 83).

[163] ATLAS Collaboration. 'Search for charged Higgs bosons through the violation of lepton universality in tt events using pp collision data at 7 TeV with the ATLAS experiment'. In: *Journal of High Energy Physics* 2013.3 (2013). DOI: 10.1007/jhep03(2013)076 (cited on page 83).

[164] ATLAS Collaboration. 'Search for charged Higgs bosons decaying via $H^{\pm} \to \tau\nu$ in fully hadronic final states using pp collision data at $\sqrt{s} = 8$ TeV with the ATLAS detector'. In: *Journal of High Energy Physics* 2015.3 (2015). DOI: 10.1007/jhep03(2015)088 (cited on page 83).

[165] CMS Collaboration. 'Search for a light charged Higgs boson in top quark decays in pp collisions at $\sqrt{s} = 7$'. In: *Journal of High Energy Physics* 2012.7 (2012). DOI: 10.1007/jhep07(2012)143 (cited on page 83).

[166] CMS Collaboration. 'Search for a charged Higgs boson in pp collisions at $\sqrt{s} = 8$ TeV'. In: *Journal of High Energy Physics* 2015.11 (2015). DOI: 10.1007/jhep11(2015)018 (cited on page 83).

[167] ATLAS Collaboration. 'Search for charged Higgs bosons decaying via $H^{\pm} \to \tau\nu$ in the τ+jets and τ+lepton final states with 36 fb^{-1} of pp collision data recorded at $\sqrt{s} = 13$ TeV with the ATLAS experiment'. In: *Journal of High Energy Physics* 2018.9 (2018). DOI: 10.1007/jhep09(2018)139 (cited on page 83).

[168] ATLAS Collaboration. 'Search for a light charged Higgs boson in the decay channel $H^{\pm} \to cs$ in $t\bar{t}$ events using pp collisions at $\sqrt{s} = 7$ TeV with the ATLAS detector'. In: *The European Physical Journal C* 73.6 (2013). DOI: 10.1140/epjc/s10052-013-2465-z (cited on page 83).

[169] ATLAS Collaboration. 'Search for a light charged Higgs boson decaying to cs in pp collisions at $\sqrt{s} = 8$ TeV'. In: *Journal of High Energy Physics* 2015.12 (2015), pp. 1–37. DOI: 10.1007/jhep12(2015)178 (cited on page 83).

[170] ATLAS Collaboration. 'Search for a charged Higgs boson decaying to charm and bottom quarks in proton-proton collisions at $\sqrt{s} = 8$ TeV'. In: *Journal of High Energy Physics* 2018.11 (2018). DOI: 10.1007/jhep11(2018)115 (cited on page 83).

[171] ATLAS Collaboration. *Search for a light charged Higgs boson in $t \to H^+b$ decays, with $H^+ \to cb$, in the lepton+jets final state in proton-proton collisions at $\sqrt{s} = 13$ TeV with the ATLAS detector*. Geneva, 2021. URL: http://cds.cern.ch/record/2779169 (cited on page 83).

[172] ATLAS Collaboration. 'Search for charged Higgs bosons in the $H^{\pm} \to tb$ decay channel in pp collisions at $\sqrt{s} = 8$ TeV using the ATLAS detector'. In: *Journal of High Energy Physics* 2016.3 (2016). DOI: 10.1007/jhep03(2016)127 (cited on page 83).

[173] A. M. Sirunyan et al. 'Search for a charged Higgs boson decaying into top and bottom quarks in events with electrons or muons in proton-proton collisions at $$ \sqrt{\mathrm{s}} $$ = 13 TeV'. In: *Journal of High Energy Physics* 2020.1 (2020). DOI: 10.1007/jhep01(2020)096 (cited on page 83).

[174] ATLAS Collaboration. 'Search for charged Higgs bosons decaying into a top and a bottom quark in the all-jet final state of pp collisions at $\sqrt{s}$ = 13 TeV'. In: *Journal of High Energy Physics* 2020.7 (2020). DOI: 10.1007/jhep07(2020)126 (cited on page 83).

[175] ATLAS Collaboration. 'Search for a Charged Higgs Boson Produced in the Vector-Boson Fusion Mode with Decay $H^{\pm} \rightarrow W^{\pm}Z$ using pp Collisions at $\sqrt{8}$ = 8 TeV with the ATLAS Experiment'. In: *Physical Review Letters* 114.23 (2015). DOI: 10.1103/physrevlett.114.231801 (cited on page 83).

[176] ATLAS Collaboration. 'Search for Charged Higgs Bosons Produced via Vector Boson Fusion and Decaying into a Pair of W and Z Bosons Using pp Collisions at $\sqrt{s}$ = 13 TeV.' In: *Physical Review Letters* 119.14 (2017). DOI: 10.1103/physrevlett.119.141802 (cited on page 83).

[177] ATLAS Collaboration. 'Search for dijet resonances in events with an isolated charged lepton using $\sqrt{s}$ = 13 TeV proton-proton collision data collected by the ATLAS detector'. In: *Journal of High Energy Physics* 2020.6 (2020). DOI: 10.1007/jhep06(2020)151 (cited on page 83).

[178] ATLAS Collaboration. 'Search for charged Higgs bosons decaying into a top quark and a bottom quark at 13 TeV with the ATLAS detector'. In: *Journal of High Energy Physics* 2021.6 (2021), p. 145. DOI: 10.1007/JHEP06(2021)145 (cited on page 83).

[179] ATLAS Collaboration. *Combination and summary of ATLAS dark matter searches using 139 fb-1 of 13 TeV pp collision data and interpreted in a two-Higgs-doublet model with a pseudoscalar mediator*. Geneva, 2021. URL: https://cds.cern.ch/record/2777863 (cited on pages 83, 127).

[180] CERN. *CERN Yellow Reports: Monographs, Vol 2 (2017): Handbook of LHC Higgs cross sections: 4. Deciphering the nature of the Higgs sector*. en. 2017. DOI: 10.23731/CYRM-2017-002. URL: https://e-publishing.cern.ch/index.php/CYRM/issue/view/32 (cited on pages 83, 109, 110, 156).

[181] ATLAS Collaboration. *Studies on top-quark Monte Carlo modelling for Top2016*. Geneva, 2016. URL: https://cds.cern.ch/record/2216168 (cited on pages 88, 90).

[182] Rikkert Frederix, Emanuele Re, and Paolo Torrielli. 'Single-top t-channel hadroproduction in the four-flavour scheme with POWHEG and aMCatNLO'. In: *Journal of High Energy Physics* 2012.9 (2012). DOI: 10.1007/jhep09(2012)130 (cited on page 88).

[183] Eric Laenen Stefano Frixione et al. 'Single-top hadroproduction in association with W boson'. In: *Journal of High Energy Physics* 2008.07 (2008), pp. 029–029. DOI: 10.1088/1126-6708/2008/07/029 (cited on pages 88, 90, 109, 155).

[184] Abdesslam Arhrib et al. 'A Guidebook to Hunting Charged Higgs Bosons at the LHC'. In: *Frontiers in Physics* 8 (2020). DOI: 10.3389/fphy.2020.00039 (cited on page 87).

[185] Céline Degrande et al. 'Heavy charged Higgs boson production at the LHC'. In: *Journal of High Energy Physics* 2015.10 (2015), p. 145. DOI: 10.1007/JHEP10(2015)145 (cited on page 87).

[186] Martin Flechl et al. 'Improved cross-section predictions for heavy charged Higgs boson production at the LHC'. In: *Phys. Rev. D* 91 (7 2015), p. 075015. DOI: 10.1103/PhysRevD.91.075015 (cited on pages 87, 125).

[187] Stefan Dittmaier et al. 'Charged-Higgs-boson production at the LHC: Next-to-leading-order supersymmetric QCD corrections'. In: *Phys. Rev. D* 83 (5 2011), p. 055005. DOI: 10.1103/PhysRevD.83.055005 (cited on page 87).

[188] Edmond L Berger et al. 'Associated production of a top quark and a charged Higgs boson'. In: *Phys. Rev. D* 71 (11 2005), p. 115012. DOI: 10.1103/PhysRevD.71.115012 (cited on page 87).

[189] A. G. Akeroyd and et al. 'Prospects for charged Higgs searches at the LHC'. In: *The European Physical Journal C* 77.5 (2017), p. 276. DOI: 10.1140/epjc/s10052-017-4829-2 (cited on page 89).

[190] Tanju Gleisberg and Stefan Höche. 'Comix, a new matrix element generator'. In: *Journal of High Energy Physics* 2008.12 (2008), pp. 039–039. DOI: 10.1088/1126-6708/2008/12/039 (cited on page 91).

[191] F. Cascioli, P. Maierhöfer, and S. Pozzorini. 'Scattering Amplitudes with Open Loops'. In: *Phys. Rev. Lett.* 108 (11 2012), p. 111601. DOI: 10.1103/PhysRevLett.108.111601 (cited on page 91).

[192] Ansgar Denner, Stefan Dittmaier, and Lars Hofer. 'Collier: A fortran-based complex one-loop library in extended regularizations'. In: *Computer Physics Communications* 212 (2017), pp. 220–238. DOI: https://doi.org/10.1016/j.cpc.2016.10.013 (cited on page 91).

[193] S Schumann and F Krauss. 'A parton shower algorithm based on Catani-Seymour dipole factorisation'. In: *Journal of High Energy Physics* 2008.03 (2008), pp. 038–038. DOI: 10.1088/1126-6708/2008/03/038 (cited on page 91).

[194] ATLAS Collaboration. *Improvements in $t\bar{t}$ modelling using NLO+PS Monte Carlo generators for Run2*. Geneva, 2018. URL: https://cds.cern.ch/record/2630327 (cited on page 95).

[195] ATLAS Collaboration. 'Measurements of top-quark pair single- and double-differential cross-sections in the all-hadronic channel in pp collisions at 13 TeV using the ATLAS detector'. In: *Journal of High Energy Physics* 2021.1 (2021), p. 33. DOI: 10.1007/JHEP01(2021)033 (cited on page 95).

[196] ATLAS Collaboration. 'Measurement of the Inelastic Proton-Proton Cross Section at $\sqrt{s} = 13$ TeV with the ATLAS Detector at the LHC'. In: *Phys. Rev. Lett.* 117 (18 2016), p. 182002. DOI: 10.1103/PhysRevLett.117.182002 (cited on page 105).

[197] 'Jet energy scale and resolution measured in proton-proton collisions at $\sqrt{s} = 13$ TeV with the ATLAS detector'. In: (July 2020) (cited on page 105).

[198] ATLAS Collaboration. 'Determination of jet calibration and energy resolution in proton–proton collisions at $\sqrt{s} = 8$ TeV using the ATLAS detector'. In: *The European Physical Journal C* 80.12 (2020). DOI: 10.1140/epjc/s10052-020-08477-8 (cited on page 105).

[199] Enrico Bothmann, Marek Schönherr, and Steffen Schumann. 'Reweighting QCD matrix-element and parton-shower calculations'. In: *The European Physical Journal C* 76.11 (2016), p. 590. DOI: 10.1140/epjc/s10052-016-4430-0 (cited on page 105).

[200] 'Electron and photon performance measurements with the ATLAS detector using the 2015–2017 LHC proton-proton collision data'. In: *Journal of Instrumentation* 14.12 (2019), P12006–P12006. DOI: 10.1088/1748-0221/14/12/p12006 (cited on page 107).

[201] 'Muon reconstruction performance of the ATLAS detector in proton–proton collision data at $\sqrt{s} = 13$ TeV'. In: *The European Physical Journal C* 76.5 (2016). DOI: 10.1140/epjc/s10052-016-4120-y (cited on page 107).

[202] Stefano Carrazza Jon Butterworth et al. 'PDF4LHC recommendations for LHC Run II'. In: *Journal of Physics G: Nuclear and Particle Physics* 43.2 (2016), p. 023001. DOI: 10.1088/0954-3899/43/2/023001 (cited on page 107).

[203] M. Beneke et al. 'Hadronic top-quark pair production with NNLL threshold resummation'. In: *Nuclear Physics B* 855.3 (2012), pp. 695–741. DOI: 10.1016/j.nuclphysb.2011.10.021 (cited on page 108).

[204] Matteo Cacciari et al. 'Top-pair production at hadron colliders with next-to-next-to-leading logarithmic soft-gluon resummation'. In: *Physics Letters B* 710.4-5 (2012), pp. 612–622. DOI: 10.1016/j.physletb.2012.03.013 (cited on page 108).

[205] Peter Bärnreuther, Michał Czakon, and Alexander Mitov. 'Percent-Level-Precision Physics at the Tevatron: Next-to-Next-to-Leading Order QCD Corrections to $q\bar{q} \to t\bar{t} + X$'. In: *Physical Review Letters* 109.13 (2012). DOI: 10.1103/physrevlett.109.132001 (cited on page 108).

[206] Michal Czakon and Alexander Mitov. 'NNLO corrections to top-pair production at hadron colliders: the all-fermionic scattering channels'. In: *Journal of High Energy Physics* 2012.12 (2012). DOI: 10.1007/jhep12(2012)054 (cited on page 108).

[207] Michal Czakon and Alexander Mitov. 'NNLO corrections to top pair production at hadron colliders: the quark-gluon reaction'. In: *Journal of High Energy Physics* 2013.1 (2013). DOI: 10.1007/jhep01(2013)080 (cited on page 108).

[208] Michał Czakon, Paul Fiedler, and Alexander Mitov. 'Total Top-Quark Pair-Production Cross Section at Hadron Colliders Through $\mathcal{O}(\alpha_S^4)$'. In: *Physical Review Letters* 110.25 (2013). DOI: 10.1103/physrevlett.110.252004 (cited on page 108).

[209] Michał Czakon and Alexander Mitov. 'Top++: A program for the calculation of the top-pair cross-section at hadron colliders'. In: *Computer Physics Communications* 185.11 (2014), pp. 2930–2938. DOI: 10.1016/j.cpc.2014.06.021 (cited on page 108).

[210] *ATLAS-CMS recommended predictions for single-top cross sections*. URL: https://twiki.cern.ch/twiki/bin/view/LHCPhysics/SingleTopRefXsec (cited on page 109).

[211] A. D. Martin et al. 'Uncertainties on α_S in global PDF analyses and implications for predicted hadronic cross sections'. In: *The European Physical Journal C* 64.4 (2009), pp. 653–680. DOI: 10.1140/epjc/s10052-009-1164-2 (cited on page 109).

[212] M. Aliev et al. 'HATHOR–HAdronic Top and Heavy quarks crOss section calculatoR'. In: *Computer Physics Communications* 182.4 (2011), pp. 1034–1046. DOI: 10.1016/j.cpc.2010.12.040 (cited on page 109).

[213] P. Kant et al. 'HatHor for single top-quark production: Updated predictions and uncertainty estimates for single top-quark production in hadronic collisions'. In: *Computer Physics Communications* 191 (2015), pp. 74–89. DOI: 10.1016/j.cpc.2015.02.001 (cited on page 109).

[214] Risto Raitio and Walter W. Wada. 'Higgs-boson production at large transverse momentum in quantum chromodynamics'. In: *Phys. Rev. D* 19 (3 1979), pp. 941–944. DOI: 10.1103/PhysRevD.19.941 (cited on page 109).

[215] W. Beenakker et al. 'NLO QCD corrections to $t\bar{t}H$ production in hadron collisions'. In: *Nuclear Physics B* 653.1 (2003), pp. 151–203. DOI: https://doi.org/10.1016/S0550-3213(03)00044-0 (cited on page 109).

[216] S. Dawson et al. 'Associated Higgs boson production with top quarks at the CERN Large Hadron Collider: NLO QCD corrections'. In: *Physical Review D* 68.3 (2003). DOI: 10.1103/physrevd.68.034022 (cited on page 109).

[217] Yu Zhang et al. 'QCD NLO and EW NLO corrections to $t\bar{t}H$ production with top quark decays at hadron collider'. In: *Physics Letters B* 738 (2014), pp. 1–5. DOI: 10.1016/j.physletb.2014.09.022 (cited on page 109).

[218] S. Frixione et al. *Electroweak and QCD corrections to top-pair hadroproduction in association with heavy bosons*. 2015. DOI: 10.48550/ARXIV.1504.03446. URL: https://arxiv.org/abs/1504.03446 (cited on page 109).

[219] John M. Campbell and R. Keith Ellis. '$t\bar{t}W^{\pm}$ production and decay at NLO'. In: *Journal of High Energy Physics* 2012.7 (2012). DOI: 10.1007/jhep07(2012)052 (cited on page 110).

[220] ATLAS Collaboration. *Multi-Boson Simulation for 13 TeV ATLAS Analyses*. Geneva, 2016. URL: https://cds.cern.ch/record/2119986 (cited on page 110).

[221] J. Alwall et al. 'The automated computation of tree-level and next-to-leading order differential cross sections, and their matching to parton shower simulations'. In: *Journal of High Energy Physics* 2014.7 (2014). DOI: 10.1007/jhep07(2014)079 (cited on page 110).

[222] Rikkert Frederix, Davide Pagani, and Marco Zaro. 'Large NLO corrections in ttW and tttt hadroproduction from supposedly subleading EW contributions'. In: *Journal of High Energy Physics* 2018.2 (2018). DOI: 10.1007/jhep02(2018)031 (cited on page 110).

[223] S. Heinemeyer, W. Hollik, and G. Weiglein. 'FeynHiggs: a program for the calculation of the masses of the neutral -even Higgs bosons in the MSSM'. In: *Computer Physics Communications* 124.1 (2000), pp. 76–89. DOI: 10.1016/s0010-4655(99)00364-1 (cited on page 125).

[224] S. Heinemeyer, W. Hollik, and G. Weiglein. 'The masses of the neutral CP-even Higgs Bosons in the MSSM: Accurate Analysis at the Two-Loop Level.' In: *The European Physical Journal C* 9.2 (1999), pp. 343–366. DOI: 10.1007/s100529900006 (cited on page 125).

[225] G. Degrassi et al. 'Towards high-precision predictions for the MSSM Higgs sector'. In: *The European Physical Journal C* 28.1 (2003), pp. 133–143. DOI: 10.1140/epjc/s2003-01152-2 (cited on page 125).

[226] T. Hahn et al. 'High-precision predictions for the light CP-even Higgs Boson Mass of the MSSM'. In: *Physical Review Letters* 112.14 (2014). DOI: 10.1103/physrevlett.112.141801 (cited on page 125).

[227] Meikel Frank et al. 'The Higgs boson masses and mixings of the complex MSSM in the Feynman-diagrammatic approach'. In: *Journal of High Energy Physics* 2007.02 (2007), pp. 047–047. DOI: 10.1088/1126-6708/2007/02/047 (cited on page 125).

[228] Henning Bahl and Wolfgang Hollik. 'Precise prediction for the light MSSM Higgs-boson mass combining effective field theory and fixed-order calculations'. In: *The European Physical Journal C* 76.9 (2016). DOI: 10.1140/epjc/s10052-016-4354-8 (cited on page 125).

[229] Henning Bahl et al. 'Reconciling EFT and hybrid calculations of the light MSSM Higgs-boson mass'. In: *The European Physical Journal C* 78.1 (2018). DOI: 10.1140/epjc/s10052-018-5544-3 (cited on page 125).

[230] Abdelhak Djouadi et al. 'HDECAY: Twenty++ years after'. In: *Computer Physics Communications* 238 (2019), pp. 214–231. DOI: 10.1016/j.cpc.2018.12.010 (cited on page 125).

[231] A. Djouadi, J. Kalinowski, and M. Spira. 'HDECAY: a program for Higgs boson decays in the Standard Model and its supersymmetric extension'. In: *Computer Physics Communications* 108.1 (1998), pp. 56–74. DOI: 10.1016/s0010-4655(97)00123-9 (cited on page 125).

[232] A. Bredenstein et al. 'Precise predictions for the Higgs-boson decay $H \to W\,W/Z\,Z \to$ 4 leptons'. In: *Physical Review D* 74.1 (2006). DOI: 10.1103/physrevd.74.013004 (cited on page 125).

[233] Axel Bredenstein et al. 'Radiative corrections to the semileptonic and hadronic Higgs-boson decays H→WW/ZZ→4 fermions'. In: *Journal of High Energy Physics* 2007.02 (2007), pp. 080–080. DOI: 10.1088/1126-6708/2007/02/080 (cited on page 125).

[234] ATLAS Collaboration. 'Search for charged Higgs bosons produced in association with a top quark and decaying via H±→τν using pp collision data recorded at $\sqrt{s}$ = 13 TeV by the ATLAS detector'. In: *Physics Letters B* 759 (2016), pp. 555–574. DOI: 10.1016/j.physletb.2016.06.017 (cited on page 125).

[235] Martin Bauer, Ulrich Haisch, and Felix Kahlhoefer. 'Simplified dark matter models with two Higgs doublets: I. Pseudoscalar mediators'. In: *Journal of High Energy Physics* 2017.5 (2017). DOI: 10.1007/jhep05(2017)138 (cited on page 127).

[236] Tomohiro Abe et al. *LHC Dark Matter Working Group: Next-generation spin-0 dark matter models*. 2018. DOI: 10.48550/ARXIV.1810.09420. URL: https://arxiv.org/abs/1810.09420 (cited on page 127).

[237] Daniel Abercrombie et al. 'Dark Matter benchmark models for early LHC Run-2 Searches: Report of the ATLAS/CMS Dark Matter Forum'. In: *Physics of the Dark Universe* 27 (2020), p. 100371. DOI: 10.1016/j.dark.2019.100371 (cited on page 127).

[238] Antonio Boveia et al. *Recommendations on presenting LHC searches for missing transverse energy signals using simplified s-channel models of dark matter*. 2016. DOI: 10.48550/ARXIV.1603.04156. URL: https://arxiv.org/abs/1603.04156 (cited on page 127).

[239] Andreas Albert et al. *Recommendations of the LHC Dark Matter Working Group: Comparing LHC searches for heavy mediators of dark matter production in visible and invisible decay channels*. 2017. DOI: 10.48550/ARXIV.1703.05703. URL: https://arxiv.org/abs/1703.05703 (cited on page 127).

[240] Tomohiro Abe, Motoko Fujiwara, and Junji Hisano. 'Loop corrections to dark matter direct detection in a pseudoscalar mediator dark matter model'. In: *Journal of High Energy Physics* 2019.2 (2019). DOI: 10.1007/jhep02(2019)028 (cited on page 127).

[241] John F. Gunion and Howard E. Haber. 'The CP-conserving two-Higgs-doublet model: the approach to the decoupling limit'. In: *Physical Review D* 67.7 (2003). DOI: 10.1103/physrevd.67.075019 (cited on page 127).

[242] ATLAS collaboration. 'Search for dark matter produced in association with a Standard Model Higgs boson decaying into b-quarks using the full Run 2 dataset from the ATLAS detector'. In: (2021). DOI: 10.1007/JHEP11(2021)209 (cited on page 128).

[243] ATLAS Collaboration. 'Search for flavour-changing neutral currents in processes with one top quark and a photon using 81 fb^{-1} of pp collisions at $\sqrt{s} = 13TeV$'. In: *Physics Letters B* 800 (2020), p. 135082. DOI: 10.1016/j.physletb.2019.135082 (cited on page 135).

[244] CMS Collaboration. 'Search for Flavor-Changing Neutral Current Interactions of the Top Quark and Higgs Boson in Final States with Two Photons in Proton-Proton Collisions at $\sqrt{s}$ = 13 TeV'. In: *Physical Review Letters* 129.3 (2022). DOI: 10.1103/physrevlett.129.032001 (cited on page 135).

[245] CMS Collaboration. 'Search for associated production of a Z boson with a single top quark and for tZ flavour-changing interactions in pp collisions at $\sqrt{s}$ = 8 TeV'. In: *Journal of High Energy Physics* 2017.7 (2017). DOI: 10.1007/jhep07(2017)003 (cited on page 135).

[246] ATLAS Collaboration. 'Search for flavour-changing neutral current top-quark decays $t \to qZ$ in proton-proton collisions at $\sqrt{s}$ = 13 TeV with the ATLAS detector'. In: *Journal of High Energy Physics* 2018.7 (2018). DOI: 10.1007/jhep07(2018)176 (cited on page 135).

[247] ATLAS Collaboration. *Search for flavor-changing neutral-current couplings between the top quark and the Z boson with LHC Run2 proton-proton collisions at $\sqrt{s} = 13$ TeV with the ATLAS detector*. Geneva, 2021. URL: http://cds.cern.ch/record/2781174 (cited on page 135).

[248] ATLAS Collaboration. 'Search for top-quark decays $t \to Hq$ with 36 fb^{-1} of pp collision data at $\sqrt{s} = 13$ TeV with the ATLAS detector'. In: *JHEP* 05 (2019), p. 123. DOI: 10.1007/JHEP05(2019)123 (cited on pages 135, 148, 170).

[249] 'Search for top quark decays via Higgs-boson-mediated flavor-changing neutral currents in pp collisions at $\sqrt{s} = 8$ TeV'. In: *Journal of High Energy Physics* 2017.2 (2017). DOI: 10.1007/jhep02(2017)079 (cited on page 135).

[250] ATLAS Collaboration. 'Search for single top-quark production via flavour-changing neutral currents at 8 TeV with the ATLAS detector'. In: *The European Physical Journal C* 76.2 (2016). DOI: 10.1140/epjc/s10052-016-3876-4 (cited on page 135).

[251] ATLAS Collaboration. 'Search for flavour-changing neutral-current interactions of a top quark and a gluon in pp collisions at $\sqrt{s} = 13$ TeV with the ATLAS detector'. In: (2021). DOI: 10.1140/epjc/s10052-022-10182-7 (cited on page 135).

[252] CMS Collaboration. 'Search for anomalous Wtb couplings and flavour-changing neutral currents in t-channel single top quark production in pp collisions at $\sqrt{s} = 8$ TeV'. In: *Journal of High Energy Physics* 2017.2 (2017). DOI: 10.1007/jhep02(2017)028 (cited on page 135).

[253] 'Search for a new scalar resonance in flavour-changing neutral-current top-quark decays $t \to qX$ ($q = u, c$), with $X \to b\bar{b}$, in proton-proton collisions at $\sqrt{s} = 13$ TeV with the ATLAS detector'. In: (Jan. 2023) (cited on page 135).

[254] Nikolaos Kidonakis. 'Two-loop soft anomalous dimensions for single top quark associated production with a W^- or H^-'. In: *Physical Review D* 82.5 (2010). DOI: 10.1103/physrevd.82.054018 (cited on page 155).

[255] Nikolaos Kidonakis. 'Next-to-next-to-leading-order collinear and soft gluon corrections for t-channel single top quark production'. In: *Physical Review D* 83.9 (2011). DOI: 10.1103/physrevd.83.091503 (cited on page 155).

[256] J. Alwall et al. 'Comparative study of various algorithms for the merging of parton showers and matrix elements in hadronic collisions'. In: (2007). DOI: 10.1140/epjc/s10052-007-0490-5 (cited on page 156).

[257] J. M. Campbell and R. K. Ellis. 'An update on vector boson pair production at hadron colliders'. In: (1999). DOI: 10.1103/PhysRevD.60.113006 (cited on page 156).

[258] 'Measurement of the $W \pm Z$ boson pair-production cross section in pp collisions at $\sqrt{s} = 13$ TeV with the ATLAS Detector'. In: *Physics Letters B* 762 (2016), pp. 1–22. DOI: 10.1016/j.physletb.2016.08.052 (cited on page 156).

[259] ATLAS Collaboration. 'Measurement of the $t\bar{t}Z$ and $t\bar{t}W$ cross sections in proton-proton collisions at $\sqrt{s} = 13$ TeV with the ATLAS detector'. In: *Physical Review D* 99.7 (2019). DOI: 10.1103/physrevd.99.072009 (cited on page 156).